Volatiles in the Moon: A sulfur and chlorine perspective

Thesis

Volatiles in the Moon:
A sulfur and chlorine perspective

Samantha Jane Faircloth
MSc, BSc (Hons), BA (Hons)

This thesis was submitted to The Open University for the degree of Doctor of Philosophy

School of Physical Sciences

February 2020

Abstract

Sulfur is a key volatile element in magmatic systems that exists in many phases (e.g. melt or gas), in multiple-oxidation states (S^{2-}, S^{4+} and S^{6+}), and has more than one stable isotope (e.g. ^{32}S and ^{34}S). Therefore, by measuring S, information regarding the conditions of a magma can be acquired. The aim of this work is to investigate what S can tell us about the behaviour of late-stage lunar basaltic magmas. An analytical protocol was developed to simultaneously measure S and Cl abundances and isotopes of lunar apatite in eleven lunar basalts with nano-scale secondary ion mass spectrometry (NanoSIMS). Additionally, a method was developed to measure the oxidation state of S in apatites of five mare basalts with X-ray absorption near-edge structure (XANES) spectroscopy at the S K-edge, making it possible to compare S oxidation state and S isotopes of lunar apatite for the first time.

Lunar apatites contain ~20–2,800 ppm S, with $\delta^{34}S$ values between -33.3 ± 3.8‰ and +36.4 ± 3.2‰ (2σ). The Cl abundance is ~350–7,230 ppm, with $\delta^{37}Cl$ values of +6.5‰ ± 0.9‰ to +36.5‰ ± 1.1‰ (2σ). All of the apatites have $S^{6+}/\Sigma S_{tot}$ ratios of >0, with average $S^{6+}/\Sigma S_{tot}$ values between 0.05 and 0.55.

An absence of correlation between S and Cl isotopes suggests a lack of evolutionary relationship between S and KREEP-rich components. The direction of S isotope fractionation, negative or positive, can be explained by degassing of H_2S and SO_2 from a relatively reduced (S^{2-}) or oxidized (SO_4^{2-}) late-stage silicate melt, respectively. The historical existence of relatively oxidized late-stage silicate melts is also evidenced by the presence of S^{6+} in lunar apatite. A positive trend is apparent between $S^{6+}/\Sigma S_{tot}$ and $\delta^{34}S$ which is indicative of the dependence of S isotope fractionation on the oxygen fugacity of the late-stage silicate melt.

Acknowledgements

I would very much like to thank my three supervisors, Mahesh Anand, Ian Franchi (The Open University) and Sara Russell (The Natural History Museum) for their time, guidance and for all of the opportunities that they have made available to me throughout my PhD. The ideas and proposals that I suggested throughout the research project (the majority of which were not planned at the beginning of the PhD) have been welcomed and encouraged (obviously after much scrutiny!). My supervisors ensured that there were no obstacles to the research that I wanted to do and had every faith in me, for which I am very grateful.

The most staggering commitment came from Mahesh, Ian and Richard C. Greenwood who took it in turns to travel to and work with me at Diamond Light Source (DLS), staying conscious until the small hours (4am was the record) to ensure that we made the most of the beamtime. A special thanks go to Richard who made an additional trip to collect some extra samples at the last hour. I would also like thank Tina Geraki (DLS) for her continual support during and long after the experiments at beamline I18.

A big thanks goes to Xuchao Zhao for endless hours of technical training and support with the nano-scale secondary ion mass spectrometer (NanoSIMS) at The Open University. Patience and cheerfulness are definitely good traits to have when using the NanoSIMS. I thank Pete Landsberg for all of the little bits and pieces and tinkering that he has done in the labs for me over the course of my project. Thank you also to Diane Johnson (previously of The Open University) for comprehensive scanning electron microscopy (SEM) training at the outset of my project.

Finally, I thank all of the people around me who have supported me and put up with me for the last three years and five months. I'm sure it cannot have been easy!

Statement of original authorship

All of the primary research presented in this PhD thesis is original and has not been submitted for a previous degree course or for publication in a peer-reviewed scientific journal.

Table of contents

List of figures

List of tables

List of acronyms

BSE	Backscatter electron
BSE	Bulk silicate Earth
BSM	Bulk silicate Moon
CDT	Canyon Diablo troilite
CAPTEM	Curation and Analysis Planning Team for Extraterrestrial Materials
CL	Cathodoluminescence
CPS	Counts per second
CRE	Cosmic ray exposure
EBSD	Electron backscatter diffraction
EDS	Energy dispersive X-ray spectroscopy
EM	Electron multipliers
EMG	Exponentially modified Gaussian
EPMA	Electron probe microanalysis
EXAFS	Extended X-ray absorption fine structure
FAN	Ferroan anorthosite
FC	Faraday cup
FMQ	Fayalite-magnetite-quartz
HSE	Highly siderophile elements
IAEA	International Atomic Energy Agency
IMB	Impact melt breccia
IMF	Instrument mass fractionation
IPA	Isopropanol
IW	Iron-wüstite
KREEP	Potassium, rare earth elements, phosphorus
LHB	Late Heavy Bombardment
LMO	Lunar magma ocean
LSPET	Lunar Samples Preliminary Examination Team
MI	Melt inclusions
MORB	Mid-ocean ridge basalt
MRP	Mass resolving power
NAM	Nominally anhydrous minerals
NanoSIMS	Nano-scale secondary ion mass spectrometry
NASA	National Aeronautics and Space Administration
PPM	Parts per million
PPB	Parts per billion
REE	Rare earth elements

ROI	Region of interest
SAU	Sayh al Uhaymir
SCSS	Sulfur concentration at sulfide saturation
SE	Secondary electron
SEI	Secondary electron image
SEM	Scanning electron microscope
SIMS	Secondary ion mass spectrometry
SMOC	Standard mean ocean chloride
V-CDT	Vienna-Canyon Diablo troilite
VHK	Very high potassium
WDS	Wavelength dispersive spectrometry
XANES	X-ray absorption near-edge structure
XRF	X-ray fluorescence

List of mineral abbreviations

Ap	Apatite
Badd	Baddeleyite
Cpx	Clinopyroxene
Crst	Cristobalite
Csp	Chromite spinel
Ilm	Ilmenite
K-spar	Potassium feldspar
Merr	Merrillite
Ol	Olivine
Plg	Plagioclase
Px	Pyroxene
Sym	Symplectite
Trd	Tridymite
Troi	Troilite
Trq	Tranquillityite
Usp	Ulvöspinel

Chapter One:

Introduction

Prior to 1969, very little was known about the formation and history of the Moon. In the last fifty years, since the return of lunar samples to Earth by the Luna and Apollo programmes, we now have a far greater understanding of the evolution of the Moon. Whilst there is still much to learn and many of the scientific ideas (particularly how the Moon formed) are still hotly debated, we now have a better understanding of how and when the Moon might have formed, how it became so heavily cratered, what its chemical composition is, whether it is a differentiated body, whether it has (or ever had) plate tectonics, whether it is still volcanically active and whether it ever experienced magmatism. Based on the lunar sample analysis of the last twenty years, this chapter introduces some of these ideas and goes on to describe how volatile elements of lunar magmas have been used to address some of the important lunar scientific questions.

1.1. Moon formation

There are four main historical theories of lunar formation. The first involves the suggestion that a segment of molten mass separated away from a rapidly rotating, large, molten proto-Earth (the fission hypothesis) which eventually formed the Moon (Darwin 1879). The second theory proposes that a body that formed elsewhere in the Solar System was gravitationally captured by the proto-Earth (Gerstenkorn, 1955; Wood, 1986). The third theory advocates a binary co-accretion, whereby the Earth and Moon formed alongside one another (Schmidt, 1959). All of these pre-Apollo theories have shortfalls when it comes to explaining the observed physical and chemical properties of the Earth-Moon system such as the Earth-Moon angular momentum (de Meijer et al., 2013), the contrasting densities (the Moon is iron-depleted) and the similar Earth-Moon isotopic signatures of oxygen (Wiechert et al., 2001; Hallis et al., 2010; Young et al., 2016), silicon (Armytage et al., 2012), chromium (Bonnand et al., 2016), titanium (Zhang et al., 2012), zirconium (Akram and Schönbächler, 2016) and tungsten (Touboul et al., 2007, 2015; Kruijer et al., 2015; Kruijer and Kleine, 2017).

The fourth theory involving a collision between a Mars-sized planetesimal (known as Theia) and the proto-Earth, whereby material ejected from the proto-Earth was flung into Earth's orbit before accreting to form the Moon (Hartmann and Davis, 1975; Cameron and Ward, 1976), has stood the test of time for explaining Earth-Moon angular momentum if a low velocity, oblique impact is assumed (Canup, 2004). If the ejected material is predominantly from the proto-Earth's mantle then there is also an explanation as to why compositional similarities are seen for the Earth and Moon (Ćuk and Stewart, 2012).

Previous hydrodynamic simulations show that the Moon should be derived primarily from impactor material and not proto-Earth material (Canup and Asphaug, 2001; Canup 2004; 2008). Compositional similarities can still be justified if the Earth and Moon were derived from a chemically related reservoir, meaning that they would have formed close to one another within the inner Solar System (Wiechert et al., 2001; Dauphas et al., 2014; Akram and Schönbächler, 2016). However, Ćuk and Stewart (2012) suggested that a giant impact involving a very fast spinning proto-Earth (resulting from a previous large impact), involving high collisional angular momentum, could account for chemical similarities because the model demonstrates that more proto-Earth material would have been ejected to

form a proto-lunar disc, with significantly less impactor material needed in the disc to eventually form the Moon.

A theory that justified the current isotopic similarity (specifically, oxygen isotope similarities) between the Earth and Moon which still allowed a giant impact was proposed by Pahlevan and Stevenson (2007), whereby the impactor and the proto-Earth initially had *distinct* isotopic compositions. Following the giant impact, melting of the silicate proto-Earth formed a deep magma ocean whilst, at the same time, lunar-forming material established itself as a magma disc surrounding the proto-Earth. The proto-Earth and proto-Moon were connected by a disc of vaporised material that was turbulently mixed by heat (released from the energy of the impact) and, therefore, permitted post-impact equilibration of the Earth's mantle with the proto-lunar disc which accounts for the observed similar isotopic compositions between the Earth and Moon. The cooling timescale for condensation of the silicate atmosphere following the giant impact was calculated to be 3,000 years and 100–1,000 years for the Earth and the Moon, respectively (Pahlevan and Stevenson, 2007).

Recent oxygen isotope analyses (Young et al., 2016) have confirmed that the oxygen isotope signatures of the Earth and Moon are virtually indistinguishable. In the same vein as Pahlevan and Stevenson (2007), Young et al. (2016) suggested that oxygen isotopes were homogenised between the impactor and the proto-Earth by vigorous mixing during the high angular momentum and high-energy giant-impact. However, Herwartz et al. (2014) reported a difference of 12 ± 3 ppm in $\Delta^{17}O$ between the Earth and Moon and concluded that the small compositional difference could be explained by a carbonaceous chondrite–dominated late veneer. The $\Delta^{17}O$ distinction has not yet been fully accepted by the scientific community.

Modelling has shown that the conditions required during the giant impact: the velocity, angle and specific size of the impactor, the imparted isotopic similarities, the angular momentum and the resulting depletion of volatiles in the Moon relative to the Earth, are so specific that the probability of achieving them is very low (Rufu et al., 2017). As an alternative, Rufu et al. (2017) modelled multiple (~20) proto-Earth impacts (Figure 1.1) from objects of 0.01 to 0.1 Earth masses which would produce the Earth's current angular momentum and the Moon's current mass. Multiple impacts would allow more of the proto-

Earth's material to be released for the formation of a Moon with similar compositional characteristics.

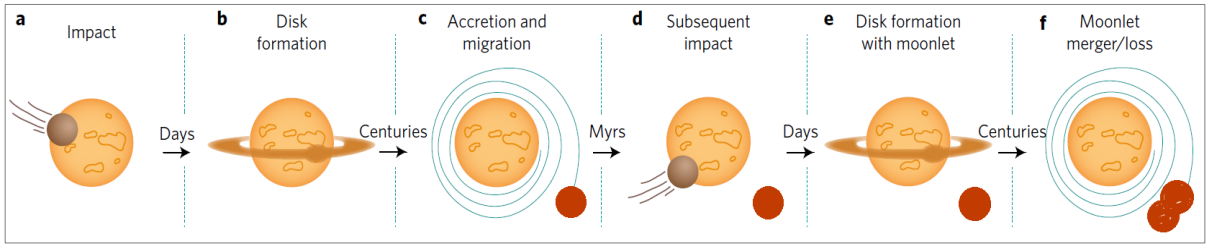

Figure 1.1. The steps involved in lunar formation involving multiple impacts to the proto-Earth. Following impact of a Moon to Mars-sized impactor (**a**), debris orbits the proto-Earth, forming a disc (**b**) which then accretes to form a 'moonlet' that begins to drift away from the proto-Earth as a result of tidal evolution (**c**). The process is repeated again after millions of years (**d**–**f**) and multiple moonlets eventually merge (**f**) to form one Moon (adapted from Rufu et al., 2017).

There was also no constraint on the angle at which the impactors could strike the proto-Earth, albeit to produce greater compositional similarities between the Earth and Moon, multiple low-angle impacts or fewer 'near' head-on impacts were required. Likewise, multiple small impacts, rather than one giant impact, were more likely to have preserved chemical heterogeneity within Earth's mantle (Rufu et al., 2017) – a property that has been suggested based on the observed differences of tungsten isotopes ($^{182}W/^{184}W$), neodymium isotopes and noble gases within deep mantle-derived terrestrial samples when compared with lunar samples (Boyet and Carlson, 2005; Mukhopadhyay, 2012; Touboul et al., 2012).

1.2. Sample return missions

Between 1969 and 1972, there were six manned sample return missions to the Moon that were part of the NASA's Apollo programme and also included Earth and Moon orbiting missions. Each Apollo mission (Apollo 11, 12, 14, 16 and 17) landed at a different location on the nearside of the Moon (the side seen from Earth) (Figure 1.2). Approximately 382 kg of lunar material, in the form of rocks, soil and core samples, was returned to Earth by the crew aboard the Apollo spacecrafts (NASA, 2016). The Soviet Luna robotic missions began in 1959, with lunar flybys and lunar landings. Between 1970 and 1976, lunar sample return missions (Luna 16, Luna 20 and Luna 24) brought ~0.3 kg of lunar soil back to Earth (NASA, 2005).

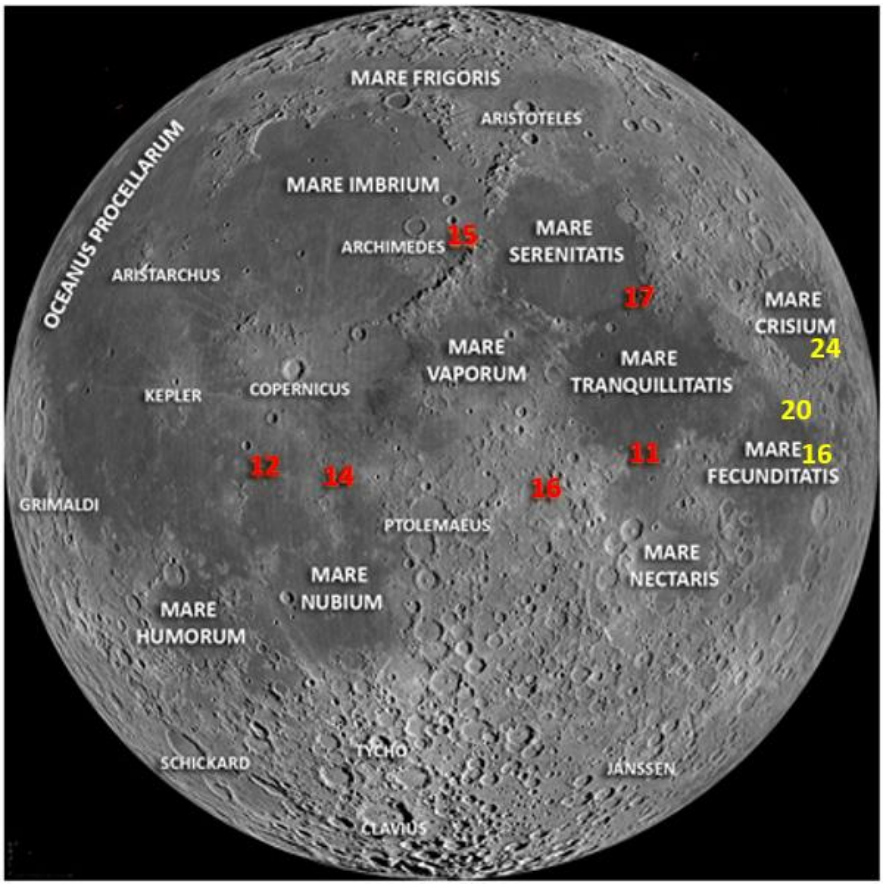

Figure 1.2. The landing sites of the lunar sample return missions. The approximate locations of the Apollo missions (red font) and the Soviet Luna missions (yellow font) are pin-pointed on the nearside of the Moon and in relation to some of the larger maria (plural for mare) (adapted from Lunar and Planetary Institute, 2018a).

All of the samples returned from the Apollo missions were categorised by the Lunar Samples Preliminary Examination Team (LSPET) and were given a five digit 'generic' number that is dependent upon such things as the Apollo mission, the location and the size of the sample. For example, to identify which mission a sample was returned from, the first one or two digits of the generic number were assigned with '10' (Apollo 11), '12' (Apollo 12), '14' (Apollo 14), '15' (Apollo 15), '6' (Apollo 16) and '7' (Apollo 17) (e.g. 10044 (for Apollo 11), 12039 (for Apollo 12), 79215 (for Apollo 17) etc.). For the Apollo 16 and 17 missions, the second digit represents the actual collection location for the sample (e.g. Apollo sample 79215 was collected at Station 9) (Vaniman et al., 1991).

For Apollo missions 15 to 17, the fifth digit is used to indicate the size of the sample (ranging from <1 mm to >10 mm) and, for lunar soils ('fines') it specifies whether it is sieved or un-sieved (e.g. a fifth digit of '1' means <1 mm sieved fraction and '5' means

>10 mm rock). Whereas, the last three digits for the Apollo 11, 12, 14 and 15 mission samples do not provide any information about the collection location or sample type (Vaniman et al., 1991).

Each sample's generic number is followed by a comma and a shorter unique number known as the 'specific' number (one to four digits long) which is used as a means to identify each subdivision (be it thin section or chip) of a particular sample (e.g. sample 79215,50 shows that there are at least 50 subdivisions of 79215, where a specific number of 0 is used for the original intact sample) (Vaniman et al., 1991).

1.3. Geological history of the Moon and lunar rock types

It has been as a direct result of the return of lunar samples from the Moon that models of Moon formation could be developed. The return of the Apollo 11 samples also led Wood et al. (1970) and Smith et al. (1970) to suggest that, following the giant Moon-forming impact, a deep, global lunar magma ocean (LMO) would have existed on the young Moon. Evidence for this came from the return of plagioclase-rich soil samples from older lunar highland terrains, which led to the suggestion that the lunar highlands could also be composed of plagioclase-rich rocks representing an early lunar crust (Grove and Krawczynski, 2009). Such primary products of crystallisation (forming the lunar crust) are recognised in the collection of samples returned from the Moon and are known as the ferroan anorthosite (FAN) suite lithologies, which are Mg-poor, Ca- and Al-rich and contain low abundances of incompatible elements (e.g. La and Th) (Warren, 1993). For plagioclase to exist in the lunar highlands, it must have floated to the surface of the LMO whilst earlier crystallising cumulates containing Fe and Mg (olivine and pyroxene) sank to form a stratified cumulate pile and an early lunar mantle (e.g. Wieczorek et al., 2006).

As crystallisation of the LMO progressed, the melt in the cumulate pile would have become more Fe-rich and, after ~90% crystallisation, titanium-bearing phases such as ilmenite ($FeTiO_3$) would have crystallised above the less dense magnesium-rich cumulates. The residual melt (1-2%) of the LMO would have been rich in incompatible elements including potassium, rare earth elements and phosphorous (KREEP) and formed a layer, known as urKREEP (Warren and Wasson, 1979), between the mantle and crust (e.g. Wieczorek et al., 2006). Rock samples from the urKREEP layer have so far not been

identified but rocks with KREEP-like components are found in most of the samples returned from the Moon, with KREEP-rich rocks having only been identified in the samples returned from the Apollo 15 mission.

The top of the cumulate pile is believed to have become unstable because of the increasing additions of later crystallised, dense Fe-bearing phases relative to the bottom of the pile. Accordingly, it has been suggested that there was an overturn event, whereby the later crystallised ilmenites and urKREEP layer would have sunk through the cumulate pile, leading to mixing with, and the ascension of, Mg-rich olivine and pyroxene cumulates (Ringwood and Kesson 1976; Hess and Parmentier, 1995; Elkins-Tanton et al., 2002, 2011). Magnesium-rich (Mg-suite) lithologies, including dunites, troctolites and norites that also contain high levels of KREEP-components have been identified in the Apollo sample collection and are believed to have formed as a result of primitive Mg-rich magmas (i.e. from decompression melting of the rising Mg-rich cumulate pile) interacting with and assimilating the urKREEP layer (Shearer and Papike, 2005). The third 'pristine', non-mare rock of the lunar highlands is the alkali-suite lithologies which are distinguished from the Mg-suite lithologies by their higher alkali (e.g. sodium and potassium) and La and Th contents and include gabbronorites, quartz monzodiorites, granitic rocks (Papike et al., 1998). It is suggested that there is a link between the alkali-suite lithologies and the magmas that formed KREEP-rich basalts, e.g. through fractional crystallisation of the magma (e.g. Wieczorek et al., 2006).

Early studies of the Apollo samples showed signs of historic impact cratering events which included alteration and impact shock metamorphism. It was suggested that, at ~3.9 Ga (Tera et al., 1974), there was a late heavy bombardment (LHB) (e.g. Norman, 2009) which delivered material to the Moon in the form of asteroids (predominantly) and comets (Bottke et al., 2010; Joy et al., 2012). The LHB is thought to have been responsible for the creation of most of the large basins on the Moon (Kring and Cohen, 2002).

The main focus of this study is the Apollo mare basalt rocks. The lunar highlands crust is thought to be up to ~4.6 Ga old, whereas the mare basalts are younger and fall primarily within the age range of ~3–3.9 Ga, but some rocks are as young as ~1 Ga (Hiesinger et al., 2014) and some are as old as 4.35 Ga (Terada et al., 2007; Snape et al., 2016). Mare basalts are richer in FeO than highlands lithologies and have variable TiO_2 contents, resulting in

what are known as the very low-Ti, low-Ti and high-Ti basalts, which do not appear to be defined by age of basalt crystallisation. It is suggested that mare basalts were formed by the partial melting of heterogeneous zones in the (overturned) mantle cumulate pile (e.g. Taylor, 2007; Hiesinger et al., 2014). Basalt lavas were erupted onto the lunar surface and infilled many of the impact craters/ basins. As part of the mare volcanism, picritic (ultra-mafic, Mg-rich) pyroclastic glasses, with a wide range of TiO_2 contents, were also erupted onto the lunar surface (e.g. Longhi, 1992). The glasses might have been formed by lunar fire-fountaining, similar to that seen on Earth, with the erupting magmas thought to have been >1,450 °C in temperature (~1,100 °C is typical on Earth). On contact with the cold, lunar vacuum, the liquid was quickly quenched to glass (Delano, 1986; Elkins-tanton et al., 2003).

The upper region of the lunar crust is known as the regolith and it is comprised of brecciated material and fragmented rocks of many sizes that include large boulders, cobbles and fine-grained particles of <1 cm (known as lunar soil). The regolith exists because of extensive meteorite impact (particularly during the LHB) and interaction with energetic particles such as the solar wind and cosmic galactic rays. Impact-melt rocks are also common in this surface layer that is thought to be between a few meters to twenty meters in depth (McKay et al., 1991). However, recent studies (Wiggins et al., 2019) suggest that large impactors (1-10 km in diameter) can fragment the lunar crust to depths of ~20 km.

1.4. Lunar volatiles

The volatility of elements within the Solar System is determined by the temperature at which they condense or vaporize. Elements classified as volatile have relatively low condensation temperatures, whereas elements classified as refractory have relatively high condensation temperatures and condensed out of the solar nebula later than the more volatile elements (Pendred and Williams, 1968). Elemental volatility is determined experimentally, commonly at pressures of $\sim 10^{-4}$ bar, and results in either a total condensation or a 50% condensation temperature (Lodders, 2003).

The study of lunar volatiles (volatile source, delivery mechanism, timing and abundance) can be used in combination with new and existing data for other inner Solar System bodies

to help solve unanswered questions regarding the origin of both volatiles and life (Anand, 2014). On the basis that volatiles (particularly water) are important for life as we know it, knowledge of their existence and the processes affecting their distribution can be used to understand when, how and why life emerged on Earth (Sarafian et al., 2014).

For the Moon, volatiles are believed to have played an important role in igneous processes such as transporting magma from depth and for determining the style of eruptions that occurred on the lunar surface (Newcombe et al., 2017). For example, lunar fire-fountaining or effusive magmatism as seen in Hawaii today is thought to have occurred on the Moon and been driven by the degassing of volatiles (Elkins-Tanton and Grove, 2011; McCubbin et al., 2015), although exactly which volatiles propelled the fire-fountaining process is debated (Elkins-Tanton et al., 2003; Elkins-Tanton and Grove, 2011; Sharp et al., 2013a). Evidence for the role of volatiles has come from the identification of relatively volatile-rich coatings of elements (e.g. S, H, Cl, F, C) on the surfaces of lunar volcanic glass beads (a product of lunar fire-fountaining (section 1.3)) (e.g. Saal et al., 2008; Ding et al., 1983).

1.4.1. Quantity and delivery of lunar volatiles

Albarède et al. (2013) has suggested that the Moon is 100 times more depleted in all volatiles when compared with the Earth. High abundances of water found in lunar volcanic glasses (Hauri et al., 2011) are thought not to be representative of the lunar interior but are a local heterogeneity found within the lunar mantle, which is otherwise a dry layer (Albarède et al., 2013; 2015). The formation of planets, via collisions and accretion, is believed to have removed most of the volatile elements from the Earth-Moon system. To account for the low abundances of volatiles, Albarède (2009) proposed that volatiles were delivered to the Earth-Moon system later in the Moon's history when material was added as a late veneer. This indeterminate period saw small additions of chondritic material, including volatiles, to the Earth and the Moon (Albarède, 2009).

Likewise, from a study of Zn abundances and isotopes of lunar basalts, Paniello et al. (2012) determined that low Zn contents and an enrichment of the heavy Zn isotope (^{66}Zn) relative to the Earth (and Mars) was due to global evaporative loss, possibly during Moon formation, leading to the suggestion that, overall, the Moon was depleted in volatiles.

However, Hauri et al. (2015) argued that the extent of volatile depletion within the bulk silicate Moon is not as high as once thought. By comparison, measurements of lunar volatiles in glasses and olivine-hosted melt inclusions have revealed lesser depletions of 2 to 10 times that of the bulk silicate Earth (BSE), leading Hauri et al. (2015) to suggest an average lunar volatile depletion factor of 0.25 times that of the BSE. One of the main questions is whether lunar volatiles were delivered and accreted before, during or after the formation of the Moon and at what stage of LMO crystallisation (Hauri et al., 2015).

It is suggested by Barnes et al. (2014) that water (volatiles) was present before the LMO fully crystallised. This suggests a delivery window of 10 Ma to 200 Ma after formation of the Moon. In addition, the similar hydrogen isotope values (section 1.5.2) for the Earth and Moon imply that volatiles existed at the time of the Moon-forming impact, which can only mean that they endured after the impact (Barnes et al., 2014).

The formation of a proto-lunar disc, consisting of ejected material from both the Earth and the impactor, was thought to have occurred over too short a timescale (centuries) for volatiles from an exogenous source to have accreted at that stage (Hauri et al., 2015). More likely, volatiles were delivered to the Moon from a heterogeneous chondritic source during the relatively large time span (~10 Ma to ~200 Ma) of LMO cooling and crystallisation. Addition of material before the creation of a hard lunar crust and lithosphere allowed volatiles to mix into the lunar interior via a process of LMO convection. This conclusion ruled out the addition of most of the Moon's volatiles during the late heavy bombardment (LHB) (~3.9 Ga) because the lunar lithosphere was in place and mantle convection had ended by the time of the LHB (Hauri et al., 2015). Tartèse and Anand (2013) also proposed that the source of lunar hydrogen was from the accretion of chondritic material, and they suggest that accretion was into the lunar interior towards the end of LMO crystallisation.

From the similarities between hydrogen, carbon and nitrogen isotopes for eucrites (stony meteorites), Earth and the Moon, Sarafian et al. (2014) concluded that all three bodies shared a common volatile source: carbonaceous chondrites. The implication of this is that the inner Solar System (including the asteroid belt) is likely to have had a common volatile origin (Sarafian et al., 2014; Barrett et al., 2016). A shared origin for volatiles within the Earth-Moon system from a chondritic source is an argument that is gaining strength within

the lunar scientific community (Saal et al., 2013; Tartèse and Anand, 2013; Tartèse et al., 2013; Füri et al., 2014).

A more recent study highlights the need for water to have already been present in the LMO as it crystallised (Lin et al., 2017) and suggests that the Moon was wet from the start. Based on high pressure and high temperature experiments to simulate LMO crystallisation, Lin et al. (2017) showed that in order to achieve an average lunar crustal thickness of ~34–43 km (based on NASA's Gravity Recovery and Interior Laboratory (GRAIL) gravity measurements), the LMO needed to have contained >500 ppm water or >1,800 ppm water if the LMO was shallow or deep, respectively, to form a plagioclase and quartz crust of the currently observed thickness.

1.4.2. Sulfur behaviour during Moon formation and evolution

The global-scale evaporation in the immediate aftermath of the Moon's formation has left the Moon sulfur-depleted relative to the bulk silicate Earth (BSE) (e.g. Day and Moynier, 2014). Whilst sulfur (S) is a chalcophile element (forming sulfides) (Day and Moynier, 2014), it also displays moderately siderophile behaviour, whereby it readily forms bonds with metallic iron (Jana and Walker, 1997). Steenstra et al. (2017a) proposed that S-depletion in the lunar mantle relative to the BSE is not caused by evaporative loss during the Moon's formation but is, in fact, because of the role it played during core-mantle differentiation of the Moon. This involved the loss of S to the lunar core by $FeS_{(liquid)}$ exsolution and segregation ($Fe^{2+} + S^{2-} \leftrightarrow FeS_{(liquid)}$), which occurs when a silicate liquid becomes supersaturated in S (Morbidelli et al., 2018) when the almost, to completely, molten Moon (LMO) was undergoing differentiation (Steenstra et al., 2017a). The high pressure metal-silicate partition experiments carried out by Steenstra et al. (2017a), using synthetic analogues of Apollo 15 glasses, demonstrated very good agreement between the required partition coefficients and the experimentally determined partition coefficients, suggesting that the abundance of S in the bulk silicate Moon (BSM) represented metal-silicate equilibration (i.e. core-mantle equilibration). Accordingly, Steenstra et al. (2017a) suggested that very little S was lost by degassing during the Moon forming event.

Previous density experiments involving lunar seismic data have estimated the S content of the core to be between 0-8 wt.% (Weber et al. 2011; Antonangeli et al. 2015). However,

using high pressure metal-silicate partition experiments, Steenstra et al. (2017b) demonstrated that <0.16 wt.% S existed in the Moon's core (if ~71–116 ppm S was assumed for the BSM) and that carbon was the dominant light element. Even if higher BSM values (~300 ppm S) were used, <0.16 wt.% S was still estimated to be in the lunar core. Assuming that there was some equilibration of S between the core and mantle, low S abundance in the core might reflect low S abundance in the lunar mantle. Therefore, only very minor S degassing (<10%, as per Wing and Farquhar, 2015) occurred during the Moon forming event with the majority of S being lost to the core during core-mantle differentiation process (Steenstra et al., 2017a, 2017b).

It is possible that $FeS_{(liquid)}$ exsolution and segregation within the remaining LMO could have continued after lunar core formation was completed (Morbidelli et al., 2018). Sulfur is an incompatible element in the silicate melt and would, therefore, have become enriched in the residual silicate melt as crystallisation of the LMO proceeded. When the S abundance in the residual silicate melt exceeded the sulfur concentration at sulfide saturation (SCSS), it is likely that FeS began to exsolve and segregate to become positioned, alongside the late-crystallising ilmenite-bearing cumulate layer, at the top of the lunar mantle. The lunar mantle overturn event is suggested to have mobilised the segregated FeS, causing it to sink to deep mantle regions (Morbidelli et al., 2018).

Based on similar metal-silicate partitioning experiments, it was suggested by Labidi et al. (2013, 2014) that core-mantle differentiation within the Earth caused a fractionation of S isotopes, whereby ^{34}S entered the core and ^{32}S became enriched in the mantle. Whilst not demonstrated, it was suggested that the core-mantle differentiation process might have involved the dissolution of S^0 (metallic form of S) rather than an exsolution/ segregation of FeS^{2-} sulfide. The dissolution would lead to a fractionation due to the different S molecular environments in a silicate melt and a metallic liquid. Compounds with a relatively high oxidation state (S^0 in this case) become more enriched in ^{34}S compared with those with a relatively low oxidized state (here, S^{2-}). The Earth's depleted mantle is ^{32}S-enriched with a S isotope value of $-1.28 \pm 3.3‰$, which led Labidi et al. (2103) to conclude that ^{34}S was removed to the core. The Moon's bulk mantle is thought to be slightly ^{34}S-enriched ($0.58 \pm 0.05‰$) (Wing and Farquhar, 2015) (see section 1.6.2), which might be a reflection of the different core-mantle formation process suggested for the Moon that involves FeS exsolution and segregation (e.g. Steenstra et al., 2017a; Morbidelli et al., 2018).

1.4.3. Chondritic delivery of sulfur

Whilst the timing of delivery of chondritic material to the Moon is debated – whether shortly after the giant impact when the LMO was cooling and crystallising (Hauri et al., 2015) or subsequent to LMO crystallisation (Morbidelli et al., 2018), ~0.1–0.4% lunar masses of chondritic material (Hauri et al., 2015), comprising 0.02–0.05% lunar masses of highly siderophile elements (HSEs) (e.g. platinum, palladium, iridium), were delivered (e.g. Day et a., 2007; Steenstra et al., 2017a; Morbidelli et al., 2018). Due to their chalcophile behaviour, HSEs can be lost to the lunar core alongside S because they preferentially partition into an FeS liquid rather than a silicate liquid. Consequently, the current HSE abundances in the lunar mantle may be a reflection of the amount of chondritic material that was delivered to the Moon after lunar core formation (Morbidelli et al., 2018). By extension, a portion of the S abundance and, therefore, the S isotope signature of the lunar mantle may reflect that of the chondritic material delivered after core formation.

Based on estimates of 0.2% lunar masses of chondritic material delivered after core formation and an initial abundance of ~300 ppm S, metal-silicate partition coefficient experiments of S by Morbidelli et al. (2018) demonstrated that ~350 ppm S would have been in the LMO following the chondritic delivery of ~180 ppm S. This estimate is slightly higher than the ~58 ppm S and ~64 ppm S estimated to have been delivered by H chondrites and CM2 chondrites, respectively, based on an initial abundance of ~250 ppm S for the bulk Moon and 0.05% lunar mass delivered (Steenstra et al., 2017a). Whilst the chondritic delivery of S, according to Steenstra et al. (2017a), is unlikely to have had a significant effect on lunar S abundance, the isotope signature of the lunar mantle may represent a combination of core-mantle differentiation process and the subsequent delivery of S to the Moon (e.g. Labidi et al., 2014; Labidi and Cartigny, 2016).

1.5. Previous laboratory analyses of lunar volatiles

1.5.1. Chlorine in lunar samples

Chlorine (Cl) is moderately to highly volatile (50% condensation temperature: 948 K), lithophile element and behaves incompatibly during partial melting (Day and Moynier, 2014). The Cl isotope composition is measured in terms of the relative abundance of its two stable isotopes, ^{35}Cl and ^{37}Cl, and is reported as $\delta^{37}Cl$, where $\delta^{37}Cl = ((^{37}Cl/^{35}Cl_{sample}/ ^{37}Cl/^{35}Cl_{SMOC}) -1) \times 1000$, and where SMOC is the 'standard mean ocean chloride'. Chlorine isotope studies indicate that the Moon has an unusually large range of $\delta^{37}Cl$ values when compared with other Solar System materials such as Earth and carbonaceous chondrites (e.g. Sharp et al. 2007, 2010b, 2013; Barnes et al., 2008, 2009), Mars (Williams et al., 2016; Sharp et al., 2016) (Figure 1.3). Terrestrial $\delta^{37}Cl$ values for mantle-derived materials closely straddle 0‰ (Sharp et al. 2013), with variations between –2.6‰ and +3.0‰ (Barnes et al., 2008, 2009) attributed to secondary processes (hydrothermal alteration), analytical errors and poor reproducibility (Barnes et al., 2009). Whereas, the $\delta^{37}Cl$ of lunar apatites is reported to lie between ~-4‰ and ~+80‰ in mare basalts, KREEP-rich basalts, highlands samples (impact breccias, Mg-suite and alkali-suite rocks), regolith breccias and lunar meteorites (e.g. Sharp et al., 2010a; Tartèse et al., 2014b; Treiman et al., 2014; Boyce et al., 2015; Barnes et al., 2016, 2019; Potts et al., 2018; Wang et al., 2019).

Apatite, the mineral analysed in this study, is a late-stage crystallising igneous mineral which has the ability to hold volatile elements within its crystal lattice, with an idealised chemical formula of: $Ca_5(PO_4)_3(F,Cl,OH)$ (Papike et al. 1991). As a result, and being a ubiquitous accessory mineral in lunar rocks, it has been targeted for measuring water and other volatiles (e.g. Cl and F) in lunar samples. The proportion of the three anions (F^-, Cl^-, OH^-) held within the anion site (*X*-site) of the apatite's crystallographic structure needs to be approximately equal to 1 (Hughes et al., 1990; Pyle 2002).

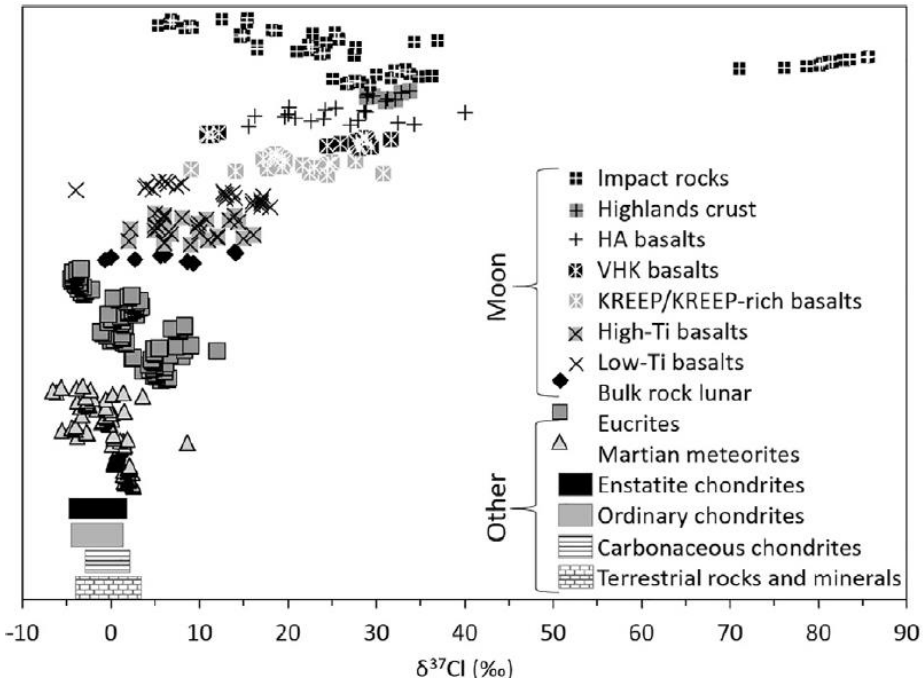

Figure 1.3. A comparison of $\delta^{37}Cl$ for Solar System materials. An increasing $\delta^{37}Cl$ trend can be seen from the bottom to the top of the graph with lunar materials, particularly KREEP-rich, highlands and impact rock samples, having far heavier $\delta^{37}Cl$ values when compared with different types of meteorites and terrestrial materials (after Barnes et al., 2019).

Sharp et al. (2010a) measured Cl isotopes for a range of glasses, apatites, bulk-rock mare basalts and soils from Apollo 11, 12, 15, 16 and 17 mission locations. Gas source mass spectrometry was used to determine Cl isotope ratios and abundances of water-soluble leachates and silicate residues from the basalts and glasses, whilst *in situ* analyses of the apatite grains were completed with secondary ion mass spectrometry (SIMS). The results revealed great variation with $\delta^{37}Cl$ values ranging from –0.7‰ to +24.5‰. There was no obvious correlation between $\delta^{37}Cl$ values and Cl abundance. Relatively heavy $\delta^{37}Cl$ values between +2‰ and +18‰ were also reported for apatites of mare basalts by Boyce et al. (2015) (also using SIMS). A positive correlation was highlighted between $\delta^{37}Cl$ and Cl abundance and it was proposed that if volatile degassing were the only process involved in Cl isotope fractionation, a negative correlation should have arisen in which reduction of Cl abundance would have led to an increase of $\delta^{37}Cl$ because the lighter ^{35}Cl would have been lost (Boyce et al., 2015).

Barnes et al. (2016) studied the apatites of mare basalts, KREEP-rich basalts and highlands rocks and reported $\delta^{37}Cl$ values of +2.2‰ to +36.3‰. The heaviest $\delta^{37}Cl$ values were found in apatites of highlands rocks (25.1‰ to +36.3‰), with the lightest $\delta^{37}Cl$ values

being found in mare basalts (+2.2‰ to +16.1‰). The KREEP-rich basalts had $\delta^{37}Cl$ values between those of the highlands and the mare basalt apatites (+14.1‰ to +33.8‰) (Barnes et al., 2016). Similar values of +7.4‰ to +19.4‰ were also derived by Barnes et al. (2019) for apatites of mare basalts.

Sharp et al. (2010a) suggested that the process of Cl isotopic fractionation on the Moon was unique in that the relative enrichment of ^{37}Cl relative to other Solar System materials was due to isotopic fractionation during degassing within a *virtually* anhydrous environment sustaining a H/Cl ratio of <1. As on Earth, the lighter ^{35}Cl isotope is preferentially lost to the vapour phase during degassing but, unlike the hydrous Earth where the H/Cl ratio is positive and a HCl gas is expected, the anhydrous volatile chloride species on the Moon was a form of metal chloride (e.g. NaCl and $ZnCl_2$) (Sharp et al., 2010a). On Earth, the amount of ^{35}Cl lost to the vapour phase is the same as the amount of ^{37}Cl lost to the HCl gas, which means that the two 'losses' cancel each other out and leave a relative fractionation of zero. In a virtually anhydrous melt, as suggested for lunar melts by Sharp et al. (2010a), metal chlorides are the dominant species, meaning that metal chlorides are lost during degassing. This results in a loss of the lighter ^{35}Cl isotope to the vapour phase without a corresponding loss of ^{37}Cl (due to similar bonding energies in the melt and vapour phases) and, therefore, the residual melt acquires a heavy $\delta^{37}Cl$ value (Sharp et al., 2010a). However, the reasoning of Sharp et al. (2010a) is at odds with the reports of up to 6,050 ppm H_2O ppm in lunar apatites (Greenwood et al. (2011), see section 1.5.2).

Boyce et al. (2015) proposed that the relatively heavy $\delta^{37}Cl$ of apatites in high and low-Ti basalts was derived much earlier in the Moon's history by metal chloride degassing (^{35}Cl loss) from the residual LMO. However, the metal chloride degassing invoked by Boyce et al. (2015) would have occurred before a crustal lid formed across the LMO, allowing degassed vapours to condense and rain straight back into the LMO, reversing any isotopic fractionation caused by evaporation (Barnes et al., 2016).

An alternative explanation for H_2O-rich contents along with heavy $\delta^{37}Cl$ values for lunar highlands and KREEP basalt apatites relies on degassing metal chlorides from a >95% crystallised LMO and a not yet solidified urKREEP layer (Barnes et al., 2016). The urKREEP layer is thought to be Cl-enriched (1,100 ppm to 1,350 ppm Cl) because it

contains the majority of incompatible lithophile volatiles that would have remained in the residual LMO melt following the early crystallisation of olivine and pyroxene (e.g. McCubbin et al., 2015). Degassing of ~80% of the initial Cl content from a deep and exposed (following giant bolide impacts) Cl-enriched urKREEP layer would have left the residual urKREEP layer ^{37}Cl-enriched (δ^{37}Cl value of ~+30‰) (Barnes et al., 2016). It was suggested by Barnes et al. (2016) that degassing of metal chlorides from urKREEP could have occurred simultaneously with the degassing of H_2O in the form of HCl and/ or H_2 based on low (pre-degassed) hydrogen isotope estimates for H_2O within urKREEP.

Evidence for interaction with the ^{37}Cl-enriched urKREEP layer came from a positive correlation between the δ^{37}Cl of apatite and bulk-rock KREEP-related incompatible trace elements (e.g. La, Sm, K and Th). Apatites of highlands samples and KREEP basalts have relatively high δ^{37}Cl and high abundances of bulk-rock trace elements, suggesting interaction with a KREEP-rich (^{37}Cl-rich) source. Whereas, apatites of mare basalts with relatively low δ^{37}Cl values have comparably low bulk-rock incompatible trace element abundances, implying less interaction with a KREEP-rich reservoir (Barnes et al., 2016, 2019).

In summary, apatites in highlands samples show enrichments of incompatible trace elements and KREEP-rich components characteristic of the urKREEP layer (e.g. ^{37}Cl-rich). Whereas, apatites of mare basalts encountered variable degassing of ^{35}Cl during basalt volcanism on the lunar surface and may have undergone some mixing between basalt source regions (Cl-poor) and varying quantities of urKREEP (Cl-rich) (e.g. Boyce et al, 2018; Barnes et al., 2016, 2019). KREEP-rich basalts are believed to have acquired a mixture of the two δ^{37}Cl signatures (highlands and mare basalts) (e.g. McCubbin et al., 2015) from the assimilation or modification of KREEP-rich material at their mantle source regions, and from degassing during eruption at the lunar surface (e.g. Tartèse et al., 2014a; Barnes et al., 2016).

Following the investigation of apatites in five Apollo 14 high-Al samples (including three basalts and two impact melt samples), Potts et al. (2018) reported very variable δ^{37}Cl values between +14.6 ± 1.6‰ and +40.0 ± 2.9‰ and Cl abundances between 580 ppm Cl and 16,149 ppm Cl. Unlike the study of Barnes et al. (2016), a positive trend was not observed between δ^{37}Cl and rare earth elements (REEs), which led to the suggestion that a

secondary process must have contributed to the Cl isotope fractionation. This involved a combination of degassing of the lighter ^{35}Cl isotope and variable interaction between a Cl-rich vapour phase and the late-stage melt. Such interaction required that there was wide-spread fumarolic activity on the nearside of the Moon at ~4 Ga which led to varying degrees of metasomatism in the studied Apollo 14 samples. Some apatites crystallised before and some after vapour phase interaction, which resulted in heterogeneous $\delta^{37}Cl$ values and Cl abundances. The Cl-rich vapour phase was produced either by an impact event and a corresponding ejecta blanket or by a lava flow – both of which could have heated the immediate region beneath, initiating the release of vapours and permitting interaction with the crystallising rock (Potts et al., 2018).

Metasomatism resulting from the transportation of element-carrying vapours through the crust and regolith was also proposed by Treiman et al. (2014) for feldspathic granulitic impactite sample 79215. An impact event was suggested to have caused the brecciated nature of the sample and, at the same time, drove the mobile vapour through the near-surface of the Moon (Treiman et al., 2014). Sample 79215 is depleted in K and REEs, whilst at the same time it has a KREEPy signature with high abundances of P, Cl and F and a heavy $\delta^{37}Cl$ value of +32.7 ±1.6‰. Treiman et al. (2014) suggested that the mobile vapour was initially derived from a KREEPy source but it subsequently underwent 'elemental fractionation' where P, Cl and F were added to the apatite but, as the vapour moved through cracks within the original granulitic protolith, 'KREE-' was carried away from the apatite to be deposited elsewhere.

In order to confirm whether the Cl isotopic fractionation process occurred prior to or during the crystallisation of the parental magma, Stephant et al. (2019) analysed silicate-hosted (olivine and pyroxene) melt inclusions (MIs) to provide information about the pre-eruptive volatile signature of a magma. From the measurement of MIs in five Apollo mare basalts, the $\delta^{37}Cl$ values of the olivine-hosted MIs were reported to be between 6.6 ± 9.0‰ and 17.1 ± 3.7‰, whereas the (relatively later crystallising) pyroxene-hosted MIs have $\delta^{37}Cl$ values between 4.5 ± 4.6‰ and 33.4 ± 4.2‰. Stephant et al. (2019) concluded that no significant Cl isotopic fractionation occurred in the melt of mare basalts subsequent to the entrapment of the MIs in the phenocrysts, be it during either further crystallisation of the magma or eventual eruption of the basalts onto the lunar surface. The Cl isotopic signature of the Moon, therefore, was acquired during the earliest stages of LMO

evolution. The Apollo 14 sample studied may, however, have been an exception where the late-stage crystallising apatite might have recorded further Cl isotopic fractionation caused by metasomatism (e.g. Potts et al., 2018).

1.5.2. Hydrogen in lunar samples

In the immediate decades following the manned Apollo missions and the robotic Luna missions to the Moon, the dominant view was that the Moon had no indigenous water (H_2O or OH). There were no water-bearing silicate minerals such as amphibole and mica within the returned lunar samples and any rare appearances of apatite were found only to contain Cl and F but not water (OH) within their crystal structures. Likewise, oxide minerals (such as the hydrated iron ore mineral limonite) were found to be completely lacking (Papike et al. 1999).

Based on the measurement of H_2O abundance and hydrogen isotopes of lunar soils and breccias, it was concluded that hydrogen was not indigenous to the Moon but, instead, had a solar wind origin. The very light hydrogen isotope values of H_2 and H_2O abundances were believed to have been inherited from the solar wind or from contamination by terrestrial meteoric waters (Epstein and Taylor, 1970; Epstein and Taylor, 1973), respectively. However, it was suggested that relatively heavy hydrogen isotope values that were observed might have been due to interactions with carbonaceous chondrite debris (Epstein and Taylor, 1973). In a review by Taylor et al. (2006), the Moon was described as being "bone-dry" and, whilst allowing for the possibility of water-ice trapped in the south polar region, the bulk Moon was said to contain <1 ppb H_2O.

However, studies published within the last decade have made use of instruments with better detection limits and have demonstrated that Apollo samples do contain measurable amounts of water (as H, H_2O or OH). Analyses of volcanic glass beads, melt inclusions, nominally anhydrous minerals (NAMs) and apatites within mare basalts, highlands rocks and KREEP basalts have confirmed the existence of significant quantities (thousands of ppm) of water (H or H_2O or OH) (e.g. Saal et al., 2008; Boyce et al., 2010; Greenwood et al., 2011; Hauri et al., 2011; Liu et al., 2012a; Hui et al., 2013; Tartèse et al., 2013, 2014a; Barnes et al., 2013, 2014, 2019, Mills et al., 2016; Robinson et al., 2016).

The study of Saal et al. (2008) reported, for the first time, absolute abundances of H_2O in Apollo 15 and 17 lunar pyroclastic glass, with very-low-Ti green glasses containing ~0.5–30 ppm H_2O, low-Ti yellow glasses containing ~20–45 ppm H_2O and high-Ti orange glasses containing ~5–15 ppm H_2O. Alongside S, Cl and F, a single very low-Ti glass bead showed H_2O to decrease from core to rim (30 ppm down to ~15 ppm H_2O) suggesting an indigenous H_2O origin and a subsequent process of volatile partial degassing. The inter-glass bead variations of H_2O was attributed to differences in the original volatile content and different degrees of volatile degassing (Saal et al., 2008)

Following the pioneering study of Saal et al. (2008), measurable quantities of water has also been detected in Apollo lunar apatites (~20–6,050 ppm H_2O) (Boyce et al., 2010; Greenwood et al., 2011; Tartèse et al., 2013, 2014a; Barnes et al., 2013, 2014, 2019; Robinson et al., 2016), melt inclusions (~270–1,200 ppm H_2O) (Hauri et., 2011) and nominally anhydrous minerals ((NAMs) such as olivine, pyroxene and feldspar) (~3 ppm to ~35 ppm H_2O) (Liu et al., 2012a; Hui et al., 2013, 2015; Mills et al., 2016).

The H isotopic composition of many lunar materials (mare basalt bulk-rocks, bulk soil and regolith breccias, apatites, volcanic glasses, NAMS (Epstein and Taylor 1970, 1971, 1972, 1973; Friedman et al. 1970, 1971; Merlivat et al. 1974a, 1974b, 1976; Hashizume et al., 2000; Greenwood et al., 2011; Liu et al., 2012b; Saal et al., 2013; Tartèse et al., 2013; Barnes et al., 2013, 2014, 2019; Robinson et al., 2016) has been used to ascertain the origin of lunar water and is reported in terms of the deuterium-hydrogen ratio (D/H) (expressed as δD, where $\delta D = ((D/H_{sample} / D/H_{SMOW}) - 1) \times 1000$ and SMOW is 'standard mean ocean water').

As the most common hydrous mineral phase, capable of holding OH within its crystallographic structure, apatite is a frequently targeted mineral for H isotopic measurements. Greenwood et al. (2011) reported the δD value of apatites in mare basalts and a highlands alkali anorthosite for the first time. The mare basalt apatites have heavier δD values from +391‰ to +1010‰, whereas the highlands apatites have lighter δD values of +240‰ to +340‰. Greenwood et al. (2011) suggested that a lack of correlation between OH and δD for the mare basalts was an indication that degassing had not occurred. Instead, the relatively high δD signatures had been derived from a lunar reservoir that had received

delivery of D-rich material from comets which have higher δD values. The lower δD of the highlands sample was thought to reflect that of the indigenous lunar interior reservoir.

According to Barnes et al. (2013), D-enrichment by the addition of cometary material to mare basalts (Greenwood et al., 2011) was unlikely because such additions have been too small to make any notable difference. According to Tartèse and Anand (2013) and Barnes et al. (2014), the mare basalt source region would have been chondritic, following the late addition of H from a chondritic source, not long after the formation of the Moon. The higher OH content and D/H ratios observed within the apatites of mare basalts, when compared with apatites of highlands (Greenwood et al., 2011; Barnes et al., 2014) and KREEP-related rocks (Tartèse et al., 2014b), might have been caused by simultaneous degassing and fractional crystallisation during eruption which acted to increase both the initial chondritic δD signature and the OH content (Tartèse and Anand, 2013). The lighter δD of apatites in lunar highlands rocks has is attributed to a lack of significant degassing, due to their igneous intrusive origin (Barnes et al., 2014).

The use of lunar apatites for studying the abundances of H, Cl and F in their parental melts has been called into question by Boyce et al. (2014) on the basis that the crystallographic site (*X*-site) of apatite that contains these three components does so in proportions that do not represent the proportions of H, Cl and F contained within the magma at the time of apatite crystallisation. The proportion of the three components held within the anion site (the *X*-site) needs to be approximately equal to 1, where F enters the *X*-site first until it is exhausted, followed by Cl and then by H (Boyce et al., 2014). As a result, it was suggested that fractionally crystallised apatite cannot be used to represent the true value of H_2O that once existed within the melt prior to crystallisation (Boyce et al., 2014).

Anand (2014) pointed out that apatite is still a useful indicator for determining water contents of mare basalt source regions as long as the textural context of the apatite is understood. Apatites which have undergone equilibrium crystallisation have been studied and are capable of recording the water contents of the melt at the time of crystallisation. Whilst apatite is a late stage crystallisation product, its use to determine the water contents of a melt can be supplemented with earlier crystallising melt inclusions, glasses and nominally anhydrous minerals (NAMs) (Anand, 2014).

1.6. Sulfur in magmas

1.6.1. Sulfur abundance of lunar samples

Sulfur is highly volatile (50% condensation temperature of 664 K), chalcophile and exists as a sulfide under reducing conditions (Day and Moynier, 2014). The primary phase of lunar sulfur is the mineral troilite (FeS), with minor and very rare phases including chalcopyrite ($CuFeS_2$), cubanite ($CuFe_2S_3$), pentlandite ($(Fe,Ni)_9S_8$), mackinawite ($Fe_{1+x}S$), sphalerite ((Zn,Fe)S) and bornite (Cu_5FeS_4) (Haskin and Warren, 1991).

There are measurable amounts of sulfur (~550 ppm to ~2,130 ppm S) in bulk-rock Apollo mare basalts (e.g. Thode and Rees, 1971, 1972; Rees and Thode, 1972, 1974; Gibson and Moore, 1974; Des Marais, 1983; Wing and Farquhar, 2015), approximately twice as much as the average terrestrial MORB contents (~730 ppm S to ~1220 ppm S) (Labidi et al., 2012). In addition, sulfur abundance has been measured in volcanic glass beads (~110 ppm to ~580 ppm S) (Ding et al., 1983; Saal et al., 2008), lunar soils (up to ~830 ppm S) (Kerridge et al., 1975a, 1975b), melt inclusions (360 ppm to 1,900 ppm S) (Bombardieri et al., 2005; Hauri et al., 2011; Chen et al., 2015a) and lunar apatite grains (~100 ppm S to 600 ppm S) (Boyce et al., 2010; Greenwood et al., 2011; Treiman et al., 2014).

The sulfur abundance of lunar pyroclastic glass beads contained within Apollo 15 and 17 soil samples was measured by Saal et al. (2008). The very low-Ti glasses were reported to have abundances between ~110 ppm S and ~270 ppm S, the low-Ti glasses have between ~520 ppm S and ~580 ppm S and the high-Ti glasses have between ~280 ppm S and ~490 ppm S. There was no apparent correlation of S and Ti content. The variable S contents between glass beads was attributed to differences in the original volatile content of S and to different degrees of S degassing experienced during rapid quenching. In addition, S abundance measurements across a single volcanic glass bead revealed a decrease of S from core to rim (Figure 1.4) of ~18% (262 ppm S to 216 ppm S). Saal et al. (2008) suggested that the S profile was evidence of an indigenous S origin and subsequent S loss during partial degassing.

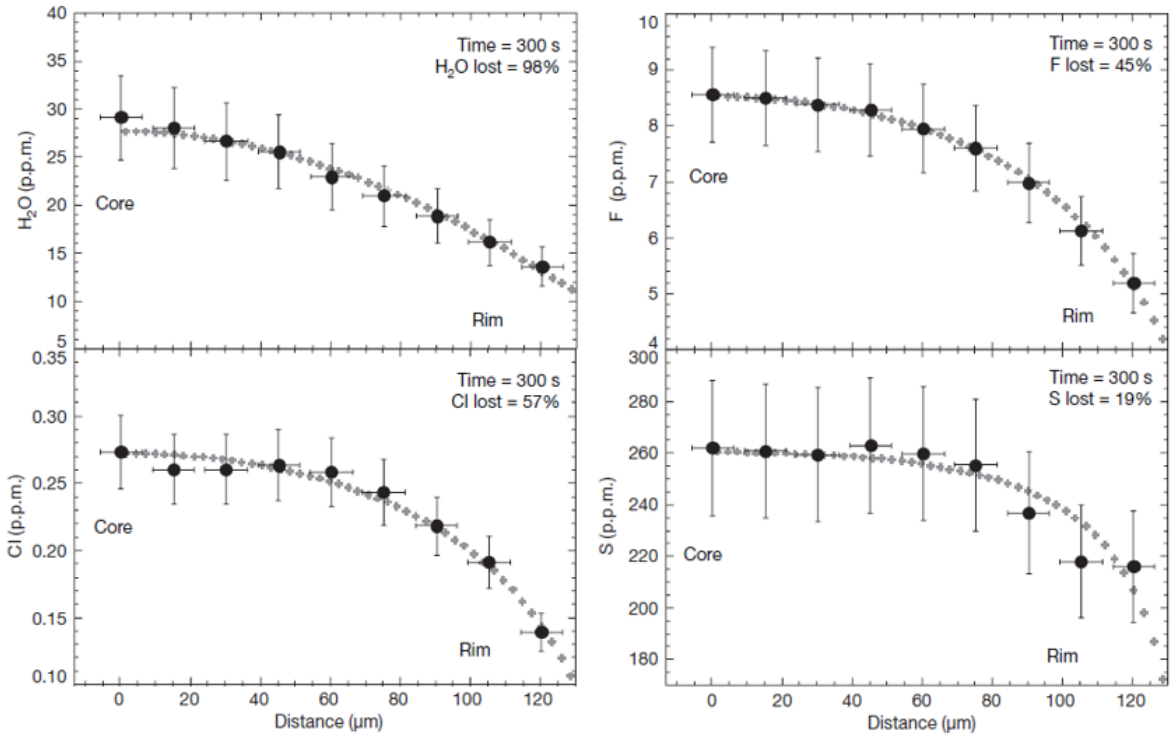

Figure 1.4. Single lunar glass bead volatile abundance as a function of core-to-rim distance. An obvious decline can be seen in the abundances of H_2O, F, Cl and S from core to rim in the very low-Ti glass bead, demonstrating the effects of degassing indigenous volatiles. The black circles are the measured data (with error bars representing 2 standard deviation), whereas the grey diamonds represent the diffusive loss model. (From Saal et al., 2008).

To remove the effects of magmatic degassing during eruption, Hauri et al. (2011) measured the S abundance of pre-eruptive olivine-hosted melt inclusions (MIs) contained within the same Apollo 17 soil sample analysed by Saal et al. (2008). The MIs were reported to contain 612–877 ppm S which was higher than the S content of the glass beads (Saal et al., 2008). Hauri et al. (2011) concluded that S abundance (along with other measured volatiles e.g. H_2O and F) of the MIs was very similar to pristine terrestrial MORB MIs, providing evidence for a reservoir within the interior of the Moon containing volatile contents that are similar to the Earth's upper mantle. By studying olivine-hosted MIs of Apollo 12 picritic basalts (Mg-rich), Bombardieri et al. (2005) reported abundances of ~500–1,200 ppm S that were similar to the findings of Hauri et al. (2011). The S content of the parental (primary) magma was calculated to have contained between ~700 ppm S and 1,200 ppm S. By way of comparison, the S abundance of the mid-ocean ridge basalt (MORB) source region is ~146 ppm S (Saal et al., 2002).

Boyce et al. (2010) measured the S, Cl and H abundances of apatite grains in a mare basalt (Apollo sample 14053) and discovered a positive correlation between S and Cl contents, although S and Cl did not correlate with H abundance. With reported abundances of ~310–460 ppm S, Boyce et al. (2010) concluded that the S of lunar apatites was comparable to that of terrestrial apatites. The range of S contents was higher than that reported by Treiman et al. (2014) for feldspathic granulitic impactite sample 79215, which was between ~100 ppm S and ~110 ppm S across three different apatite grains.

Sulfur abundance measurements for primary igneous highlands rocks are limited but Kerridge et al. (1975b) reported a slightly lower range of ~530–1030 ppm S when compared with mare basalts (~550–2,130 ppm S). The lowest S contents are found in highlands ferroan anorthosites, with some abundances of just 10 ppm S (Haskin and Warren, 1991).

1.6.2. Sulfur isotopes of lunar samples

The sulfur isotope composition is measured in terms of the relative abundance of its two stable isotopes, ^{34}S and ^{32}S, (with the ratio $^{34}S/^{32}S$) and is represented by $\delta^{34}S$, where $\delta^{34}S = ((^{34}S/^{32}S_{sample}/ {}^{34}S/^{32}S_{V\text{-}CDT}) - 1) \times 1000$ and where V-CDT is Vienna-Canyon Diablo troilite (an iron meteorite) (Marini et al., 2011).

On Earth, sulfur isotopes fractionate due to the constant cycling of sulfur through the Earth's geological and biogeochemical environments. The fractionation process involves hydrothermal activity and alteration at mid-ocean ridges, precipitation of sulfur ores (following interaction with saline liquids), interactions with organic matter and microbial reduction reactions of sulfide (Peters et al., 2010; White, 2013). Overall, S cycling within and on the Earth leads to a non-chondritic S isotopic signature for the Earth's silicate mantle with a slightly negative $\delta^{34}S$ value (e.g. Labidi et al., 2013) when compared with the bulk Moon (Wing and Farquhar, 2015) (Figure 1.5). Unlike Earth, microbial activity and plate tectonics are not observed on the Moon, suggesting that the causes of sulfur isotopic fractionation of lunar magmas may be related to the vaporization of sulfur by magmatic degassing (Wing and Farquhar, 2015) and/ or the presence of multi-valent phases of S. Mixing of magmas may also result in variable $\delta^{34}S$ values (e.g. Economos et al., 2017).

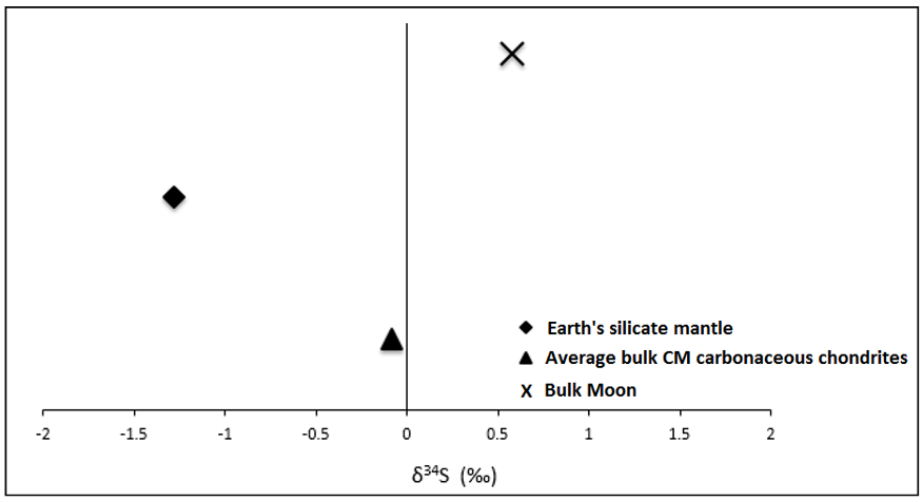

Figure 1.5. A comparison of the $\delta^{34}S$ value. The graph puts the bulk Moon $\delta^{34}S$ value into perspective with the $\delta^{34}S$ values of the Earth's silicate mantle and the average bulk CM carbonaceous chondrites. (Data from Labidi et al., 2013, 2017; Wing and Farquhar, 2015).

In some of the earlier bulk-rock sulfur isotope analyses of Apollo 12 basalts, Thode and Rees (1971) developed an acidification technique to extract sulfur and used gas-source mass spectrometry to measure four different S isotopes (^{32}S, ^{33}S, ^{34}S and ^{36}S). The authors reported relative enrichment of $\delta^{34}S$ in all (five) rock samples with a range of +0.37‰ to +0.68‰ (relative to the historically used Canyon Diablo troilite (CDT) meteorite reference standard) that was considered large enough to demonstrate considerable $\delta^{34}S$ variation within the Apollo 12 basalts. Using the same analysis method as Thode and Rees (1971), Rees and Thode (1972) reported S isotope values for Apollo 12 and Apollo 14 basalts. The $\delta^{34}S$ for the Apollo 12 basalts ranged from +0.47‰ to +0.65‰, whereas the Apollo 14 basalt produced varied values of +0.90‰ and +1.44‰. Rees and Thode (1972) also noted $\delta^{34}S$ heterogeneity within the individual Apollo 12 basalt samples and within the same basalt samples reported by Thode and Rees (1971).

Rees and Thode (1974) continued the work of Rees and Thode (1972) and investigated Apollo 16 and Apollo 17 samples with the majority of the work being focussed on lunar fines of <1 mm. The only Apollo 16 anorthosite rock analysed was the first rock reported to have a negative $\delta^{34}S$ of –0.1‰. Whilst Rees and Thode (1974) provided no interpretation of the negative result, Petrowski et al. (1974) subsequently noted a negative $\delta^{34}S$ value of –5.2‰ from an Apollo 17 anorthositic brecciated gabbro (using a method of acid hydrolysis and mass spectrometry) which they believed might either have been caused

by the addition of fractionated S from an extra-lunar source or it could have been a signal that indigenous S isotopes are more heterogeneous than previously thought.

Using a method of acid hydrolysis to measure the $\delta^{34}S$ values of fifteen Apollo 15 and 16 mare basalts, Gibson et al. (1975) reported $\delta^{34}S$ values ranging from –1.6‰ to +0.9‰, with some results found to be different from those of Rees and Thode (1974) and Petrowski et al. (1974) for the same samples. The reason for this was unknown, but Des Marais (1983) later attributed such $\delta^{34}S$ variations to discrepancies in measurement methods between different laboratories.

The S isotopes of secondary 'vein and replacement troilite (FeS)' from Apollo 16 lunar highlands clasts were measured by Shearer et al. (2012), with negative $\delta^{34}S$ values ranging from $–3.3 \pm 1.6$‰ to $–1.0 \pm 1.6$‰ (2σ) reported for the troilite (the bulk-rock $\delta^{34}S$ was $–3.4 \pm 0.6$‰ to 0‰ with 0.5–1.3 wt.% S). The $\delta^{34}S$ depletions in the troilite were attributed to an interaction between the plutonic lithologies of the shallow lunar crust and a sulfur-enriched vapour with elevated ^{32}S contents. The sulfur-rich vapour was believed to have originated from degassing of shallowly emplaced magma intrusions (possibly from Mg-suite magmatism or early-stage basaltic magmatism) or from the breakdown and evaporation of troilite within the shallow crust, possibly triggered by a crustal heat source.

Similar to troilite, volcanic orange and black glass beads collected from the Apollo 17 site are reported to have light $\delta^{34}S$ signatures (Ding et al., 1983) with values between –2.62‰ and +2.57‰. The majority of small glass grain sizes were observed to have lighter $\delta^{34}S$ values and higher S abundances when compared with the larger grain sizes. It was suggested that the glass beads were a product of lunar fire-fountaining and had undergone the preferential loss of ^{32}S to the vapour phase during extrusive volcanism. The smaller glass beads, having a larger surface area to volume ratio, experienced greater levels of ^{32}S condensation from the vapour cloud onto their surfaces as they cooled.

In a more recent study, Wing and Farquhar (2015) measured four different S isotopes (^{32}S, ^{33}S, ^{34}S and ^{36}S) of ten bulk-rock mare basalts from the Apollo 11, 12 and 17 missions, using a similar analysis method to that of Thode and Rees (1971). Finding $\delta^{34}S$ to be heterogeneous within the established CDT standard, Wing and Farquhar (2015) adopted an alternative, the Vienna-Canyon Diablo troilite (V-CDT) scale, which is now the

internationally recognised reference standard to use for S isotope analyses. The majority of lunar mare basalts measured by Wing and Farquhar (2015) have very restricted, homogeneous $\delta^{34}S$ values with a mean of +0.57 ± 0.07‰ (spanning +0.443‰ to +0.686‰). The homogeneity was despite the large range of ages, different sampling locations and estimated formation depths of the mare basalts. The bulk Moon was estimated to have a $\delta^{34}S$ value (+0.58 ± 0.05‰) that was very similar to the mare basalts.

Wing and Farquhar (2015) suggested that the reduced nature of the basaltic magma from which the mare basalts had formed meant that sulfide existed as the dominant S-bearing species in the melt. Such dominance limited the fractionation of sulfur isotopes because the existence of other S-bearing species (gases or melts) which might have promoted sulfur isotope fractionation, were in the minority. As a result, the mare basalts demonstrate a fairly uniform $\delta^{34}S$ value which has been preserved since the giant moon-forming impact (Wing and Farquhar, 2015).

Four of the ten mare basalts studied had $\delta^{34}S$ depletions (albeit still positive) relative to the mare basalt population average and were thought to have originated from a magma that contained a sulfide melt and a gaseous S-bearing phase which permitted S isotope fractionation (Wing and Farquhar, 2015). Evidence for volcanic degassing of sulfur retained in olivine melt inclusions of mare basalts, based upon the work of Bombardieri et al. (2005), was cited by Wing and Farquhar (2015) as evidence for the possible presence of a gaseous sulfur species. It was proposed that S could have been lost via COS (from a hydrogen-poor melt) or H_2S (from a hydrogen-rich melt) degassing below the lunar surface to account for the four negative $\delta^{34}S$ mare basalt values, with potentially 40–60% of S lost from either of the degassing methods to result in a $\delta^{34}S$ decrease of ≈0.2‰–0.3‰. The sulfur loss was suggested to have occurred during the magma stage which allowed the preservation of the isotopic signature after eruption onto the lunar surface (Wing and Farquhar, 2015).

When compared with the mean terrestrial MORB $\delta^{34}S$ value of −0.91 ± 0.50‰ (Labidi et al., 2012) and with the Earth's depleted mantle $\delta^{34}S$ value of −1.28 ± 0.33‰ (Labidi et al., 2013), lunar mare basalts and the bulk Moon have a relatively enriched $\delta^{34}S$ mean value. The enrichment suggests degassing and loss of ≤ ~10% S during the Earth-Moon impact-forming event (Wing and Farquhar, 2015).

Lunar soils have much heavier $\delta^{34}S$ values when compared with bulk-rocks, from which the soils are thought to have formed. For example, values between +5.3‰ and +13.5‰ have been reported (Thode and Rees, 1971; Rees and Thode, 1972, 1974; Kerridge et al., 1975a, 1975b; Kaplan et al. 1976) with the suggestion that the ^{34}S-enrichment is related to the maturity of the lunar soil and was a result of S loss and S isotope fractionation through vaporization caused by micrometeorite impacts (Kerridge et al., 1975a, 1975b).

At the time of writing, only one *in situ* lunar apatite study of sulfur isotopes is known to us. Treiman et al. (2014) used SIMS (Cameca 7f-GEO) to measure the S abundance and isotopes (along with hydrogen and chlorine abundances and isotopes) of apatites from granulite breccia 79215. The average sulfur contents from measurements of three apatite grains was 106 ± 8 ppm S, with an average $\delta^{34}S$ value from measurements of just one apatite grain of +10.5 ± 3‰. When compared with the homogeneous bulk-rock $\delta^{34}S$ value (+0.57 ± 0.07‰) of Wing and Farquhar (2015), the apatite showed considerably higher S isotope fractionation. An interpretation of the heavy $\delta^{34}S$ value was not provided.

To the best of our knowledge, only one study has been published that reports the S isotope data of terrestrial apatite and the study was not available at the time that this PhD project started (Economos et al., 2017). When compared with lunar apatites, the terrestrial apatite $\delta^{34}S$ values are exclusively positive with values between 1.0‰ and 8.5‰. The $\delta^{34}S$ range was suggested to have been caused by the presence of multiple oxidation states of sulfur (most likely S^{6+} and S^{2-}) accompanied by varying degrees of ascent-driven degassing.

1.6.3. Oxidation state of sulfur

Sulfur solubility in a magma depends on temperature, pressure, oxygen fugacity and melt composition (e.g. Carroll and Webster, 1994). The relationship between S solubility and magma oxidation state means that S predominantly dissolves as a sulfide (S^{2-}) species in reduced melts (as expected for the lunar environment, Equation 1.1) and as a sulfate (S^{6+}) species in more oxidized melts (Equation 1.2). The proportions of S^{6+} and S^{2-} in a melt are controlled by the equilibrium shown in Equation 1.3 (Fincham and Richardson, 1954; Carroll and Webster, 1994).

$$O^{2-}_{(\text{silicate melt})} + \frac{1}{2}S_{2(gas)} = \frac{1}{2}O_{2(gas)} + S^{2-}_{(\text{silicate melt})} \quad \text{Equation 1.1}$$

Where S^{2-} (sulfide) replaces O^{2-} anions in a melt/ magma.

$$\frac{3}{2}O_{2(gas)} + \frac{1}{2}S_{2(gas)} + O^{2-}_{(melt)} = SO_4{}^{2-}_{(\text{silicate melt})} \quad \text{Equation 1.2}$$

Where $SO_4{}^2$ (sulfate) replaces O^{2-} on the anion sub-lattice in a melt/ magma.

$$S^{2-}_{(\text{silicate melt})} + 2O_{2(gas)} = SO_4{}^{2-}_{(\text{silicate melt})} \quad \text{Equation 1.3}$$

Sulfur loss from lunar magmas occurs during eruption and cooling, with the amount of loss being affected by pressure, lava viscosity (Gibson et al., 1975) and impact heating (Papike et al., 1991). Sulfur gas contained within lunar magma was thought to have been historically lost as it helped to propel pyroclastic eruptions on the Moon (Papike et al., 1991) (section 1.3).

Sulfur abundance in terrestrial apatite is thought to be related to temperature, pressure, S content of the melt and oxygen fugacity (fO_2). Both increases and decreases of temperature have been cited as causes of increasing S abundance in apatite (Peng et al., 1997; Parat and Holtz, 2004; Humphreys et al., 2006; Parat et al., 2011), whereas an increase of pressure is thought to increase S abundance (Peng et al., 1997; Carroll and Rutherford, 1985). Increasing fO_2 and/ or higher levels of S content in the melt lead to increased S abundance in apatite (Peng et al., 1997; Streck and Dilles, 1998; Parat and Holtz, 2004; Parat et al., 2011).

For terrestrial apatites, two possible S substitution reactions (Equations 1.4 and 1.5) involving phosphorous (P) are thought to occur (Peng et al., 1997) at the tetrahedral (*T*) cation site (Hughes and Rakovan, 2015) of the apatite crystallographic structure:

$$S^{6+} + Si^{4+} \leftrightarrow 2P^{5+} \quad \text{Equation 1.4}$$

and

$$S^{6+} + Na^{+} \leftrightarrow P^{5+} + Ca^{2+} \quad \text{Equation 1.5}$$

However, these occur under more oxidising conditions where SO_3 contents are relatively high (e.g. Peng et al., 1997). For lunar apatites, it was suggested by Boyce et al. (2010) that, under the reducing conditions of the lunar environment, S within a melt that coexisted with apatite should have been in a sulfide form (S^{2-}). Boyce et al. (2010) speculated that S^{2-} might be incorporated into the *X*-site (the anion column) of the apatite crystallographic structure. This suggestion has so far only been synthesized in a laboratory and has not been seen in nature (Henning et al., 2000).

Recent work (Konecke et al., 2017a) has demonstrated experimentally that S^{6+} can exist alongside dominant S^{2-} in the apatite crystallographic structure under relatively reduced conditions (fayalite-magnetite-quartz (FMQ)). By positioning an electron beam parallel to or perpendicular to the c-axis of the experimentally crystallised apatite, Konecke et al. (2017a) observed S^{6+} at different orientations to S^{2-} and concluded that they were held in different crystallographic sites. Thermodynamic modelling has also shown that S^{2-} might be stable in the *X*-site of apatite (Kim et al., 2017).

1.7. Research justification

Sulfur is a key volatile in planetary formation, differentiation and dynamic processes such as degassing, element mobility and volcanism (Ding et al., 2018). Therefore, by measuring the S of lunar materials, information can be acquired about both how the Moon formed and how the lunar interior evolved.

Very few lunar S studies have been performed *in situ*, with the majority of research having so far been focussed on lunar soil and bulk-rock samples. In particular, with the exception of one study that measured a single lunar apatite grain (Treiman et al., 2014), the S isotopes of lunar apatite, so far, remain understudied. This means that there is a missing part of the S evolutionary story of the Moon. As a late-stage crystallising mineral phase, apatite can reveal the behaviour of S in some of the last magmas and melts that were to exist on the Moon. By measuring S and Cl on the same spot of the same apatite grains, a better understanding of the behaviour of S in the late-stage magmas can be achieved through comparisons with what is already known for Cl in lunar apatite.

1.7.1. Research aim

The aim of this project is to, therefore, answer the broad research question:
What can S tell us about the behaviour of late-stage lunar basaltic magmas?

To answer this question, the following sub-questions will be addressed:

1. Is there evidence for S isotope fractionation in lunar apatites? If yes:
    - Are fractionation patterns unique to lunar apatites or are similar trends observed in terrestrial apatites?
    - Do the S isotope values in lunar apatites vary across different sample types?
    - Can the existence of different magma sources explain the observed S isotope fractionation?
    - Can 'groupings' of samples be identified (i.e. some with low, medium and high S isotope fractionations)?
2. Which mechanisms are causing extreme fractionation of Cl isotopes in lunar samples?
    - Is fractionation linked to secondary processes within the lunar environment or is it a signature of the original magma source region?
3. Do any correlations exist between S and Cl abundances and isotopes?
4. Does any evolutionary relationship exist between S and urKREEP?
5. What was the nature of the S species in the late-stage silicate melt?
6. What was the nature of the degassing S species?
7. Can S be used to determine the oxidation state of the late-stage silicate melt at the time of apatite crystallisation?
8. Does oxygen fugacity correlate with S isotope fractionation?
9. Is S homogeneously or heterogeneously distributed within the lunar interior?

1.7.2. Research objectives

In order to answer the research questions, the following objectives will be pursued during this research project:

1. Develop an analytical routine to measure S abundances and $^{34}S/^{32}S$ ratios of lunar apatite using the Cameca NanoSIMS 50L at The Open University.

2. Refine the analytical routine to measure Cl abundances and $^{37}Cl/^{35}Cl$ ratios of lunar apatite within the same samples that undergo S analyses using the Cameca NanoSIMS 50L at The Open University.
3. In order to be as representative as possible, analyse lunar apatites of mare basalt samples from all five Apollo landing sites (11, 12, 14, 15 & 17).
4. Positively identify apatites in mare basalt thin section samples and determine the chemical and petrological details of samples with scanning electron microscopy (SEM) and energy dispersive spectroscopy (EDS).
5. Apply the new S and Cl protocols to the identified apatite grains of Apollo mare basalt samples.
6. Develop a new protocol for measuring the oxidation state of S in lunar apatite at the UK's synchrotron facility, Diamond Light Source.

1.8. Personal contribution

In all cases, sample preparation for analysis with SEM, electron probe microanalysis (EPMA), nano-scale secondary ion mass spectrometry (NanoSIMS) and X-ray absorption near-edge structure (XANES) spectroscopy was undertaken by the author. Acquisition and processing of SEM and EPMA data was performed by the author, whereby SEM data collection far exceeded that of EPMA and, from year two, was ongoing over the course of the research project, with each sample (including unsuitable samples not reported here) requiring ~2-3 days of time. Acquisition and processing of NanoSIMS data was predominantly performed by the author but considerable support was provided by the NanoSIMS operative, Xuchao Zhao, particularly during the development of the new S protocol, which took ~6 months to optimise. The combined S and Cl analysis time for a single apatite grain (67 grains were analysed) took ~2-4 days. NanoSIMS data reduction (including S and Cl abundance and isotope data) was performed by the author and required ~2 months of time, which involved self-teaching of the software 'OriginPro' (for abundance data). The XANES spectroscopy was performed by the author, who was assisted by Mahesh Anand, Ian Franchi and Richard C. Greenwood. There were 7 full days (168 hours) of analysis time at the beamline. Data reduction was undertaken by the author, which involved self-teaching of the software 'Athena' and also discovering, trialling and self-teaching of the software 'Fityk', all of which required ~10 weeks' of time.

Chapter Two:

Analytical methods

This chapter describes the methods used for identification of target phases and for characterising and analysing the samples used in this research project. Each analytical technique and specific method involved in the lead up to, and the actual measurement of, sulfur and chlorine abundance and isotopes is detailed. In particular, this chapter outlines a new protocol for measuring sulfur isotopes in apatite that has been developed using an existing chlorine isotope protocol. The latter sections of the chapter provide information regarding the procedures used for data reduction and they are followed by a discussion relating to the overall reproducibility of the abundance and isotope measurements performed.

2.1. Optical microscopy

Throughout the research project, a Nikon Eclipse LV100 polarizing microscope fitted with a Nikon DS-Fi1 camera was used regularly at The Open University to investigate the samples analysed. The initial usage was to determine the texture of the samples which included assessing the size of the grains, what they were (if they showed characteristic interference colours under crossed polars) and what their modal abundance and distribution was. It was very difficult to identify apatite grains with optical microscopy before they had been located exactly with, for example, scanning electron microscopy (SEM) (see section 2.2) which not only has a superior resolution and magnification but is also equipped with an energy dispersive detector for quick identification of phases.

The analytical techniques used within this project required carbon and/ or gold coats to be applied to a sample. Optical microscopy was used to check for any old residual coating before sample analysis that might have led to inferior conductivity of a sample and, likewise, it was used afterwards to ensure that no carbon or gold had been left on the sample. In addition, a significant amount of time was spent searching for very small apatite grains, typically ~20 μm in the longest dimension, and capturing images with the optical microscope prior to work carried out at the beamline at Diamond Light Source (see Chapter Five). The camera used for mineral pinpointing at the beamline was based on optical light which meant that the preparations avoided wasting valuable beamline time (i.e. time not spent running the experiments) searching for and trying to recognise apatite grains that looked much smaller and very different under optical light when compared with the original images acquired from SEM.

2.2. Secondary Electron Microscopy

2.2.1. Fundamental principles

Secondary electron microscopy (SEM) is a high-resolution technique used to analyse whole rock sections and individual minerals on a micro-scale. The SEM is fitted with an electron gun which generates electrons that are accelerated to form a focussed electron beam with energy of between 0.1 keV to 30 keV. Electron lenses within the instrument de-magnify the electron beam so that, under vacuum conditions, the spot size of the beam that

interacts with a sample surface (down to ~1 µm in depth) is very small (nanometres) (Chen et al., 2015b).

2.2.1.1. Backscattered electrons

SEM is able to contextualise a sample through the use of backscattered electrons (BSE). When an electron beam is raster-scanned (steady to and fro movement) across a solid sample, it causes some electrons to interact with the atomic nuclei of the sample and undergo a sling-shot action whereby they effectively circle the nucleus and exit the atom with an elastic scattering action (a change in trajectory without losing energy) (Figure 2.1). These 'backscattered' electrons produce signals that are collected by a detector and are converted into a BSE image which is viewable in real-time on a computer screen (Chen et al., 2015).

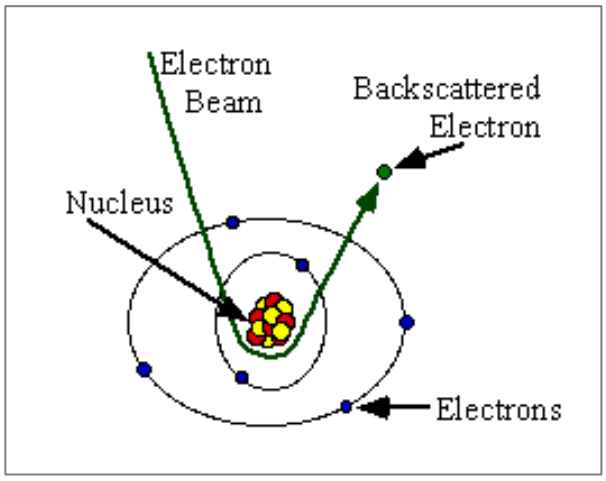

Figure 2.1. The generation of backscattered electrons. An incident electron beam penetrates a sample and causes some of the electrons to interact with the atomic nuclei of the sample. Those electrons undergo a sling-shot action and are sent rapidly out of the atom as backscattered electrons (adapted from Iowa State University, 2017.).

BSE images are useful because different mineral phases and compositions are represented by different shades of grey, with heavy elements (larger atomic masses) producing brighter contrasts and light elements (smaller atomic masses) producing darker contrasts (Chen et al., 2015). This occurs because the yield of backscattered electrons increases with atomic number, whereby more incident electrons are elastically scattered and reach the detector (Reed, 2005). A bright contrast, therefore, represents less absorption from elements with a larger atomic mass (Chen et al., 2015).

2.2.1.2. Energy dispersive X-ray spectroscopy (EDS)

The bombardment by an incident electron beam with sufficient energy (exceeding the electron binding energy) can excite an electron within a target sample from its restful ground state to a higher energy state, resulting in a vacancy. The absorption of energy by an inner orbital shell electron, for example, the K-shell, leads to a transit of that electron to a higher energy state and, in turn, the atom becomes ionised due to the raised energy state. To compensate, there is an inward movement of an outer L-shell electron to fill the K-shell vacancy (Reed, 2005) (Figure 2.2). The de-excitation energy of the electron transitioning from an outer orbital shell is converted into an X-ray photon which has an energy equal to the energy difference between the two electrons involved in the overall X-ray generation. The X-ray energy is, therefore, greatest for electrons transitioning from the M-shell to the K-shell (generating a Kβ X-ray) when compared with transitions from the L-shell to the K-shell (generating a Kα X-ray) (Zhou and Wang, 2006). Unlike BSE, X-rays are created by inelastic scattering (very little change in trajectory but a loss of energy) of the electron beam due to the transfers of energy involved (Reed, 2005).

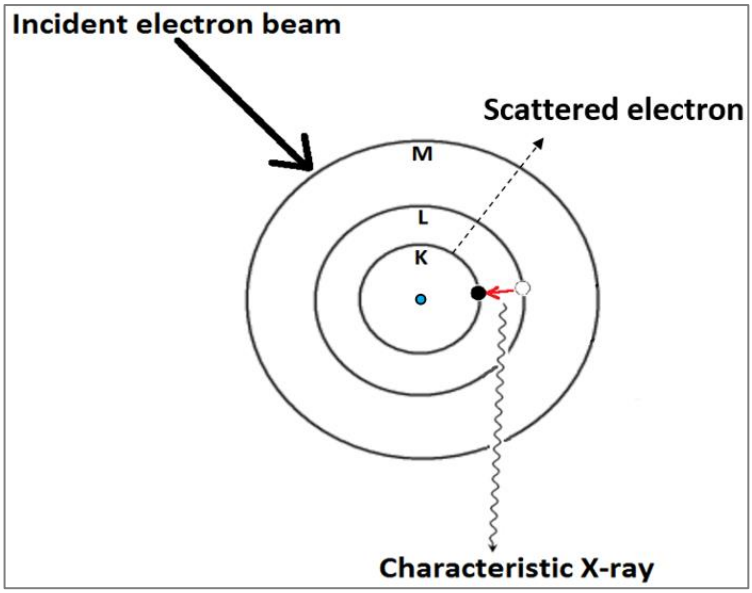

Figure 2.2. The X-ray generation process. An incident electron beam excites a K orbital shell electron within a sample, driving it to a higher energy state (dashed arrow) (the M- and L-shells are actually divided into several sub-shells with different energy levels that are not shown here). The resulting vacancy is filled as an electron from the L-shell (open small white dot) falls to the K orbital shell (small black dot). De-excitation energy of the transitioning electron is converted into a characteristic X-ray, here, a Kα X-ray. The light blue dot represents the nucleus (adapted from the Lunar and Planetary Laboratory, 2007).

The X-rays given off by a sample are analysed with energy dispersive X-ray spectroscopy (EDS). The Open University has a FEI Quanta 3D Dual beam Scanning Electron Microscope fitted with an Oxford Instruments silicon X-ray detector. The emitted X-rays produce characteristic wavelengths and spectrum lines for each element (Reimer, 1998) that are separated and identified by the detector to provide quantitative compositional information for a sample (Chen et al., 2015). With guidance from a BSE image, it is possible to use EDS for spot analysis (a few microns) to target specific mineral phases and identify what the elements are (Chen et al., 2015).

EDS enables the creation of grey-scale elemental distribution maps by combining the X-ray spectra with the corresponding backscattered electron image for a whole sample. The Open University uses Oxford Instruments INCA software (with SmartMap function) that permits chemical analysis of samples by 'montaging' a map to identify individual elements and mineral grains (via the present elements). False colours can be applied to the montaged map where specific colours are allocated to different elements to easily and qualitatively confirm the elements and composition of the grains (Oxford Instruments, 2017).

2.2.1.3. Secondary electrons

A different type of electron that is detectable by SEM is the secondary electron (SE) which is released from the first few nanometres of a sample surface when an incident primary electron beam interacts with the electrons within an atom. The interaction causes repulsion and inelastic scattering of electrons within the K orbital electron shell and, with enough energy, may lead to electrons escaping out of the atom and away from the sample surface (Figure 2.3) (Reimer, 1998). The secondary electron has relatively less energy (< 50 eV) than the backscattered electron which means that it can be differentiated from backscattered electrons by the SEM detector (Chen et al., 2015). Whilst a lower energy means that only shallow electrons will escape from a sample surface, secondary electrons are also produced when backscattered electrons travelling from greater depths within an atom make their way back out of a sample (Reimer, 1998).

Due to the lower energies involved with SEs, secondary electron images (SEIs) are useful for highlighting sample surface topography at a higher resolution than BSE because only

the secondary electrons near the surface escape to be detected. Such topographical information can be beneficial for further analyses with nanoscale secondary ion mass spectrometry (NanoSIMS) (see section 2.4) because unsuitable analysis areas, such as those containing small fracture lines, holes or contaminants, can be identified and avoided (Reed, 2005).

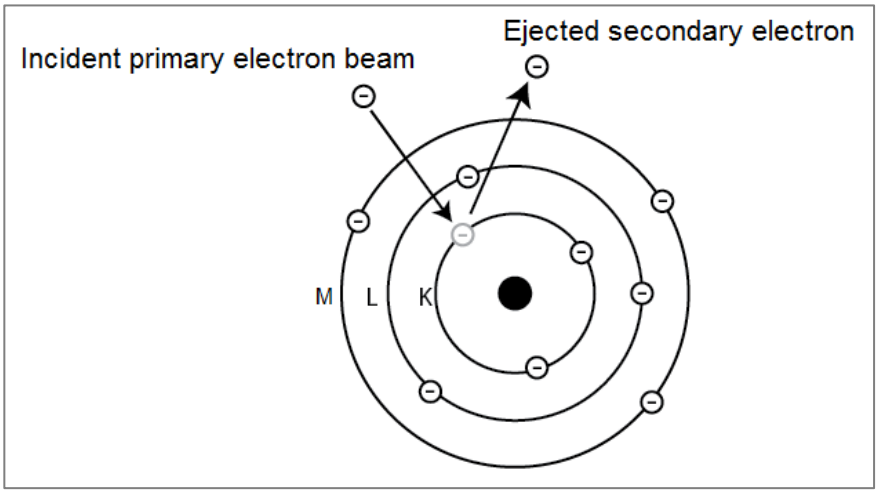

Figure 2.3. Secondary electron generation. An incident primary electron beam interacts with the electrons (circles enclosing negative symbols) within an atom. An electron from the K-shell is excited by the interaction and escapes from the atom and then the target sample surface (adapted from CCWJ, 2012).

2.2.1.4. Cathodoluminescence

The SEM at The Open University is also fitted with a Deben Centaurus cathodoluminescence panchromatic detector with Photo Multiplier Tube (PMT) that detects wavelengths of light between 185 nm – 850 nm and makes use of a manually retractable cathodoluminescence (CL) detector arm. When compared with optically-based CL instruments, SEM-CL instruments have a very high spatial resolution that permits observation of a sample at the micrometre- to nanometre-scale (Robertson and Gibson, 2014). A panchromatic detector detects the sum of all of the visible wavelengths of light emitted from a sample, which are split by a parabolic mirror according to their wavelength. The emitted light signal is multiplied by the PMT, which enables an image with contrasting (panchromatic) shades of grey (where lighter shades represent more intense luminescence and darker shades represent less intense luminescence) to be acquired (Hamers and Drury, 2011). Luminescence occurs when a non-metallic material (insulator) is bombarded with an incident electron beam (to a depth of ~2–8 μm) that causes an

increase in energy within an atom, leading to the outermost electrons transitioning to an unstable, excited state. Surplus energy is released as the electrons relax back to a lower energy state (often the ground state) which results in the emission of photons of visible light from luminescent materials (Mason, 2014).

When an electron beam is focussed onto a sample via an objective lens, it interacts with the atoms of a sample which leads to energy being absorbed by electrons that reside within a lower energy valence band (highest energy band occupied by electrons for non-metals) (Figure 2.4). The electrons become excited and transition to a higher energy state in the conduction band (an empty band for non-metals). The excited state is unstable, so the electrons relax down from the conduction band back to the lower energy valence band by releasing the excess energy (a few eV) as emitted light (a photon) with a wavelength equal to the band gap energy (Götze and Kempe, 2009). For the purpose of CL detection, the wavelength and corresponding energy of the photons is within the visible portion of the electromagnetic spectrum and the luminescence is generated when a photon is released (Mason, 2014).

The band gap (or, 'forbidden gap') is sandwiched between the valence and conduction bands (Figure 2.4) and can be occupied if there are crystal lattice defects, for example, substitution of ions such as Mn^{2+} for Ca^{2+} could cause a distortion and defect within a lattice, as could the existence of interstitial ions – all of which have their own energy levels (Reed, 2005). The occupants of the band gap can trap electrons for a few microseconds as they relax back down to the valence band and, depending upon the density of the defects or impurities, varying intensities of CL can be emitted due to the energy released when electrons are liberated from the temporary entrapment(s) (Götze and Kempe, 2009).

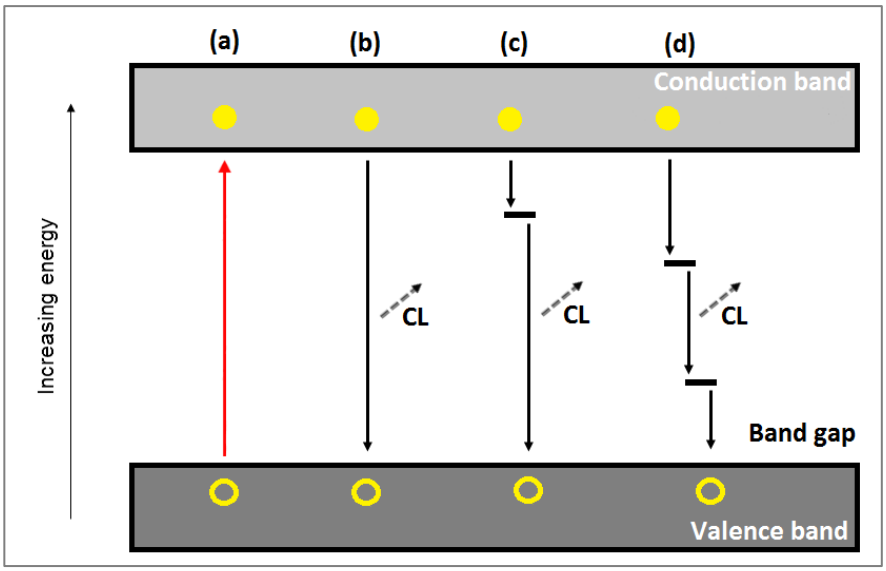

Figure 2.4. The process of energy transfer and generation of luminescence. An electron residing within the valence band (**a**) is initially excited by an incident electron beam and rises (red arrow) to the higher energy conduction band, leaving a hole in the valence band (open yellow circle). The unstable electron relaxes straight back down (**b**) to the valence band and a photon is released which generates CL. An alternative pathway for the relaxing electron (**c**) involves interaction with defects in the band gap which momentarily trap the electron and alter the intensity of the CL emitted. The final pathway (**d**) demonstrates that an electron can be trapped multiple times by defects within the band gap (adapted from Reed (2005) and Götze and Kempe (2009)).

Certain impurity ions (such as Mn^{2+}, Cr^{3+}, Ca^{2+} and rare earth elements Nd^{3+} and Sm^{3+}), known as activators, can substitute for other cations and increase the intensity of the CL emitted because they are readily excited. However, some impurity ions (notably Fe^{2+}), known as quenchers, can inhibit or completely block CL emission by trapping some of the excitation energy absorbed by activator ions (Boggs and Krinsley, 2006). Instead of the excitation and relaxation pathway taken by activators (described above), quenchers relax back to a ground state without emitting radiation. The intensity of CL, therefore, depends upon the presence and balance of activators and quenchers which can vary between different specimens of the same mineral. Additionally, a greater concentration of activator ions does not necessarily mean a more intense CL emission because if there is more than one activator present, the excited state may be passed from activator to activator rather than resulting in an emission of CL (Mason, 2014).

SEM-CL is, therefore, able to highlight heterogeneities within a sample through variations in the intensity of CL caused by crystal defects, different compositions (through substitution) or varying quantities of the same trace elements within a mineral (Reed,

2005). As a result, the use of CL can highlight the existence of micro-textures such as zonation within minerals which would otherwise not be observable with BSE and SE images or EDS. When apatite is studied with CL, it is seen to have varying degrees of luminesce which has been attributed to the replacement of Ca within the apatite crystal structure with the REEs Sm^{3+}, Dy^{3+}, Tb^{3+}, Mn^{2+} and, to a lesser extent, Ce^{3+}, whereas, La^{3+}, Ce^{4+}, Nd^{3+}, Gd^{3+}, Yb^{3+}, Pr^{3+}, Eu^{3+} and Lu^{3+} either do not contribute or are very weak contributors. At the other extreme, Fe in many lunar minerals is thought to act as a quencher of CL emissions (Götze and Kempe 2008; Götze 2009) and it is suggested that this may also occur in lunar apatite that contains trace amounts of FeO, leading to the observation of less intense luminescence (Černok et al., 2019). Likewise, trace element Mn^{2+} is a significant activator (Mitchell et al. 1997; 2014) with a characteristic yellow luminescence (if colour filters are used) which, when seen alternating (zoned) with blue and violet luminescence, can be a sign of magma mixing (acidic and basic magmas) during apatite crystallisation (Götze, 2012) or is as a result of secondary metasomatic interaction (Mitchell et al., 1997).

2.2.2. Analytical methods and sample preparation for SEM-CL

All of the Apollo samples used within this project had been previously mounted as polished rock thin-sections of ~30 μm thickness by NASA's Curation and Analysis Planning Team for Extra-terrestrial Materials (CAPTEM).

In readiness for SEM and CL analyses, all samples were inspected with optical microscopy to check for any previous carbon/ gold coats and for any surface dust. Samples were cleaned with isopropanol (IPA) and laser sealed wipes before being dried with an air hose. The samples were coated with ~20 nm of carbon with the EMITECH K950X Turbo Evaporator in order to dissipate any excess charge caused by the SEM electron beam. The optical microscope was used regularly to check the quality of the carbon coating as well as to check samples once the carbon coats had been removed. To aid conductivity and dissipate charge, aluminium tape was positioned at the edge of each sample before being fastened to a specimen stub and placed on the stage within the SEM sample chamber.

The FEI Quanta 3D Dual beam Scanning Electron Microscope (SEM) fitted with Oxford Instruments X-ray detector at The Open University was used for all SEM and CL analyses.

For the Apollo samples, elemental montage maps (using EDS) of the whole sample were acquired first in order to identify phosphorous (P) and calcium (Ca) hotspots that could potentially be apatite sites within a sample. This was achieved by using the INCA X-ray SmartMap function which permitted parameters such as the magnification, the dwell time, the number of frames and the resolution of the final map to be adjusted. For the Apollo samples, the settings depended upon the size of the sample because the use of greater magnification and longer dwell times, for example, resulted in longer instrument analysis time and ultimately a larger file for montaging. Maps created with an accelerating voltage of 20.05 kV and a current (incident beam) of ~0.6 nA, along with a working distance of ~15 mm and a resolution of 1024 x 896 pixels were suitable for observing minerals within the sample and for the identification of P and Ca.

The INCA software was used to stitch the map together (montage) to produce a BSE image for the whole sample. Elements of interest were selected (such as P, Mg, Ca, Fe, and Ti) and assigned different colours (Figure 2.5) which appeared on the montaged BSE maps and assisted with mineral identification and apatite detection. Once potential apatite sites had been located, EDS was used in 'point & I.D.' mode to acquire individual elemental spectra for the P- and Ca-bearing grains in order to rule out the other phosphate-bearing mineral, merrillite (containing Mg and Na) and confirm that the grain was apatite. The positively identified apatites were checked for their suitability for use with NanoSIMS which meant using SEIs to assess the grain size (NanoSIMS analysis required an area to be at least 5 μm x 5 μm) and the grain topography (Figure 2.6), which included eliminating grains with cracks and holes that might interfere with analyses. Likewise, high resolution BSE and SE images of the apatite grains and EDS were used to identify possible impurities representing sample contamination on the grain surface that would adversely affect the quality of NanoSIMS data.

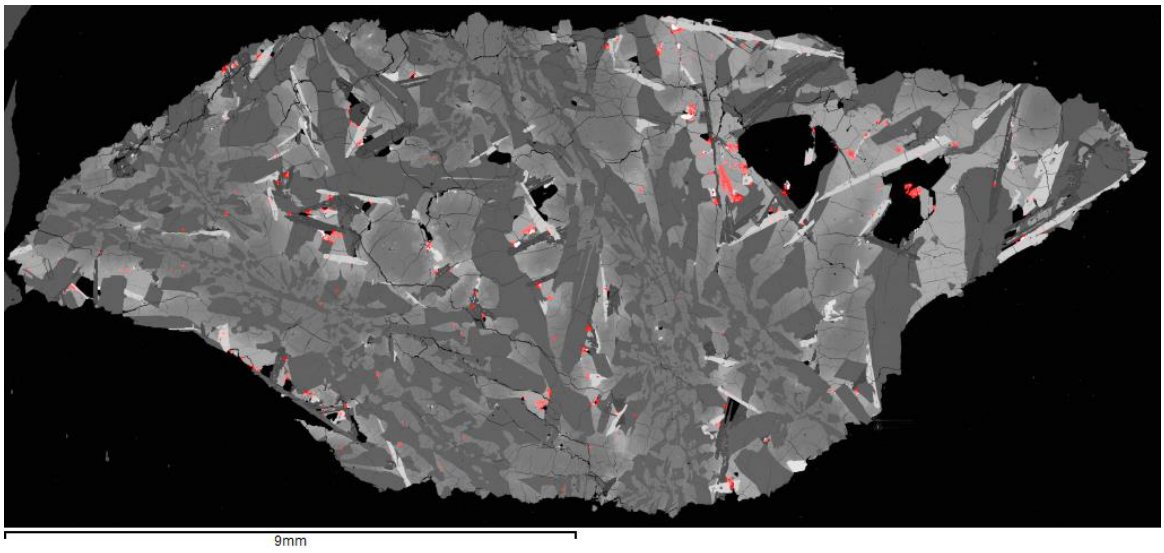

Figure 2.5. An example of a false colour X-ray map for the whole section of Apollo sample 12039,45 with phosphorous highlighted red. The highlighted grains were investigated in detail at a higher resolution and element spectra were acquired in order to positively identify apatite.

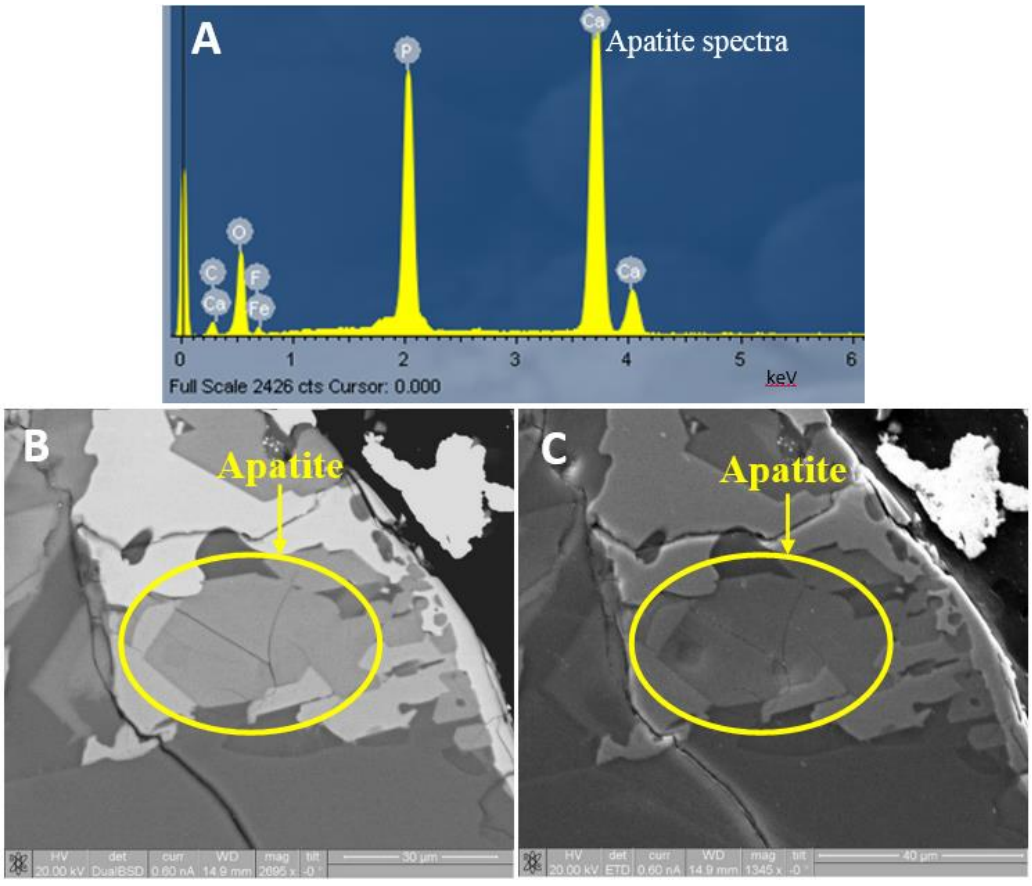

Figure 2.6. Identification and suitability of apatite. **A)** The spectra acquired for a grain in Apollo sample 14053,19 allowed positive identification of apatite, with dominant Ca and P (but lacking Mg and Na, characteristic of merrillite). **B)** and **C)** are BSE and SE images (note slightly different magnification), respectively, for the acquired spectra. The grain was a good candidate for subsequent NanoSIMS analysis due to its size (>30 μm), lack of large cracks, holes and impurities.

The Deben Centaurus cathodoluminescence panchromatic detector with Hamamatsu Photo Multiplier Tube (fitted to the FEI scanning electron microscope) at The Open University was employed in this research project in order to determine whether zoning and/ or micro-textures observed with CL in lunar apatite displayed any quantitative chemical relationship with lunar volatiles, in particular, the abundances and isotopic composition of S and Cl measured using NanoSIMS.

Once appropriate apatite grains had been selected for further investigations with CL, the sample chamber was vented and the BSE detector within the chamber was removed before the retractable CL detector 'arm' could be manually inserted. No further sample preparation was required. During this short time (~2 minutes to complete) the sample remained in place on the sample stub. The vacuum was then reapplied to bring the pressure down to ~10^{-5} mbar and the detector was set to 'External'. The settings used for acquiring CL images varied depending upon the composition of the apatite grain and the CL intensity, however, apatites within the Apollo samples responded well to an accelerating voltage of 7 kV – 10 kV and an incident electron beam with a current of 0.7 nA – 1.5 nA. Likewise, a working distance between ~12 mm and ~13 mm achieved some of the best images. The brightness and contrast settings were adjusted to achieve the optimal CL images (Figure 2.7).

Secondary electron images could still be viewed 'live' alongside the CL images which helped with locating the apatite grains (some only ~10 μm in across) quickly (to limit exposure) within the samples and it ensured that the correct regions of interest within the apatite grains were being analysed with CL. The acquired CL images were used during NanoSIMS so that regions of zonation could be targeted within the apatite grain in order to identify any variation in both the S and Cl abundance and the corresponding isotope values.

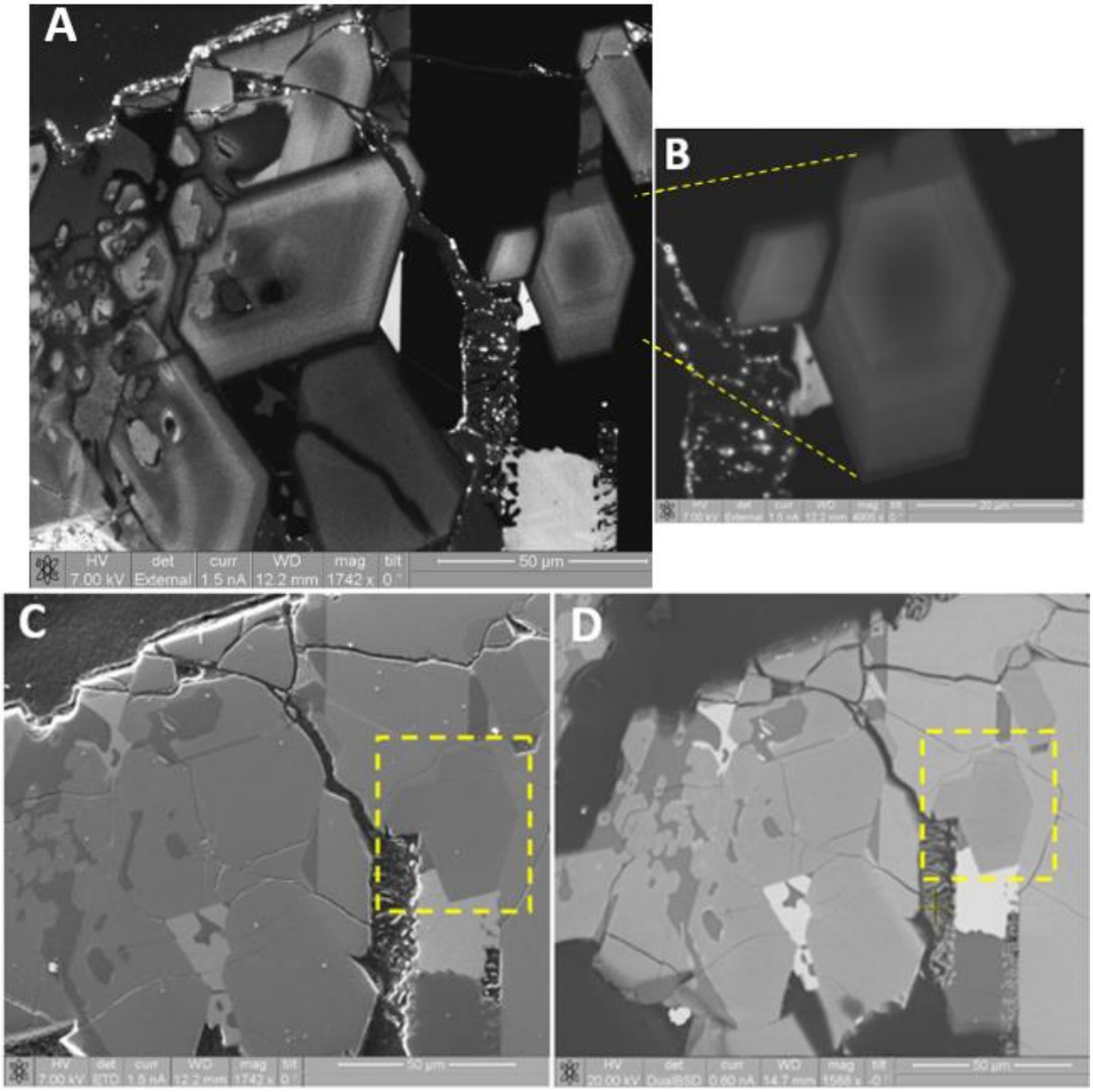

Figure 2.7. An example of a cathodoluminescence image. **A)** Cathodoluminescence (CL) for multiple apatite grains in Apollo sample 12039,45 with clear concentric zonation patterns. **B)** Highlights a perfectly euhedral zoned apatite grain (dashed yellow lines pinpoint the location in A). **C)** Secondary electron (SE) and backscattered electron (BSE) images, respectively, showing a more magnified version of A) to demonstrate that, without use of CL, the zonation patterns are not detectable with BSE or SE. For comparison, the yellow dashed boxes in C) & D) pinpoint the apatite shown in B).

2.3. Electron probe microanalysis (EPMA)

2.3.1. Fundamental principles

Electron probe microanalysis (EPMA) is used to determine the chemical composition of individual minerals within a sample. As with SEM, EPMA involves an electron gun and a beam of accelerated and focussed electrons (between 5 keV – 30 keV) which is directed onto the surface of a polished, solid sample that is under vacuum in a sample chamber. Unlike SEM, the electron microprobe is also fitted with an optical microscope and CCD camera with which to locate areas of interest. Upon interaction with an electron beam, X-ray photons are generated from a sample that are characteristic of individual elements and are detected by the spectrometer(s).

EPMA is based upon wavelength dispersive spectrometry (WDS), therefore, X-rays are dispersed according to their wavelength by a process of Bragg reflection (refraction), with the spectra of each X-ray being detected and identified by a wavelength dispersive spectrometer (Reed, 2005). The Cameca SX100 at The Open University is fitted with five WDS multi-crystal spectrometers, each of which uses different analytical crystals that have a certain lattice plane spacing which diffracts specific X-rays generated from within a sample. Only the X-rays that encounter the analytical crystal at a specific angle (the Bragg angle) and obey Bragg's law (Equation 2.1) are diffracted and exit the crystal at an angle equal to the incident X-ray beam to reach the detector (Hammond, 2009).

Bragg's Law: $n\lambda = 2d \sin\theta$ Equation 2.1

Where λ is the X-ray wavelength, n (an integer) is the order of reflection, d is the lattice plane spacing and θ is the angle of incidence/ reflection to the planes (Hammond, 2009).

The angle of the analytical crystal(s) can be changed with respect to the sample and the detector so that the X-rays specific to one particular element can be selected on one of the five analytical crystals and, therefore, be detected in accordance with Bragg's law. For example, the position of the crystal can be set to reflect (refract) the Na X-rays into the detector and these X-rays are counted over a predetermined amount of time. As a result, the X-rays generated by different elements cannot be collected simultaneously by one

spectrometer but must be collected sequentially. Likewise, any one analytical crystal cannot satisfy Bragg's law for the full spectrum of wavelengths emitted by all elements (Lunar and Planetary Laboratory, 2007). Alongside five WDS multi-crystal spectrometers, the EPMA at The Open University has 11 standard Cameca analysing crystals (with different *d*-spacings) allowing the collection of multiple elements when WDS is set to run in a sequence involving a cycling of different crystals for each analysis run. Most commonly, five of these crystals are employed for analysis: pseudo crystals PC0 and PC2 (W/Si and Ni/C synthetic multi-layer crystals, respectively), thallium acid phthalate (TAP), pentaerythritol (PET) and lithium fluoride (LIF).

The advantage of using WDS over EDS (as found on the SEM) is that the former allows precise (to within ± 1%) quantitative chemical analysis of elements with atomic numbers greater than that of boron (>5), with a spectral resolution of ~1 μm and a low elemental detection limit in the tens of parts per million (ppm), compared with hundreds to thousands of ppm for EDS (Reed, 2005). In order to obtain precise and high quality EPMA data, well characterised reference standards must be used to convert X-ray counts per second into element concentration levels for an unknown sample. For example, the X-ray count rate for an element of interest within a standard (with a known elemental abundance) is compared with the X-ray count rate of the unknown sample and, after adjusting for any interferences from other elements, the element abundance level for the unknown sample can be calculated (Lunar and Planetary Laboratory, 2007).

2.3.2. Analytical methods and sample preparation for EPMA

EPMA was employed to acquire the quantitative chemical composition of the apatite grains such as the major element oxides and the rare earth elements (REEs). EPMA was used before NanoSIMS for lunar meteorite sample SaU 169 and Apollo sample 79215,50 in order to determine whether S abundance within the apatite grains was quantitatively adequate to determine the S isotope values with sufficient precision using NanoSIMS. EPMA and NanoSIMS were carried out on SaU 169 first (the lunar meteorite was used as a proof of concept for measuring S isotopes – see Appendix A) and, once shown to be successful, sample 79215 was investigated with the same techniques. Sample preparation was identical to that employed for SEM except a thicker coat of carbon (~30 nm) was applied to the samples to reduce charge build-up during analysis.

It is suggested that anion mobilisation of F and, to a much lesser extent, Cl within apatite can be caused by the implantation of electrons or the heating of the sample via exposure to an electron beam, whereby X-ray intensities of F are seen to increase as a function of time under routine analytical conditions (e.g. Goldoff et al., 2012; McCubbin et al., 2010a; Stock et al., 2015; Stormer et al., 1993). There is debate as to the cause of volatile mobilisation, however, the mobilisation magnitude has been shown to be linked to the orientation of the apatite grain relative to the incident electron beam, whereby a beam positioned perpendicular to the c-axis [001] had a greater effect compared with a beam positioned perpendicular to the a-axis [100], under the same analytical conditions (Stormer et al., 1993). As a result of electron implantation, F is mobilised (rather than lost/ volatilized) to the surface of an apatite grain which can both cause the count-rate of F to appear falsely higher than it really is during analysis and make the anions within the X-site (the crystallographic position where F, Cl and OH reside within a apatite structure) non-stoichiometric, i.e. not add up to 1 (Pyle et al., 2002).

Tests carried out by Barnes et al. (2013), also using routine measurement conditions, found that beam exposure from EPMA had no effect on hydrogen isotope (δD) values (any potential effects were well within the current level of uncertainty in the measurement of H isotopes) or OH contents unless, in the case of OH abundance, a relatively stronger beam current was used and, in which case, OH counts were seen to increase marginally. Likewise, it has been shown that mobilisation of S during EPMA of melt inclusions is non-existent, with the S remaining stable for long counting times (12,000 seconds) when analysed with a beam current of 30 nA and beam diameter of 15 μm (Métrich and Clocchiatti, 1996). In order to prevent potential mobilisation of S (as well as other volatile elements) in apatite, Konecke et al. (2017a) employed an accelerating voltage of 15 keV, a beam current of 10 nA and beam diameter of 2 μm for all electron probe analyses.

To prevent volatile element mobilisation, two different beam conditions were employed for apatite analysis with the electron probe in this project. For the first condition, just F was analysed (to reduce any possibility of prolonged exposure to the beam) with an accelerating voltage of 10 keV, a beam current of 4 nA and beam diameter of 10 μm, making use of the PC0. The remaining elements were measured as part of the second condition which involved an accelerating voltage of 20 keV, a beam current of 20 nA and

beam diameter of 10 μm and included Na, Mg and Si (LTAP crystal), Ca, P, S and La (PET crystal), Cl, Y and Ce (LPET crystal) and Fe, Mn and Nd (LLIF crystal).

Reference standards that contained the relevant elements studied within the apatites were used during EPMA. These included strontium fluoride (F), jadite (Na), forsterite (Mg), feldspar (Si), bustamite (Ca, Mn), yttrium phosphate (Y and P), Barite (S), sylvite (Cl), haematite (Fe), cerium metal (Ce), lanthanum metal (La) and neodymium metal (Nd). In addition, laboratory apatite and olivine secondary reference standards were used during EPMA to provide reproducibility checks and to maintain the quality of the apatite measurements made.

Upon analysing sample 79215 with NanoSIMS (see section 2.4), it became clear from the images that S hotspots (suspected to be contamination and/ or inclusions) were present within the apatite grains and that S abundance measurement with EPMA was not entirely reliable because of the risk of unknowingly selecting a point on the apatite grain that was in fact a S hotspot containing far higher S abundances (thousands of ppm). As a result, in the latter stages of the project, EPMA was not used prior to (or after) NanoSIMS as a method of gauging the S abundance within the apatite grains of the remaining thirteen Apollo samples studied in this project.

It also became clear that there was a great risk of beam damage from prolonged exposure with EPMA which could lead to photo-reduction or oxidation of S (e.g. $S^{6+} \rightarrow S^{4+}$ and $S^{2-} \rightarrow S^{6+}$) resulting in erroneous $S^{6+}/\Sigma S$ calculations (Métrich et al., 2009; Wilke et al., 2008). This was a particularly important consideration because of the S oxidation investigations that were carried out at Diamond Light Source (see Chapter Five) after NanoSIMS work had been completed.

For the two samples that underwent EPMA, the data reduction process involved normalising the acquired data to a total of 13 anions (Deer et al., 2013) found within the apatite structural formula ($Ca_5(PO_4)_3(F,Cl,OH)$) which are made up of $12O^{2-}$ and $1X^{-}$, where 'X' is primarily a combination of F, Cl and OH in an apatite structure that has no vacancies in the X-site, giving a total charge per formula unit (pfu) of -25 (McCubbin et al., 2011). This method allows the abundance of the missing component in the X-site to be estimated stoichiometrically, i.e., on the basis that OH cannot be measured directly with

EPMA, if F and Cl are measured accurately, stoichiometric calculations that define which elements can be held at certain crystallographic sites are used to estimate the abundance of OH – believed to be the only and most likely missing component in lunar apatite (McCubbin et al., 2011). This method assumes that the X-site is filled with F, Cl and OH only and that the total of the three anions equals one atom per formula unit (apfu). Appendix B, Table B.1 shows how stoichiometric calculations were performed subsequent to EPMA and Appendix B, Table B.2 contains the EPMA results.

2.4. Nano-scale Secondary Ion Mass Spectrometry (NanoSIMS)

2.4.1. Fundamental principles

In the field of planetary science, secondary ion mass spectrometry (SIMS) is used to determine elemental abundance and isotopic composition of solid samples, such as rocks and minerals, with use of an ion microprobe. All elements can be analysed with SIMS except for the noble gases which do not ionise. Due to a sub-micron probe size, only a small amount of sample is required for SIMS analysis which, despite it being a destructive technique, allows better preservation of the petrological context. SIMS, therefore, has an advantage over other isotope analysis methods, such as laser ablation inductively coupled plasma mass spectrometry (LA-ICP-MS), which entails destruction of a larger sample volume (Wei et al., 2015).

For SIMS, a primary ion beam with a typical energy of 1 keV to 20 keV is directed at a 90˚ angle or an inclined angle onto a flat sample surface which transfers kinetic energy to the target atoms of the upper few atomic layers of a sample. The imparted energy causes the target atoms to collide and jostle with one another in all directions (the collision cascade) (Figure 2.8) and, for every incident primary ion, one to tens of secondary particles are sputtered (ejected) from a sample surface into a very high or ultra-high vacuum (Stern, 2009). Of the ejected particles, only a small fraction (<<10%) becomes ionised because of the dependence upon, for example, the sample composition, the ionisation efficiency of the elements within the sample and the ion beam energy used for analysis (Stern, 2009; Kilburn and Wacey, 2015).

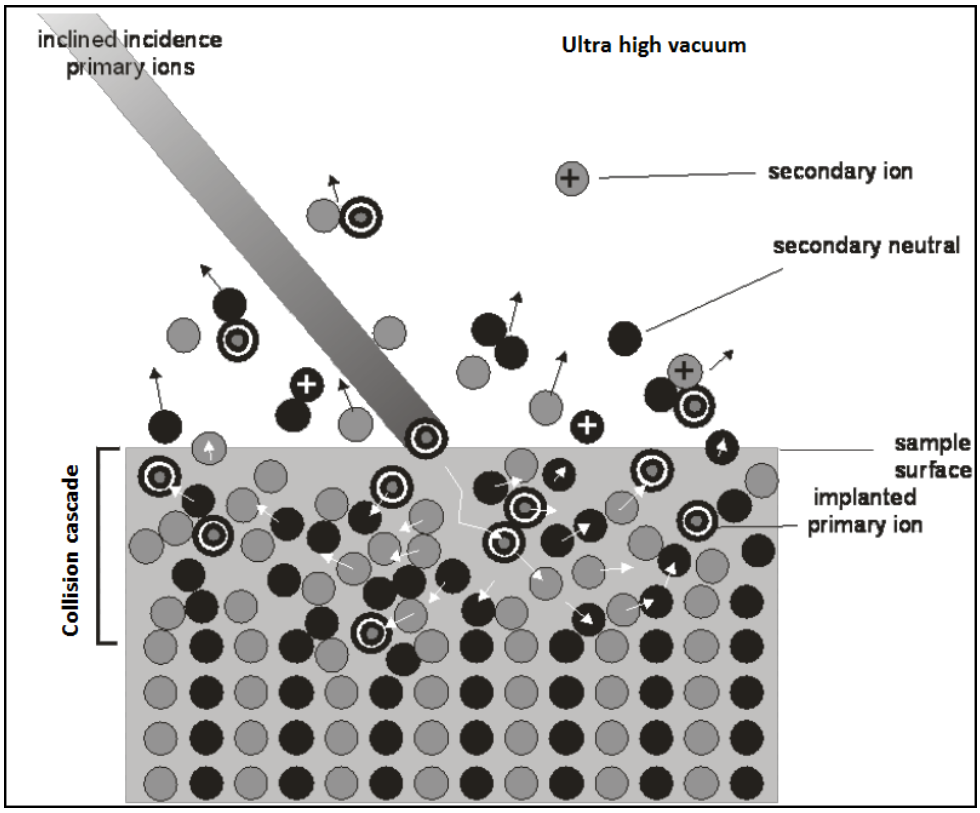

Figure 2.8. The fundamental process of SIMS analysis. The primary ion beam (here shown as inclined) travels through the ultra-high vacuum to reach the solid sample surface. The imparted energy causes random jostling (collision cascade) of atomic species (movement represented by small white arrows) within the surface layers and the ejection (sputtering) of particles, 'some' of which are ionised (secondary ions) (adapted from Stern, 2009).

The ionised particles, known as 'secondary ions', are physically separated by a magnetic field (the magnetic sector) within the mass spectrometer which deflects the ions according to their mass-to-charge ratios, where ions with the greatest mass and the smallest charge are deflected the least, into a detector (Faraday cup or electron multiplier) where the ions are counted (Hoppe et al., 2013). To have high mass resolution is to have the ability to detect and separate any isobaric interferences from species that have the same mass as the element of interest. For example, with a mass resolving power of ~4,000, ^{33}S can be differentiated from $^{32}S^{1}H$ within a mass spectrometer. The magnetic sector of the Cameca NanoSIMS 50L, which was used in this project, is capable of high mass resolution (mass resolving power (MRP)) of >7,000 '$m/\Delta m$', where m is the detected (mean) mass and Δm is the mass difference between two species that are to be separated (Zhang et al., 2014).

The Cameca definition of MRP is as Equation 2.2.

$$MRP_{Cameca} = \frac{1}{4} \text{ x } \frac{r}{L} \qquad \text{Equation 2.2}$$

Where, *r* is the turning radius of mass *m* in the magnet and *L* is the width of the portion of the mass peak between 10% and 90% of the maximum intensity (a measure for the steepness of the peak flanks) (Hoppe et al., 2013).

For analytically precise isotope measurements, it is desirable to have a high transmission, whereby a large number of secondary ions generated from the sample surface pass through the mass spectrometer to then actually reach the detectors. On the other hand, in order to achieve high spatial resolution, precision might be compromised because a lower primary beam current is required which results in fewer secondary ions and, therefore, reduces the probability of the ions reaching the detector. The Cameca NanoSIMS 50L has 7 detectors (1 Faraday cup (FC) and 6 electron multipliers (EM)), allowing 7 different isotopes or species to be studied simultaneously but, due to the finite size of the magnet, the ratio of maximum to minimum masses under simultaneous investigation cannot be greater than 21 (Hoppe et al., 2013).

Both the primary ion beam and the extracted secondary ions travel through the same coaxial lens stack design (Figure 2.9), consisting of the EOS, EOW, EOP and L4 lenses (Figure 2.10) and, as a result, the polarity of the primary beam is opposite to that of the extracted secondary ions. The coaxial design allows a closer working distance between the objective lens of the primary ion column and the sample (0.4 mm) and also permits simultaneous focusing of the instrument optics for the primary ion beam and the extracted secondary ions. The design leads to a higher spatial resolution (a greater number of pixels due to the ability to separate signals in close proximity to each other) than could be attained with LA-ICP-MS techniques and it is achieved with a probe diameter as small as 30 nm - 50 nm (Hauri et al., 2016; Wei et al., 2015; Zhang et al., 2014).

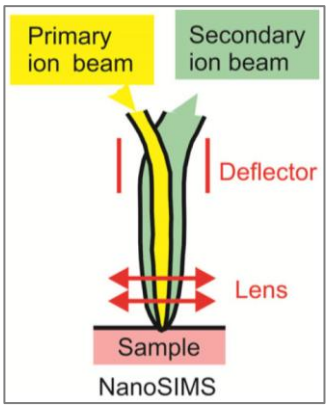

Figure 2.9. NanoSIMS coaxial lens design. The primary ion beam travels through a lens stack at 90˚ to the target sample surface and the secondary ions (those particles ionised) pass back through the same optical system. The deflection plates (P1 in Figure 2.10) separate the oppositely charged primary and secondary ions (Wei et al., 2015).

The Cameca NanoSIMS 50L (Figure 2.11) has two primary ion beam sources, Cs^+ or O^-, which generate negative and positive secondary ions, respectively, from a sample surface (Kilburn and Wacey, 2015). Having been derived from the source, the primary ion beam is de-magnified by the lenses L0, L1 and L2 and is guided through the primary optical column by an electrostatic spherical sector (SS30) (an electric field that turns the beam 78° (Hoppe et al., 2013)) and an octopole (8 rods (lenses)) (Figure 2.10) before it is deflected by a set of P1 deflector plates which align the beam perpendicularly to the sample surface. Before reaching the sample surface, the angular distribution of the primary ion beam and, therefore, the current and probe size, is reduced with a selection of different sized diaphragm apertures (D1) until finally the beam is focussed onto the sample surface with the EOP lens (Hoppe et al., 2013).

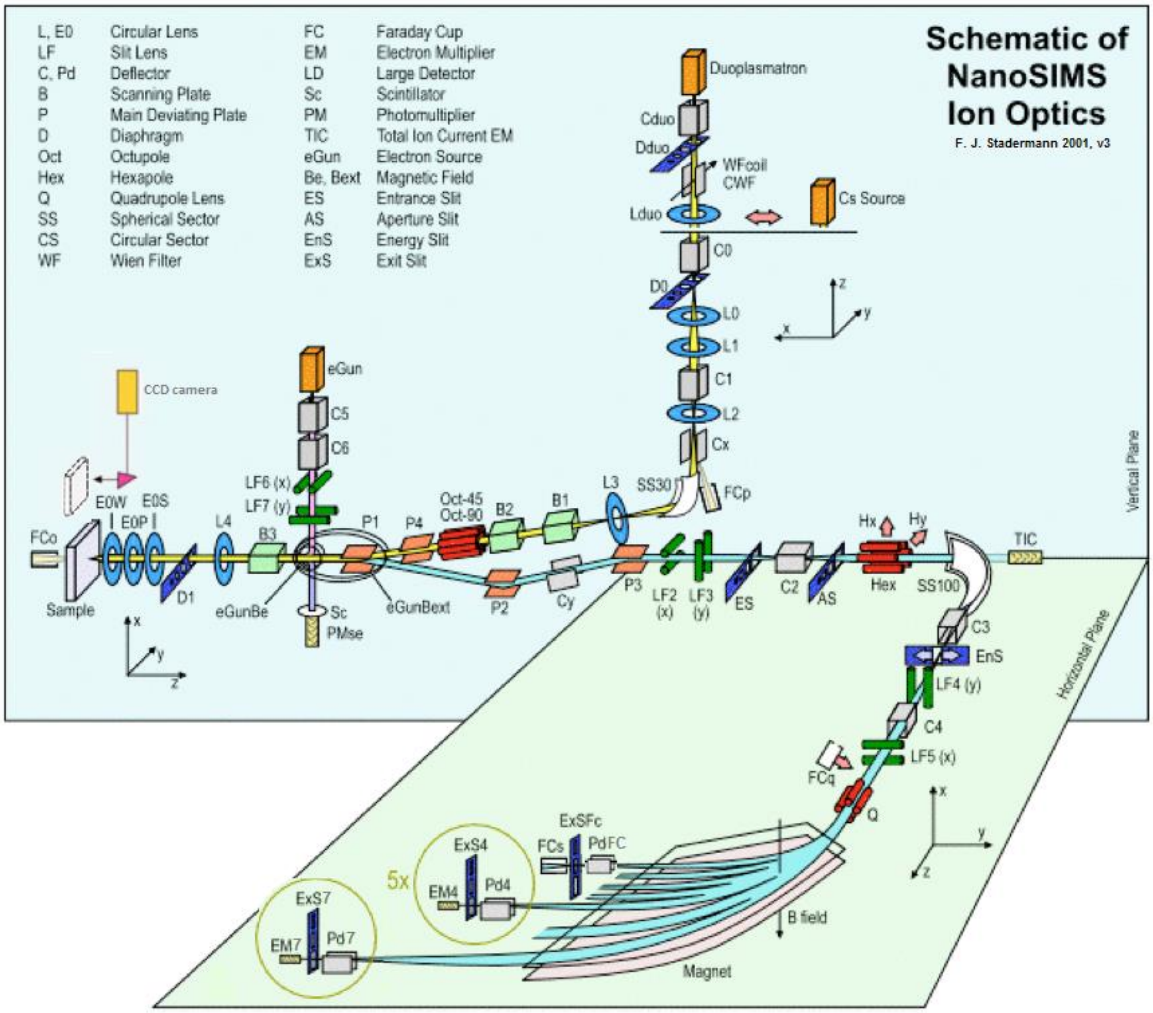

Figure 2.10. Schematic of the NanoSIMS 50L ion optics. The vertical column (vertical plane of diagram) shows the primary ion optics through which the primary beam passes - the lenses, apertures and plates of which are referred to within this chapter. The column can be followed round through the coaxial optics to reach the sample. See also the key in the top left for reference. The column travelling towards the right of the image (moving away from the sample and coming out of the page – the horizontal plane) shows the secondary ion optics through which the secondary ions travel, having passed back through the coaxial optics and on through plates and apertures to eventually arrive at the detectors: the electron multipliers (EMs) and the Faraday cup (FC) (adapted from schematic by Frank Stadermann, 2001).

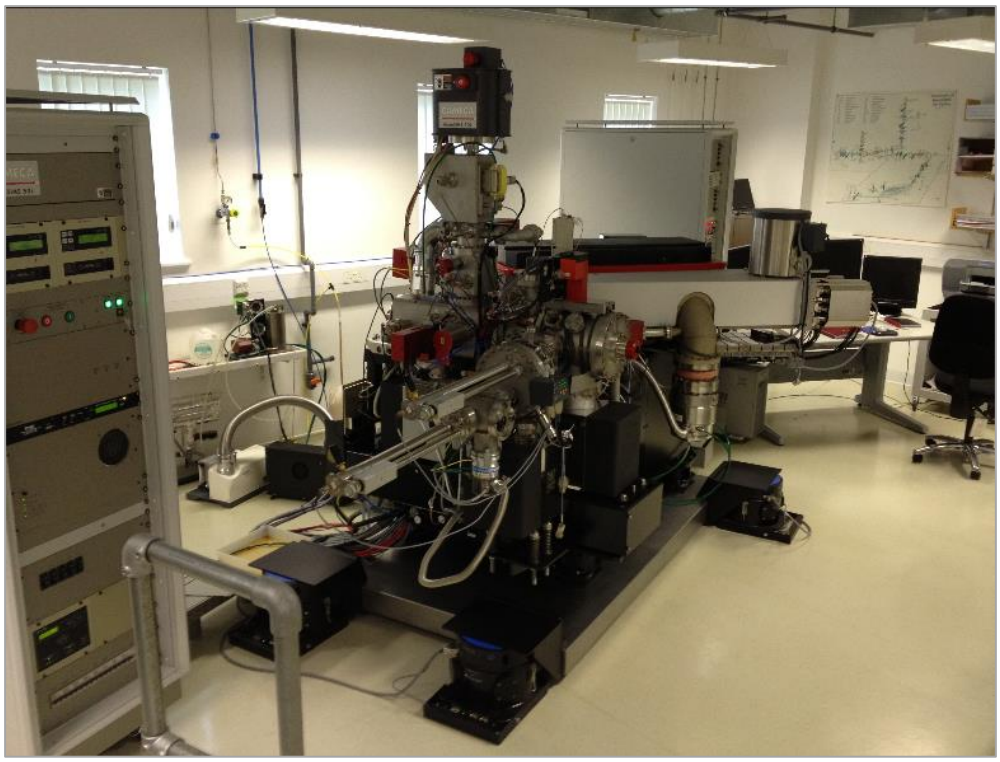

Figure 2.11. Photograph of the Cameca NanoSIMS 50L at The Open University. The instrument airlocks (accessed by long silver arms) and sample chamber are at the image centre (Chapter Two). The primary ion beam source is at the very top of the image. (Image courtesy of Natalie Starkey, The Open University).

Secondary ions extracted from the sample surface are also focussed with the lens stack (EOW, EOP, EOS and LF4) and reduced with the diaphragm D1. The secondary ions are separated from the primary ions by the set of deviating P1 plates (used to rotate and separate primary and secondary ions). In order to prevent mass fractionation of the secondary ions at the entrance slit (ES) of the mass spectrometer, a pair of external coils (Bf-vert and Bf-hor) at P1 is calibrated by monitoring the automated vertical and horizontal scans of the P2, Cy and P3 plates. P1, P2 and P3 centre the secondary ion beam through the lens and entrance slits (LF2 and ES, respectively) in the vertical direction, whilst the Cy centres the secondary ion beam through both the lens slit LF3 and the ES in a horizontal direction. The secondary ions are, therefore, guided into the mass spectrometer via the ES where the size and lateral energy distribution of the secondary ion beam is reduced before it passes through the aperture slit (AS) (both ES and AS have adjustable, different sized, lens widths) to limit the angular dispersion of the secondary ion beam. The electrostatic spherical analyser (SS100) (producing an electric field) disperses the secondary ions according to their energy before they pass through the energy slit (EnS) which filters the secondary ions according to their energy. The beam is then directed through two slit lenses (LF4 and LF5), a deflector (C4) and a quadruple lens (Q) which

perform angular and energy focussing before the ions enter the magnetic field. It is within the magnetic field that mass separation occurs before ions pass through the exit slit (ExS) to finally reach the detectors (EMs and FC) (Hoppe et al., 2013).

The Cameca NanoSIMS 50L is capable of high sensitivity, giving it the ability to detect many elements at the parts per billion (ppb) level and measure very small changes in element abundance which cannot be detected by other methods such as electron probe microanalysis (EPMA). The sensitivity of the instrument depends upon the number of secondary ions produced and the transmission efficiency (how many generated secondary ions reach the detector). Ultimately, transmission is dependent upon the correct tuning of the instrument, via the ion optics (Figure 2.10), which needs to be carried out frequently to adjust for any changes in conditions such as changing the sample field of view (Wei et al., 2015).

In order to quantify the detected secondary ion signals, it is necessary to use reference materials (standards) with known elemental abundances and isotope values in order to calculate the unknown abundances and isotope values of a sample (Stern, 2009). Quantifying the measurements acquired from secondary ion mass spectrometry analysis can be problematic due to unwanted interferences such as from 'matrix effects' which refer to the influence that a sample matrix (consisting of other minerals with a different composition surrounding the mineral of interest within a rock sample) has on the number of secondary ions generated per sputtered atom (the ion yield). A variable sample composition and/ or surface structure can be responsible for unpredictable and varied secondary ion yields (van der Heide, 2014) which results in extreme fractionation of elements and mass fractionation of isotope ratio measurements (Hoppe et al., 2013).

Additionally, for isotope ratio analyses, instrument mass fractionation (IMF) must be taken into account. IMF is introduced during sample analysis (sputtering and ionization) and leads to systematic errors in the derived isotope ratios. For example, lighter isotopes falsely appear to be more abundant relative to heavier isotopes due to small differences with the detection and transmission efficiencies for each isotope (Hoppe et al., 2013). By measuring a matrix-matched standard at the same time as a sample, both matrix effects and IMF can be removed if the standard has an identical composition to, or one that brackets, the unknown composition of the sample of interest. An appropriate standard is one where, for

the element of interest, the elemental abundance and isotope values have been well characterised and independently verified (van der Heide, 2014).

2.4.2. Analytical method

2.4.2.1. Quantification of standards used for NanoSIMS analyses

Four terrestrial apatite grains with known volatile abundances (including S and Cl) were used as reference standards for the measurements made on samples using the NanoSIMS within this research project. These included an apatite from Durango, Mexico ('Ap003'), an apatite from the Atlas Mountains, Morocco ('Ap004'), an apatite from the Crystal Lode Pegmatite Mine, Colorado, USA ('Ap005') and apatite from Lake Baikal, Sludyanka, Russia ('Ap018') (Figure 2.12). Francis McCubbin (Johnson Space Centre, *pers. comm.*) quantified the abundances of the two elements of interest for this project (S and Cl) (Table 2.1) via electron probe microanalysis at the Department of Earth and Planetary Sciences at the University of New Mexico and NASA JSC. Additionally, a nominally anhydrous ('dry') San Carlos olivine reference standard was used in order to both assess, and correct for, the total instrumental S and Cl background contribution resulting from measurement with NanoSIMS.

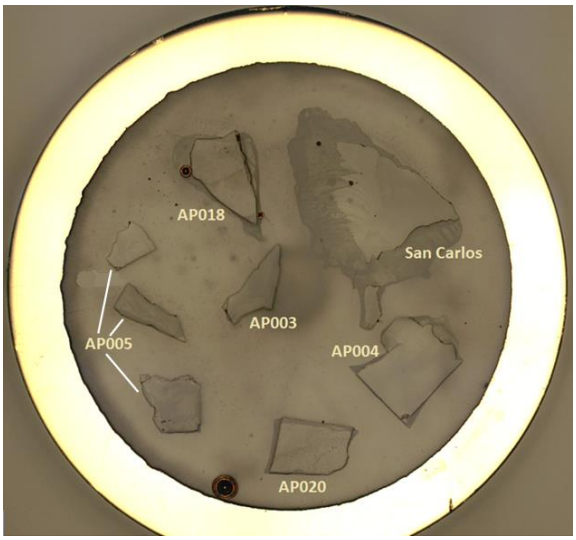

Figure 2.12. Photograph of mounted apatite reference standards. The 10 mm brass ring contains the apatite reference standards used regularly within this project, Ap003, Ap004, Ap005 and Ap018 (4 homogeneous grains) mounted in indium metal. Ap020 was used to demonstrate the ability to measure low abundance precisely. The large San Carlos olivine reference standard was used for background S and Cl measurements (image courtesy of Jessica Barnes, The Open University).

Table 2.1. Quantification of terrestrial apatite standards. The weight % oxide for S and Cl were determined by EPMA. The values in parenthesis are the 2σ standard deviation from the mean for all the analyses from each sample (Francis McCubbin, Johnson Space Centre, *pers. comm.*).

Reference standard	Location	SO_3 (wt.%)	Cl (wt.%)
Apatite Ap003	Durango, Mexico	0.36 ± 0.06	0.42 ± 0.07
Apatite Ap004	Atlas Mountains, Morocco	0.41 ± 0.06	0.32 ± 0.04
Apatite Ap005	Crystal Lode pegmatite mine, Colorado, U.S.A	0.10 ± 0.02	0.90 ± 0.13
Apatite Ap018	Lake Baikal, Sludyanka, Russia	0.96 ± 0.06	0.15 ± 0.03
Apatite Ap020	Unknown pegmatite region, India	0.0075 ± 0.012	0.0078 ± 0.016
San Carlos olivine	San Carlos, Arizona, USA	b.d.†	b.d. [a, †]

[a] Mosenfelder et al. (2011); † Determined by electron probe microanalysis (EPMA) at The Open University. b.d. = below detection.

2.4.2.2. Sample and standard preparation

The apatite standards (Ap003, Ap004, Ap005 and Ap018) used within this project were mounted and pressed into a 10 mm brass ring filled with indium metal and polished to leave a flat surface which is necessary for NanoSIMS to limit charge build up and improve precision (Barnes et al., 2014).

Subsequent to the SEM and EPMA work carried out within this project, all samples were gently cleaned with isopropanol (IPA) and laser sealed wipes to remove the previously applied carbon coat (from SEM/ EPMA analyses). Samples were then put into a beaker of IPA and placed in an ultrasonic bath (Bandelin SONOREX Digital DK 255 P) for 10 minutes at 60% vibrational power (at room temperature) for a thorough clean with use of sound energy vibrations. Samples were dried thoroughly with an air hose before being baked in a vacuum oven (along with the standard block) with a temperature of ~55° C for ~2-3 days in order to limit the absorption of any contaminating atmospheric gases prior to analysis with NanoSIMS.

Immediately after removal from the oven, samples and the mounted standards block, were coated with ~30 nm of gold using the EMITECH K575X peltier cooled gold sputter coater in order to make sample surfaces conductive for NanoSIMS analysis. Conductivity is required in order to remove any excess charge, following the build-up of ions, from an electrically non-conductive sample surface which would otherwise lead to measurement interference from local electrical fields (Höschen et al., 2015). Once gold coated, samples were loaded into a 'Geology' NanoSIMS sample holder which was positioned in the NanoSIMS airlock, where the surrounding pressure was reduced from ~10^{-5} mbar to ~10^{-7} mbar, to bake at 60 ˚C for ~2-3 days and degas any remaining surface contamination. The samples were subsequently moved into the vessel chamber (also under vacuum), where the pressure was reduced to ~10^{-8} mbar, to undergo further degassing in preparation for analysis. The last stage involved the transfer of samples into the analysis chamber where the pressure was ~10^{-9} mbar.

Following analysis, the gold coats that had been applied to the samples were removed with a 0.25 μm diamond paste and corresponding polishing Alpha Cloth. It was important to perform the task gently because there was a risk of plucking out or rounding off some of the grains from the thin section. Samples were then put in a beaker of IPA and placed in the ultrasonic bath to remove any residual diamond paste, following the method outlined above.

2.4.3. Analytical techniques

With guidance from the backscattered electron images (BSE) and secondary electron images (SEIs) acquired previously, the NanoSIMS reflected light camera (CCD camera) was used to locate the apatite regions of interest (ROIs) and to ensure that both sample and standard surfaces were in focus. Cross-referencing with the SEIs and cathodoluminescence (CL) meant that any cracks and holes within the apatite grains were avoided and zoned regions could be selected when choosing where exactly to position the primary ion beam on the sample.

The NanoSIMS 'imaging mode' was used throughout the project to measure both S and Cl which involved scanning (rastering) the focussed primary ion beam across the surface of the sample to detect and record the number of secondary ions that arrived at the electron

multipliers (EM) for each pixel of the scan (Kilburn and Wacey, 2015). The ion images consisted of a rastered area of 10 µm x 10 µm, with a resolution of 128 pixels x 128 pixels or 256 pixels × 256 pixels (depending upon the aperture slit (AS) settings). Each image consisted of between 50 and 500 measurement cycles (horizontal frames that accumulated with depth, typically leading to a pit depth of < ~1 µm), dictated by the counts per second achieved for the isotope of interest and the corresponding precision (e.g. longer measurement times were needed for samples with low counts of S ions to improve precision). The imaging mode produces elemental and isotopic distribution maps from which isotope ratios and element abundance can be calculated (Hoppe et al., 2013). Imaging mode was used throughout this project because of the heterogeneous nature of the apatite grains under investigation. It also made complex compositional structures easily observable and permitted areas containing hotspots to be de-selected with use of the data processing software 'L'image' (developed by Larry Nittler and marketed by the Carnegie Institution of Washington) (see section 2.4.3.3).

It was important to adjust the NanoSIMS tuning parameters to achieve the highest mass resolving power (MRP) for the highest number of ion counts. For example, where appropriate, the entrance, aperture and energy slit (ES, AS and EnS, respectively) widths were increased in order to raise the MRP (through separating/ resolving peaks) whilst the width of diaphragm D1 was increased in order to increase the number of ion counts (where D1-1 is the largest and D1-4 is the smallest aperture width which afford greater and lesser counts per second, respectively). Use of D1, ES and AS also permitted secondary ion beam focussing, whilst the exit slit (ExS) was used for beam positioning.

Throughout the analytical sessions, the EOS lens (Figure 2.10) was continually adjusted for optimal primary and secondary ion beam focussing. The centre line position of each mass was determined both vertically and horizontally by scanning the Cy, P2 and P3 deflectors before the secondary ions entered the ES and the mass spectrometer. The slit lens LF4 and the deflectors C3 and C4 were then adjusted to optimise the shape of the peak after ions had passed through the ES. Fine focussing of the secondary ion beam was achieved by the adjustment of the quadruple lens (Q). The aperture and slit settings used for all of the analytical sessions are detailed Table 2.2, where the parameters and the probe size were adjusted each session to be optimal for the source condition, sample elemental abundance and complexity of the sample's structure (e.g. zoned or containing hotspots).

Table 2.2. Summary of NanoSIMS settings used for analysis throughout the project.

Session	Vacuum (mbar)	Cs^+ probe current (pA) (approx.)	Diaphragm (D1)*	Entrance Slit (ES)*	Aperture Slit (AS)*
January 2018_S&Cl	3.5×10^{-9}	10	D1-4	ES-3	AS-2
May 2018_S&Cl	1.6×10^{-9}	25	D1-4	ES-3	AS-0
August 2018_S&Cl	3.6×10^{-9}	25	D1-4	ES-3	AS-0
October 2018a_Cl	3.6×10^{-9}	25	D1-4	ES-3	AS-0
October 2018b_Cl	2.9×10^{-9}	2	D1-3	ES-3	AS-0
November 2018_Cl&S	1.1×10^{-9}	2	D1-3	ES-4	AS-0
December 2018_Cl	1.1×10^{-9}	2	D1-2	ES-4	AS-0
March 2019_S	1.7×10^{-9}	40	D1-3	ES-4	AS-2
April 2019_Cl	1.6×10^{-9}	20	D1-4	ES-4	AS-0
April 2019_S	1.3×10^{-9}	40	D1-3	ES-4	AS-2
August 2019_S	-	20	D1-4	ES-4	AS-2
August 2019_Cl	-	20	D1-4	ES-4	AS-0

Four terrestrial apatite standards (Ap003, Ap004, Ap005 and Ap018 (Table 2.1) with known volatile abundances (Francis McCubbin, Johnson Space Centre, *pers. comm*.) were used during the analytical sessions to calibrate the unknown volatile abundances and isotope values of the samples. For all reference standard and sample analyses, a positive caesium (Cs^+) primary beam source with a probe current of 200 pA was used to 'pre-sputter' the target surfaces prior to isotope measurement so that the gold coat and any remaining surface contamination was removed. This was achieved by rastering the beam over an area of 12 μm x 12 μm or 15 μm x 15 μm for ~3-5 minutes.

Before pre-sputtering the sample, real time secondary ion images were monitored with the use of either ^{31}P (used in earlier analyses sessions) or $^{40}Ca^{16}O$ to ensure that the probe was correctly positioned on the desired apatite grain. Likewise, real time monitoring of ^{32}S during pre-sputtering ensured that cracks and sulfur hotspots that might have interfered with the analysis were avoided as much as they possibly could be.

As a proof of concept, measurement of S and Cl abundance and isotopes in the apatite grains of lunar meteorite SaU 169 with NanoSIMS were performed before measuring any of the apatite grains in the Apollo samples. This was to ensure that the modified

NanoSIMS S and Cl protocols adopted for this project were feasible and would result in worthwhile and reproducible volatile measurement results with respect to the Apollo samples (Appendix A).

2.4.3.1. Chlorine protocol

The Cl protocol adopted for this project was based on a modified, existing Cl protocol that had previously been shown to be successful (Tartèse et al., 2014b; Barnes et al., 2016). For the analysis of Cl with NanoSIMS, a mass resolving power of ~8,000 (Cameca definition) was achieved, which was sufficient to resolve isobaric interferences, such as from $^{36}S^{1}H^{+}$ for measurement of isotope ^{37}Cl, and from $^{16}O^{18}O^{1}H^{+}$ for measurement of ^{35}Cl. Peak centring for Cl analysis was always performed on ^{35}Cl which had an easily discernible peak and sufficient counts per second (cps).

The NanoSIMS instrument was set up in the multi-collection mode to simultaneously collect negative secondary ions of ^{18}O, ^{32}S, ^{34}S, ^{35}Cl, ^{37}Cl and $^{40}Ca^{16}O$ on electron multipliers (EM) (with detector position numbers 2 to 7, respectively). Following pre-sputtering, the Cs^{+} primary beam rastered area was reduced to 10 μm x 10 μm and $^{18}O^{-}$ was monitored to ensure that ~20,000 cps were achieved (although not always possible with the lower probe sizes) by using the most optimal focus and alignment for the secondary ion beam (e.g. through automated scanning of the EOS lens and vertical and horizontal scans of the deflector plates P2/P3 and Cy).

To offset any positive electrical charge deposited by the ion beam onto the sample surface, the electron gun (e-gun) settings were adjusted, when necessary, until the counts reaching the detectors were stable. Chlorine hotspots were few and far between but any small and faint hotspots that were apparent were easily avoided by moving the primary beam (probe) to more homogeneous areas whilst remaining fully on the apatite grain.

The use of a suitable probe current was very dependent upon the source condition and how Cl-rich the sample was likely to be and, therefore, how many cps were measured. Scientific literature was used as a guide for the abundance of Cl within apatite where SIMS measurements had been previously performed by other researchers. As a result, the probe current used for Cl measurement varied between 2 pA and 25 pA (Table 2.2 settings)

throughout the project. The lowest probe current of 2 pA was employed for a small apatite grain (not quite filling the 10 μm x 10 μm area) with a particularly complex, zoned structure because it allowed any high counts of Cl coming from nearby cracks to be included within the 10 μm x 10 μm image without jeopardising the precise measurement of Cl counts from the apatite grain. The typical Cl analysis time across all analysis sessions was between ~30 minutes and two hours which involved 50 to 200 measurement frames. The number of measurement frames used for the apatite reference standard always matched those used for the sample.

2.4.3.2. Sulfur protocol

The S and Cl NanoSIMS isotope analyses were performed on the same spot, with Cl measurements always carried out first. There were two reasons for this, the first was so that the abundance of S within a sample could be gauged from the Cl analyses sessions (^{32}S ions were collected as part of the Cl protocol), and the second was so that any possible residual S contamination on the sample surface could be removed during the Cl sputtering process. This meant that the S isotope measurements started at a slightly deeper level within the sample, with a typical depth of < ~1 μm – representing the deepest pit created during the longest Cl analyses (~200 measurement frames in January 2017) (Barnes, 2014).

The Cl protocol was modified so that, rather than the NanoSIMS tuning being applied to the peak positions of Cl within the apatite standards, the instrument was optimally tuned for S, to ensure greater precision and reproducibility for S isotope measurements. For example, the NanoSIMS ion optics were tuned (section 2.4.3) to achieve a mass resolving power (MRP) between ~7,000 and 11,000 (Cameca definition (Equation 2.2)) which was sufficient to resolve isobaric interferences for S isotope measurements such as $^{31}P^{1}H$ and O_2 when measuring ^{32}S, and ^{34}O ($^{16}O + {}^{18}O$) and $^{33}S^{1}H$ when measuring ^{34}S. Peak centring for the S measurements was conducted on either ^{32}S or ^{18}O, depending upon the cps achieved for S, because a clear single peak was easily discernible for either with the MRP achieved.

Initially, the NanoSIMS was set up to simultaneously collect the negative secondary ions of ^{18}O, ^{31}P, ^{32}S, ^{33}S, ^{34}S, and $^{40}Ca^{16}O$ on electron multipliers (EM) (with detector position

numbers 2 to 7, respectively). As with Cl analysis, the Cs^+ beam rastered area was reduced to 10 μm x 10 μm following pre-sputtering, and $^{18}O^-$ was monitored to ensure that, typically, ~20,000 counts per second were achieved (dependent upon probe size) by tuning the secondary ion beam and adjusting the e-gun to offset charge. The typical analysis time varied between ~1 and ~5 hours, where longer times were necessary due to low count rates of ^{32}S, which amounted to 100 to 500 measurement frames. The number of measurement frames used for the apatite reference standard always matched those used for the sample.

The S protocol was continually improved throughout the project and, from the second S analysis session in May 2018, the protocol was modified in order to counteract the tremendous ionisation of the sample surface caused by very high counts of ^{31}P reaching the detector. By removing ^{31}P, the collected negative secondary ions became ^{18}O, ^{32}S, ^{33}S, ^{34}S, ^{35}Cl and $^{40}Ca^{16}O$ (substituting ^{35}Cl for ^{37}Cl whenever the counts of ^{35}Cl became too high relative to ^{32}S).

As with the Cl analysis, the probe current used for the S measurements (Table 2.2) depended upon the instrument source conditions, how S-rich the sample was and how small (e.g. <10 μm x 10 μm) and complex the structure of the apatite grain was. The probe size was particularly important for S with regards to high cps of S because hotspots of S, some with >100,000 cps S, were far more prevalent than for Cl. If the S hotspots could not be completely avoided, for example, if moving away from the hotspot would have meant that the beam was not solely on an apatite grain, then a lower probe size could be used. During post-analysis processing, it was also possible to use only signals (counts) collected from the most homogeneous portions of the apatite grain (achieved with the L'image software – section 2.4.3.3).

2.4.3.3. Image processing

Each ion imaging analysis performed with NanoSIMS typically consisted of between 50 and 500 frames (dependent upon the S or Cl abundances within the sample) which were stitched together and processed using the L'image software (Larry Nittler, Carnegie Institution of Washington) to form one image. Unlike the Faraday cup (FC) which measures secondary ions directly, the electron multipliers (EM) used throughout all of the analytical sessions for this project measure an amplified electrical pulse produced by the

arriving ions, therefore, the software was used to correct each individual pixel for detector dead time to determine the true secondary ion count rate. This process corrects for the under-recording of new secondary ions reaching the EM detectors in quick succession which can happen if a previous secondary ion signal is still being processed and may result in two or more ions being recorded as only one ion (Kilburn and Wacey, 2015). Additionally, any sample drift that may have occurred with depth during the analysis, (e.g. due to stage or primary ion beam shifts) was corrected with a sample alignment operation within the software.

From the acquired sample images, homogeneous regions of interest (ROI) could be selected by using the 'ratio profile' function within the L'image software which highlighted variations in ratios, for example, $^{32}S/^{18}O$, $^{34}S/^{32}S$, $^{35}Cl/^{18}O$ and $^{37}Cl/^{35}Cl$, across the 10 μm x 10 μm image. Typically, the homogeneous region of interest selected for an apatite standard was ~7 μm x 7 μm (Figure 2.13). For the samples, only regions with little, to negligible, variation were isolated and used for data processing, with heterogeneous regions being excluded. The software permitted the easy removal of regions containing hotspots of S or, to a lesser extent, Cl, which presented clear differences in isotope ratios relative to the remaining homogeneous apatite grain. Hotspots were deemed to be surface contamination or unrepresentative inclusions within the apatite grains because they were found to disappear with analysis depth, which was obvious to see with the images. Likewise, cracks or apatite grain boundaries that could not be avoided within the original 10 μm x 10 μm analysis area were also excluded from the main region of interest with use of the software. If the sample image showed clear apatite zoning, the software was used to determine whether S and Cl abundance and isotopic differences existed between the zones.

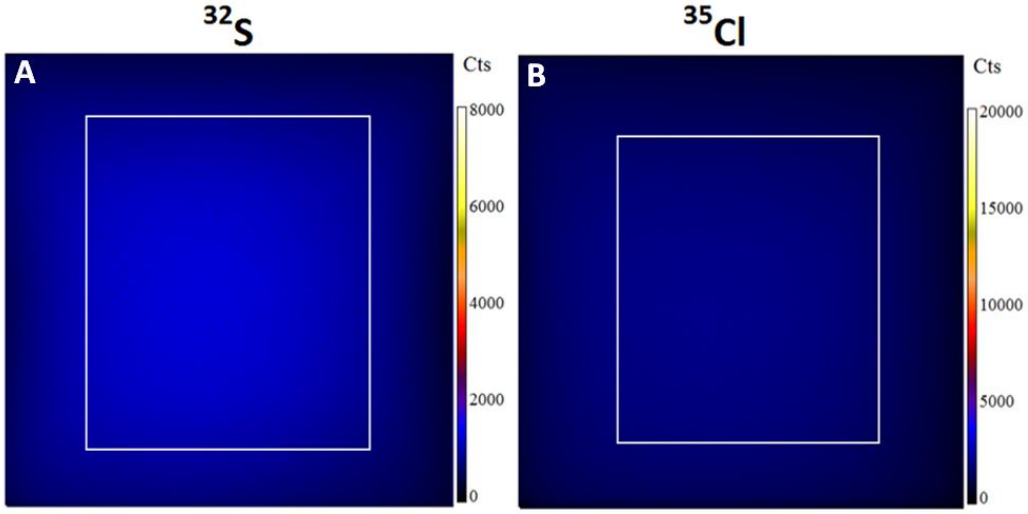

Figure 2.13. Examples of homogeneous apatite reference standard images acquired by NanoSIMS and processed with L'image. **A)** Illustrates a typical area (white outline) selected for ^{32}S (apatite standard Ap005 run on the 29th August 2018), whereas **B)** shows a typical area selected for ^{35}Cl (apatite standard Ap004 run on 15th August 2018). Each full ion image is 10 µm x 10 µm. The selected areas were used for processing the acquired data to calculate S or Cl abundance and isotope values of the unknown sample.

2.4.4. Data Reduction

2.4.4.1. Calibrating for abundance and assessment of background

In order to use the primary reference standards to calculate the unknown abundances of S and Cl within the samples and within the San Carlos olivine used for assessing the total instrumental S and Cl background contribution, multiple terrestrial apatite standards (typically Ap004, Ap005 and Ap018, with Ap003 occasionally included) were measured during each analytical session to produce a graph with a calibration gradient. This was achieved by plotting the known (true) abundances of S or Cl (ppm) for the apatite standards (Francis McCubbin, Johnson Space Centre, *pers. comm*.) against the corresponding measured isotope ratios $^{32}S/^{18}O$ or $^{35}Cl/^{18}O$ (for S and Cl analyses, respectively) for those standards. Once plotted, linear regression of the two variables (true abundance and measured ratios) was performed using the OriginPro software, whereby a linear best-fit line was forced through the origin of the graph. The unknown sample abundances (S or Cl in ppm) were calculated by multiplying the measured $^{32}S/^{18}O$ or $^{35}Cl/^{18}O$ ratios of the samples by the gradient of the calibration line. Likewise, in order to determine the total instrumental background (S and Cl in ppm), the measured $^{32}S/^{18}O$ or $^{35}Cl/^{18}O$ ratios of the San Carlos olivine were also multiplied by the calibration gradient

with the resulting value being subtracted from the calculated S or Cl abundance (ppm) of the sample(s) (Equation 2.3 in section 2.4.4.2). The total background for both S and Cl was calculated to be ~0.1 ppm.

Depending upon whether S or Cl abundance was being measured within an analytical session, an apatite standard with an abundance closest to that of the unknown sample was typically measured more than once during a 24 hour period. For example, one of Ap003, Ap004 or Ap005 was run for S measurements (with abundances between 392 ppm S and 1627 ppm S), however, Ap005 was most commonly used due to the low abundance of S within the majority of samples (Table 2.1). Likewise, for Cl measurements, Ap004 (with an abundance of 3,182 pm Cl) was typically measured more than once during a 24 hour period because the Cl abundance within the apatite standard was closest to that of the unknown samples. Where multiple measurements of the standards existed, they were included within the linear regression so that quantitative variations in the measured ratios during an analytical session were incorporated into the uncertainty attributed to the calibration gradient (see Equation 2.4 in section 2.4.4.2).

Figures 2.14 and 2.15 show examples of the calibration lines generated for both Cl and S during the course of this project (all of the calibration data are presented in Appendix B, Tables B.3 and B.4). The gradient derived from the best-fit lines for Cl and S varied between different analytical sessions. The possible reasons for the variation are that different primary and secondary ion optic settings were employed (e.g. different aperture widths or distances between apatite surface and main lenses) depending upon the instrument conditions (Greenwood et al., 2011) or because there were differences in the ionisation of the apatite surface (e.g. due to nanometre-scale features such as inclusions or contamination or micro-scale topography) (Mosenfelder et al., 2011) or that there were differences in the charge compensation related to the e-gun settings (Hauri et al., 2002).

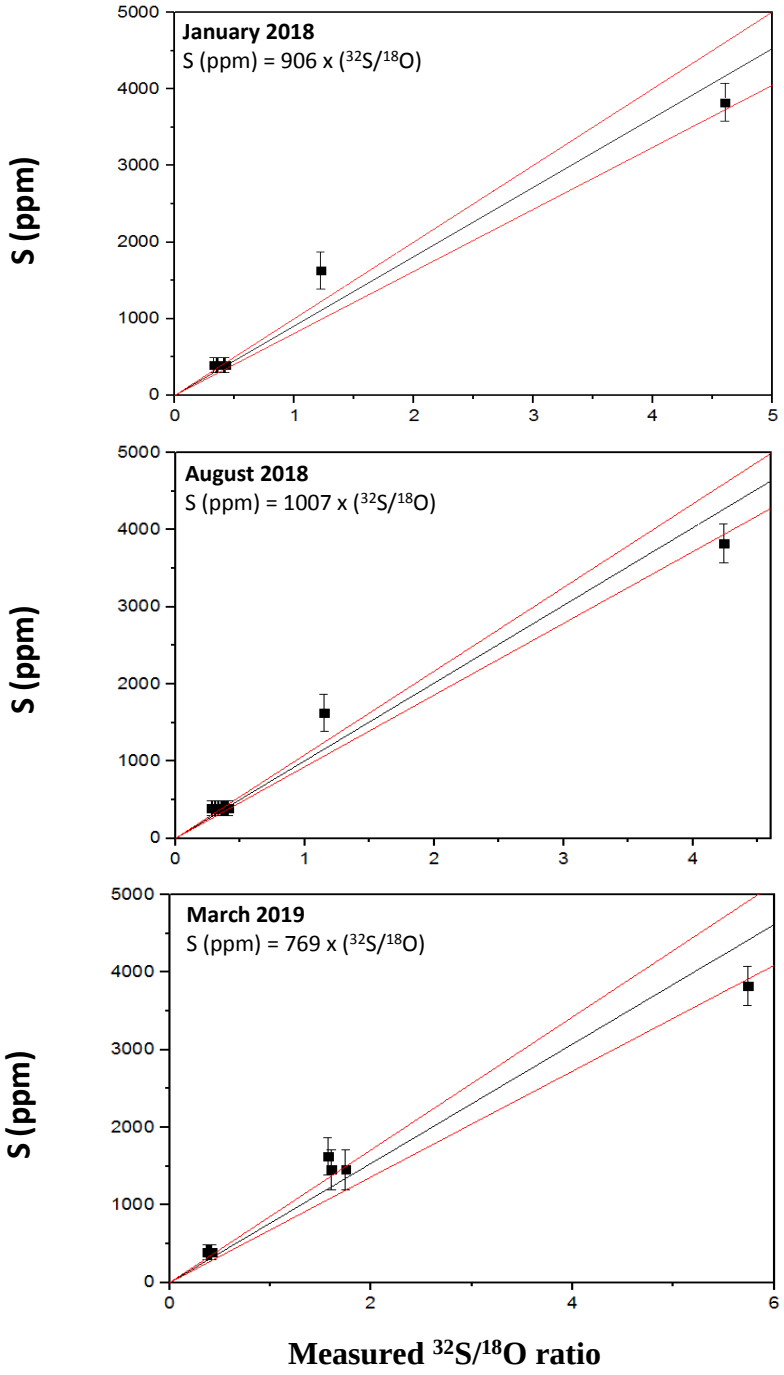

Figure 2.14. Calibration graphs for S apatite standards. The graphs show typical calibration lines generated for S during the course of NanoSIMS analysis (January 2018–March 2019). Black squares represent known S (ppm) abundance (Francis McCubbin, Johnson Space Centre, *pers. comm.*) for apatite standards Ap005, Ap004, Ap003 and Ap018 (in ascending order) plotted against the $^{32}S/^{18}O$ ratio measured during an analytical session. The black line is the gradient used to calculate S abundance (see section 2.4.4.2.) and the red lines are the upper and lower 95% confidence levels. The error bars are 2σ standard deviation.

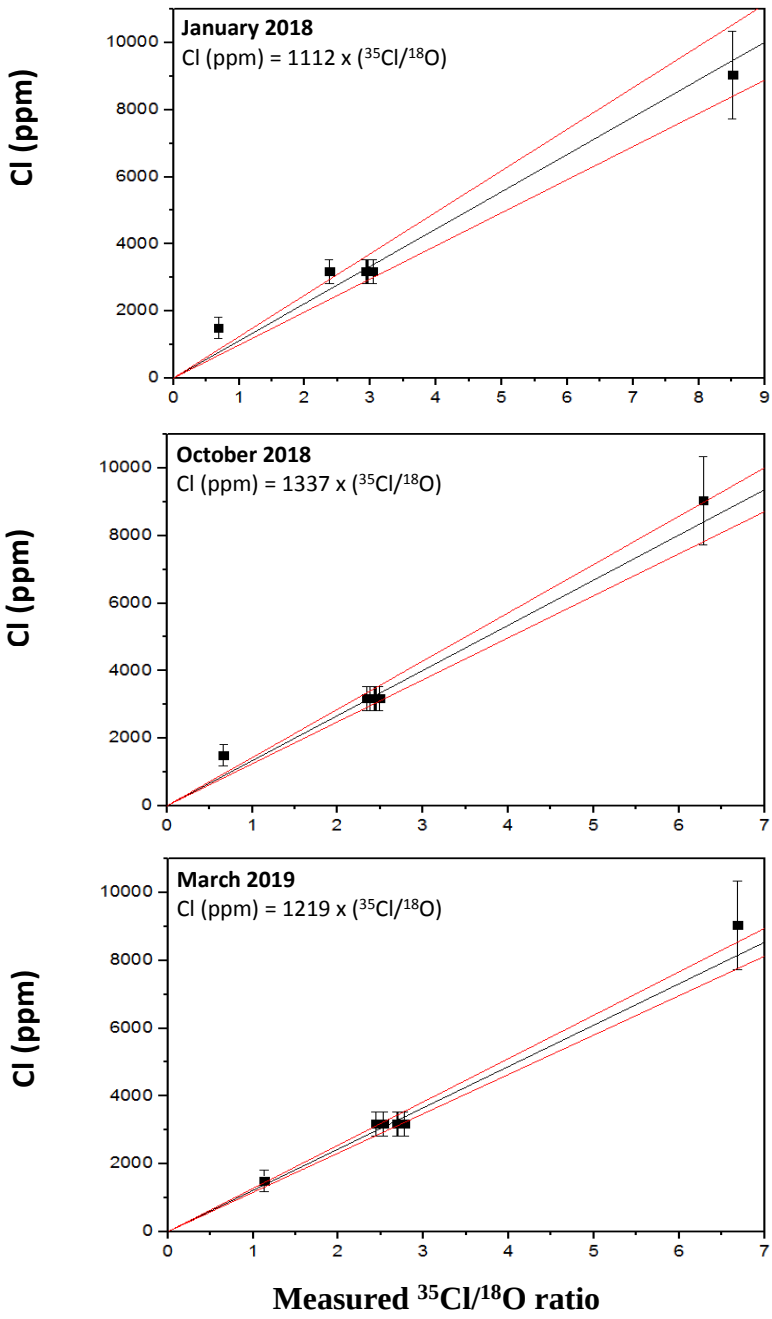

Figure 2.15. Calibration graphs for Cl apatite standards. The graphs show typical calibration lines generated for Cl during the course of NanoSIMS analysis (January 2018 – March 2019). The black squares represent the known Cl (ppm) abundance values (Francis McCubbin, Johnson Space Centre, *pers. comm.*) for the apatite reference standards Ap018, Ap004 and Ap005 (in ascending order) plotted against the $^{35}Cl/^{18}O$ ratio measured during an analytical session. The graph symbols and error bars are as Figure 2.14.

2.4.4.2. S and Cl abundance measurements and calculations

Daily measurement of a standard enabled the stability of the instrument to be confirmed by checking the position of the peaks (e.g. ^{18}O, ^{32}S, ^{33}S and ^{34}S for a sulfur session) and, if necessary, adjusting the lenses (EOS) and deflector plates (P2, Cy and P3) so that the MRP was optimal for the isotopes of interest. The checks also ensured that the number of ions reaching the electron multipliers were similar across different days within an analytical session.

The gradient(s) determined from the calibration lines(s) was used to calculate the corresponding unknown S and Cl abundances of the samples (Equation 2.3).

$$\text{Abundance (ppm)} = (m \times r_m) - b \qquad \text{Equation 2.3}$$

Where, m = gradient of the calibration line produced with the known apatite standards; r_m = measured ratio ($^{32}S/^{18}O$ or $^{35}Cl/^{18}O$ for S or Cl abundance, respectively) for the (unknown) sample under investigation; b = total instrumental background contribution (S or Cl) calculated from the San Carlos olivine (~0.1 ppm for S and Cl).

The percentage uncertainty associated with the calibration line was calculated by taking the percentage difference between the gradient and the 95% upper confidence level (Equation 2.4) of the gradient. To calculate the total uncertainty for derived sample abundances, the square root of the sum of the squares (Equation 2.5) was adopted which combined the uncertainty related to the calibration gradient (slope error) with the poisson uncertainty associated with the measured isotope ratios which was generated by the software (L'image) used to process the NanoSIMS images.

$$\text{Calibration gradient uncertainty (2}\sigma\text{ \%)} = \frac{(UCL - m)}{m} \times 100 \qquad \text{Equation 2.4}$$

Where, *UCL* = the 95% upper confidence level of the calibration line gradient.

$$\text{Abundance uncertainty (2}\sigma\text{ ppm)} = \sqrt{\left(\left(\frac{a}{100} \times 2\right)^2 + \left(\frac{b}{100}\right)^2\right)} \times c \qquad \text{Equation 2.5}$$

Where, *a* = the poisson error associated with the measured ratio for the sample (generated by L'image software); *b* = calibration gradient uncertainty (2σ) calculated in Equation 2.4; and *c* = abundance calculated in Equation 2.3.

2.4.4.3. Measurement and calculation of the unknown S and Cl isotope values

For the Cl isotope measurements, the apatite standard Ap004 (measured on a daily basis) was used within the calculations to determine the unknown isotope Cl value of the sample. The standard has a previously determined $\delta^{37}Cl$ value of +0.11‰ (Barnes et al., 2016), relative to the $^{37}Cl/^{35}Cl$ value of 0.31977 for standard mean ocean chloride (SMOC), and is reported in parts per thousand ('per mil': ‰). The delta (δ) notation (Equation 2.6) is used to report the isotope composition of Cl for all of the samples throughout this project relative to the $^{37}Cl/^{35}Cl$ value of SMOC.

$$\delta^{37}Cl_{(SMOC)}\ (‰) = [(^{37}Cl/^{35}Cl)_{sample} / (^{37}Cl/^{35}Cl)_{SMOC} - 1] \times 1000 \qquad \text{Equation 2.6}$$

For S isotopic measurements, the apatite standard Ap003 (from Durango, Mexico) was used within the calculations to determine the unknown S isotope value of the sample. Standard Ap003 ('Durango') has a previously determined $\delta^{34}S$ value of +0.34‰ ± 0.02‰ (Economos et al., 2017) (reported in parts per thousand ('per mil': ‰)), relative to the International Atomic Energy Agency (IAEA) Vienna-Canyon Diablo Troilite (V-CDT) standard that has a $^{34}S/^{32}S$ value of 0.04416 (Ding et al., 2001; Hauri et al., 2016). The conventional delta (δ) notation (Equation 2.7) is used to report the isotopic composition of S for all of the samples in this project relative to the $^{34}S/^{32}S$ value of V-CDT.

$$\delta^{34}S_{(V\text{-}CDT)}\ (‰) = [(^{34}S/^{32}S)_{sample} / (^{34}S/^{32}S)_{V\text{-}CDT} - 1] \times 1000 \qquad \text{Equation 2.7}$$

As previously stated, an apatite standard with a known S abundance closest to that of the unknown sample was measured on a daily basis, with Ap005 (lowest S abundance) being most commonly used due to the relatively low S abundance within most samples. In order to determine the S isotope value for the majority of samples that were not measured alongside Ap003 (with a known $\delta^{34}S$ value), the $\delta^{34}S$ values of secondary apatites Ap005 and Ap004 were calculated by using Ap003 as a primary reference standard. This was achieved with NanoSIMS through use of the 'spot analysis' mode to repeatedly measure

the $^{34}S/^{32}S$ ratio of Ap003, Ap004 and Ap005. For this purpose, spot analysis (rather than the imaging mode used for complex Apollo sample analysis) could be used because of the homogenous nature of the standards. The negative secondary ions of ^{18}O, ^{32}S, ^{33}S, ^{34}S, and $^{40}Ca^{16}O$ were collected using a probe size of ~40 pA, with each standard repeatedly measured for 6 frames (lasting ~20 minutes) under identical measurement conditions within the space of 24 hours.

The S spot analysis was repeated on different days, spanning two different months in order to acquire a reproducible $^{34}S/^{32}S$ ratio value for all three standards. The average of the measured $^{34}S/^{32}S$ ratio of Ap004 and Ap005 was corrected against Ap003 for instrument mass fractionation (IMF) (Equation 2.8) and was then referenced to the known $\delta^{34}S_{(V\text{-}CDT)}$ value of Ap003 (+0.34‰ ± 0.02‰ (Economos et al. 2017)) (Equation 2.9) to give a $\delta^{34}S_{(V\text{-}CDT)}$ value of +18.6‰ ± 0.8‰ and +10.7‰ ± 0.87‰, for Ap004 and Ap005, respectively.

In order to calculate the true S isotope value for the samples, the average $^{34}S/^{32}S$ value of the standard measured (whether Ap003, Ap004 or Ap005) within a 24 hour period (where both sample and standard were analysed with the imaging mode) was used to correct the sample $^{34}S/^{32}S$ ratio measured within the same period for IMF, according to Equation 2.8. Likewise, to calculate the true Cl isotope value for the samples, the average $^{37}Cl/^{35}Cl$ value of the reference standard Ap004, measured within a 24 hour period, was used to correct the sample $^{37}Cl/^{35}Cl$ ratio measured within the same period for instrument mass fractionation (Equation 2.8).

$$a = \left(\frac{b}{c} - 1\right) \times 1000‰ \qquad \text{Equation 2.8}$$

Where, a = the corrected measured ratio ($^{34}S/^{32}S$ or $^{37}Cl/^{35}Cl$) of the (unknown) sample; b = the measured ratio ($^{34}S/^{32}S$ or $^{37}Cl/^{35}Cl$) of the sample; c = the average measured $^{34}S/^{32}S$ or $^{37}Cl/^{35}Cl$ ratio of the apatite standard.

The corrected ratios (Equation 2.8) were then referenced to the known $\delta^{34}S_{(V\text{-}CDT)}$ and $\delta^{37}Cl_{(SMOC)}$ values of Ap003 (+0.34‰) and Ap004 (+0.11‰), respectively, according to Equation 2.9.

$$\delta x\ (‰) = (a + y) + \left(\frac{a \times y}{1000}\right) \quad \text{Equation 2.9}$$

Where, δx = the standardised isotope value of the sample ($\delta^{34}S_{(V\text{-}CDT)}$ or $\delta^{37}Cl_{(SMOC)}$); a = the corrected measured ratio of the sample (Equation 2.8); y = the known $\delta^{34}S_{(V\text{-}CDT)}$ or $\delta^{37}Cl_{(SMOC)}$ value of apatite standards Ap003 or Ap004, respectively.

The daily ratio measurements of the apatite reference standard (Ap003, Ap004 or Ap005) were used to assign a per mil (‰) reproducibility uncertainty to the isotope values derived for the samples. The uncertainty was calculated by dividing the standard deviation (2σ) of the ratio ($^{37}Cl/^{35}Cl$ or $^{34}S/^{32}S$) measured on the standard by the average ratio ($^{37}Cl/^{35}Cl$ or $^{34}S/^{32}S$) measured on the standard and multiplying by 1000‰. In order to calculate the total uncertainty of the sample measurements, error propagation (Equation 2.10) was used to combine the external reproducibility error of the reference standard with the internal uncertainty generated by the NanoSIMS software (L'image) for the analytical measurements.

$$\delta x\ 2\sigma\ (‰) = \sqrt{((f)^2 + (g \times 2)^2)} \quad \text{Equation 2.10}$$

Where, $\delta x\ 2\sigma$ = the total uncertainty (‰) for the measured isotope values, $\delta^{37}Cl$ or $\delta^{34}S$, expressed as 2σ; f = the error from the measured ratio of the apatite standard (‰) (derived by dividing the average by the standard deviation (2σ) and multiplying by 1000‰; g = the error (‰) generated by the NanoSIMS L'image software (given as 1σ, therefore, multiplied by 2 in the above equation).

2.4.5. Reproducibility: abundance and isotope measurements

2.4.5.1. Sulfur

In order to confirm the reproducibility of the measurements carried out with NanoSIMS, repeated S abundance (ppm) measurements of the main apatite standard, Ap005, with a known value (392 ± 100 ppm S) were performed during the March 2019 analytical session (Figure 2.16). The error attributed to the measurements combines both the 2 sigma (2σ)

uncertainty associated with the analytical measurement of the $^{32}S/^{18}O$ ratio and the 2σ uncertainty related to the gradient of the calibration line.

The typical precision (shown here for the March 2019 analytical session) was ~11 ppm. This was calculated by taking the standard deviation (2σ) of the average measured $^{32}S/^{18}O$ ratios (n = 4) for Ap005. Figure 2.16 shows that, within error, the measurements performed were also accurate based on the external abundance measurements of Ap005 by Francis McCubbin (Johnson Space Centre, *pers. comm.*).

Likewise, the reproducibility of the $^{34}S/^{32}S$ ratio measurements can be demonstrated with the repeat measurement of the secondary standard Ap005 (Figure 2.16) (with a value of +10.7‰ ± 0.87‰, derived by S spot analysis in previous section 2.4.4.3) that was performed during the August 2019 analytical session. The $\delta^{34}S$ value of Ap005 was calculated by correcting the $^{34}S/^{32}S$ ratio measurements for IMF and then referencing to the primary standard Ap003 (+0.34‰ ± 0.02‰ (Economos et al., 2017)). The uncertainty (2σ) combines the reproducibility associated with the $^{34}S/^{32}S$ ratio measurement of the primary standard Ap003 and the internal analytical uncertainty of the $^{34}S/^{32}S$ ratio measurement of Ap005.

The typical precision, demonstrated here for the August 2019 analytical session, was 0.2‰. This was calculated by taking the standard deviation (2σ) of the average measured $^{34}S/^{32}S$ ratios (n = 4) for Ap005. Figure 2.16 shows that, within error, the measurements performed were also accurate based on the known S isotope value of Ap005.

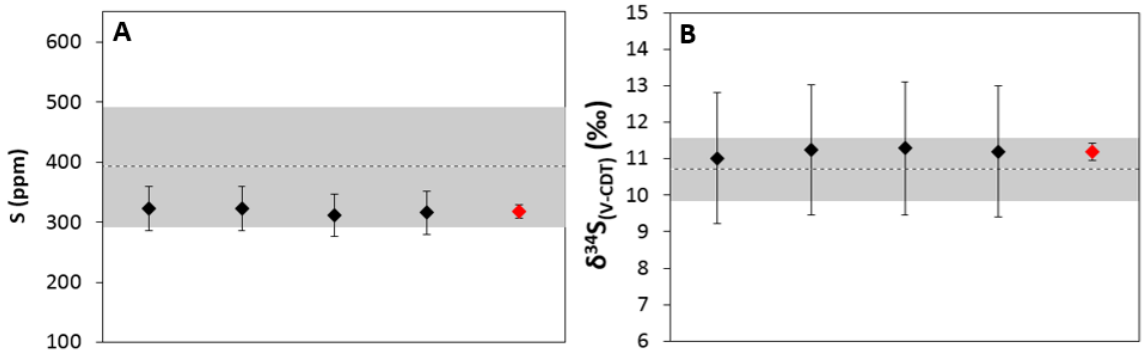

Figure 2.16. The precision and accuracy of S measurements. **A)** S abundance (ppm) of Ap005 (black diamonds) from the March 2019 analytical session. The dashed line at 392 ± 100 ppm represents the true (known) S abundance of Ap005, where the grey band denotes the 2σ uncertainty (Francis McCubbin, Johnson Space Centre, *pers. comm.*). **B)** S isotope ($\delta^{34}S_{V\text{-}CDT}$ (‰)) values of Ap005 (black diamonds) from the August 2019 analytical session. The dashed line at +10.7‰ ± 0.87‰, represents the known S isotope value of Ap005, with the grey band representing the 2σ uncertainty (derived in this project). For both **A)** and **B)**, the errors associated with each measurement point represent the 2σ uncertainty and the red diamond is the average of the measurements (n = 4), where the error bars represent the standard deviation (2σ) (see text for details).

2.4.5.2. Chlorine

Similarly to S, in order to confirm the reproducibility of the Cl measurements performed with NanoSIMS, repeated Cl abundance (ppm) measurements of the main apatite standard, Ap004, with a known value (3,182 ± 351 ppm Cl), were performed during the March 2019 analytical session (Figure 2.17). The error attributed to the measurements combines both the 2 sigma (2σ) uncertainty associated with the analytical measurement of the $^{35}Cl/^{18}O$ ratio and the 2σ uncertainty related to the gradient of the calibration line.

The typical precision (shown here for the March 2019 analytical session) was ~104 ppm at 2σ. This was calculated by taking the standard deviation (2σ) of the average measured $^{35}Cl/^{18}O$ ratios (n = 4) for Ap004. Figure 2.17 demonstrates that, within error, the measurements performed were also accurate based upon the external abundance measurements of Ap004 by Francis McCubbin (Johnson Space Centre, *pers. comm.*).

The reproducibility of the $^{37}Cl/^{35}Cl$ ratio measurements can be demonstrated with the repeat measurement of the secondary standard Ap004 (Figure 2.17) (with a value of +0.11‰ (Barnes et al., 2016)) that was performed during the August 2019 analytical

session. The $\delta^{37}Cl$ value of Ap004 was calculated by correcting the $^{37}Cl/^{35}Cl$ ratio measurements for IMF and then referencing to the primary standard Ap003 with a value of +0.3‰ (Barnes et al., 2019)). The uncertainty (2σ) combines the reproducibility associated with the $^{37}Cl/^{35}Cl$ ratio measurement of the primary standard Ap003 and the internal analytical uncertainty of the $^{37}Cl/^{35}Cl$ ratio measurement of Ap004.

The typical Cl isotope precision, demonstrated here for the August 2019 analytical session, was 0.4‰, calculated by taking the standard deviation (2σ) of the average measured $^{37}Cl/^{35}Cl$ ratios (n = 4) for Ap004. Figure 2.17 shows that, within error, the measurements performed were also accurate based on the known Cl isotope value of Ap004.

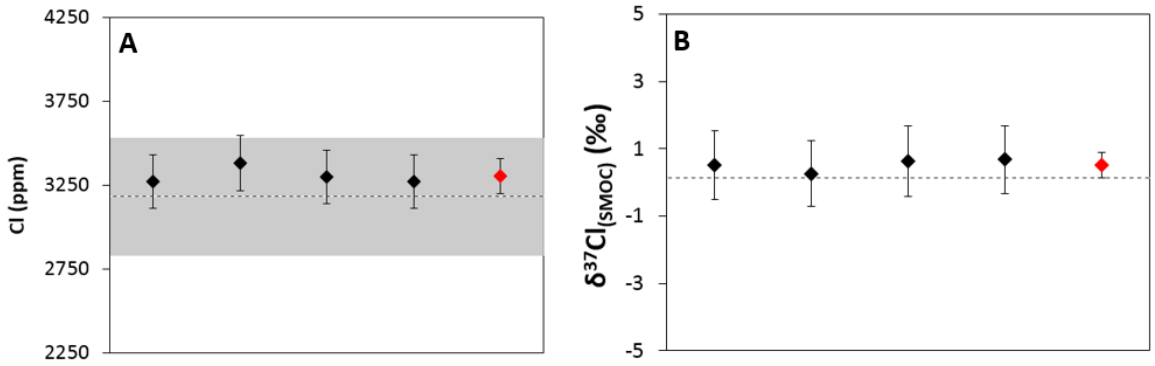

Figure 2.17: The precision and accuracy of Cl measurements. **A)** Cl measurements (ppm) of Ap004 (black diamonds) based on the March 2019 analytical session. The dashed line at 3,182 ± 351 ppm Cl represents the true (known) Cl abundance of Ap004, where the grey band denotes the 2σ uncertainty (Francis McCubbin, Johnson Space Centre, *pers. comm.*). **B)** Cl isotope ($\delta^{37}Cl_{SMOC}$ (‰)) values of Ap004 (black diamonds) from the August 2019 analytical session. The dashed line at +0.11‰ represents the known Cl isotope value of Ap004, (Barnes et al., 2016). For both **A)** and **B)**, the errors associated with each measurement point represent the 2σ uncertainty and the red diamond is the average of the measurements (n = 4), where the associated error bars represent the standard deviation (2σ) (see text for details).

In order to demonstrate the ability of the NanoSIMS technique to measure isotopes precisely for samples with very low abundance levels, an experiment to confirm measurement reproducibility was devised to repeatedly measure the $^{37}Cl/^{35}Cl$ ratio of apatite Ap020, which is a known to have a very low abundance of 78 ± 162 ppm Cl (Francis McCubbin, Johnson Space Centre, *pers. comm.*). The $\delta^{37}Cl$ value of Ap020 was calculated by correcting the $^{37}Cl/^{35}Cl$ ratio measurements for IMF and then referencing to the primary standard Ap003 (known value of +0.3‰ (Barnes et al., 2019)). The uncertainty (2σ) combines the reproducibility associated with the $^{37}Cl/^{35}Cl$ ratio

measurement of the primary standard Ap003 and the internal analytical uncertainty of the $^{37}Cl/^{35}Cl$ ratio measurement of Ap020. The isotopic precision attained for Ap020 was 0.3‰, calculated by taking the standard deviation (2σ) of the average measured $^{37}Cl/^{35}Cl$ ratios (n = 4) for Ap020 (Figure 2.18). In addition, the Cl abundance calculated for Ap020 was 14 ± 6 ppm Cl (2 σ) which is within the error of the value reported (78 ± 162 ppm Cl) by Francis McCubbin (Johnson Space Centre, *pers. comm.*) which also demonstrates the ability of the NanoSIMS technique to accurately measure low abundance levels. Whilst the total uncertainty of each measurement is higher due to poorer counting statistics on low abundance samples, there is no obvious isotopic effect when measuring samples with low abundances.

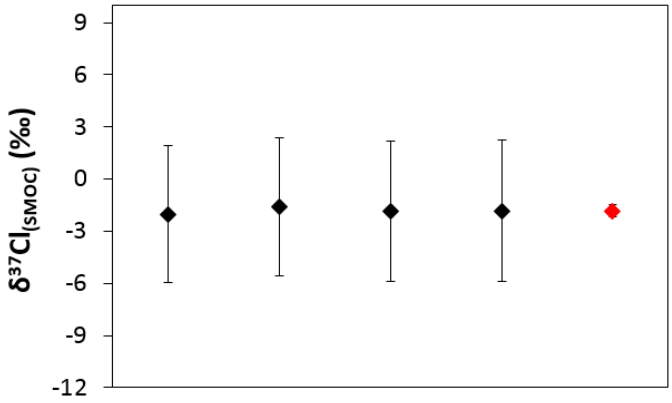

Figure 2.18. The reproducibility of $^{37}Cl/^{35}Cl$ ratio measurements for low Cl abundance. Black diamonds show the Cl isotope ($\delta^{37}Cl_{SMOC}$ (‰)) values of Ap020 measured during the August 2019 analytical session. The errors associated with each measurement point represent the 2σ uncertainty and the red diamond is the average of the measurements (n = 4), with the associated (barely visible) error bars representing the standard deviation (2σ) (see text for details).

Chapter Three:

The Apollo samples

This chapter describes the petrography of fourteen Apollo rock samples that were studied in this research project. The chemical and petrological details of each sample that have been reported in the scientific literature are provided within each sample sub-section of the chapter. This includes the major elements content and the modal mineralogy of each rock, together with available petrological interpretations from the literature. Moreover, the regions where the mineral apatite is commonly located and the different types (size/ shape) of apatite grains that are found within the Apollo samples studied in this project are also described in the chapter.

3.1. Sample significance

The fourteen Apollo samples studied within this research project (Table 3.1) were collected during the NASA Apollo missions to the Moon between 1969 and 1972. All of the samples were supplied by NASA's Curation and Analysis Planning Team for Extraterrestrial Materials (CAPTEM). The samples selected for this project represent five of the six Apollo landing sites in order to include as diverse a sampling area of the Moon as possible. The studied samples exist as polished rock thin-sections of ~ 30 μm thickness.

In this study, the focus has been on the analysis of the mineral apatite in lunar mare (pronounced 'mar-ray') basalt rocks and a potassium (K), rare earth element, and phosphorous (KREEP) rich basalt that were erupted onto the lunar surface ~3–3.9 Ga ago. Mare basalts are products of mantle partial melting, making them significant samples for investigating the indigenous inventory of volatile elements in the lunar interior and, therefore, understanding the chemical evolution of the Moon. The cause of partial melting of the lunar mantle and, ultimately, mare basalt generation, is not fully understood (e.g. Grove and Krawczynski, 2009). The current theories involve either increasing activity from hot, deep magmas, possibly due to heating from tidal friction, or partial melting caused by prolonged periods of material (e.g. meteorites, asteroids, comets) impacting the Moon (e.g. Grove and Krawczynski, 2009), known as the Late Heavy Bombardment (between ~4.0 Ga and 3.8 Ga) (e.g. Morbidelli et al., 2012). The different basaltic source regions are estimated to have been at a depth of between 150 km (Papike et al., 1976) and 700 km below the lunar surface (Hess, 1991).

3.2. Sample selection

Initially, apatites ($Ca_5(PO_4)_3(F,Cl,OH)$) of mare basalt samples that already had published chlorine and hydrogen isotope data were selected for this project so that comparisons and contrasts could be drawn between the existing results and the findings of this project. Low levels of sulfur (S) in many mare basalt apatites investigated meant that analysing samples for which data already existed was not always possible. Importantly, the rock samples selected needed to contain the phosphate mineral apatite that was suitable for further analyses. For example, an additional 16 Apollo samples not detailed here underwent preliminary investigations (with optical and scanning electron microscopy) as part of this

project but they were excluded because they were found not to contain apatite, or the apatite grains were too small or were unsuitable due to the presence of multiple cracks.

The samples investigated in this study were selected to demonstrate a diversity of mare basalts that include low-Ti basalts (pigeonite basalts, olivine basalts and gabbroic basalts) and high-Al basalts, with a range of crystallisation ages from ~3.1 Ga to ~3.9 Ga (Table 3.1). With the exception of sample 14053, all of the mare basalts are pristine with no signs of alteration from secondary processes such as metamorphism or impact shock. Different quantities and combinations of the element oxides SiO_2, Al_2O and FeO have been reported to affect S solubility in a sulfide saturated melt that forms mare basalts (e.g. Ding et al., 2018). Therefore, a variety of basalts were chosen based upon the bulk-rock major element oxide contents reported in the scientific literature (Table 3.2).

In addition to the mare basalts (and KREEP basalt), apatites in a feldspathic granulitic impactite rock (79215) were analysed as part of this project because, to the best of our knowledge, it is currently the only sample for which S isotopes and abundance in lunar apatite have been reported in the scientific literature (Treiman et al., 2014). By analysing 79215, it was possible to confirm the reproducibility of published data and perform inter-laboratory comparisons. Furthermore, apatites in a lunar meteorite, Sayh al Uhaymir (SaU) 169, a hot desert 'find' from Oman, were analysed as proof of concept for the newly developed nano-scale secondary ion mass spectrometry (NanoSIMS) S isotope protocol (see Chapter Two for more details).

Table 3.1. An overview of the lunar samples used in the research project that includes rock type, crystallisation ages and modal mineralogy.

Collection location site	Sample identity number	Sample specific identity number	Rock type	Crystallisation age/ Ga	CRE age/ Ma	Modal mineralogy*	Mesostasis region
Apollo 11	10044	645	Ilmenite basalt - high-Ti	3.69 [a]	79	45 vol.% px, 35 vol.% plg, 13 vol.% ilm,	silica, ilm, troi, ap, sym, trq, Fe-metal, K-rich glass.
Apollo 12	12031	7	Pigeonite basalt - low-Ti	3.23 [b]	N.R.	49 vol.% pyroxene, 40 vol.% plg, 4 vol.% ilm,	troi, silica, ap & ilm.
Apollo 12	12039	45	Pigeonite basalt - low-Ti	3.13 ± 10 [c, a]	N.R.	50 vol.% px, 26 vol.% plg, 8 vol.% ilm & 7 vol.% trd.	K- & Si-glass, trd, trq, troi, badd, K-spar & ap.
Apollo 14	14053	19	High-Al basalt – low-Ti	3.92 [d]	21	50 vol.% px, 40 vol.% plg, <10 vol.% ilm & ol.	ap, usp, ilm, troi, k-spar, sym, badd, Fe-metal, px, plg.
Apollo 15	15016	7	Olivine basalt - low-Ti	3.29 [e]	~378–422	65 vol.% px, 21 vol.% plg, 7 vol.% ol, 6 vol.% ilm	ap, troi, silica, ilm & Fe-Ni metal inclusions.
Apollo 15	15058	15	Pigeonite basalt – low-Ti	3.4 [f, g]	135	70 vol.% cpx, 24 vol.% plg, <5 vol.% silica & ilm.	silica, ilm, troi, ap & sym.
Apollo 15	15065	85	Gabbroic basalt – low-Ti	3.35 [h]	N.R.	60 vol.% cpx, 35 vol.% plg, 1 vol.% silica & ilm.	K-spar, ilm, trd, ap & troi, px & plg.
Apollo 15	15085	15	Pigeonite basalt – low-Ti	3.40 [i]	N.R.	40-66 vol.%, px, 22-60 vol.% plg, 4 vol.% trd, 1.5 vol.% ilm.	ap, usp, csp, troi, silica, ilm, k-spar, sym & Fe-Ni metal.
Apollo 15	15386	46	KREEP basalt	3.88 [a]	~235 ± 5[†]	35-50 vol.% plg, 50 vol.% px, 10 vol.% crst, 3 vol.% ilm.	troi, ap, merr, k-spar, trq, badd, ilm, plg, px, silica.

Table 3.1. Continued

Collection location site	Sample identity number	Sample specific identity number	Rock type	Crystallisation age/ Ga	CRE age/ Ma	Modal mineralogy*	Mesostasis region
Apollo 15	15475	17	Porphyritic pigeonite basalt - low-Ti	~3.4 [j]	473 ± 20	64-74 vol.%, px, 10-45 vol.% plg, 2 vol.% ilm.	ap, usp, csp, troi, silica, ilm, plg, px & k-spar
Apollo 15	15545	7	Olivine normative basalt-low-Ti	~3.3[†]	~2[††]	50 vol.%, px, 22-60 vol.% plg, 4-11 vol.% ol, 3 vol.% ilm, 3 vol.% usp.	ap, usp, troi, ilm, k-spar, ol, px & Fe-Ni metal.
Apollo 15	15555	991	Olivine-normative basalt - low-Ti	3.32 [k]	81	40-65 vol.% px, 25-35 vol.% plg, 5-20 vol.% ol	silica, ilm, troi, ap & usp.
Apollo 15	15556	137	Vesicular olivine normative - low-Ti basalt	3.4 ± 0.1 [m]	~508	50 vol.% px, 25-35 vol.% plg, 5 vol.% ol, 2.1 vol.% ilm, <1 vol.% usp & chromite.	ap, ilm, troi, silica, K-spar, plg & px.
Apollo 17	79215	50	Feldspathic granulitic impactite	3.9 [n]	339 ± 24.2	Matrix portion (72 vol.%): 79 vol.% plg, 13 vol.% ol, 7 vol.% px, <0.4 vol.% spinel, ilm, metal & troi.	N/A
Oman [#]	SaU 169	N/A	Lunar meteorite: Impact melt breccia	N.R.	N.R.	px, plg, ol, K-glass, Ca-glass, ilm, ap & merr.	N/A

[a] Snape et al. (2016); [b] Nyquist et al. (1979); [c] Nyquist et al. (1977); [d] Papanastassiou and Wasserburg (1971); [e] Evensen et al. (1973); [f] Birck et al. (1975); [g] Husain (1974); [h] Nakamura et al., (1977); [i] Papanastassiou and Wasserburg (1973); [j] Synder et al. (1997); [k] Wasserburg and Papanastassiou (1971); [m] Kirsten et al. (1972); [n] Hudgins et al. (2008), McGee et al. (1978), Oberli et al. (1979). [#] = non-Apollo sample – full description is in Appendix A, section A.1.1. * = references provided within the text under the detailed individual sample descriptions. N.R. = not reported. [†] = the age is assumed to be the same as KREEP basalt 15382 (see main 15386 description). [††] = the age has been interpreted from published isotope data (see main 15545 description). Table abbreviations: ap = apatite, badd = baddeleyite, cpx = clinopyroxene, crst = cristobalite, csp = chromite spinel, ilm = ilmenite, K-spar = potassium feldspar, merr = merrillite, ol = olivine, plg = plagioclase, sym = symplectite, trd = tridymite, troi = troilite, trq = tranquillityite, usp = ulvöspinel.

Table 3.2. Major element bulk-rock compositions of the Apollo samples studied in this project, as reported in the scientific literature.

Sample identity number	SiO_2/ wt.%	FeO/ wt.%	MgO/ wt.%	Al_2O_3/ wt.%	CaO/ wt.%	K_2O/ wt.%	Na_2O/ wt.%	TiO_2/ wt.%
10044 [a]	42.2	17.9	6.0	10.4	12.1	0.03	0.50	10.2
12031 [b]	47.0	16.8	7.1	12.6	12.3	0.05	0.33	2.9
12039 [b]	46.1	20.3	5.8	10.5	11.7	0.1	0.3	4.5
14053 [c]	46.3	16.8	8.72	13.6	11.2	0.12	N.R.	2.6
15016 [c]	44.0	22.6	11.1	8.4	9.4	0.03	0.21	2.3
15058 [d]	47.8	20.0	9.0	8.9	10.3	0.03	0.28	1.8
15065 [e]	48.5	19.3	10.6	9.3	9.9	0.05	0.34	1.48
15085 [f]	46.4	26.8	8.2	5.8	9.1	0.07	0.21	3.07
15386 [d]	50.8	10.6	8.2	14.8	9.7	0.7	0.7	2.2
15545 [d]	45.0	22.0	10.4	8.77	9.9	0.03	0.21	2.33
15555 [c]	44.2	22.4	11.1	8.48	9.5	0.03	0.24	2.3
15475 [d]	47.8	20.0	8.3	9.5	10.7	0.04	0.24	2.0
15556 [f]	46.2	21.7	8.0	9.9	10.7	0.09	0.3	2.6
79215 [g]	43.8	4.6	6.3	27.7	15.9	0.1	0.5	0.3

[a] Beaty and Albee (1978); [b] Rhodes et al. (1977); [c] Hallis et al. (2014); [d] Rhodes and Hubbard (1973); [e] Cuttita et al. (1973); [f] Mason et al. (1972); [g] Bickel et al. (1976). N.R. = not reported.

3.3. Sample descriptions and mineralogy

3.3.1. Ilmenite basalt: 10044,645

Apollo sample 10044 was collected during the Apollo 11 mission of 1969 from an unknown area immediately to the southwest of the Lunar Module (McGee et al., 1977). The sample is thought to be very similar to two other rock samples found at the same location (10047 and 10058) which led Beaty and Albee (1978) to suggest that the rocks originate from the same large block that possibly broke during collection. The crystallisation age of sample 10044 has been determined using $^{207}Pb/^{206}Pb$ dating to be 3.69 ± 0.005 Ga (Snape et al., 2016) and, by using the abundance of cosmogenic ^{81}Kr, the cosmic ray exposure age (CRE) has been reported as ~79 Ma (Hohenberg et al., 1970).

Described as a high-Ti (low-K) coarse-grained porphyritic ilmenite basalt, 10044 is predominantly composed of pyroxene (~45 vol.%), plagioclase (~35 vol.%) and ilmenite (~13 vol.%) (McGee et al., 1977; Beaty and Albee, 1978). The pyroxene grains are subhedral to anhedral phenocrysts (1.0–2.0 mm) (McGee et al., 1977) and have augite in the cores that become increasingly Fe-rich and Ca-poor towards the grain rims which are composed of intermittent pyroxferroite (Fe-rich pyroxene) (Beaty and Albee, 1978) (Figure 3.1). There is very little pore space within the matrix which otherwise contains tightly packed sub-ophitic plagioclase (up to 2 mm in the longest dimension) which is also observed to be zoned with decreasing Ca from the core to the rim. Lath-and irregularly-shaped ilmenite grains of up to 1.6 mm in the longest dimension appear as intergrowths between the pyroxene and plagioclase grains (McGee et al., 1977; Beaty and Albee, 1978). Other minor minerals in the rock include silica (cristobalite and tridymite) (~7 vol.%) and, representing <1 vol.% of the sample, fayalite, troilite, Fe-metal and ulvöspinel (Beaty and Albee, 1978).

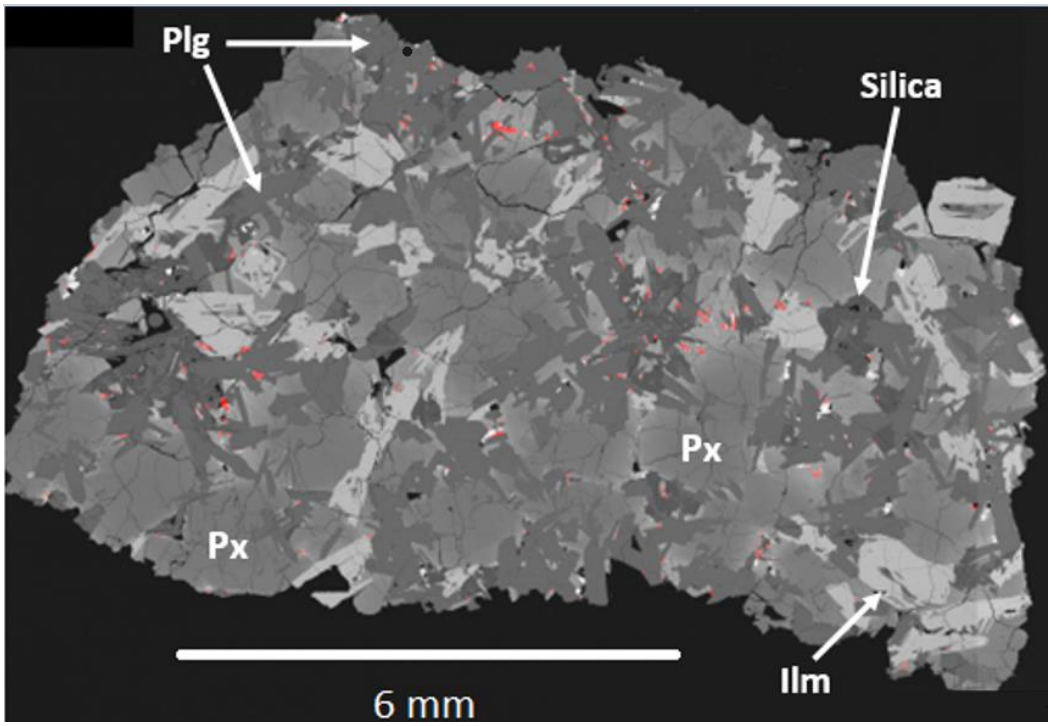

Figure 3.1. Apollo sample 10044,645. A false colour whole sample X-ray map, where red highlights regions containing phosphorous (confirmed as apatite). Large, faintly zoned pyroxene (Px) grains dominate the image. Abundant, but smaller plagioclase (Plg) exist within the matrix set around the pyroxenes. The less frequent lath- and irregularly-shaped ilmenite (Ilm) intersect and cross-cut the pyroxene grains. Relatively large silica (up to 1 mm) grains are easily visible in this image.

Mesostasis is a late-stage crystallisation region from which minerals containing incompatible elements crystallise within the gaps (interstices) of the earlier formed major minerals (Haskin and Warren, 1991). Phosphate minerals, such as late-stage crystallising apatite and merrillite ($Ca_9NaMg(PO_4)_7$) are commonly found within this region in lunar basalts (Papike et al., 1991) which means that the mesostasis is an important region for this research (Figure 3.2). The mesostasis of 10044 is composed of silica, troilite, Fe-metal, K-rich glass, tranquillityite (rare) and apatite (McGee et al., 1977). Symplectite is also observable within the mesostasis region which represents the breakdown of unstable phases that become replaced by one or more (different) minerals to give a replacement texture e.g. pyroxferroite can be replaced by an assemblage of fayalite, cristobalite and Fe-rich pyroxene.

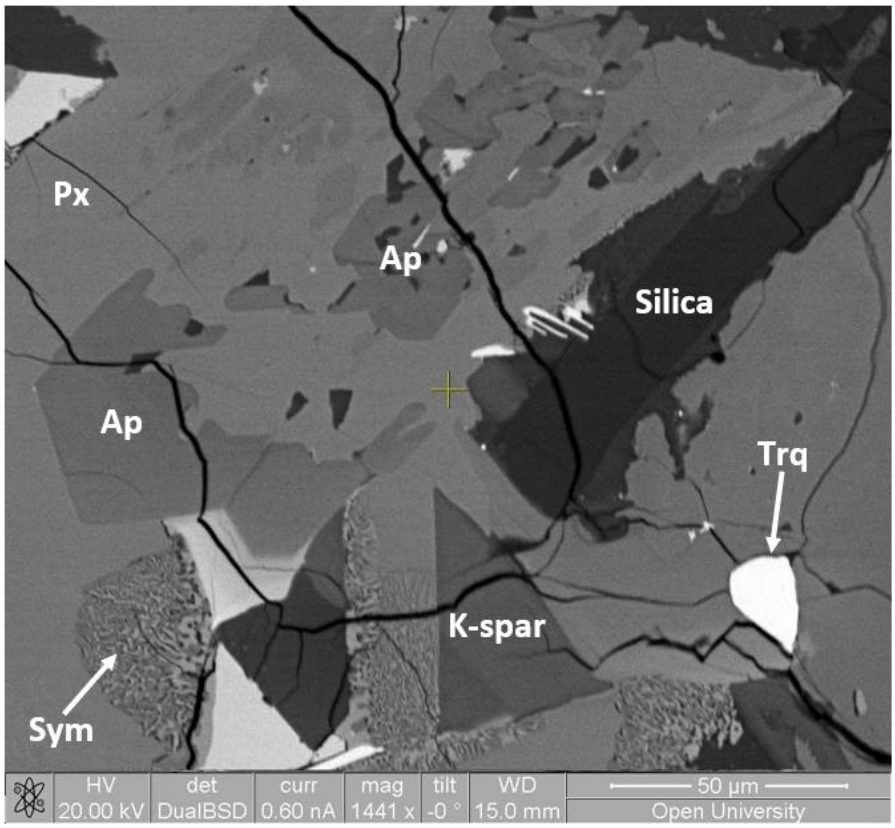

Figure 3.2. Mesostasis region in Apollo sample 10044,645. The backscatter electron (BSE) image shows a typical mesostasis region for the sample with apatite (Ap) appearing left of centre (subhedral grain), and just above centre (anhedral grain). Other mesostasis minerals include Ilm = ilmenite, Px = pyroxene, K-spar = potassium feldspar, Trq = tranquillityite and Sym = symplectite. (Image courtesy of Jessica Barnes, The Open University).

The apatite grains in 10044,645 are commonly subhedral to anhedral (Figure 3.2) and can vary considerably in size from <10 µm to >~200 µm in the longest dimension. The

acquisition of cathodoluminescence (CL) images of apatites in 10044 reveal diffuse zoning of the grains that is not apparent in the backscatter electron (BSE) images (Figure 3.3). It is suggested that zonation within apatite is as a result of lattice defects such as broken bonds, vacancies or the incorporation and variation of trace elements (e.g. rare earth elements, Mn^{2+}, Cr^{3+}) into the crystal structure during crystal growth (Götze, 2012).

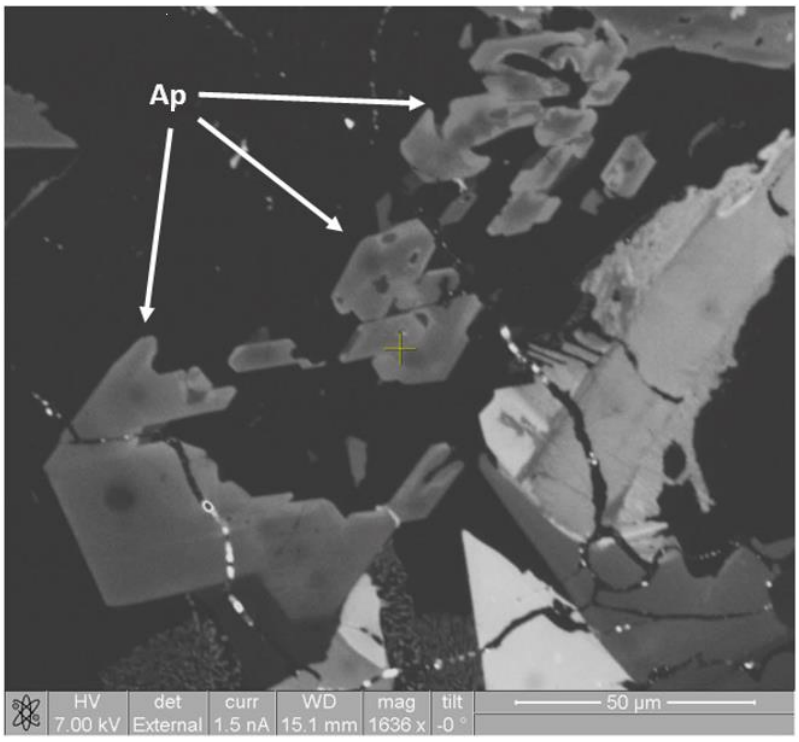

Figure 3.3. Zoned apatite grains in sample 10044,645. With the use of cathodoluminescence (CL), diffuse zoning can be seen within the apatite (Ap) grains. Silica also has CL properties and can be seen to the right of the image but has no zonation (the image area is the same as Figure 3.2).

3.3.2. Pigeonite Basalt: 12031,7

Apollo sample 12031 was collected during the Apollo 12 mission of 1969 on the north rim of Head Crater, but no exact location details were recorded (LSPET, 1970). The crystallisation age of 12031 has been determined using Rb-Sr isochron dating and was reported to be 3.23 ± 0.007 Ga (Nyquist et al., 1979). A cosmic ray exposure (CRE) age has not yet been reported. Since the 1970s, very few scientists have studied and characterised 12031 (e.g. Meyer, 2011). There has been some debate about whether 12031 is a feldspathic basalt (Beaty et al., 1979; Rhodes et al., 1977), a Pigeonite basalt (Nyquist et al., 1979) or an ilmenite basalt (e.g. Neal et al., 1994) based upon studies using modal and chemical data, Rb/Sr ratios and the Mg-number (Mg#).

Sample 12031 is a coarse-grained basalt, predominantly composed of large pyroxene (up to 3 mm in the longest dimension) and plagioclase (up to 3.5 mm in the longest dimension) grains (constituting ~49 vol.% and ~40 vol.%, respectively) (Beaty et al., 1979; Rhodes et al., 1977; Neal et al., 1994; Nyquist et al., 1979). The plagioclase grains are complexly twinned and demonstrate compositional normal zoning (An_{91}-An_{76}). The plagioclase grains are also inter-grown with the pyroxene grains (Figure 3.4) which have complicated compositional zoning that becomes increasingly Fe-rich from the core to the rim of the grain, with diffuse boundaries between pigeonite, augite and pyroxferroite (Beaty et al., 1979).

Contrasting gabbroic and graphic textures were seen within the specific sample 12031,7 by Beaty et al. (1979) (this is also the section studied in this project) involving the juxtaposition of more granular textures against regular intergrowths of plagioclase and pyroxene (Figure 3.4). The remainder of the rock consists of ilmenite (~3.8 vol.%), minor silica (tridymite laths and interstitial cristobalite) and a trace of fayalite (Beaty et al. 1979). It is suggested by Beaty et al. (1979) that the cause of the coarseness of 12031 is similar to that suggested for coarse Apollo 15 basalts (Grove and Walker, 1977), whereby the rocks crystallised under slow cooling rate conditions.

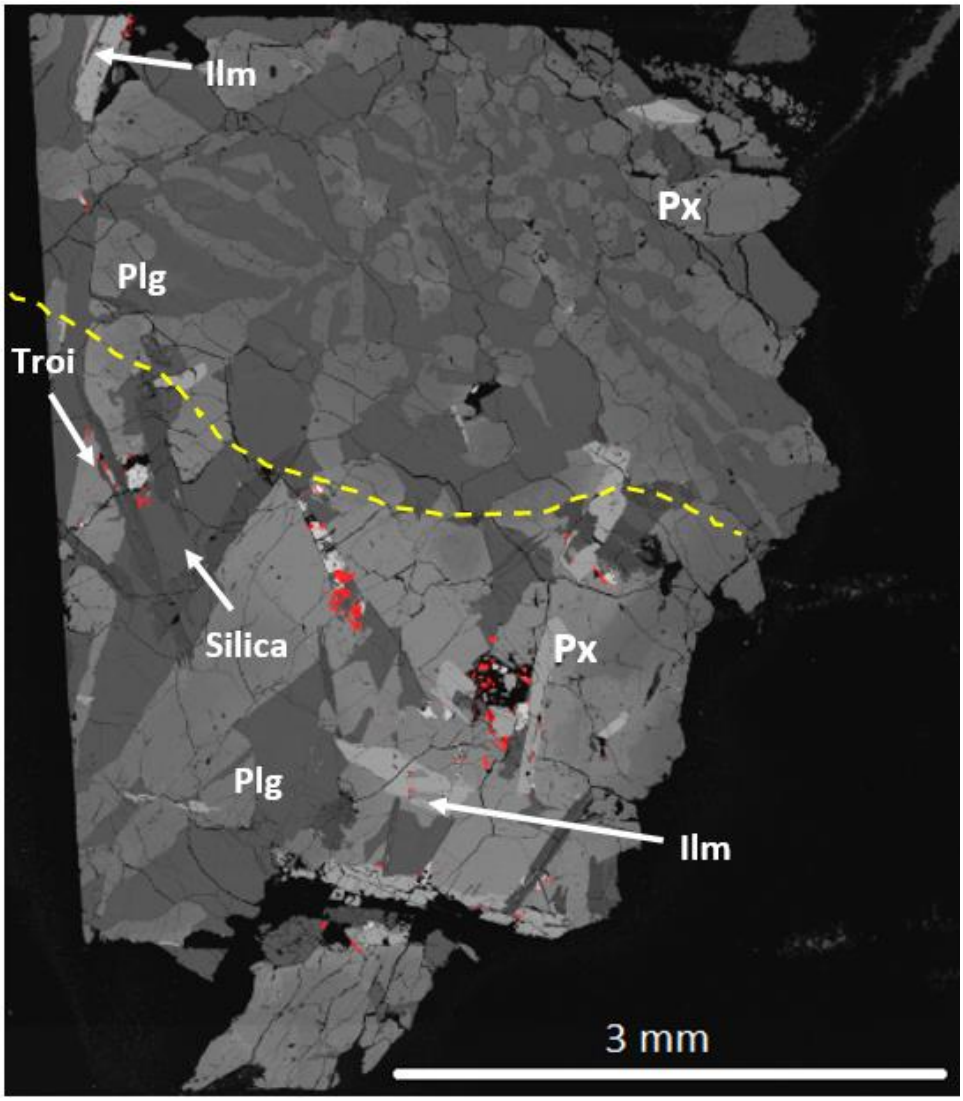

Figure 3.4. Apollo sample 12031,7. A false colour whole sample X-ray map, where red = phosphorous regions (confirmed as apatite) that highlight the large and coarse grained mesostasis regions. The image shows the intergrowth of plagioclase (Plg) with pyroxene (Px) grains and the clear divide between the regular intergrowths with graphic textures (above the yellow dashed line) and the more granular, gabbroic textures (below the yellow dashed line). Lath-shaped silica grains cross-cut the plagioclase and pyroxene, whereas, ilmenite (Ilm) is predominantly found within the pyroxene grains.

For the sample studied within this project (12031,7), the mesostasis regions are very coarse grained and contain large apatite grains (~75 μm in the longest dimension) (Figure 3.5). The apatite grains within the mesostasis regions are rarely euhedral, with most being subhedral to anhedral and they are found alongside large grains of troilite (some >100 μm in the longest direction), ilmenite and silica. However, apatite grains are also found to exist within non-mesostasis pyroxene grains, which suggests that apatite was not solely an interstitial crystallising mineral. Whilst symplectite has been identified in 12031,7, it is not directly associated with apatite. The majority of apatite grains showed no signs of zoning

when analysed with CL but, for a few grains, incredibly faint and non-distinct zone boundaries could be seen.

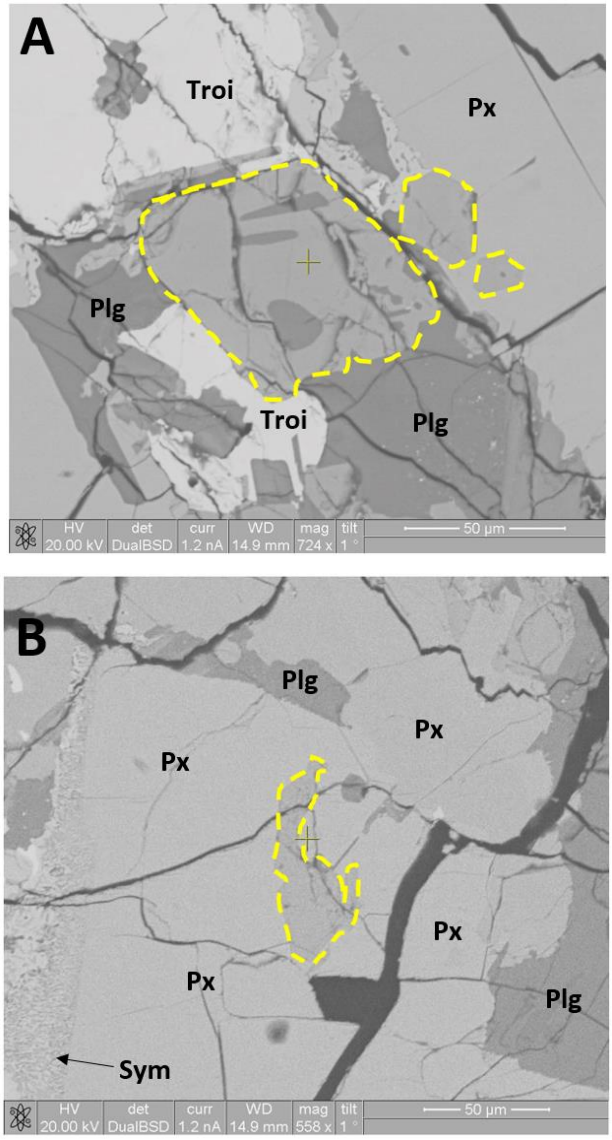

Figure 3.5. Apatite regions in Apollo sample 12031,7. **A**) The BSE image shows a large (~70 µm in the longest dimension) apatite at the centre (surrounded by dashed yellow lines), next to smaller subhedral apatite grains, contained within the mesostasis region. **B**) The BSE image shows an apatite grain (enclosed by dashed yellow line) wholly surrounded by pyroxene grains. Where Troi = troilite, Plg = plagioclase, Px = pyroxene and Sym = symplectite.

3.3.3. Pigeonite Basalt: 12039,45

Apollo sample 12039 was collected during the Apollo 12 mission of 1969 from the west rim of Bench Crater, although the exact site has not been recorded (McGee et al., 1977). Based upon the Rb-Sr dating system and Pb-Pb isochron dating, the crystallisation age for

12039 was reported to be 3.13 ± 0.1 Ga (Nyquist et al., 1977; Snape et al., 2016). The cosmic ray exposure (CRE) age has not yet been reported for this sample.

Described as a microgabbro and a low-Ti mare basalt, 12039 is a coarse grained ophitic rock, predominantly composed of pyroxene (~50 vol.%) and plagioclase (~26 vol.%) where the pyroxene completely or partially enclose laths of plagioclase (Figure 3.6) (Bunch et al., 1972). Both pyroxene (0.8 mm – 4 mm) and plagioclase (0.8 mm – 2 mm) are often cross-cut by ilmenite (0.8 mm – 2 mm) and tridymite (SiO_2) (< 1 mm) which make up ~8 vol.% and ~7 vol.%, respectively (Bunch et al., 1972; McGee et al., 1977). Ilmenite is frequently intergrown with ulvöspinel (McGee et al., 1977). Negligible pigeonite has been detected (Keil et al., 1971) within the sample with suggestions that a relatively low (1,140 ˚C) liquidus temperature was experienced in the melt that, instead, resulted in the crystallisation of augite as the major pyroxene phase (Bunch et al., 1972).

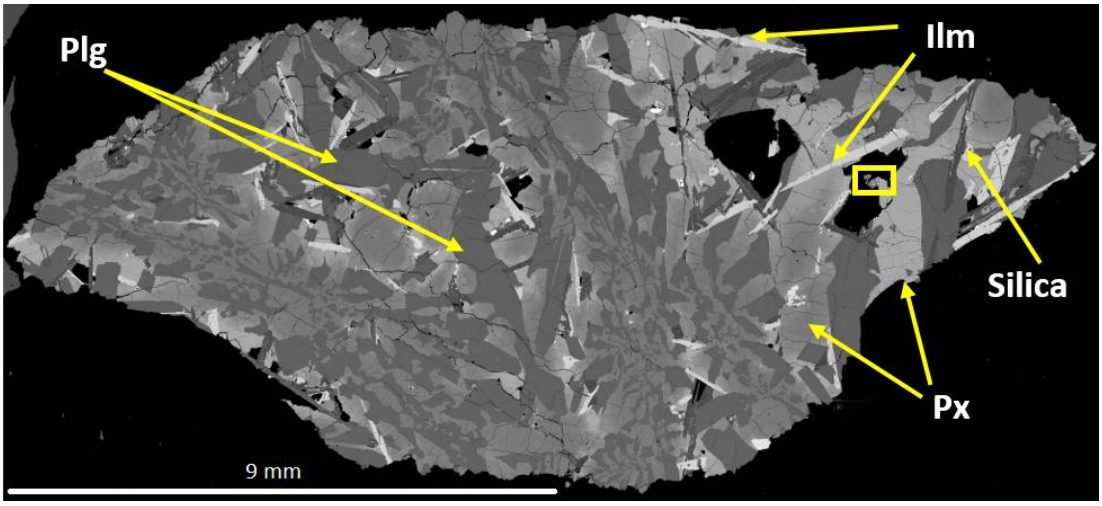

Figure 3.6. Apollo sample 12039,45. BSE montage map showing the large dominant plagioclase (Plg) and pyroxene (Px) grains with lath-shaped ilmenite (Ilm) and silica grains that cut across the plagioclase and pyroxene. The yellow rectangle highlights the region for both Figures 3.7 and 3.9.

The clinopyroxene grains within 12039 show significant optical zonation from core to rim with zone colour changes accompany changes in chemistry and mineralogy from augite, to ferroaugite (Fe-rich), to ferrohedenbergite (Fe- and Ca-rich augite), to (very rare) pyroxferroite crystals, resulting in an oscillation between Ca-rich and Ca-poor minerals. Likewise, significant zonation within plagioclase has been recorded, but for proportionally fewer grains, and has been explained by a depletion of Ca from the core to an enrichment of Na and K towards the rim (Bunch et al., 1972). The zonation is thought to be evidence for the rapid cooling (not enough time for re-equilibration) and fractional crystallisation of

sample 12039 (Bunch et al., 1972). The specific sample analysed in this project (12039,45) also revealed notable concentric and oscillatory zoning within multiple apatite grains (Figure 3.7). Such clear apatite zoning was not observed in any of the other lunar samples studied in this project.

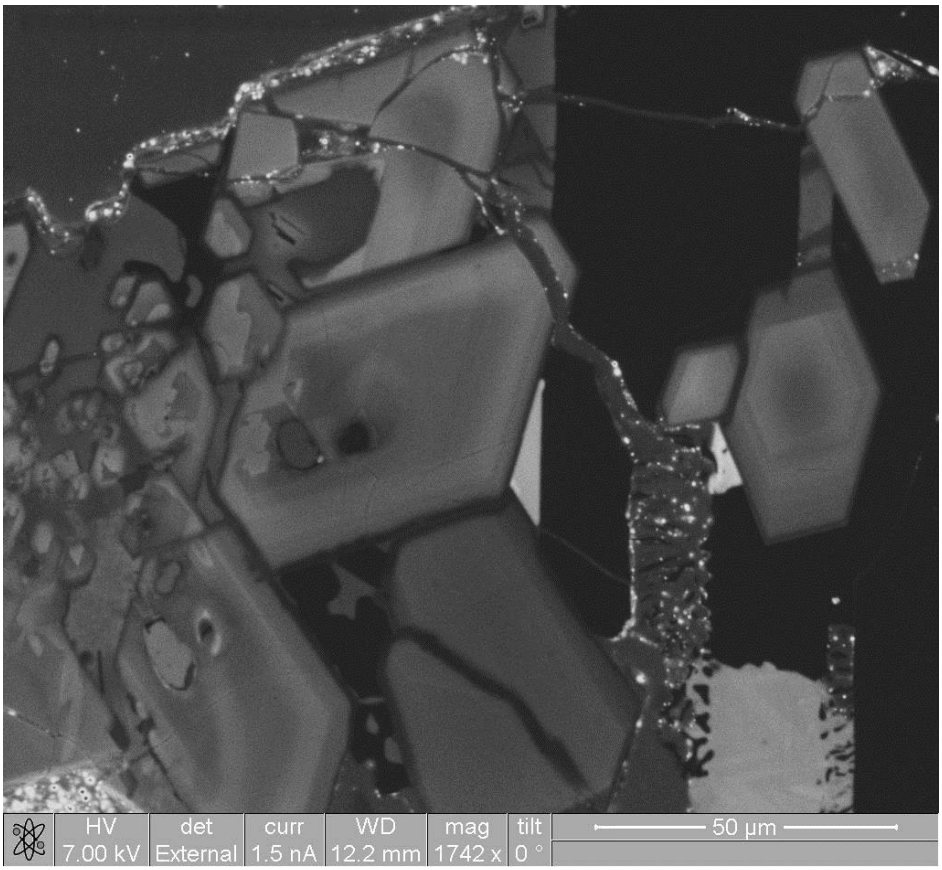

Figure 3.7. Zoned apatite grains in sample 12039,45. With the use of cathodoluminescence (CL), both concentric and oscillatory zoning can be clearly seen within the apatite grains that fill this image. Likewise, apatite grain boundaries are easily discernible when CL is employed to analyse the apatite grains.

Sample 12039 has been classified as one of the most Mg-depleted rocks analysed from the Apollo 12 mission with a very high FeO/ (MgO + FeO) ratio (Rhodes et al., 1977) of ~21 wt.% FeO and ~5 wt.% MgO (Bunch et al., 1972) (Figure 3.8). Sample 12039 is olivine-poor and also has the highest levels of SiO_2 (~47 wt.%) of analysed Apollo 12 samples which, when all taken into consideration, led Keil et al. (1971) to conclude that the parental melt of sample 12039 was one of the most differentiated of all Apollo 12 samples analysed.

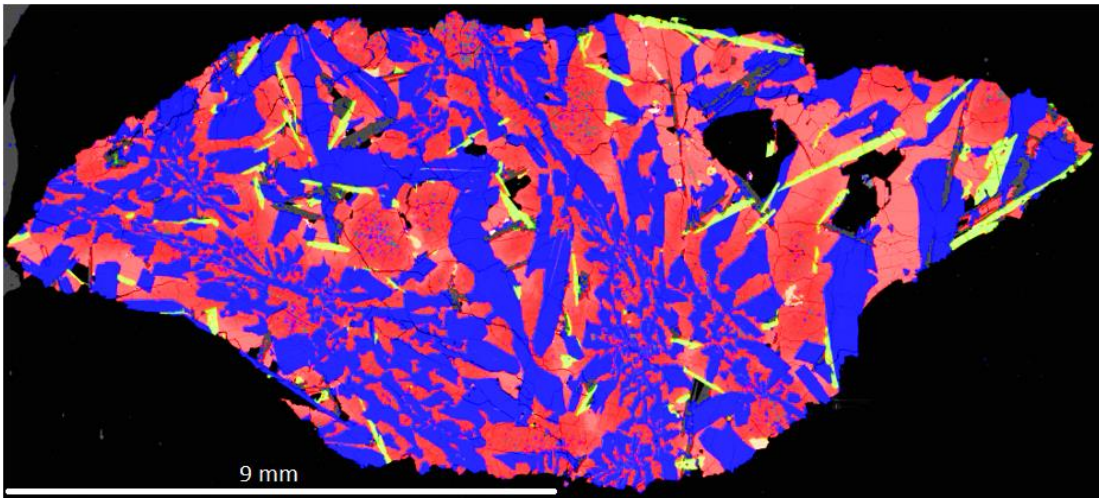

Figure 3.8. Apollo sample 12039,45 false colour X-ray map. The image shows the dominance of Fe (red (pyroxene)) and clearly highlights the laths of ilmenite (Ti represented by yellow). Blue is Al and represents plagioclase.

Within the mesostasis of sample 12039 is an intersertal K- and Si-rich glassy texture which very irregularly surrounds tridymite, tranquillityite, troilite, apatite, baddeleyite, barian potassium feldspar and pyroxferroite (McGee et al., 1977; Bunch et al., 1972; Greenwood et al., 2011) (Figure 3.9). The apatite grains found within the mesostasis region of the specific sample analysed in this project (12039,45) are predominantly euhedral-basal with the remaining few being subhedral crystals. The grains occur as clusters, with sizes ranging from <20 μm up to ~60 μm in the longest dimension, that are surrounded by similarly sized potassium feldspar, troilite, tridymite and tranquillityite grains that are adjacent to large pyroxene grains.

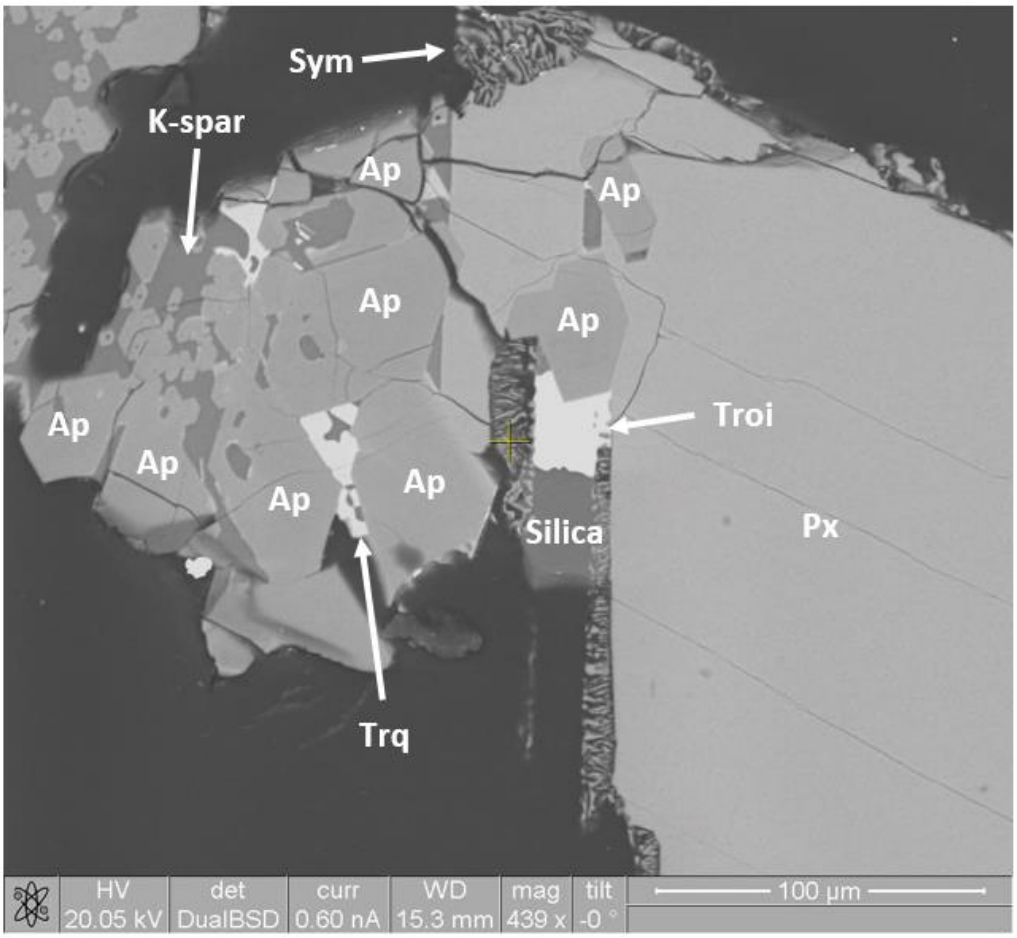

Figure 3.9. Apatite in Apollo sample 12039,45. The BSE image shows the clustered apatite (Ap) grains. Some grains are so close together that the BSE image is unable to show clear boundaries (c.f. cathodoluminescence Figure 3.7). Euhedral and anhedral apatite grains are visible in the BSE image. The textural relationship between apatite grains and other minerals is shown, where Troi = troilite, Trq = tranquillityite, Sym = symplectite (Si and Fe), K-spar = potassium feldspar, Px = pyroxene.

3.3.4. High-Al Basalt: 14053,19

Apollo sample 14053 was collected during the Apollo 14 mission in 1971 from the Fra Mauro highlands (Swann et al., 1971a) and is one of only four basalt rocks returned from the mission (Taylor et al., 2004). The sample was found in and amongst a boulder and ejecta blanket region near to a young crater (Cone Crater) (Swann et al., 1971a). The crystallisation age for 14053 is ~3.92 Ga (Papanastassiou and Wasserburg, 1971) and the cosmic ray exposure age is ~21 Ma (Eugster et al., 1984).

An Al-rich sample, 14053 has been described as an ophitic coarse-grained low-Ti basalt (Figure 3.10) with ~50 vol.% of large pyroxene grains (up to 5 mm) alongside lesser quantities (~40 vol.%) of plagioclase grains (up to 2 mm) (Papike et al., 1976; Taylor et

al., 2004). Approximately 10 vol.% of the sample is composed of ilmenite and fayalitic olivine.

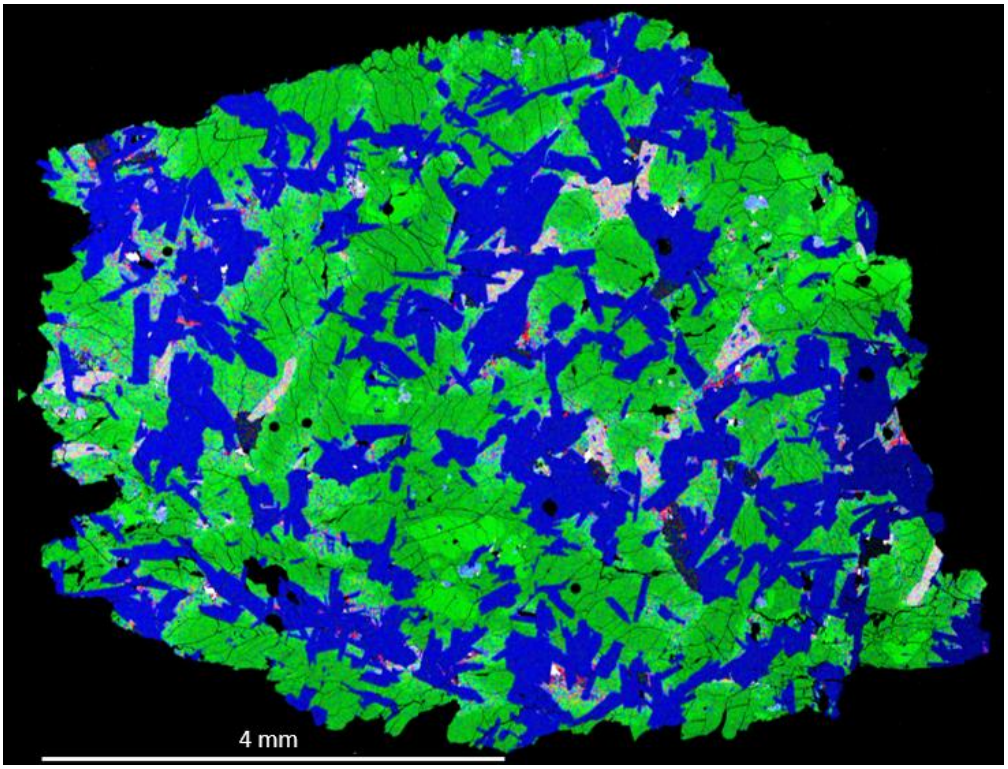

Figure 3.10. Apollo sample 14053,19. **A**) A false colour whole sample X-ray map, where green = Mg (representing pyroxene and minor olivine), blue = Al (plagioclase), greyish-white = Ti (ilmenite) and red = P. (Image courtesy of Romain Tartèse, The Open University).

14053 has been dubbed the most reduced rock from the Moon because mineral reduction reactions, such as the breakdown of fayalitic olivine to Fe-metal + silica and the breakdown of chromite-ulvöspinel to ilmenite + Ti-Al-chromite + Fe, have been observed within the rock. A symplectite region is visible within Figure 3.11, which represents the breakdown of unstable phases (e.g. pyroxferroite). As no impact-melt texture has been detected within the sample, the cause of the reduction is thought to have been due to subsequent solar wind (hydrogen) implantation to the exterior of the rock, post-crystallisation. Solar wind implantation was made possible by a reheating stage, perhaps triggered by an impact event that led to the burial (and heating) of 14053 (Taylor et al., 2004).

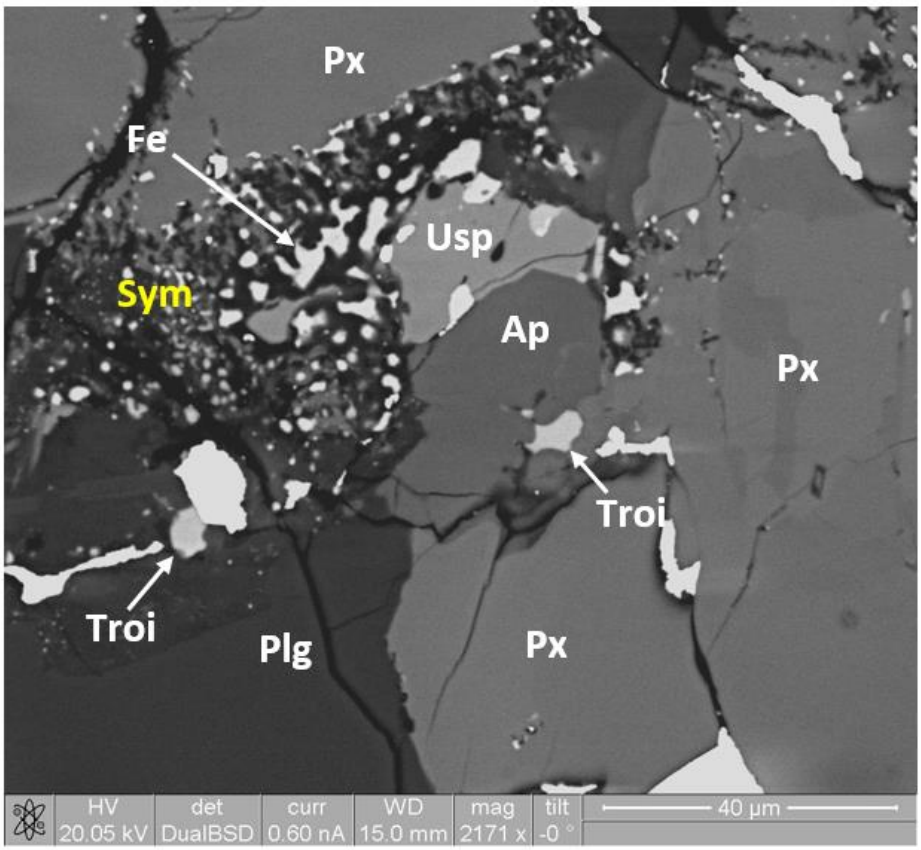

Figure 3.11. Mesostasis region of Apollo sample 14053,19. The BSE image shows a typical mesostasis region found within 14053,19, where Ap = apatite, Usp = Ulvöspinel, Px = pyroxene, Plg = plagioclase, Troi = troilite, Ilm = ilmenite, Sym = symplectite and Fe = Fe-metal. A scallop-shaped apatite is shown at the centre adjacent to the symplectic region.

Chlor- and fluor-apatite have been identified within mesostasis regions alongside potassium feldspar, silica (tridymite), Fe-metal, chromite-ulvöspinel, troilite, baddeleyite (ZrO_2), Si-, K- and Ba-enriched glasses, merrillite and symplectite (Taylor et al., 2004; McCubbin et al., 2010b). Typically, apatite grains directly adjacent to reduced minerals, e.g. chromite-ulvöspinel, are observed to be anhedral with more curvaceous "scalloped" grain boundaries (Taylor et al., 2004). The apatite grains present within the sample studied in this project (14053,19) are euhedral (sparse), subhedral and anhedral and are between 20 µm and 100 µm in size (Figure 3.11), although McCubbin et al. (2010b) reported sizes of up to 200 µm in the longest dimension.

3.3.5. Olivine basalt: 15016,7

Apollo sample 15016 was collected during the 1971 Apollo 15 mission to the Moon. It was found approximately 1.5 km to the north-north-east of Elbow Crater in the Hadley-

Apennine region at the rim of a 50 cm diameter crater at a site designated as Station 3. A traverse to the location where the sample was found had not been part of the planned schedule but was a detour when returning to the experiment deployment site from Station 2. Sample 15016 was the only material to have been collected from Station 3 (Lunar and Planetary Institute, 2018b).

The crystallisation age of the rock was reported to be 3.29 ±0.05 Ga based upon the Rb-Sr dating method (Evensen et al., 1973) and 3.38 ±0.08 Ga based upon the Ar-Ar dating system (Kirsten et al., 1973). However, the consistency of the plateau for the latter method was questioned by Husain et al. (1974) who employed K-Ar dating which gave an age of 2.90 ±0.04 Ga and led them to conclude that radiogenic ^{40}Ar had been lost. Cosmic ray exposure ages of 285 Ma and 315 Ma were determined for the sample by Kirsten et al. (1972) and Husain et al. (1974), respectively and, more recently, Füri et al., (2017) derived a much higher CRE age of between ~378–422 Ma.

Sample 15016 is described as a low-Ti medium-grained, olivine-normative, vesicular basalt that contains large vesicles from 0.7 mm to 5 mm in diameter (Figure 3.12) (McGee et al., 1977). Vesicles comprise ~60% of the rock and are so numerous that they intersect one another. Many vesicles are thinly lined with black glass and ilmenite plates within their interior walls (Butler, 1971; Bence and Papike, 1972; Ryder, 1985a). The vesicles are believed to have been formed as a result of gaseous release during very fast cooling of the basalt in a low pressure environment (Bence and Papike, 1972; Rhodes and Hubbard, 1973).

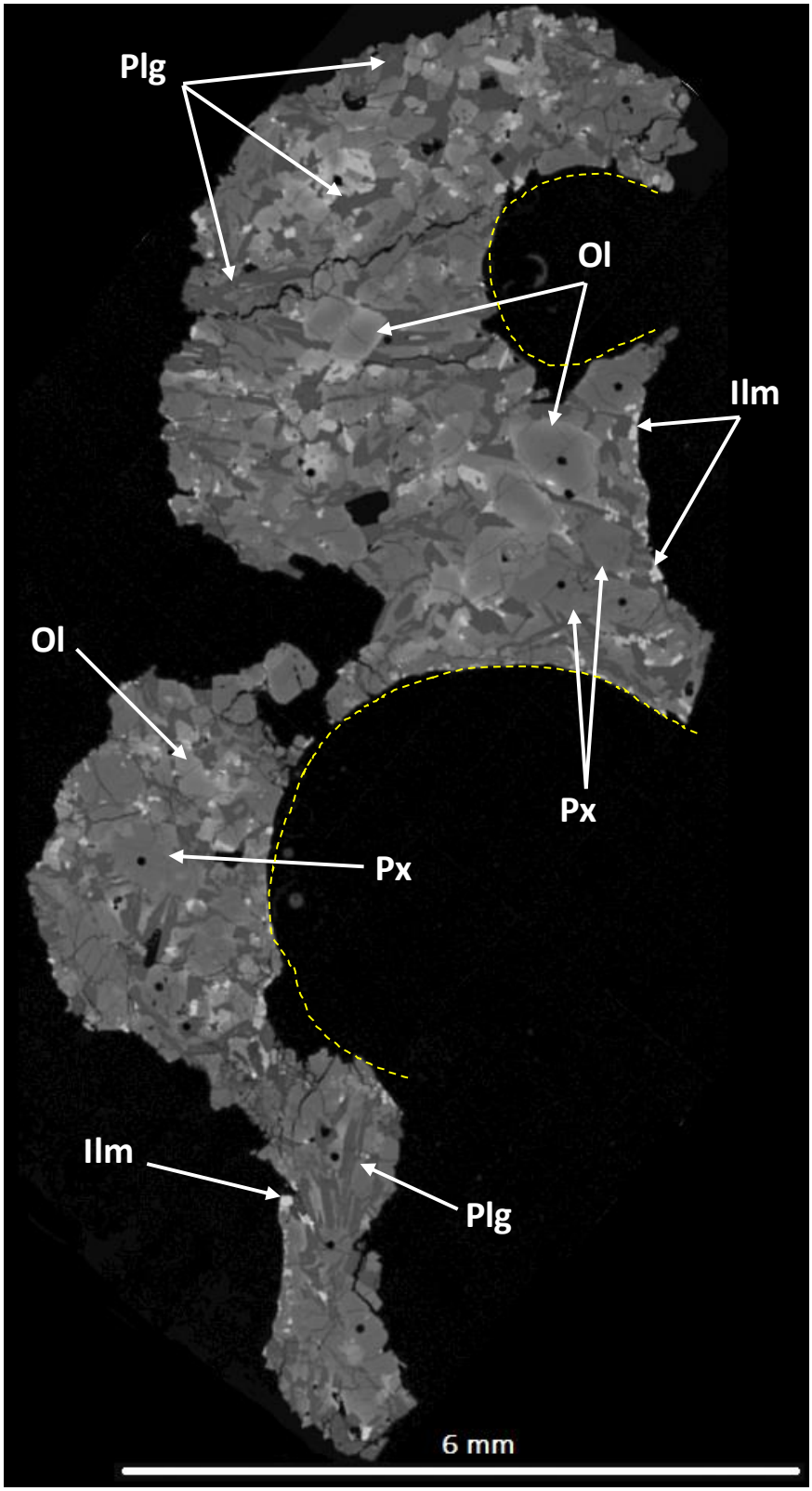

Figure 3.12. Apollo sample 15016,7. BSE montage map showing large pyroxene (Px) and olivine grains (Ol), lathed-shaped plagioclase (Plg) grains and much smaller ilmenite (Ilm) grains along the sample edges. The yellow dashed semi-circle lines highlight the outline of vesicle edges.

Sample 15016 is also described as porphyritic due to its large phenocrysts of pyroxene (1 – 2 mm) and olivine (0.8 – 1 mm) (Figure 3.12) (McGee et al., 1977). The pyroxene grains, which account for ~63–67 vol.% of the rock (Rhodes and Hubbard, 1973; Papike et al., 1976; McGee et al., 1977), are highly zoned from Ca-rich pigeonite at the core to (more abundant) augite at the rim, and it is this zonation that is thought to reinforce the conclusion that the rock cooled very quickly because the growing/ crystallising grain did not have enough time to re-equilibrate with the surrounding magma. Plagioclase crystallisation is marked by a reversal from augite to a Ca-poor, Fe-rich augite (Bence and Papike, 1972; Ryder, 1985a). The plagioclase grains, which make up ~20–22 vol.% of the rock (Rhodes and Hubbard, 1973; Papike et al., 1976; McGee et al., 1977), are predominantly lath-shaped (up to 1 mm in length) and also display zonation (An_{81-94} (Ryder, 1985a)) as well as intergrowths of pyroxene (McGee et al., 1977).

After plagioclase, olivine is the most abundant mineral within sample 15016, comprising 7-8 vol.% (Rhodes and Hubbard, 1973; Papike et al., 1976; McGee et al., 1977), and was the first to have fully crystallised, followed by pyroxene and then plagioclase (Bence and Papike, 1972). The olivine grains are also zoned with a range of Fo_{72-75} reported by Rhodes and Hubbard (1973), where Fo_{75} was stated as the maximum possible olivine forsterite composition based on melting experiments carried out on a synthetic 15016 composition by Kesson (1977). From the melting experiments of both Kesson (1975) and Kesson (1977), sample 15016 is thought to have been formed by the partial melting of an olivine-pyroxenite source, possibly within the lunar upper mantle, at a depth of 200 km – 500 km.

The remainder of sample 15016 is comprised of ilmenite (~6 vol.%) and lesser amounts of Cr-spinel, ulvöspinel, troilite and cristobalite which, when combined, represent <1 vol.% of the rock (Rhodes and Hubbard, 1973; Papike et al., 1976; Ryder, 1985a). Mesostasis regions (~0.3 vol.%) contain troilite and traces of Fe-Ni metal inclusions (McGee et al., 1977) and, within the specific sample studied for this project (15016,7), this is the region where apatite is predominantly found but it also occurs in non-mesostasis regions where it is surrounded by pyroxene and plagioclase (Figure 3.13). There are many small euhedral, basal sections of apatite as well as anhedral grains in 15016,7 with sizes ranging from <10 μm to ~40 μm in the longest dimension.

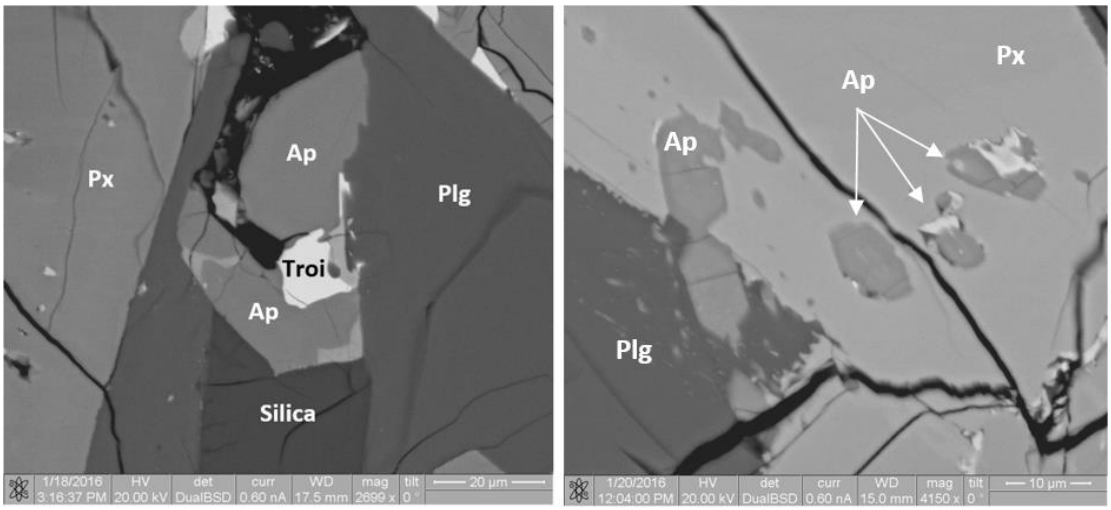

Figure 3.13. Apatite grains in Apollo sample 15016,7. **A)** The BSE image shows a scalloped-shape anhedral apatite grain within a mesostasis region typical for this sample. **B)** The BSE image shows euhedral apatite grains in a non-mesostasis region that has grown into plagioclase and pyroxene grains. Ap = apatite, Px = pyroxene, Plg = plagioclase and Troi = troilite (Images courtesy of Jessica Barnes, The Open University).

3.3.6. Pigeonite basalt: 15058,15

Apollo sample 15058 was collected during the Apollo 15 mission of 1971 from the south-eastern margin of the Mare Imbrium Basin, within the Hadley-Apennine region (the foot of the Apennine Mountains) (Lunar and Planetary Institute, 2018b). One of the largest basalts returned from the Apollo 15 mission (weighing ~2.7 kg), the exact situation of sample 15058 is uncertain but is thought to have been collected ~30 m east-northeast of the Apollo Lunar Surface Experiments Package (ALSEP) central station (used to power scientific instruments) and designated 'Station 8' (LSPET, 1972). Sample 15058 has a crystallisation age of ~3.4 Ga, determined using both the Rb-Sr isochron and Ar-Ar age dating systems (Birck et al., 1975; Husain, 1974), and has a cosmic ray exposure age of ~135 Ma (Husain, 1974).

Sample 15058 is a coarse-grained, porphyritic basalt (Bass, 1971) with phenocrysts of clinopyroxene (10 mm to 20 mm in the longest dimension) and laths of plagioclase (up to 4 mm in the longest dimension), some of which enclose smaller pyroxene grains (Ryder, 1985a). The sample contains ~24 vol.% plagioclase within a coarse matrix but is otherwise dominated by clinopyroxene grains (~70 vol.%) which are zoned from Mg-pigeonite within the cores through to sub-calcic augite at the rims, with relative Al-depletion throughout the zones (Bence and Papike, 1972; Ryder, 1985a) (Figure 3.14). Silica (tridymite and cristobalite) and opaque minerals (e.g. ilmenite) exist in the rock at <5

vol.% and, whilst it is considered to be a quartz-normative rock, trace amounts of olivine have been reported by a few authors (Rhodes and Hubbard, 1973; Meyer, 2010).

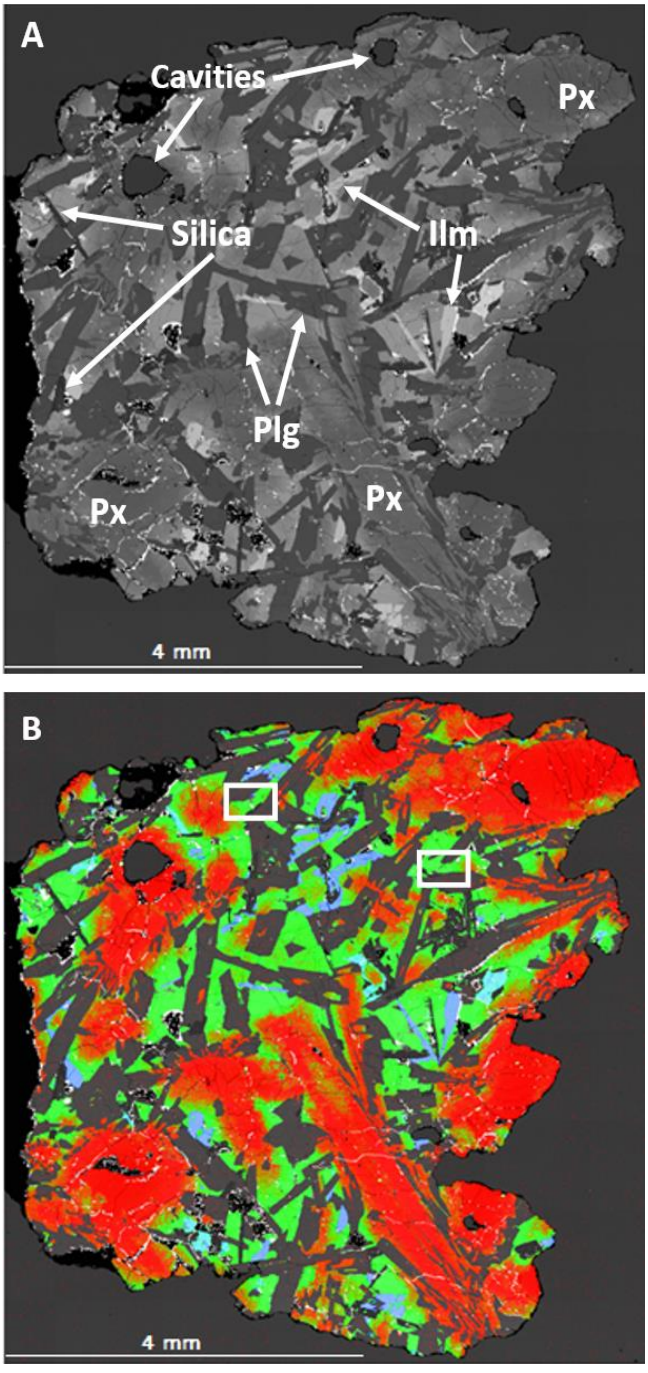

Figure 3.14. Apollo sample 15058,15. **A**) BSE montage map showing the dominance of pyroxene (Px), intersected by plagioclase (Plg), ilmenite (Ilm) and silica laths. The vuggy texture (cavities) (see text) is clear to see, particularly within large pyroxene grains. **B**) False colour X-ray map, where red = Mg (Mg-rich pyroxene), green = Fe (Fe-rich pyroxene), grey = Al (plagioclase) and blue = Ti (ilmenite). Plagioclase laths in the image centre enclose small Mg-rich pyroxene grains. The pyroxene zonation is more visible using false colour with Mg-rich and Fe-rich pyroxene in the core and mantle, respectively. The two white rectangles represent the apatite regions shown below in Figure 3.15.

The sample is described as ‘vuggy’ (cavity-ridden) (Figure 3.14) with ~5 vol.% of the rock containing cavities (LSPET, 1972), some of which contain pyroxene and plagioclase crystals, giving it a diktytaxitic texture: one that now has abundant gas cavities (Bass, 1971). The coarseness of sample 15058 has been attributed to a two-stage slow cooling of the rock, with an experimentally derived (using Apollo sample 15597 as the basis for chemical comparison) early-stage pyroxene phenocryst cooling rate of ~0.96–4.8 ˚C day^{-1} and a later, relatively faster, cooling-stage of the groundmass, which incorporates the plagioclase, at a rate of ~2.4 ˚C day^{-1} (Grove and Walker, 1977).

The specific sample 15058,15 studied in this project contains apatite grains that range from euhedral, to subhedral, to anhedral and grains that have a very thin and long straw-like appearance, all of which are predominantly found surrounded by pyroxene and potassium feldspar grains. Some apatite grains are immediately adjacent to silica, ilmenite, troilite and, occasionally, symplectite (containing a breakdown of pyroxferroite), typical of late-stage mesostasis regions within Apollo mare basalts (Figure 3.15). Some apatite grains of <5 μm in size are found clustered together, making their boundaries harder to discern, whereas other straw-like apatite grains are up to 200 μm in the longest dimension.

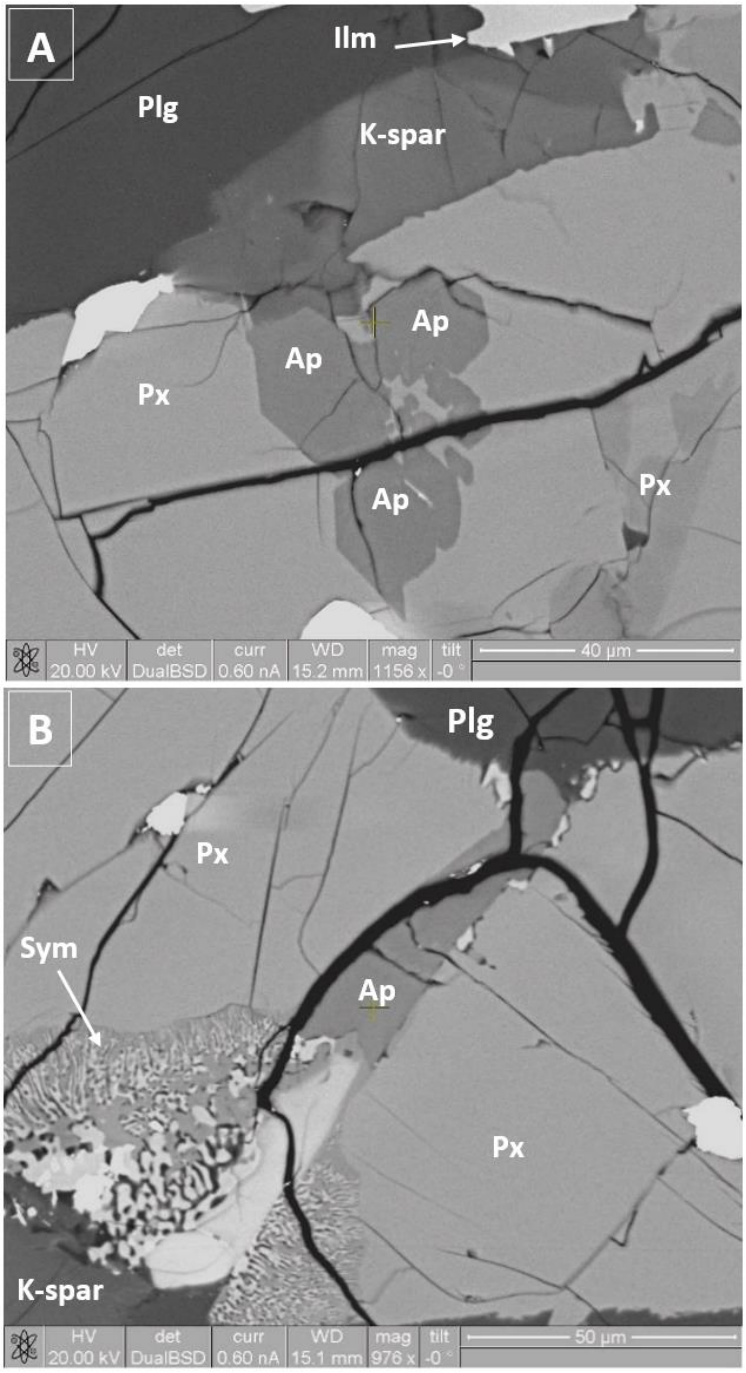

Figure 3.15. Apatite in Apollo sample 15058,15. **A**) The BSE image shows subhedral apatite grains surrounded by pyroxene and potassium feldspar grains. **B**) The BSE image shows an apatite grain within a typical mesostasis region, where Ap = apatite, Px = pyroxene, Plg = plagioclase, Ilm = ilmenite, K-spar = potassium feldspar and Sym = symplectite. Large fracture lines can be seen throughout this vuggy rock sample in both A) and B).

Whilst the pyroxene grains are found to be markedly zoned within sample 15058,15, there is very limited zonation seen within the apatite grains when cathodoluminescence (CL) is used for grain analyses (Figure 3.16). Unlike the pyroxene grains, zoning in the apatite is not detectable with BSE, suggesting that the zoning is caused by a variation of trace

elements that are too small to detect. The minority of apatite grains that do appear to be zoned show very diffuse zone boundaries with the resolution available for such small grains (<20 μm) (Figure 3.16).

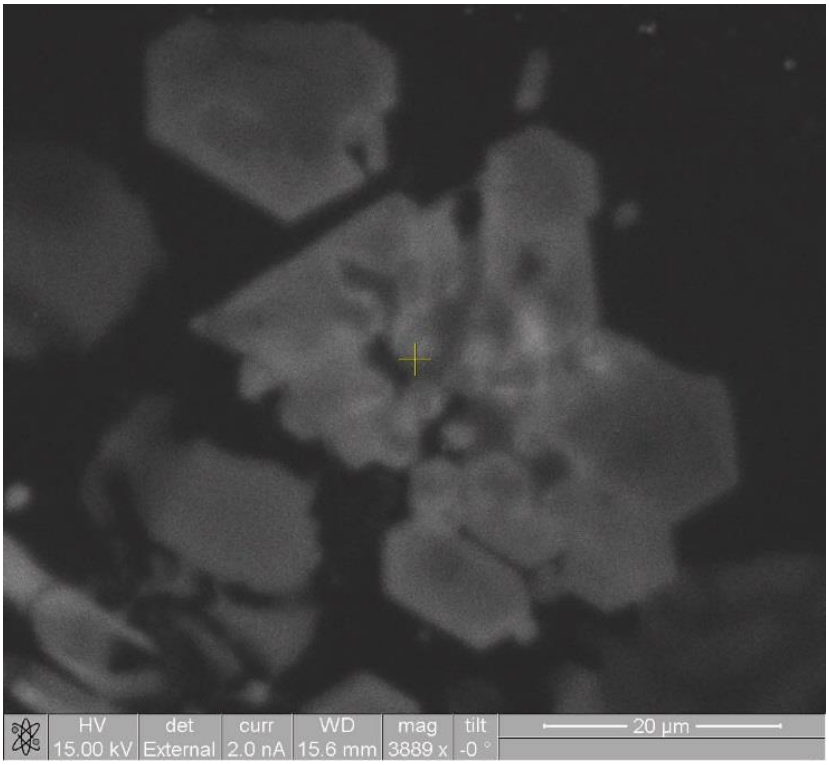

Figure 3.16. Cathodoluminescence in Apollo sample 15058,15. Very faint and diffuse zoning is apparent within this cluster of small apatite grains but the region of zonation is rare for apatite in this Apollo sample.

3.3.7. Gabbroic basalt: 15065,85

Apollo sample 15065 was discovered during the Apollo 15 mission of 1971 and was collected, as part of a suite of samples, from a location (designated 'Station 1') close to the rim of Elbow Crater (Lunar and Planetary Institute, 2018b). Sample 15065 has a crystallisation age of ~3.35 Ga which was determined using Sm-Nd dating system (Nakamura et al., 1977), whilst the cosmic ray exposure age remains undetermined (Meyer, 2010).

Described as a coarse-grained, low-Ti mare basalt (Nava, 1974), sample 15065 is composed of 60 vol.% zoned clinopyroxenes (3 mm – 5 mm in the longest dimension), 35 vol.% plagioclase (~2 mm in the longest dimension), with minor (~1 vol.%) silica (tridymite and cristobalite) and opaque minerals (e.g. ilmenite) (Ryder, 1985a; Morrison and Silver, 1971). The pyroxene is zoned with Mg-rich pigeonite forming the core of the

mineral which gives way to augite and then ferroaugite in the direction of the mineral rim (Figure 3.17) (Walker et al., 1977). Based upon major element oxides, 15065 is classified as a quartz-normative gabbro (Rhodes and Hubbard, 1973), however, minor and relatively small olivine grains (~60 μm) are found enclosed within pyroxene grains and are reported to have intra-grain homogeneity with (~50% forsterite) but small (~2%) inter-grain variations in forsterite (Ryder, 1985a; Walker et al., 1977).

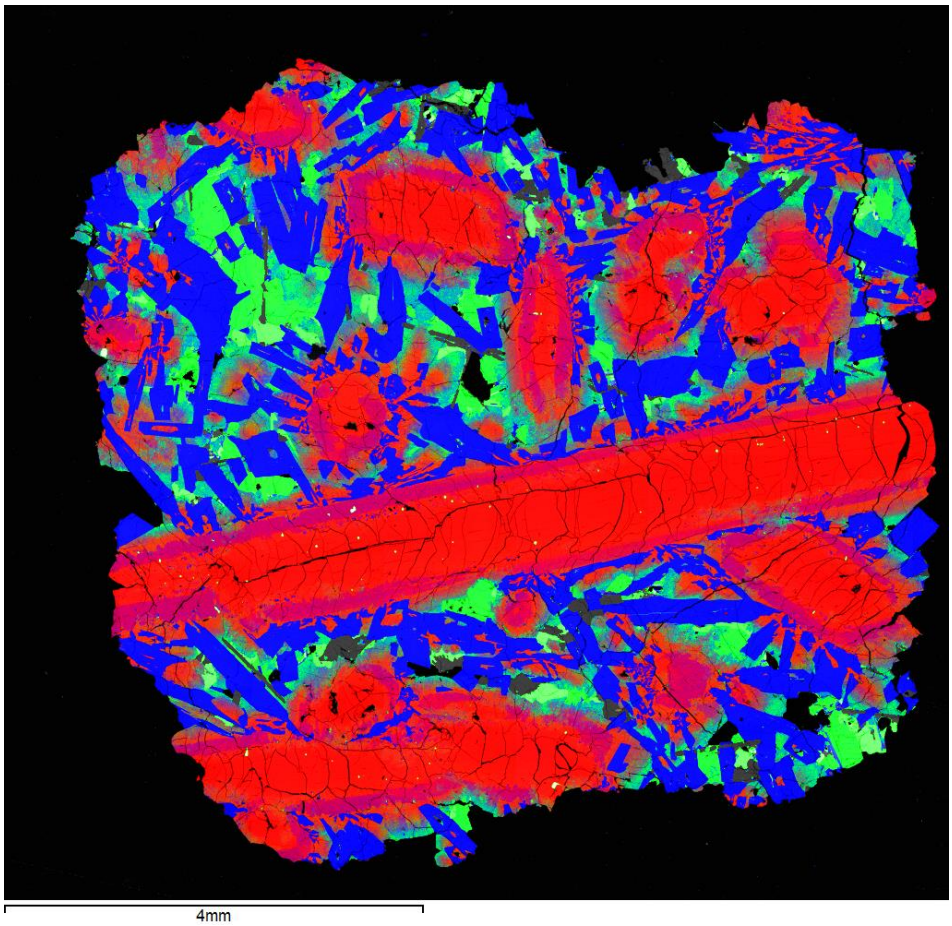

Figure 3.17. Apollo sample 15065,85 false colour X-ray map where red = Mg (Mg-rich pyroxene), green = Fe (Fe-rich pyroxene) and blue = Al (plagioclase). A very large pyroxene grain running across the centre of the sample (~8 mm) shows very clear zoning with a deepening of red to purple-red from pigeonite to ferroaugite, respectively. Plagioclase (Al-rich) is the second most abundant mineral with grains up to ~2 mm in the longest dimension.

There are numerous fractures throughout sample 15065, giving it a vuggy texture (Morrison and Silver, 1971) (Figure 3.18). The complete rock is reported to have two distinct regions: one of mafic and one of felsic composition with a diffuse boundary between the two regions (Morrison and Silver, 1971). Nava (1974) analysed two separate portions, 10 cm apart in the original intact specimen, and noted that the more mafic section

had higher FeO and TiO contents but lower Al_2O_3 relative to the other section which contained more plagioclase. Reasons suggested for the differences include magma chamber zoning or contamination from non-gabbroic material (Cuttita et al., 1973). The coarseness of the rock is thought to be due to its very slow cooling rate which was estimated to have been ~0.3 ˚C day^{-1}, based upon olivine diffusion modelling (Walker et al., 1977).

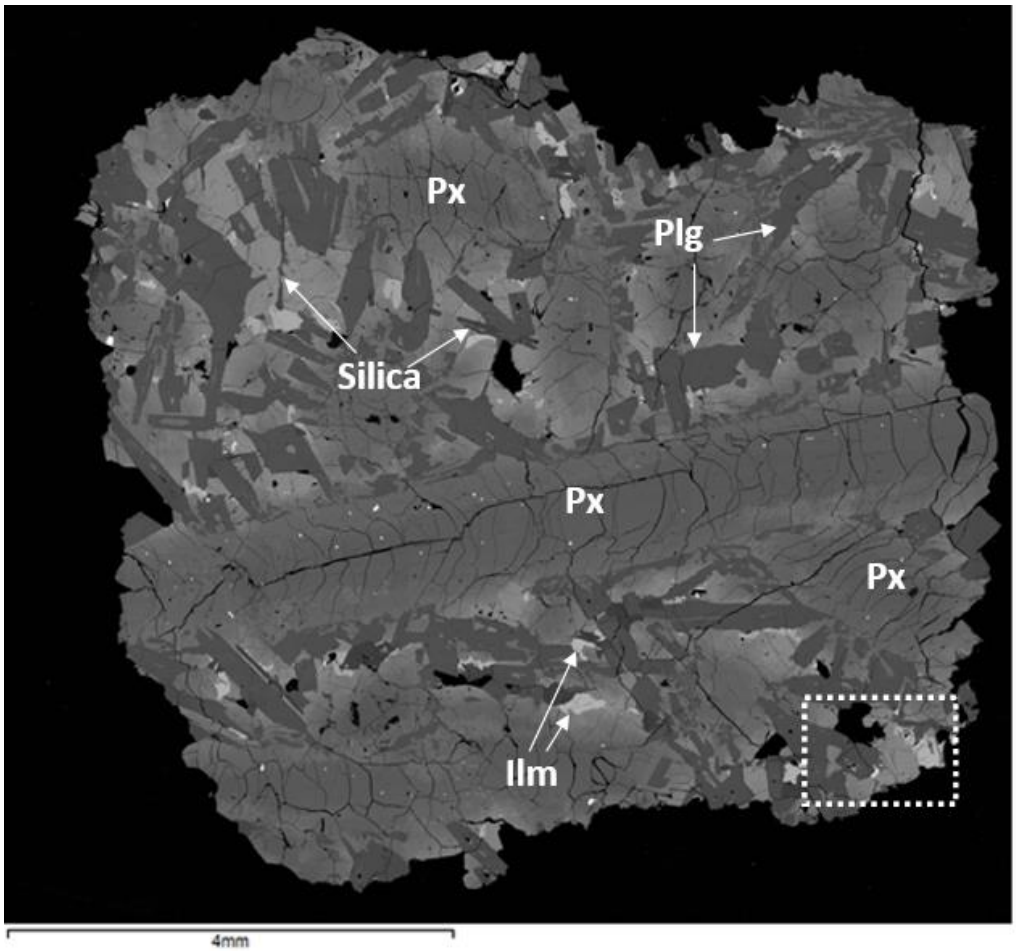

Figure 3.18. Apollo sample 15065,85. The BSE montage map shows the pyroxene zonation clearly (darker and lighter grey contrasts at core and rim, respectively) in the very large grains, where Px = pyroxene, Plg = plagioclase and Ilm = ilmenite. Infrequent laths of silica are detectable. The vuggy texture is very apparent and small vugs are particularly prominent within the large pyroxenes. The dashed white box represents the apatite region shown in Figure 3.19.

In 15065, prominent apatite is reported to occur alongside accessory minerals such as ilmenite, troilite, ulvöspinel, silica (cristobalite and tridymite), Ca-poor ferroaugite, metal and Fe-Ti oxides (Ryder, 1985a; Taylor and McCallister, 1972). The apatite analysed in this project (15065,85) is found in and amongst pyroxene grains (Figure 3.19) and in contact with plagioclase, potassium feldspar, ilmenite, tridymite and troilite.

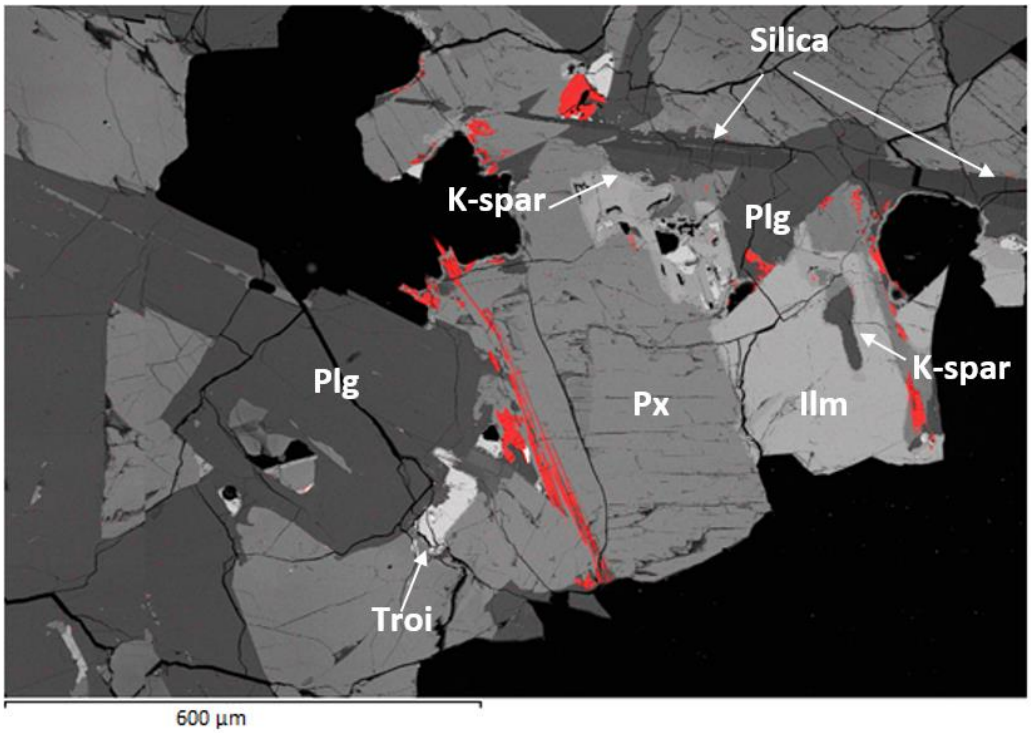

Figure 3.19. The position of apatite in Apollo sample 15065,85. False colour X-ray map, where red represents phosphorous, which has been positively identified as apatite. Very long (~200 µm) and very fine apatite laths are visible in this image. Px = pyroxene, Plg = plagioclase, Ilm = ilmenite, K-spar = potassium feldspar, Troi = troilite.

The apatite grains in 15065,85 frequently exist in tight clusters (Figure 3.20) where they are found to be relatively small (<2 µm – ~80 µm in the longest dimension) and are euhedral to anhedral. However, larger apatite grains, up to 200 µm in the longest dimension, are found as very fine laths that cross-cut pyroxene (Figure 3.19). As with pyroxene, apatite is also zoned but the zoning is only detectable when analysed with cathodoluminescence and not seen in BSE images (Figure 3.21). Like sample 15058,15, this suggests that the zoning is caused by different trace elements contained within the individual zones.

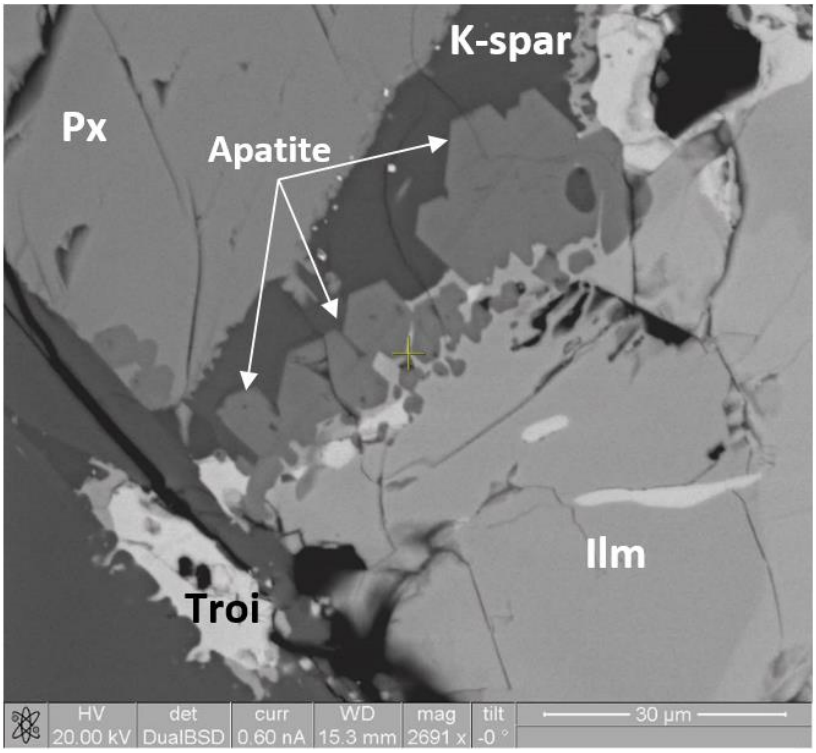

Figure 3.20: Apatite clusters in Apollo sample 15065,85. Some of the apatite (Ap) grains in this BSE image are <2 µm with others ~20 µm in the longest dimension. Apatites exist as tight clusters of apatite but their euhedral shapes can easily be seen in the BSE image. Px = pyroxene, Ilm = ilmenite, K-spar = potassium feldspar and Troi = troilite.

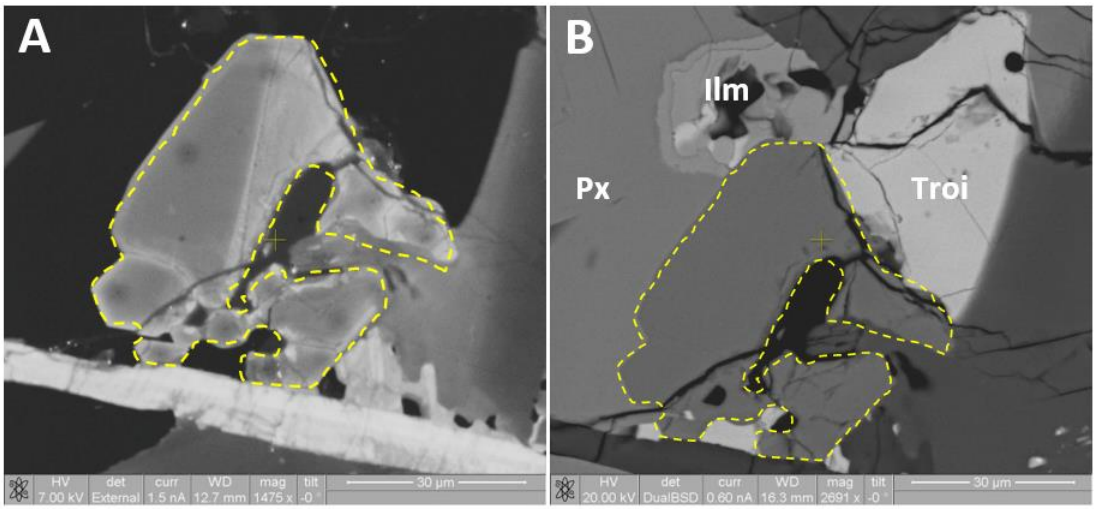

Figure 3.21. Zoned apatite grain in sample 15065,85. **A)** Cathodoluminescence image showing a zoned apatite grain (within yellow dashed line) with both diffuse and sharp zone boundaries. The luminescing lath of a tridymite is seen running beneath the apatite and a plagioclase is situated to the right of the apatite. **B)** BSE image does not detect the compositional zoning within the same apatite grain. Labels are as per Figure 3.20.

3.3.8. Pigeonite Basalt: 15085,15

Apollo sample 15085 was discovered during the Apollo 15 mission of 1971 and, as with sample 15065, was collected as part of a suite of samples from a location (designated 'Station 1') 60 m east of the rim of Elbow Crater (LSPET, 1972; Lunar and Planetary Institute, 2018b). Sample 15085 has a crystallisation age of ~3.40 ± 0.04 Ga which was determined using Rb-Sr isochron dating (Papanastassiou and Wasserburg, 1973). The cosmic ray exposure age for this sample has not been determined.

Sample 15085 is a coarse-grained, low-Ti basalt which contains vugs of a few milimeters in size that represent ~3–5 vol.% of the rock (LSPET, 1972). As a quartz-normative basalt that lacks olivine, 15085 is predominantly composed of very large pyroxene and plagioclase grains of up to 10 mm in the longest dimension (Ryder, 1985a) (Figure 3.22). Comprising ~40–66 vol.% of the rock, the pyroxenes have simple twins and are extensively zoned from Ca-poor pigeonite cores to Ca-poor, Fe-rich ferroaugite rims (Ridley and Bass, 1971; Wilshire and Brett, 1971). The anhedral plagioclase grains are slightly zoned and cut into the large pyroxene grains. The plagioclase content in separate thin sections of 15085 is reported to represent ~22–60 vol.% of the rock (Ridley and Bass, 1971; Wilshire and Brett, 1971; Papike et al., 1976). The very large and zoned crystals in 15085 have been attributed to a very slow subsolidus cooling rate of ~7 °C per day (Papike et al., 1976). Tridymite (silica) laths and blades are a common accessory mineral (~4 vol.%) in 15085 that cross-cut pyroxene, plagioclase and ilmenite (1.5 vol.%) grains (Wilshire and Brett, 1971; Ryder, 1985a).

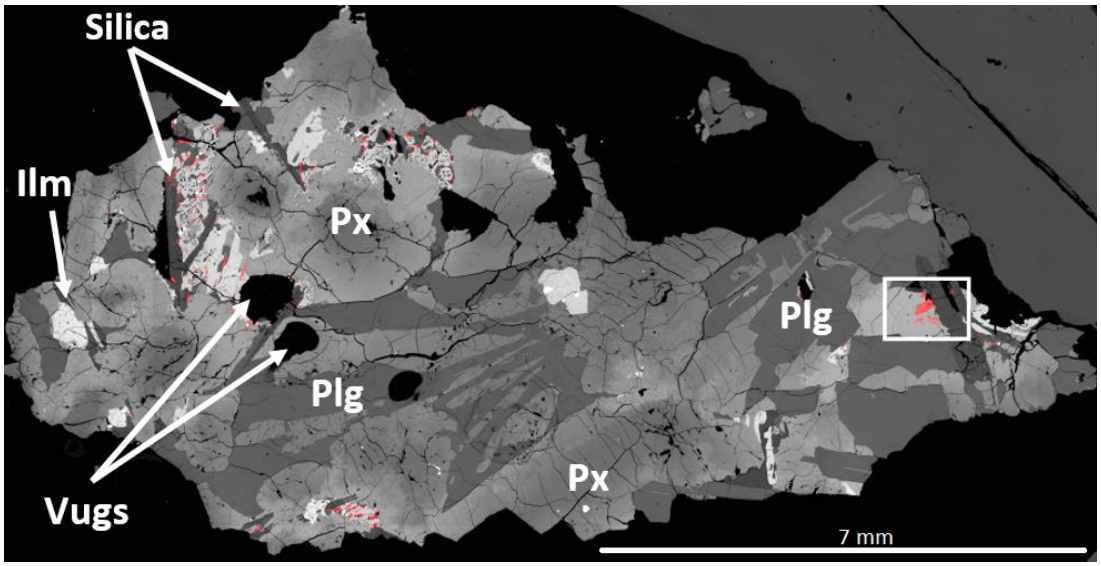

Figure 3.22. Apollo sample 15085,15. The false-colour image (where red = phosphorous-rich regions that highlight the position of apatite) shows the very large, zoned pyroxene (Px) grains (lighter and darker grey contrasts are discernible for the larger pyroxene grains which represent crystal zoning) and plagioclase grains (Plg), both of which enclose vugs. The white rectangle highlights the large apatite surrounded by pyroxene and silica in Figure 3.23. Ilmenite (Ilm) and blades of silica are also visible in this image.

The minor components of 15085 are found in the mesostasis regions and include ulvöspinel (~1.5 vol.%) and <1 vol.% troilite, Fe-Ni metal (found as blebs in troilite) and chromite spinel (Wilshire and Brett, 1971). Apatites are located within the mesostasis regions of the sample studied in this project (15085,15) alongside large troilite grains (often up to ~50 μm), ilmentite, silica, potassium feldspar and symplectite. However, the majority of the apatites are positioned away from mesostasis regions and are enclosed in pyroxene grains (Figure 3.23). Sample 15085 contains the largest apatite grain studied in the mare basalts of this project: ~200 μm in longest dimension but there are also much smaller grains of <~10 μm. The apatites vary in shape from small euhedral to (predominantly) anhedral and lath-shaped. Only incredibly faint diffuse zoning was seen to exist in a few apatite grains when viewed with cathodoluminescence.

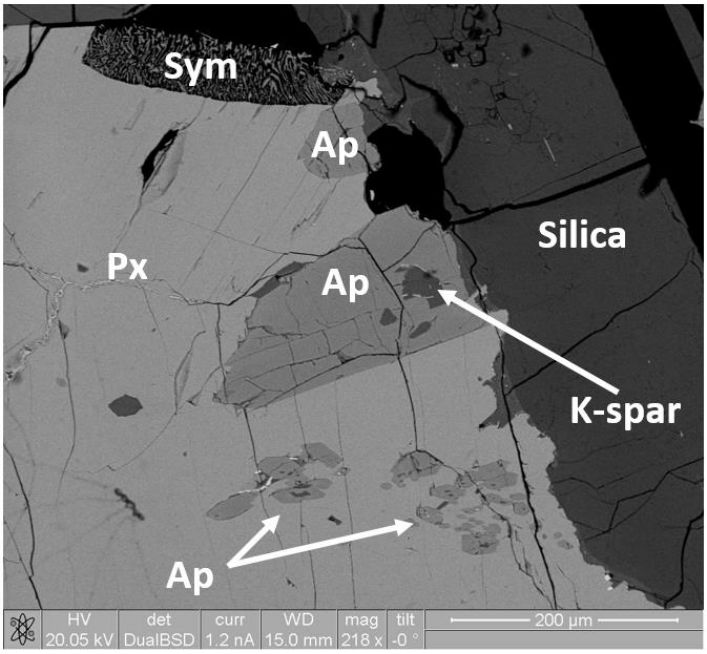

Figure 3.23. Apatite in Apollo sample 15085,15. BSE image of very large apatite (Ap) grains (in the longest dimension: ~200 µm in the centre and ~50 µm at the top of the image) enclosed within a pyroxene (Px) and bordering silica. The largest apatite has potassium feldspar (K-spar) inclusions.

3.3.9. KREEP basalt: 15386,46

Apollo sample 15386 was collected in a soil rake sample (mostly consisting of breccias and soil fragments), on the northeast rim of Spur Crater, along the Apennine Front (Station 7), during the Apollo 15 mission of 1971 (Swann et al., 1971b). The crystallisation age of 15386 is ~3.88 ± 0.25 Ga (weighted average age of Rb-Sr and Sm-Nd isochron dates (Tartèse et al., 2014a)). There is no cosmic ray exposure age (CRE) reported for 15386, albeit values of ~235 ± 5 Ma (based on KREEP basalt 15382) have previously been used for spallation corrections (Tartèse et al., 2014a).

Potassium, rare earth element, phosphorous (KREEP) basalt 15386 is a non-mare basalt sample that has incompatible trace element enrichment of 100 to 150 times that of chondritic (primitive) meteorite compositions (e.g. Wieczorek et al., 2006). Sample 15386 is described as a subophitic (small grained), pristine (i.e. endogenous to the lunar interior) volcanic basalt. Plagioclase is reported to comprise ~35–50 vol.% of the rock sample with grains of up to ~2 mm in the longest dimension. Interstitial pyroxene is observed between the plagioclase grains and represents ~50 vol.% of the sample (Figure 3.24). Olivine has not been found in the sample and it is suggested that plagioclase and pyroxene crystallised together as a result of rapid cooling which also led to the relatively small grain sizes in the

sample. Approximately 10 vol.% cristobalite has been reported along with ~3 vol.% ilmenite (Ryder, 1985c).

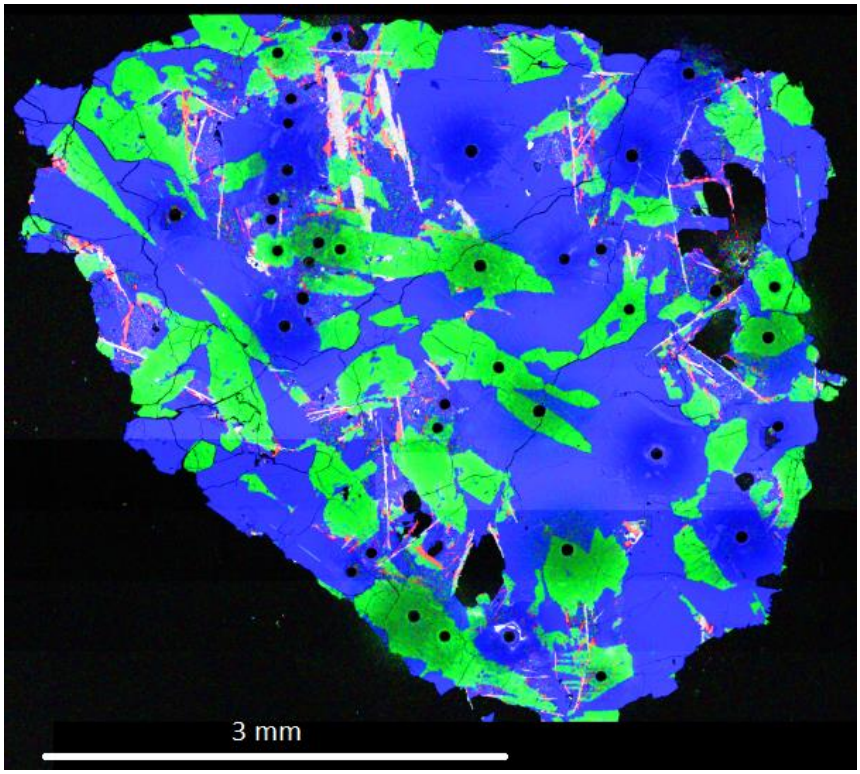

Figure 3.24. Apollo sample 15386,46. A false colour X-ray map where: blue = Al (plagioclase), green = Mg (pyroxene), red = phosphorous (apatite) and white = Ti (ilmenite). Plagioclase dominates this image with interstitial pyroxene and blades of ilmenite intersecting the plagioclase. (Image courtesy of Jessica Barnes, The Open University).

The minor mineral phases of 15386, such as troilite, Fe-metal and phosphates are found within mesostasis regions (Ryder, 1985c). The mesostasis in the specific sample studied in this project (15386,46) also include potassium feldspar, tranquillityite, baddeleyite, apatite, merrillite, ilmenite, plagioclase and silica. Exclusively found in mesostasis pockets, the apatite is between ~25 μm and ~250 μm in the longest dimension (Figure 3.25) and varies from subhedral to anhedral or appears as long, straw-shaped grains. When viewed with cathodoluminescence, zoning is either absent or is incredibly faint at the edges of the apatite grains.

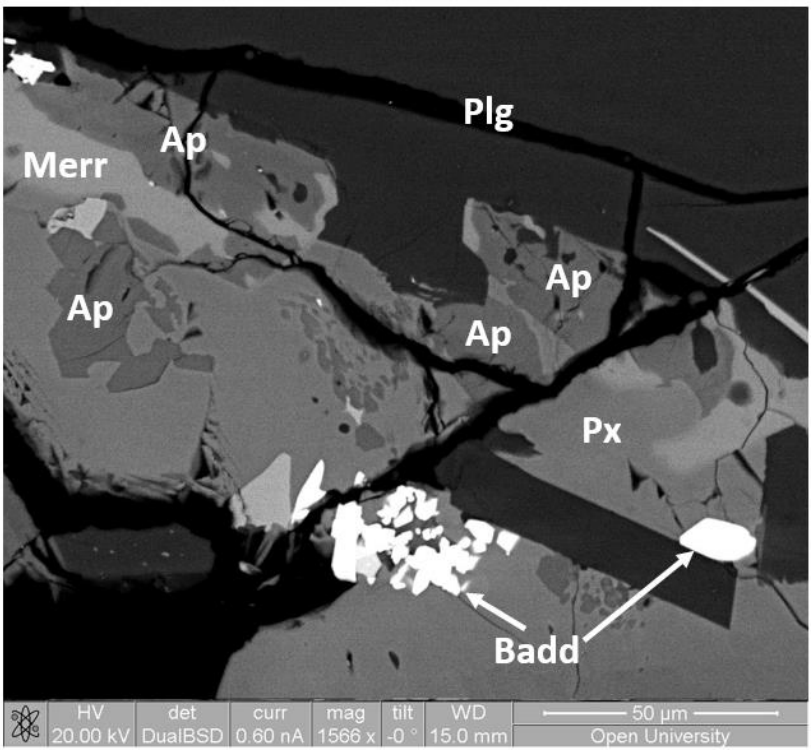

Figure 3.25. Apatite in Apollo sample 15386,46. BSE image of apatite (Ap) grains contained within a typical mesostasis region. The apatites are subhedral to anhedral and range from <5 μm to >50 μm in the longest dimension. The image also contains the other phosphate mineral merrillite (Merr) that is adjacent to apatite in the top-left corner. Other mineral phases include pyroxene (Px), plagioclase (Plg) and baddeleyite (Badd). (Image courtesy of Jessica Barnes, The Open University).

3.3.10. Porphyritic Pigeonite Basalt: 15475,17

Apollo sample 15475 was discovered approximately 30 meters south-southeast from the rim of Dune Crater, in an area designated Station 4, during the Apollo 15 mission of 1971. It was collected alongside four other mare basalt rocks (15476, 15485, 15495 and 15499) (Swann et al., 1971b). The crystallisation age of 15475 has been determined using Rb-Sr dating as 3.43 ± 0.15 Ga and using Sm-Nd dating as 3.37 ± 0.05 Ga (Synder et al., 1997). The sample was exposed to cosmic rays at the surface for a relatively long time of 473 ± 20 Ma (determined using the noble gas $^{81}Kr/^{83}Kr$ technique (Drozd et al., 1974; Pepin et al., 1974)) and there are some micrometeorite impacts on the surface of the rock, accompanied by notable fractures (two pieces of the rock have broken away from the main mass) (e.g. Ridley and Bass, 1971; Morrison and Silver, 1971; Ryder, 1985b).

Described as a coarse-grained (porphyritic), low-Ti, quartz-normative mare basalt, 15475 contains 2–20 vol.% vuggy pore space and is visibly fractured at the scale of the thin

sections (Ridley and Bass, 1971; Jakes, 1971; Morrison and Silver, 1971) (Figure 3.26). As with many of the Apollo 15 samples studied in this project, the mineralogy of 15475 is dominated by large pyroxene and plagioclase grains. Pyroxene represents ~64–74 vol.% (Silver and Brett, 1971; Rhodes and Hubbard, 1973) of the sample with large grains of up to 15 mm (Ryder et al., 1985b) that are twinned and zoned from pigeonite cores to augite or Ca-poor, Fe-rich pyroxferroite rims (Schnare et al., 2008; Brown et al., 1972).

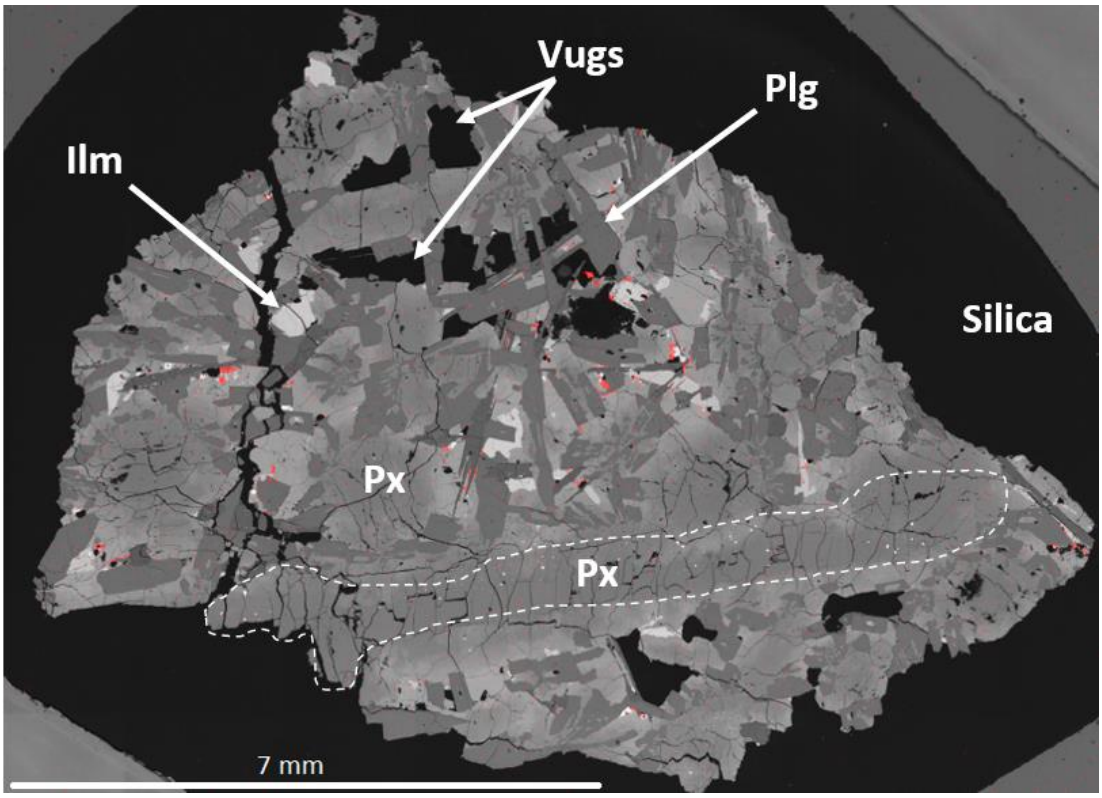

Figure 3.26. Apollo sample 15475,17. The false-colour image, where red = phosphorous-rich regions that highlight the position of apatites, shows very large, zoned subhedral pyroxene grains (lighter and darker grey contrasts are discernible for the larger pyroxene grains which represent crystal zoning) with a grain of ~10 mm in the longest dimension (dashed oval white line). The vuggy nature of the grain is clear to see and there is a notable fracture on the left-hand-side of the sample.

As with the abundance of vugs and clinopyroxene, the plagioclase content is found to be quite varied depending upon the thin section studied, with 10–45 vol.% reported by different investigators (Ridley and Bass, 1971; Jakes, 1971; Morrison and Silver, 1971; Rhodes and Hubbard, 1973). Lath- and tabular-shaped plagioclase grains are typically up to 2 mm in the longest dimension (Morrison and Silver, 1971). Overall, the large grain sizes in 15475 have been attributed to a very slow cooling rate of 0.05 °C per hour and 0.1 °C per hour during the early and late stages of cooling, respectively (Grove and Walker, 1977).

Often found being cross-cut by plagioclase, ilmenite grains of up to 0.5 mm in the longest dimension (Silver and Brett, 1971) exist within the rock matrix of 15475 and represent ~2 vol.% of the sample. Minor mineral phases include laths of cristobalite (~0.8 vol.%), ulvöspinel (~0.6 vol.%), chromium spinel (~0.4 vol.%) and troilite (~0.1 vol.%) (Rhodes and Hubbard, 1973). Mesostasis regions represent ~1 vol.% of the sample and are exclusively where apatite grains in the specific sample (15475,17) studied in this project are situated (Figure 3.27). The mesostasis regions contain silica, ilmenite, potassium feldspar, troilite, plagioclase and pyroxene. Potassium feldspar commonly appears as inclusions within apatite grains (Figure 3.27). The apatites are mostly euhedral to subhedral and are some of the largest observed in the samples studied in this project (second to sample 15085,15) being ~50 μm to ~100 μm in the longest dimension. Zoning was not apparent when the apatites were investigated with cathodoluminescence.

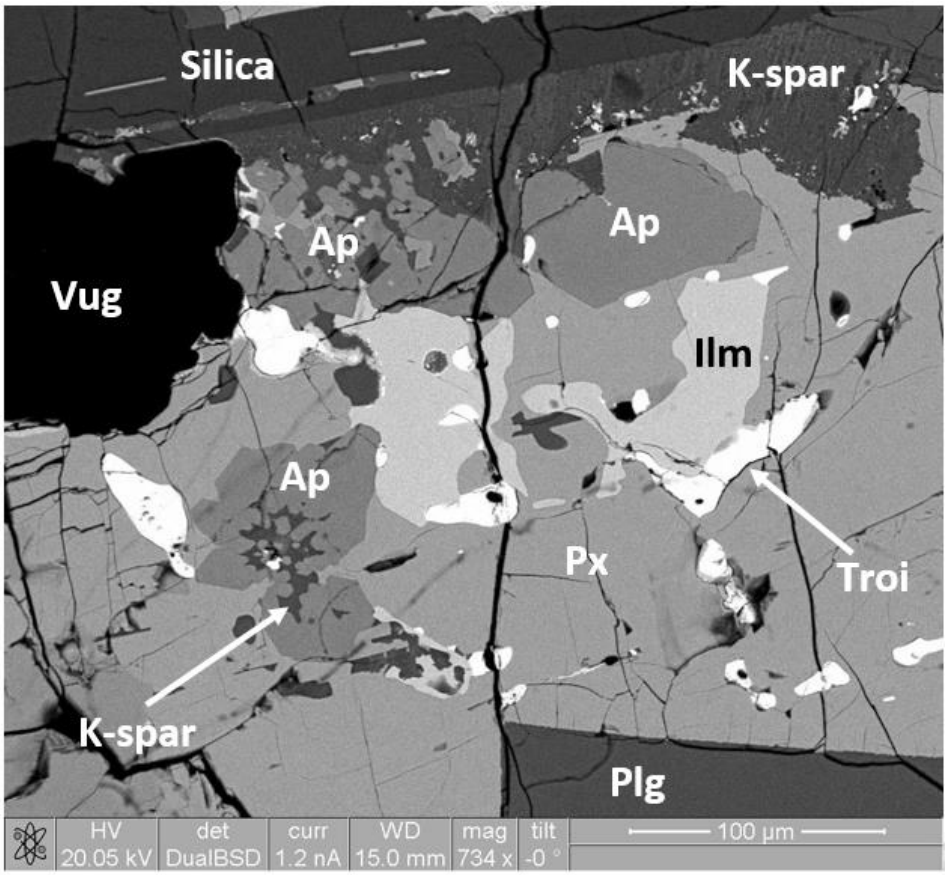

Figure 3.27. Apatite in Apollo sample 15475,17. BSE image of apatite (Ap) grains contained within a typical mesostasis region. The top-right apatite is ~90 μm in the longest dimension. Potassium feldspar (K-spar) inclusions can be easily seen within the apatite grain left of centre. A large vug (>100 μm across) in the top-left corner and cracks and fractures throughout the mineral phases can be clearly seen. Px = pyroxene, Plg = plagioclase, Troi = troilite, Ilm = ilmenite.

3.3.11. Olivine normative basalt: 15545,7

Apollo sample 15545 was collected from 'The Terrace', near to the edge of Hadley Rille, from Station 9A, during the Apollo 15 mission of 1971 (Swann et al., 1971b). From a petrological point of view, 15545 is a relatively unstudied sample. Whilst previous studies have published Rb-Sr and Na-Al isotopic data (e.g. Nyquist et al., 1973; Yokoyama et al., 1974), the crystallisation age and cosmic exposure age of 15545 was not explicitly reported. However, the data has been interpreted by other authors to give a crystallisation age of ~3.3 Ga and a cosmic ray exposure age of ~2 Ma (e.g. Ryder et al., 1985b; Meyer, 2010).

Sample 15545 is described by Silver and Brett (1971) as a porphyritic olivine mare basalt with late-stage interstitial plagioclase. Olivine comprises ~4–11 vol.% of the rock and can be 1.5 mm in the longest dimension with zoning from Fo_{56} to Fo_{17} or Fo_{7}. The plagioclase grains are larger at 3 mm in the longest dimension and represent ~24–30 vol.% of the sample (Figure 3.28). Pyroxene grains are the most abundant with ~50 vol.% but they are the smallest of these three minerals being only ~0.2 mm in the longest dimension. The pyroxenes are zoned from pigeonite at the core through to Ca-poor augite at the rim (Silver and Brett, 1971; Rhodes and Hubbard, 1973; Ryder et al., 1985b).

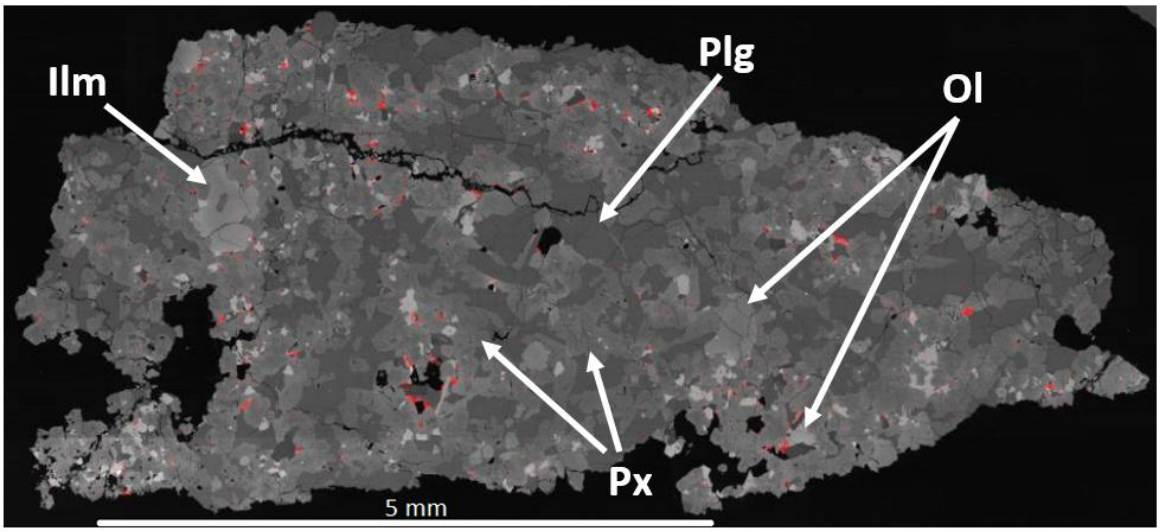

Figure 3.28. Apollo sample 15545,7. The false-colour image shows the locations of apatites (red = phosphorous-rich regions) and relatively large plagioclase (Plg) grains set in a matrix of smaller but more abundant pyroxene (Px) and ilmenite (Ilm) grains. The olivine (Ol) grains are small and less abundant. A clear fracture runs from top left to top right of the sample.

The minor constituent minerals that form part of the rock matrix include ulvöspinel (3 vol.%), ilmenite (3 vol.%), cristobalite (1.5 vol.%), and <1 vol.% is represented by troilite, Fe-Ni metal, glass and chromite spinel. Vugs represent ~10-15% of the rock and are surrounded by pyroxene (Silver and Brett, 1971). Mesostasis regions are scattered throughout the thin section sample studied in this project (15545,7) and are where all of the analysed apatites are located. The typical mesostasis regions include potassium feldspar, ilmenite, troilite, Fe-Ni metal, olivine and pyroxene (Figure 3.29). Many of the apatites were too small for further analysis (<10 μm) but other grains of up to ~30 μm in the longest dimension also exist in the sample. The majority of apatites are anhedral and contain inclusions of potassium feldspar or are surrounded by intricate lace patterns of potassium feldspar. Only very faint zoning was seen at the very edge of two apatite grains when viewed with cathodoluminescence (Figure 3.30).

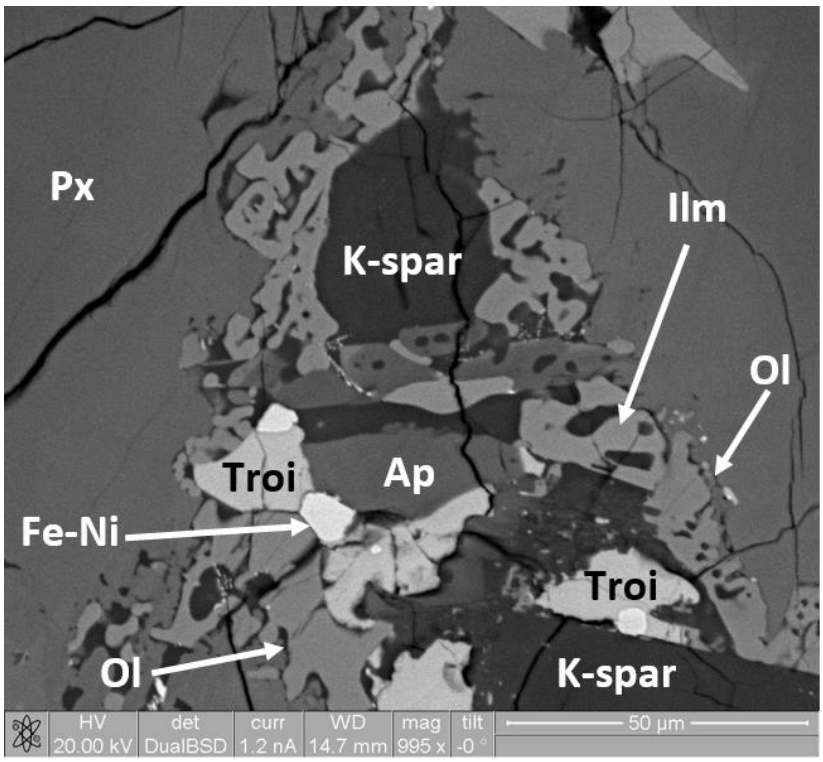

Figure 3.29. Apatite in Apollo sample 15554,7. BSE image of a typical mesostasis region. Apatite (Ap) is in the centre of the image and is immediately surrounded by potassium feldspar (K-spar), troilite (troi), ilmenite (Ilm) and Fe-Ni metal (Fe-Ni). Olivine (Ol) and pyroxene (Px) also feature within the mesostasis region.

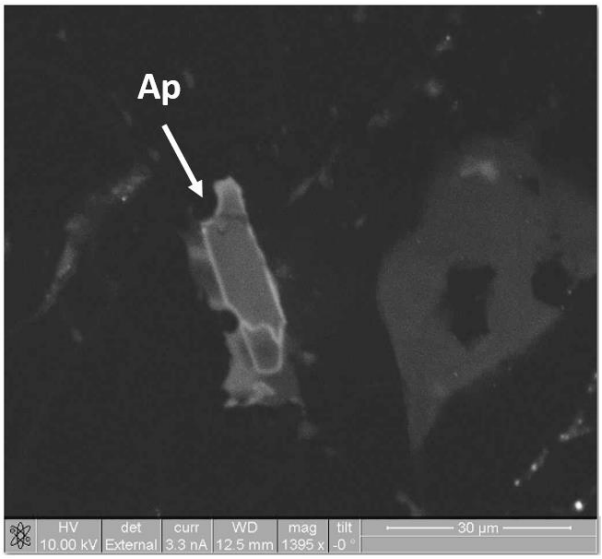

Figure 3.30. Zoned apatite grain in sample 15545,7. Cathodoluminescence (CL) image showing sharp zonation all the way around the far edge of the apatite grain. The halo to the left and below the apatite is luminescence from the adjacent potassium feldspar grain. The large, light grey, shape to the right of the image is a luminescing vug (cavity).

3.3.12. Olivine normative basalt: 15555,991

Apollo sample 15555 was collected ~12 meters to the north of the rim of the Hadley Rille (a great valley in the lunar surface) during the Apollo 15 mission of 1971 (Lunar and Planetary Institute, 2018b) from Station 9A. The sample was the largest of those returned from the Apollo 15 landing site, weighing ~9.6 kg (LSPET, 1972) and has become the most extensively studied.

The crystallisation age of sample 15555 has been reported as 3.32 ± 0.06 Ga, based on the Rb-Sr dating method (Wasserburg and Papanastassiou, 1971). However, up to fifteen different authors have calculated the crystallisation age using Rb-Sr, Ar/Ar, U/Pb, Pb/Pb and Sm/Nd dating methods during the early 1970s (Meyer, 2010) and reported ages from 3.23 ± 0.02 Ga (Nyquist et al., 1991) up to 3.54 ± 0.13 Ga (Chappell et al., 1971). The cosmic ray exposure age of 81 Ma was determined using the noble gas $^{81}Kr/^{83}Kr$ method by Marti and Lightner (1972).

Sample 15555 is a large coarse-grained (porphyritic), vuggy, low-Ti olivine-normative basalt (Rhodes and Hubbard, 1973). Having been extensively studied, a very wide range of compositional values are reported for 15555 from different authors, with olivine content between 5-20 vol.%, pyroxene content between 40-65 vol.% and plagioclase content

between 25-35 vol.% (e.g. Nord et al., 1973; Bence and Papike, 1972; Rhodes and Hubbard, 1973; McGee et al., 1977). The minor components of 15555 are silica (cristobalite) (0.2-3 vol.%), ilmenite (1 vol.%), opaque minerals (chromite and ulvöspinel) (~5 vol.%) and mesostasis (0.2-5 vol.%) (Rhodes and Hubbard, 1973; McGee et al., 1977).

Quantitative differences between reported measurements are also apparent for major element oxides and rare earth element (REE) content for 15555 (Mason et al., 1972). Such differences have been attributed to the proportionally small size of the sub-samples allocated to investigators relative to the large size of the crystals contained within the individual samples. The outcome is that the results are not necessarily representative of the whole rock but are a reflection of only a few large grains contained within the allocated sub-samples (Mason et al., 1972).

On average, the olivine, pyroxene and plagioclase grains in 15555 are 0.8-1.0 mm, 0.5-2.0 mm and 0.9-3 mm, respectively, in the longest dimension (Ryder, 1985b; McGee et al., 1977) (Figure 3.31). The majority of olivine grains are zoned from a Mg-rich core out to a Fe-rich rim (Fo_{67-29}) (Dalton and Hollister, 1974). Pyroxene grains that crystallised early are relatively coarse with zoning patterns from pigeonite to augite, whereas the fine-grained pyroxene that crystallised later are augites enclosed in a plagioclase matrix (Bence and Papike, 1972). The plagioclase grains enclosing small olivine and pyroxene grains are relatively homogeneous in the cores (An_{94-91}) but the rims have a zonation pattern of decreasing anorthite (An_{91-78}) (Ryder, 1985b).

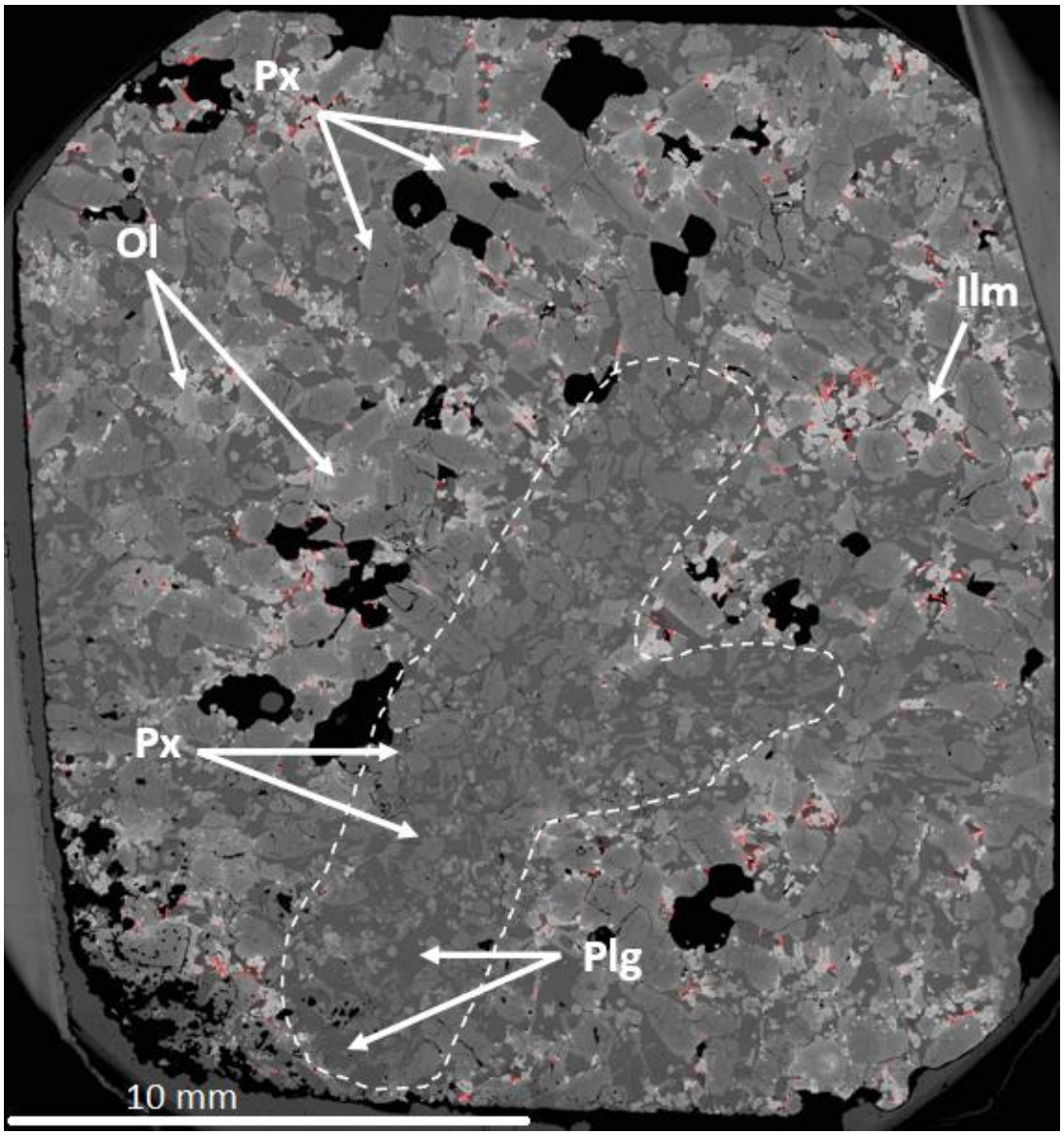

Figure 3.31. Apollo sample 15555,991. The false-colour image (red = phosphorous-rich regions and apatite locations) shows the vuggy nature of the rock and the two different relationships of pyroxene (Px) with plagioclase (Plg). The area within the white dashed line highlights the later crystallising pyroxene which is finer-grained and enclosed in a plagioclase matrix, whereas the rest of the sample contains the larger, earlier crystallising pyroxene. Lighter and darker grey contrasts are discernible for the larger pyroxene grains which represent crystal zoning. Where, Plg = plagioclase, Ol = olivine and Ilm = ilmenite.

The cooling rate for sample 15555 has been determined to be between ~5 °C and 24 °C per day (Walker et al., 1977; Taylor et al., 1977; Bianco and Taylor, 1977). Bence and Papike (1972) have stated that 15555 and 15016 (see earlier description) are "identical in every respect but texture", where the differences in texture were attributed to slower and faster cooling rates, respectively.

The apatite grains of the specific sample studied within this project (15555,991) are predominantly located within the mesostasis regions (0.2-5 vol.%) alongside troilite, potassium feldspar, silica and ilmenite (Figure 3.32) but apatite is also found enclosed within Fe-rich pyroxene grains, often with plagioclase inclusions. The majority of the apatite grains are between <5 μm and ~40 μm in the longest dimension and appear as clusters of small euhedral or larger anhedral grains. It is also quite typical for apatite grains in 15555 to have long, thin straw-like appearances (up to ~100 μm in the longest dimension) that give the impression of having been splashed into the rock (Figure 3.32(B)). Whilst zoning of olivine, pyroxene and plagioclase grains is prevalent (apparent in BSE images), the apatite grains were rarely seen to be zoned when observed under cathodoluminescence imaging.

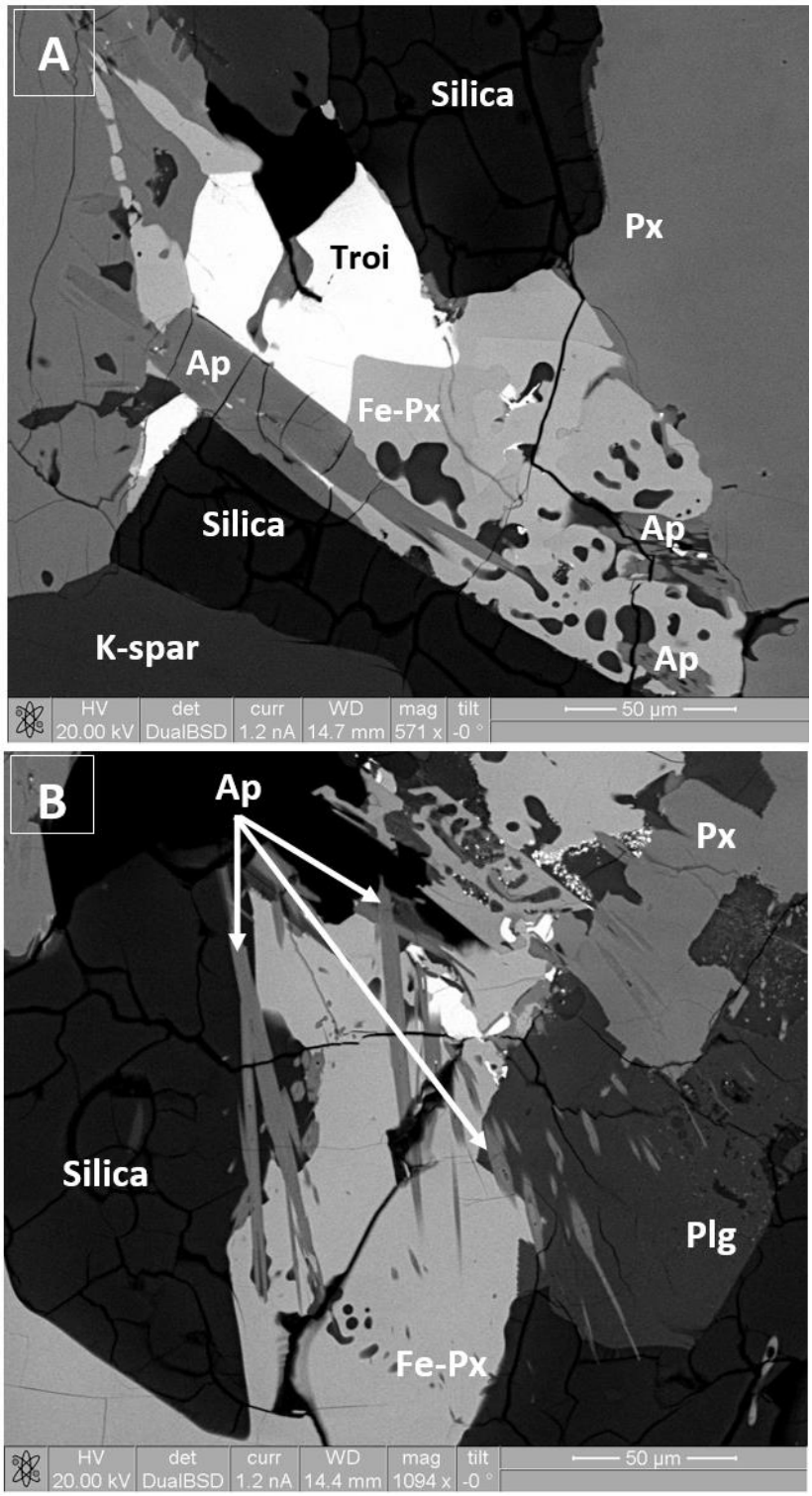

Figure 3.32. Apatite in Apollo sample 15555,991. **A)** BSE image of a relatively large (~25 µm) apatite (Ap) in a typical mesostasis region. Blebs of potassium feldspar (K-spar) are also seen within the Fe-rich pyroxene (Fe-Px) grain. **B)** BSE image shows the dominant type of apatite found in 15555 with its straw-like, dripped/ splashed appearance as it dissects silica, Fe-Px and Plg (abbreviations are as per image A).

3.3.13. Vesicular olivine normative basalt: 15556,137

Apollo sample 15556 was collected from the same area as sample 15545 at 'The Terrace', ~60 meters north-east of the rim of Hadley Rille (Station 9A) during the Apollo 15 mission of 1971 (Swann et al., 1971b). The crystallisation age of 15556 has been determined using K-Ar dating as 3.4 ± 0.1 Ga. A relatively long cosmic ray exposure time of 490 ± 50 Ma (determined by both ^{3}He and ^{38}Ar isotope analyses) to 525 ± 40 Ma was reported by Kirsten et al. (1972).

Sample 15556 is a fine-grained, low-Ti mare basalt. It is highly vesicular with ~50 vol.% of the rock containing vesicles of up to ~5 mm (Figure 3.33) that are often lined with opaque minerals (e.g. ilmenite) or glass (McGee et al., 1977). Olivine phenocrysts (~0.1 – 0.4 mm) comprise ~5 vol.% of the sample and appear to be less abundant and smaller in regions of the rock where there are more vesicles (Ryder, 1985b). Approximately 50 vol.% of the sample is composed of pyroxene phenocrysts (up to ~0.5 mm in the longest dimension) which are found to be very weakly zoned (Reid and Brett, 1971). The matrix of the rock contains granular pyroxene and tabular-shaped plagioclase. Glass and opaque minerals of ilmenite (~2.1 vol.%), ulvöspinel and chromite (totalling <1 vol.%) are also found in the matrix between the larger silicate grains (Rhodes and Hubbard, 1973; McGee et al., 1977).

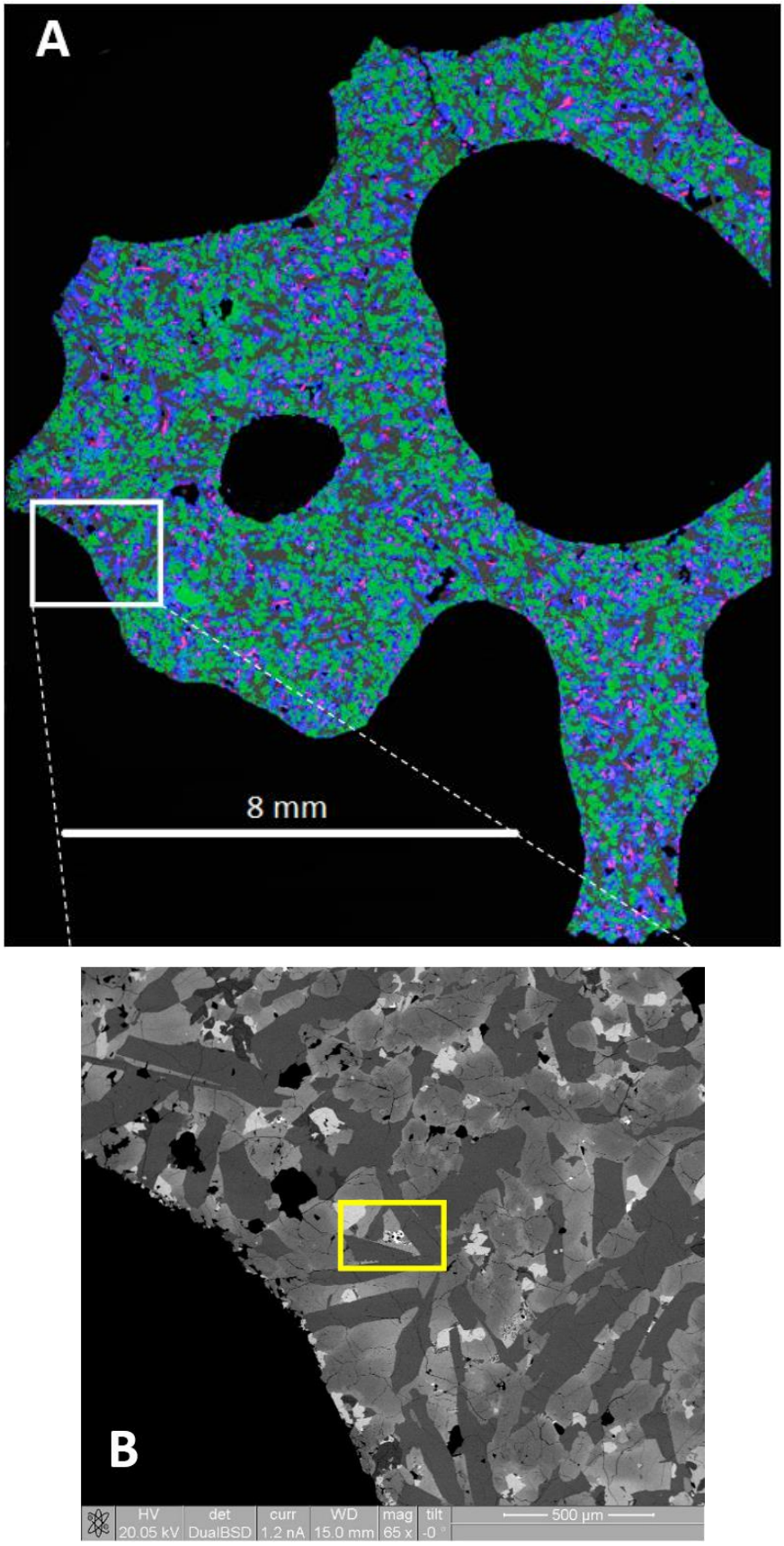

Figure 3.33. Apollo sample 15556,137. **A**) The false colour X-ray map shows the fined grained nature of the sample, where blue = Fe and green = Mg (pyroxene and olivine), grey = Ca (plagioclase) and pink = Ti (ilmenite). **B**) A higher resolution BSE image showing the mineral phases more clearly, where the yellow box highlights the apatite region shown in Figure 3.34.

As with vesicular olivine basalt 15016, sample 15556 is thought to have acquired its vesicles as a result of the eruption style, whereby vesicles are believed to have formed from gaseous release during very fast cooling of the basalt in a low pressure environment. Based on physical investigations of the vesicles, Garvin et al. (1982) suggested that the magma from which 15556 formed, ascended at a rate of 0.2 ms^{-1}. Unlike 15016, sample 15556 is very low in MgO with only ~8 wt.% compared with ~11 wt.% for 15016 (Table 3.2) (Rhodes and Hubbard, 1973), which suggests that it might be from a more evolved magma. Mason et al. (1972) has suggested that 15556 is related to sample 15555 by olivine fractionation, whereby a decreasing MgO and olivine (16% less) trend in the magma can account for the difference between 15555 and 15556.

The mesostasis regions of the specific sample studied in this project (15556,137) typically contain ilmenite, troilite, silica, potassium feldspar, plagioclase and pyroxene. There are very few apatites in 15556,137 but the three that were analysed are located in mesostasis regions. The apatites are anhedral or straw-like and relatively small with sizes ranging from <5 μm to ~30 μm in the longest dimension (Figure 3.34). Zoning of the apatite grains was not observed when viewed with cathodoluminescence.

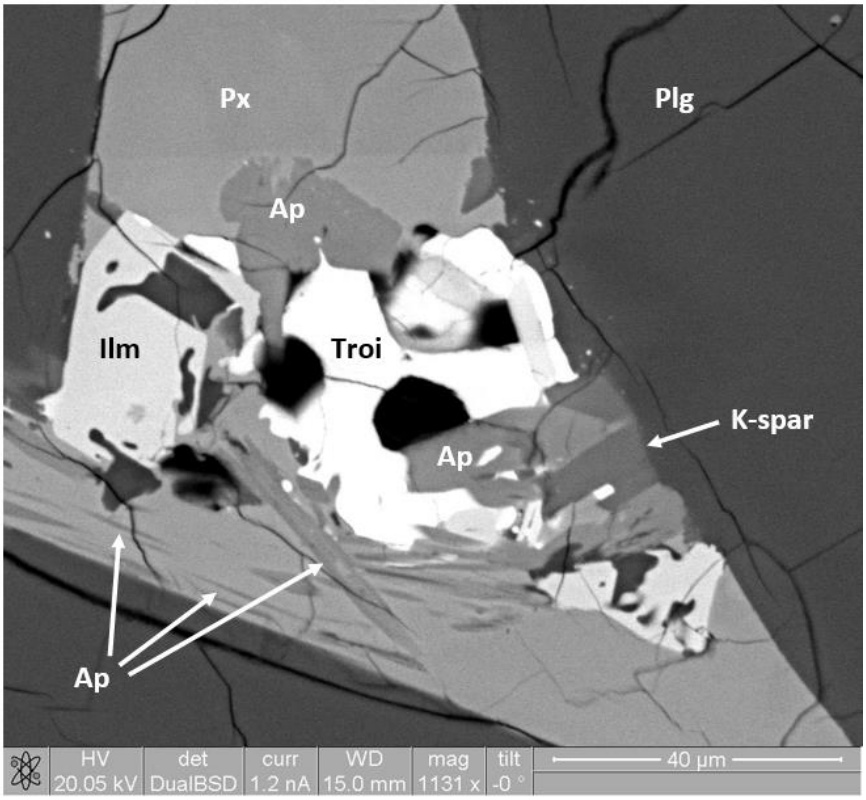

Figure 3.34. Apatite in Apollo sample 15556,137. BSE image of a typical mesostasis region containing anhedral and very thin, straw-shaped apatite (Ap) grains. The mesostasis also contains a large troilite (troi) in the centre, ilmenite (ilm), potassium feldspar (K-spar), pyroxene (Px) and plagioclase (Plg). The location of this mesostasis area is highlighted in Figure 3.33(B).

3.3.14. Feldspathic granulitic impactite: 79215,50

Apollo sample 79215 was collected during the Apollo 17 mission of 1972 where it was found loose at the lunar surface within the Taurus-Littrow Valley, southeast of the Van Serg Crater (Muehlberger et al. 1973). The valley is set within the mountainous highlands region that makes up the east rim of the Serenitatis basin (Lunar and Planetary Institute, 2018c).

A KREEP-poor sample, 79215 has been described as a holocrystalline (entirely crystal based), feldspar-rich rock that consists of both relict lithic and single mineral clasts that intermingle with a crushed, mixed and annealed granoblastic matrix (having a polygonal morphology with grain boundaries intersecting at triple junctions of ~120° (Best, 2003)) (Bickel et al., 1976; McGee et al., 1978). Proposed to have originally been a plagioclase-olivine cumulate derived from the global, primitive lunar melt and subsequent lunar crust (Warner, et al., 1977), the sample is believed to have experienced high temperature

metamorphic deformation during an event of unknown origin (perhaps single or multiple meteorite impacts) prior to the terminal lunar cataclysm (the formation of many large basins at ~3.9 Ga – 4 Ga) (Bickel et al., 1976). The crystallisation age for 79215 has been calculated as approximately 3.9 Ga (Hudgins et al., 2008; McGee et al., 1978; Oberli et al., 1979), whereas the cosmic ray exposure age is ~339 ± 24.2 Ma (McGee et al., 1978).

The highly siderophile trace element abundance has been used as evidence for meteoritic interaction, with the highly siderophile element (HSE) ratios being characteristic of CM carbonaceous chondrites (Fischer-Gödde and Becker 2012). However, the preservation of major element chemistry and relict grains within the sample, indicate that the rock retains some of its primitive chemistry (Bickel et al., 1976). During the deformation, the sample was heated to a high temperature which, during re-crystallisation, removed or rearranged any imposed crystal defects (a process known as annealing (Humphreys et al., 2017)) and led to the growth of larger grains. The annealing occurred over a prolonged period with an estimated temperature range between ~660 °C and ~1000 °C as indicated by geothermometry (e.g. via mineral pairs such as low and high Ca pyroxene, olivine–orthopyroxene and olivine–spinel) (Bickel et al., 1976; McGee et al., 1978; Andersen and Lindsley, 1979; Cushing et al., 1999).

Sample 79215 has a matrix accounting for ~72% of the rock which was formed by prolonged annealing, crushing and limited mixing (Bickel et al., 1976) of clasts of anorthite plagioclase (~79 vol.%), olivine (~13 vol.%), orthopyroxene (~5 vol.%), clinopyroxene (~2 vol.%) and small quantities (≤0.1 vol.% each) of spinel, ilmenite, metal and troilite (McGee et al., 1978). Phosphate (apatite) is almost completely lacking within the matrix (Figure 3.35).

The remaining ~28% of the rock is composed of mafic (troctolitic-noritic-gabbroic) (3 vol.%), anorthositic (20 vol.%) and mineral clasts (5 vol.%). The mafic clasts consist of plagioclase (~42 vol.%), olivine (~30 vol.%), orthopyroxene (~21 vol.%) and clinopyroxene (~6 vol.%), and have quite indistinct, gradational boundaries with the matrix. The anorthositic clasts consist of anorthitic plagioclase (~93%), olivine (~6%) and minor (both <1%) orthopyroxene and clinopyroxene (McGee et al., 1978). These clasts are found either completely surrounded by matrix with distinct boundaries, or as cross-cutting, irregular bands that mingle with the matrix at gradational boundaries and suggests some

level of interaction between the clasts and the matrix. Large phosphate (apatite) clasts contribute to ~8% of the mineral clasts which are otherwise dominated by plagioclase (68%) and olivine (~19%) (McGee et al., 1978).

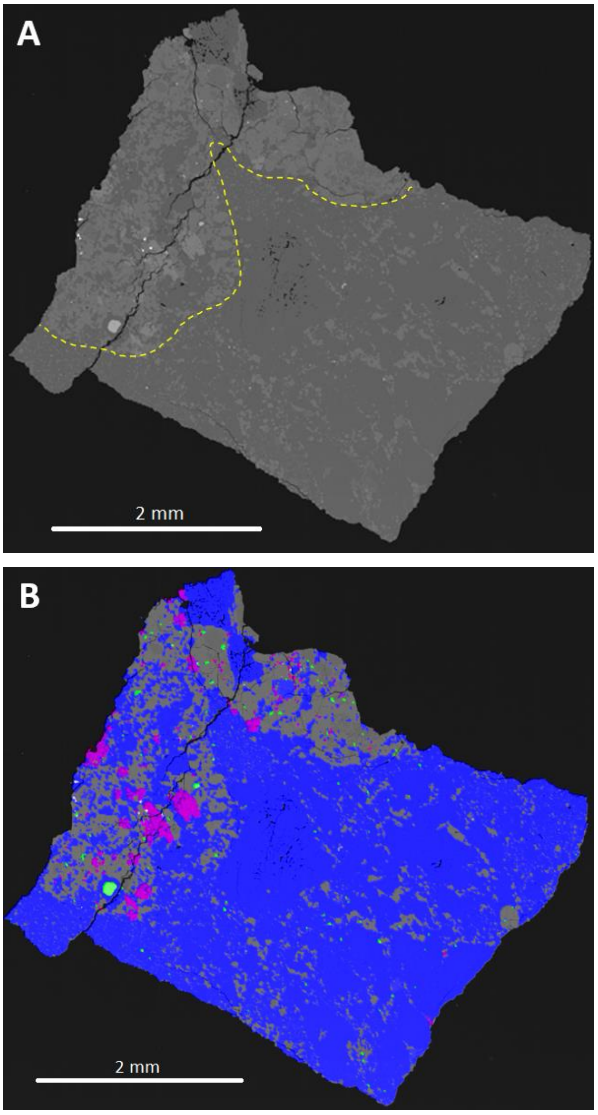

Figure 3.35. Apollo sample 79215,50. **A)** BSE montage map showing the larger mafic clasts (to the left of the dashed yellow line) and the relatively smaller clasts intermingled within the matrix (to the right of the dashed yellow line). **B)** False-colour X-ray map, where blue is Ca (plagioclase), grey is Mg (Mg-rich pyroxene), green is Cr (spinel) and pink is P (apatite). (Image A courtesy of Jessica Barnes, The Open University).

As shown in Figure 3.36, for the sample studied within this project (79215,50) apatite exists as large (up to ~500 μm in the longest dimension) subhedral to anhedral grains, located almost exclusively outside of the main matrix area. The apatites are predominantly found as megacryst clasts (smaller ones are ~10 μm) and are believed to have formed

during the annealing process because they are observed to enclose some of the matrix material (Bickel et al., 1976) such as plagioclase and olivine (Treiman et al., 2014).

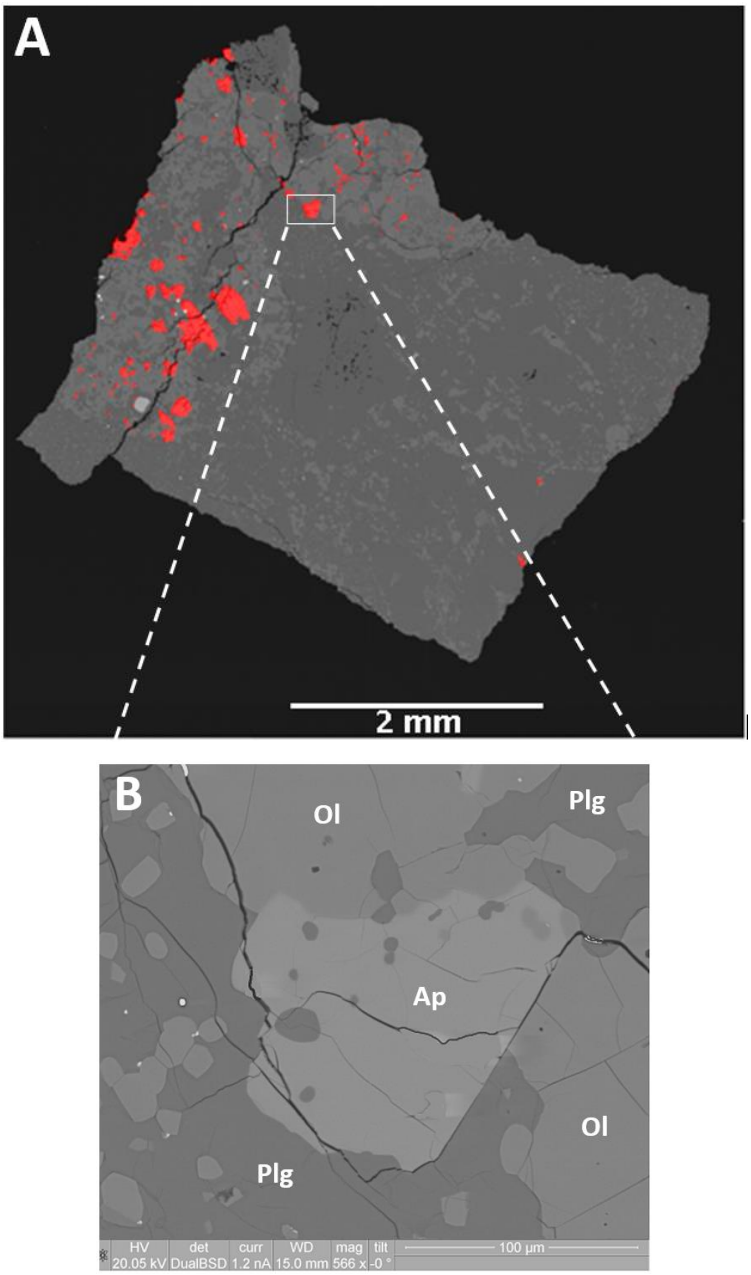

Figure 3.36. Apatite in Apollo sample 79215,50. **A**) The false colour X-ray map shows the phosphorous content (red) which was positively identified as apatite (no merrillite was detected in this thin section). **B**) A BSE image of a subhedral apatite grain (indicated by the white rectangular box in A)) and the textural relationship with other minerals is shown, where Ap = apatite, Ol = olivine and Plg = plagioclase.

Chapter Four:

Sulfur and chlorine in lunar apatite

The first part of this chapter separately presents the results of the sulfur and chlorine abundance and isotope measurements performed with nano-scale secondary ion mass spectrometry (NanoSIMS) for fourteen Apollo samples and one lunar meteorite studied in this project. The second part of the chapter consists of an evaluation of the newly acquired chlorine data and a discussion of the sulfur and chlorine results in combination, with a view to understanding the behaviour of sulfur in lunar apatite. The third part of the chapter focusses on sulfur data and an evaluation of how it compares with the existing literature. The final part of the chapter provides an interpretation of the sulfur results and discusses the behaviour of sulfur within late-stage lunar magmas.

4.1. The abundance and isotopic composition of sulfur and chlorine in lunar apatite

The abundance and isotopic composition for both sulfur and chlorine in lunar apatite, as measured by nano-scale secondary ion mass spectrometry (NanoSIMS) are reported in Table 4.1. The sulfur data were acquired from twelve different Apollo samples, representing four different Apollo landing sites (Apollo missions 12, 14, 15 and 17). In addition, the apatites in lunar meteorite SaU 169, were measured as a proof of concept study for measuring S within the Apollo samples. An image of each individual Apollo apatite grain refered to in Table 4.1 is shown in Appendix C, Figure C.1. At the time of writing, the abundance and isotopic composition of S in apatite grains in just one (Apollo sample 79215) out of the twelve Apollo samples analysed in this project have been published (Treiman et al., 2014). Therefore, our S data on eleven Apollo samples (ten mare basalts and one KREEP basalt), and the lunar meteorite, SaU 169, constitute the first comprehensive dataset of its type.

In addition to the same 12 Apollo samples and lunar meteorite studied for S, a further two Apollo samples were analysed for Cl which included a sample from the Apollo 11 mission and another sample from the Apollo 15 mission. It was hoped that it would be possible to measure S for a sample returned from the Apollo 11 mission but, following Cl measurements (where the protocol included the measurement of ^{32}S and ^{18}O), it became clear that the S ion counts within the Apollo 11 sample were too low (hundreds to tens of counts) across all of the measured apatite grains, precluding any reliable S measurements. The additional Apollo 15 sample measured for Cl was also found to have very low S ion counts across all apatite grains. At the time of writing, Cl measurements for five Apollo samples not previously reported in the scientific literature (12031, 15085, 15475, 15545 and 15556) are presented for the first time in this project.

In some cases, it was not possible to measure both S and Cl for an individual apatite grain within any one sample, either because the S ion counts were very low (e.g. some grains in sample 15085) or the acquired NanoSIMS images did not have a satisfactory resolution (e.g. Apollo sample 15556). As a result, such samples have no associated data for the concerned element in the relevant column of Table 4.1.

Table 4.1. NanoSIMS data for both sulfur and chlorine abundances and isotopes. $\delta^{34}S$ is calculated from the measurement of $^{34}S/^{32}S$ ratios and $\delta^{37}Cl$ is calculated from the measurement of $^{37}Cl/^{35}Cl$ ratios, where $\delta^{34}S$ is relative to V-CDT and $\delta^{37}Cl$ is relative to SMOC. Sulfur and chlorine abundances are calculated relative to apatite standards with known values. All results are reported at the 2σ uncertainty level (which includes internal and external measurement uncertainties).

Sample type	Sample I.D.	Analysis I.D.	$\delta^{34}S_{(V\text{-}CDT)}$ (‰)	2σ (‰)	S (ppm)	2σ (ppm)	$\delta^{37}Cl_{(SMOC)}$ (‰)	2σ (‰)	Cl (ppm)	2σ (ppm)
Ilmenite basalt	10044,645	Ap1_001	-	-	-	-	9.3	1.3	471	33
		Ap5	-	-	-	-	6.3	1.4	464	32
		Ap6	-	-	-	-	10.4	1.4	470	33
		Ap8_1_001	-	-	-	-	11.7	1.1	1188	83
Pigeonite basalt	12031,17	Ap001a	2.0	2.8	193	15	16.5	2.5	2521	112
		Ap001b	0.2	3.4	151	12	16.5	2.6	2775	123
		Ap002_002	0.6	3.1	255	20	17.1	2.5	3490	155
		Ap003	2.2	6.3	28	2	16.9	2.7	551	25
		Ap004	0.7	5.1	35	3	10.4	1.3	578	26
		Ap005	5.3	5.2	34	3	9.6	1.4	402	18
Pigeonite basalt	12039,45	Ap001_a	9.0	9.2	47	5	12.5	2.0	1280	49
		Ap001_c	8.0	10.5	33	3	14.8	1.4	879	33
		Ap001_b	1.2	13.6	19	2	17.0	2.9	667	25
		Ap001_d	4.2	13.7	36	4	17.6	2.7	464	18
		Ap001_f	-2.1	7.0	112	12	18.5	1.0	2988	113
Hi-Al Basalt	14053,19	Ap010	0.6	4.6	162	17	18.1	1.9	3071	348
		Ap005	3.8	6.2	219	23	16.9	1.8	3481	394
		Ap003c	2.4	8.1	48	5	18.2	2.8	1363	154
		Ap003a	-5.9	10.5	41	4	21.3	3.0	1081	122
		Ap008	3.1	5.9	229	24	17.4	1.6	3108	352
Olivine basalt	15016,7	Ap5	32.9	5.9	181	42	6.5	0.9	2629	183
		Ap28	32.7	6.4	311	73	6.7	1.4	7228	503
		Ap42_rim	30.5	5.1	2,763	645	19.1	3.8	687	48

Table 4.1. Continued.

Sample type	Sample I.D.	Analysis I.D.	$\delta^{34}S_{(V\text{-}CDT)}$ (‰)	2σ (‰)	S (ppm)	2σ (ppm)	$\delta^{37}Cl_{(SMOC)}$ (‰)	2σ (‰)	Cl (ppm)	2σ (ppm)
Olivine basalt	15016,7	Ap42_core	28.9	8.3	1,212	283	17.4	2.1	3191	222
		Ap6	36.4	3.2	2,797	653	12.5	2.9	350	24
Pigeonite basalt	15058,15	Ap016	-0.2	2.7	301	49	8.8	1.3	818	31
		Ap017	4.1	5.8	51	8	12.3	0.9	818	31
		Ap002	6.5	5.2	98	16	9.3	0.9	1215	46
		Ap003	1.5	3.5	186	30	10.0	0.7	2652	101
		Ap007	-10.5	5.9	64	10	10.3	0.9	1701	65
		Ap012a	-7.9	3.2	472	76	9.5	1.5	2307	88
Gabbroic basalt	15065,85	Ap001b	-18.0	2.8	341	55	10.7	1.4	5373	204
		Ap003	-14.1	2.6	978	158	10.0	1.5	2778	105
		Ap004	-22.0	4.4	72	12	8.2	1.6	802	30
		Ap005b_core	-18.0	2.4	1,501	243	8.2	1.2	1449	55
		Ap005b_rim	-27.4	6.5	412	67	8.7	1.8	2016	77
		Ap006	-33.3	3.8	67	11	13.0	1.4	1050	40
		Ap007	-29.1	2.4	903	146	7.0	1.0	2686	102
Pigeonite basalt	15085,15	Ap001a	-11.4	2.4	59	7	36.5	1.1	1874	91
		Ap001b	-10.8	2.4	63	7	28.3	1.1	2097	101
		Ap012a	-	-	-	-	17.7	2.1	564	27
KREEP-basalt	15386,46	Ap1	-1.4	4.4	77	6	20.4	2.6	3189	142
		Ap3	-3.9	4.2	51	4	20.1	2.6	2623	117
		Ap6	-0.4	3.8	89	7	18.7	2.6	2978	132
Porphyritic pigeonite basalt	15475,17	Ap002	-0.2	2.3	128	14	13.8	1.0	4070	197
		Ap003b	-2.3	2.0	348	39	22.7	1.6	4316	209
		Ap004a	-8.8	2.5	87	10	34.4	2.7	1235	60
		Ap005a	-7.8	2.4	71	8	14.4	1.2	1718	83

Table 4.1. Continued.

Sample type	Sample I.D.	Analysis I.D.	$\delta^{34}S_{(V\text{-}CDT)}$ (‰)	2σ (‰)	S (ppm)	2σ (ppm)	$\delta^{37}Cl_{(SMOC)}$ (‰)	2σ (‰)	Cl (ppm)	2σ (ppm)
Porphyritic pigeonite basalt	15475,17	Ap001a	-7.0	2.8	49	5	16.3	1.4	1126	54
		Ap004b	2.6	2.5	115	13	15.2	1.6	1979	96
Olivine normative basalt	15545,7	Ap005	-	-	-	-	23.7	4.8	682	90
		Ap003	-	-	-	-	23.1	2.9	1364	180
		Ap006	-	-	-	-	23.4	2.3	2708	356
		Ap001	-	-	-	-	13.0	3.4	1465	193
Olivine normative basalt	15555,991	Ap005a	-14.7	2.8	157	18	21.1	1.6	2354	310
		Ap013a	3.4	4.6	48	5	10.4	2.3	1028	135
		Ap017	5.5	4.2	47	5	11.7	1.4	1900	250
Olivine normative basalt	15556,137	Ap001	2.7	1.2	2,806	317	14.6	2.2	853	41
		Ap003	6.4	1.2	1,473	167	29.5	1.9	2365	114
		Ap002	10.6	3.2	119	13	-	-	-	-
Feldspathic granulitic impactite	79215,50	Ap001a	5.6	4.4	141	15	34.6	0.9	5766	219
		Ap002	4.8	7.7	96	10	33.7	0.9	5758	218
		Ap004	-3.6	5.1	144	15	33.5	0.8	5880	223
		Ap005	3.1	5.2	126	13	34.4	0.9	5751	218
		Ap009	5.0	7.7	124	13	35.6	0.8	5917	225
		Ap010	-6.4	4.9	123	13	34.9	0.8	5871	223
Impact melt breccia	SaU 169	Ap7	1.4	4.2	245	19	12.3	0.4	9978	444
		Ap14	6.8	3.6	340	26	14.0	0.4	12063	537
		Ap15	29.9	3.5	477	37	15.9	0.5	10741	478
		Ap20	-1.6	3.3	241	19	19.8	0.6	10751	478

4.1.1. Sulfur results

Overall, the minimum and maximum S abundance for the apatites of ten different Apollo mare basalt samples measured (excluding KREEP-rich sample 15386 and granulitic impactite 79215) is ~20 ppm and ~2,800 ppm, respectively. The S isotope range ($\delta^{34}S_{(V\text{-}CDT)}$) is ~70‰, with a minimum and maximum S isotope value of -33.3 ± 3.8‰ (2σ) and +36.4 ± 3.2‰ (2σ), respectively (Table 4.1).

The S data acquired in this study are plotted in Figure 4.1. Vesicular basalts 15016 and 15556 and gabbroic basalt sample 15065 (all low-Ti basalts) have apatites that contain the highest abundances of S with ~2,800 ppm, ~2,800 ppm and ~1,500 ppm, respectively. These samples show heterogeneity with respect to S abundance, whereby individual apatites within each sample display a very wide range of values. For example, the difference between the highest and lowest S abundance measured across four different apatite grains in sample 15016 is >2,500 ppm S (~2,800 – 180 ppm S). In addition, one apatite grain in 15016 (Ap42) with notable S zoning, apparent from NanoSIMS images, has very different S abundance within the core (1,212 ppm S) versus the rim (2,763 ppm S) but with identical (within 2σ error) corresponding $\delta^{34}S$ values of +28.9 ± 8.3‰ and +30.5 ± 5.1‰, respectively. Sample 15556 has the largest range in S abundance across the three grains measured with a difference of ~2,700 ppm S (~2,800 – 120 ppm S) compared with all of the other analysed samples. For the six different apatites analysed in sample 15065, the range of S abundance between the highest and lowest (~1,500 – 70 ppm S) grain is 1,430 ppm. Similarly to 15016, one grain (Ap005b) in 15065 is zoned with respect to S but, unlike 15016, the core contains more S (~1,500 ppm) than the rim (~410 ppm) and has a less negative $\delta^{34}S$ value of -18.0 ± 2.4‰ when compared with the rim value of -27.4 ± 6.5‰.

As well as having high S abundances, samples 15016 and 15065 have significantly different S isotope values when compared with the other eight mare basalts, KREEP basalt and granulitic impactite. By some margin, 15016 has the heaviest S isotope values with a very restricted $\delta^{34}S$ range across four different grains where values are between +28.9 ± 8.3‰ and +36.4 ± 3.2‰. At the other extreme, 15065 has the lightest $\delta^{34}S$ values, albeit with a larger spread across the six different grains, with a range from -33.3 ± 3.8‰ to -14.1 ± 2.6‰. These six grains (including the zoned grain) show a faint positive correlation

between $\delta^{34}S$ and S abundance. Whilst 15556 is one of the few samples (along with 15016 and 12031) to have exclusively positive $\delta^{34}S$ values (+2.7 ± 1.2 to 10.6 ± 3.2‰), the values are within error (2σ) of the $\delta^{34}S$ values of the remaining seven mare basalts, KREEP basalt and granulitic impactite and cannot, therefore, be said to be significantly different (Figure 4.1).

Apatites of mare basalts 15085 (low-Ti) and 15555 (low-Ti and low-Al) have far less spread in S abundance with values between 59 ppm and 63 ppm for only two measured grains in sample 15085 and values between 47 ppm and 157 ppm across three grains measured in 15555. Both samples have negative S isotope values, with 15085 displaying the smallest $\delta^{34}S$ spread of all samples measured with values of -11.4 ± 2.4‰ and -10.8 ± 2.4‰. However, in addition to one negative value of -14.7 ± 2.8‰, 15555 also has two positive $\delta^{34}S$ values of +3.4 ± 4.6‰ and +5.5 ± 4.2‰, giving it the largest S isotope spread (~20‰) measured for any one sample in this study. Interestingly, the most negative S isotope value measured for 15555 is from the same grain that has the highest S abundance (157 ppm) relative to the other two grains (47 ppm and 48 ppm).

The remaining five low-Ti mare basalts (all pigeonite basalts, except for high-Al basalt 14053) all have, within error, apatites with $\delta^{34}S$ values that straddle 0‰. However, the corresponding heterogeneity of S abundance within these samples is clearly visible in Figure 1. Of those, only sample 12031 has exclusively positive S isotope values with a small range from 0.2 ± 3.4‰ to 5.3 ± 5.2‰ (albeit with high statistical uncertainty) but a larger range of S abundance from ~28 ppm to ~255 ppm across six apatites. Sample 12039 has both positive and negative $\delta^{34}S$ values, across five different grains, that straddle 0‰ from -2.1 ± 7.0‰ to 9.0 ± 9.2‰ and have a difference of ~90 ppm S between grains with the highest (~110 ppm) and lowest (~20 ppm) S abundance. Positive and negative $\delta^{34}S$ values are also seen in high-Al sample 14053, ranging from -5.9 ± 10.5‰ to +3.8 ± 6.2‰ with a large S abundance spread from ~40 ppm to ~230 ppm across five apatite grains. The apatites of samples 15058 and 15475 have, respectively, the highest and largest range of S abundances among these five mare basalts, with ~420 ppm (~50–470 ppm) and ~300 ppm (~50–350 ppm), where six grains were measured for each sample. The $\delta^{34}S$ spread is similar for both samples with 15058 displaying a minimum of -10.5 ± 5.9‰ and a maximum of +6.5 ± 5.2‰, and 15475 displaying a minimum of -8.8 ± 2.5‰ and a maximum of +2.6 ± 2.5‰.

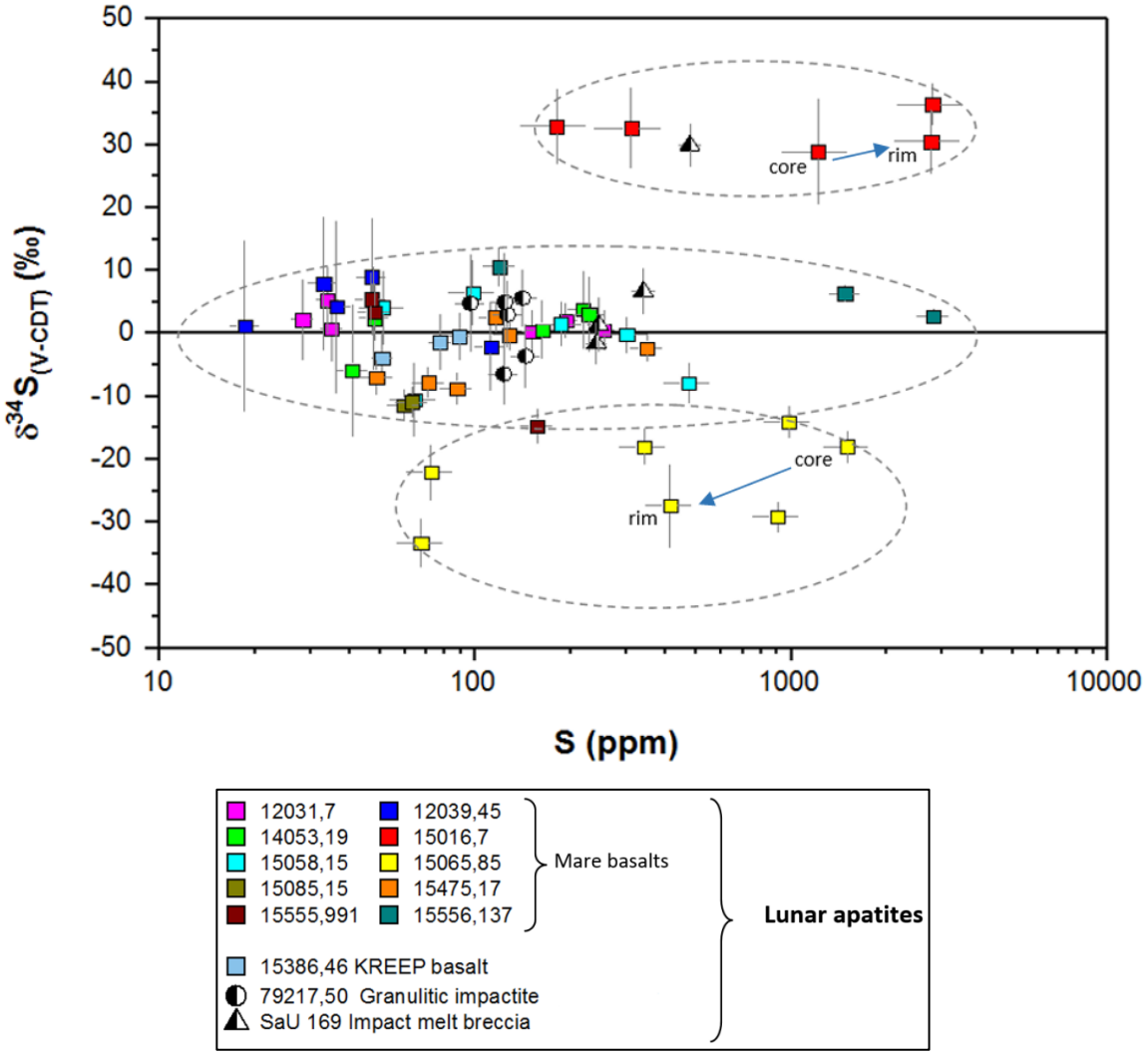

Figure 4.1. Plot of S isotopes ($\delta^{34}S_{(V\text{-}CDT)}$) against S abundance (ppm) in apatite for the analysed lunar samples. The graph shows the results of S measurements performed with NanoSIMS for ten Apollo mare basalts, a KREEP basalt, a granulitic impactite and a lunar meteorite (impact melt breccia) during this project. Note the log scale on the x-axis. The three distinct groups for S isotopes have been highlighted with oval, dashed lines (see text for details). Two blue arrows highlight the direction of the apatite core-rim S variations. The error bars are at the 2σ uncertainty associated with the measurements.

The (non-mare) KREEP basalt (15386) and granulitic impactite (79215) apatites demonstrate no discernible S isotopic differences either relative to each other or to apatites in eight of the mare basalt samples (excluding 15016 and 15065). Within error, the $\delta^{34}S$ values of 15386 and 79215 straddle 0‰ with a minimum and maximum of -3.9 ± 4.2‰ and -0.4 ± 3.8‰, respectively, for 15386 (across three grains) and a minimum and maximum of -6.4 ± 4.9‰ and +5.6 ± 4.4‰, for 79215, respectively (across six grains). Both samples do, however, have a very tight range of S abundance from ~50 ppm to ~90 ppm and from ~100 ppm to ~140 ppm S for 15386 and 79215, respectively. The lunar meteorite (SaU 169) also falls into the restricted S abundance category (~240 ppm to ~480

ppm) for the four grains measured, but it has a marked S isotope variation with three grains having values from -1.6 ± 3.3‰ to +6.8 ± 3.6 ‰ but then a fourth grain having a value of +29.9 ± 3.5‰, the latter value being very similar to apatites in 15016.

Using the S results, potential relationships between lunar apatite S and other quantifiable sample properties were investigated in order to identify possible processes that might have affected both the incorporation and fractionation of S in apatite. For example, comparisons were made between bulk-rock S content (known from the scientific literature) and both the S abundance and S isotope composition of lunar apatites. Likewise, comparisons were made between bulk-rock major element contents (e.g. SiO_2, FeO, MgO, Al_2O_3, CaO, K_2O, Na_2O and TiO_2 (with the exception of Apollo sample 79215, all of the Apollo samples displayed in Figure 4.1 are classified low-Ti basalts)) and both the S abundance and S isotope composition of lunar apatites. For each of these scenarios, positive or negative correlations are not observed. In addition, a relationship between bulk-rock abundances of rare earth elements (REEs) (e.g. Hallis et al., 2014) and S (both abundance and isotope composition) in lunar apatite was investigated because, for terrestrial apatite, S is incorporated into the crystal structure by multiple substitution reactions involving REEs (e.g. Peng et al., 1977). A correlation is absent. The crystallisation and, where available, cosmic ray exposure (CRE) ages of the samples (Chapter Three) were also compared with the S abundance and S isotope composition but, as with the other sample properties, no correlation is observed for the S in the apatite studied in this research project.

However, what is clear from the S results is that S is heterogeneously distributed across the samples and that there are 3 distinct S isotope groups: those with heavy $\delta^{34}S$ values, those with $\delta^{34}S$ values than straddle ~0‰, covering the region of ~+10‰ to ~-10‰, and those with light $\delta^{34}S$ values which are enriched in ^{32}S and depleted in ^{34}S. Sample 15555 is the only sample to straddle the two groups: the ~0‰ and the light $\delta^{34}S$ isotope groups. There appears to be no systematic positive or negative correlation between S abundance and S isotope values within and across the three groups.

4.1.2. Chlorine results

Overall, the range of Cl abundance for apatites of the twelve different Apollo mare basalt samples studied (excluding KREEP-rich sample 15386 and granulitic impactite 79215) is

~6,900 ppm, with a minimum and maximum value of ~350 ppm and ~7,230 ppm, respectively. The isotope range ($\delta^{37}Cl_{(SMOC)}$) for the samples is ~30‰, with a minimum and maximum Cl isotope value of +6.5‰ ± 0.9‰ (2σ) and +36.5‰ ± 1.1‰ (2σ), respectively (Table 4.1). The Cl data listed in Table 4.1 are displayed in Figure 4.2. No systematic correlation is discernible between Cl abundance and the corresponding Cl isotope values and, unlike the S results, no notable groupings of the data are apparent.

Vesicular basalt 15016 has the highest abundance of Cl measured (~7230 ppm) from apatite grain Ap28 but, at the same time, this sample also has an apatite grain (Ap6) with the lowest Cl abundance measured (~350 ppm), giving it a large range of ~6,900 ppm Cl and making it very heterogeneous with respect to Cl. The $\delta^{37}Cl$ for 15016 varies from +6.5 ± 0.9‰ to +19.1 ± 3.8‰, whereby the latter value is from the rim of zoned apatite Ap42 which displays small intra-grain variability with a core value of +17.4 ± 2.1‰. The intra-grain abundance variability is far greater with ~3,200 ppm and ~700 ppm Cl recorded for the core and rim, respectively.

One apatite in gabbroic basalt 15065 has the second highest measured Cl abundance (~5400 ppm Cl in Ap001b) and also has a large spread of ~4,600 ppm (~5400 – 800 ppm Cl) across the other five grains. The $\delta^{37}Cl$ values range from +7.0 ± 1.0‰ to +13.0 ± 1.4‰. Just like 15016, the intra-grain variability for zoned apatite (Ap005b) is small for $\delta^{37}Cl$ but large for Cl abundance with +8.2 ± 1.2‰ and ~1,450 ppm Cl recorded in the core, and +8.7 ± 1.8‰ and ~2,000 ppm Cl in the rim.

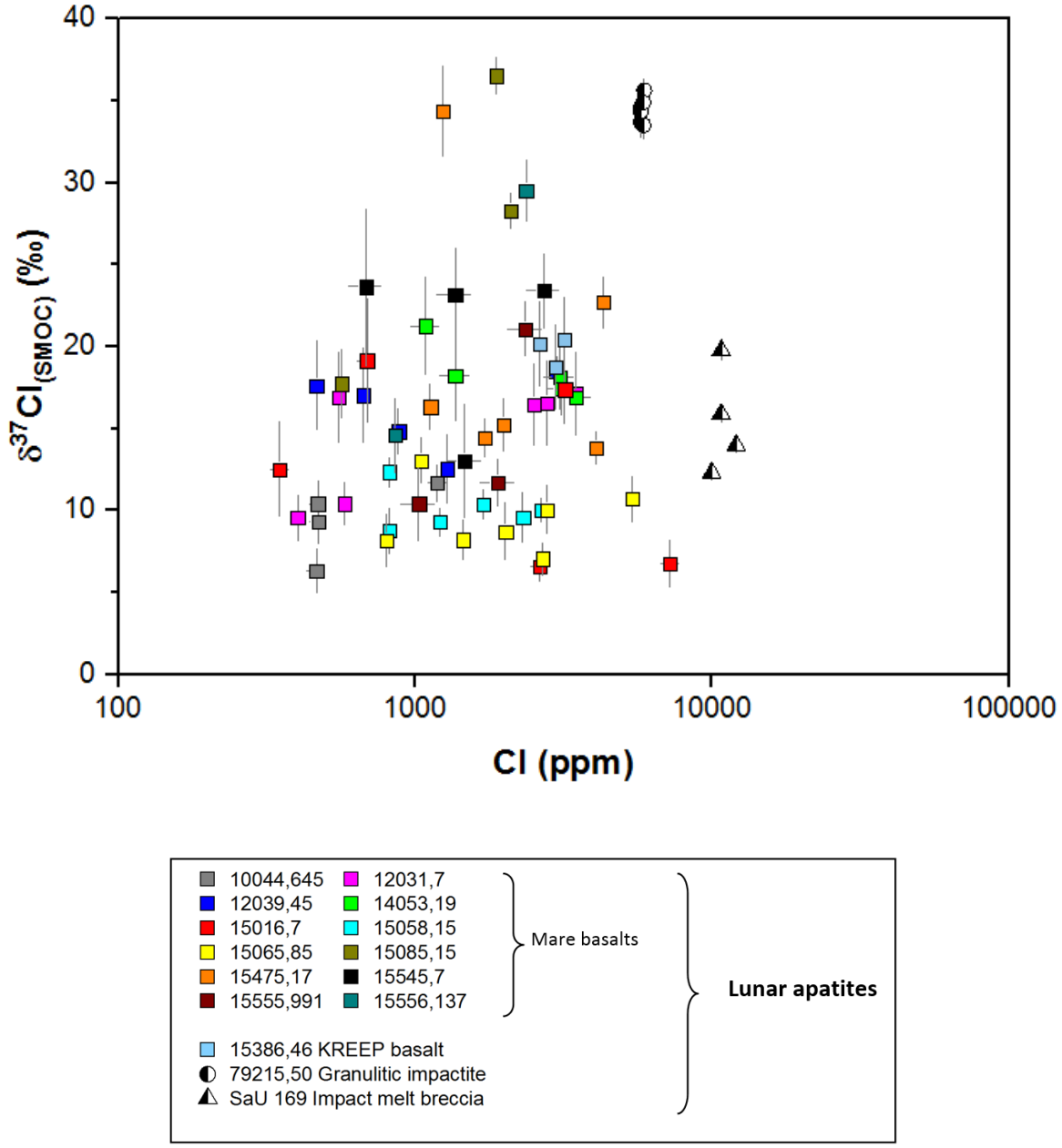

Figure 4.2. Plot of Cl isotopes ($\delta^{37}Cl_{(SMOC)}$) against Cl abundance (ppm) in apatite for the analysed lunar samples. The graph shows the results of Cl measurements performed with NanoSIMS for apatites of twelve Apollo mare basalts, a KREEP basalt, a granulitic impactite and a lunar meteorite (impact melt breccia) during this project. Note the log scale on the x-axis. The error bars are at the 2σ uncertainty associated with the measurements.

As seen from Figure 4.2, the chlorine isotope and abundance results for apatites of the five newly analysed low-Ti mare basalts (12031, 15085, 15475, 15545 and 15556) are very spread out and scattered across the graph. Individual apatites from 15085, 15475 and 15556 have $\delta^{37}Cl$ values of >~+23‰, which appear to be much higher than the majority of other apatite data points shown on the graph. Three apatite grains in sample 15085 have a $\delta^{37}Cl$ range from +17.1 ± 2.1‰ up to the highest $\delta^{37}Cl$ value recorded for all of the lunar

samples, +36.5 ± 1.1‰. The minimum and maximum abundances are ~560 ppm and ~2,100 ppm Cl, respectively. Apatites in sample 15475 have a very high δ^{37}Cl value of +34.4 ± 2.7‰ but also a much lower value of +13.8 ± 1.0‰ with a similarly large range of abundances from ~4,100 ppm Cl down to ~1,130 ppm Cl. Only two apatite grains were measurable for Cl within sample 15556 giving a δ^{37}Cl of +14.6 ± 2.2‰ and +29.5 ± 1.9‰ and corresponding abundances of ~850 ppm and ~2,400 ppm Cl. The apatites within all three of these mare basalts samples show heterogeneity with respect to both Cl abundance and δ^{37}Cl.

The other two newly analysed samples display less variation in δ^{37}Cl values but are still heterogeneous with respect to Cl abundance. Spanning six apatite grains, sample 12031 has δ^{37}Cl values from +9.6 ± 1.4‰ to +17.1 ± 2.5‰ and a large spread in abundance from ~400 ppm to ~3490 ppm Cl. Sample 15545 has three apatite grains with very uniform values of +23.7 ± 4.8‰, +23.1 ± 2.9‰ and +23.4 ± 2.3‰ and corresponding Cl abundances of ~680 ppm, ~1,360 ppm and ~2,700 ppm, respectively. The fourth grain has similar Cl contents (~1,465 ppm) but a lower δ^{37}Cl value of +13.0 ± 3.4‰.

The apatites of the remaining five low-Ti mare basalts (10044, 12039, 14053 (also high-Al), 15058 and 15555) have δ^{37}Cl values spanning ~15‰, where the lowest value is +6.3 ± 1.4‰ (for a grain within 10044) and the highest is +21.3 ± 3.0‰ (for a grain within 14053). Of these five basalts, the inter-grain δ^{37}Cl variability is greatest for 15555 with a difference of ~10.7‰ between the lowest (+10.4 ± 2.3‰) and the highest (+21.1 ± 1.6‰) δ^{37}Cl values. The δ^{37}Cl inter-grain variation is smallest for 15058 with a range of ~3.6‰ (from +12.3 ± 0.9‰ to +8.8 ± 1.3‰). The Cl abundance in apatites from the five samples spans ~3,000 ppm, with a minimum content of ~460 ppm (for a grain in both 10044 and 12039) and a maximum of ~3,480 ppm Cl (for a grain in 14053). Sample 10044 has the smallest range of Cl contents across its four grains with a difference of ~730 ppm Cl (~1,190 – 460 ppm).

KREEP basalt 15386 displays very restricted but relatively high δ^{37}Cl and Cl abundance with very little inter-grain variability. Within error, there is no statistically significant difference between the δ^{37}Cl values for the three different apatite grains (+20.4 ± 2.6‰, +20.1 ± 2.6‰ and +18.7 ± 2.6‰) and all three grains have Cl abundances between ~2,600 ppm and ~3,200 ppm. There is no inter-grain heterogeneity for granulitic impactite 79215

and no statistically significant difference in $\delta^{37}Cl$ or Cl abundance. Across all six grains, 79215 has consistently much higher $\delta^{37}Cl$ and Cl abundances compared with all of the other samples, with minimum and maximum $\delta^{37}Cl$ of +33.5 ± 0.8‰ and +35.6 ± 0.8‰, respectively. The six grains are very homogeneous with respect to Cl abundance with minimum and maximum values of ~5,750 ppm and ~5,900 ppm, respectively. Lunar meteorite SaU 169 has similar but slightly varied $\delta^{37}Cl$ values (+12.3 ±0.4‰ to +19.8 ± 0.6‰) to the mare basalts and KREEP basalt (Figure 4.2) and relatively higher Cl abundances (~10,000-12,000 ppm) across the four apatite grains.

4.2. A comparison of sulfur and chlorine systematics in lunar apatite

4.2.1. Chlorine isotopes and abundances compared with the existing literature

As was detailed in Chapter One, Cl is reported to have a relatively heavy $\delta^{37}Cl$ signature in lunar materials when compared with the majority of planetary materials, where values of ~-4‰ to ~+80‰ are reported for lunar apatites (the primary lunar mineral phase for Cl (Haskin and Warren, 1991)) of mare basalts, KREEP-rich basalts, highlands samples (impact breccias, Mg-suite and alkali-suite rocks), regolith breccias and lunar meteorites (e.g. Sharp et al., 2010a; Tartèse et al., 2014b; Treiman et al., 2014; Boyce et al., 2015; Barnes et al., 2016, 2019; Potts et al., 2018; Wang et al., 2019). Briefly (see Chapter One for more details), to explain the heavy $\delta^{37}Cl$ signature of highlands samples, fractionation of Cl is thought to have been caused by the volatilization of ^{35}Cl, in the form of metal chlorides (e.g. NaCl, $ZnCl_2$), from a deep but exposed (possibly due to crust-breaching impact event(s)) Cl-enriched urKREEP layer. This occurred at a time when the lunar magma ocean (LMO) was >95% crystallised and it left the final dregs of the urKREEP layer ^{37}Cl-enriched. The highlands samples show enrichments of incompatible elements and KREEP-rich components characteristic of this layer (e.g. Boyce et al., 2015; Barnes et al., 2016).

Likewise, to explain the relatively less fractionated $\delta^{37}Cl$ signature of lunar basalt samples, it was suggested that some ^{35}Cl was lost via degassing during basalt volcanism on the lunar surface (e.g. Barnes et al., 2016) and it was also speculated that there was some mixing between basalt source regions (Cl-poor) and varying quantities of urKREEP (Cl-rich) (e.g. Boyce et al, 2018; Barnes et al., 2019). KREEP basalts are believed to have acquired a

mixture of the two $\delta^{37}Cl$ signatures (highlands and basalt) (e.g. McCubbin et al., 2015) from the assimilation or modification of KREEP-rich material at their mantle source regions, and from degassing during eruption at the lunar surface (e.g. Tartèse et al., 2014a; Barnes et al., 2016).

For apatites in seven mare basalts, the KREEP basalt and the granulitic impactite analysed in this project, data are available in the literature for the same samples. The data are plotted in Figure 4.3 to compare the reproducibility and accuracy of the measurements made in this study with previous measurements made in the same laboratory (The Open University: Barnes et al., 2016; Potts et al., 2018; Barnes et al., 2019) and in other laboratories (Treiman et al., 2014; Boyce et al., 2015). Overall, there are two clear groups: one for mare basalts and one for the granulitic impactite, with relatively low $\delta^{37}Cl$ and Cl abundance and relatively high $\delta^{37}Cl$ and Cl abundance, respectively. The mare basalt group is slightly split with high-Al basalt 14053 (measured by Potts et al., 2018) having marginally higher $\delta^{37}Cl$ values. In fact, one of the data points for 14053 measured by Potts et al. (2018) appears to be an outlier with ~>7,000 ppm Cl and is plotted in the granulitic impactite group. The apatites from KREEP basalt 15386 otherwise represent an intermediate $\delta^{37}Cl$ group with ~20‰.

When the $\delta^{37}Cl$ values of apatites in this study are compared with those of the same samples reported in other studies, with the exception of 14053, 15016, 15555 (possibly due to quantitative chemical differences between individual thin sections, see Chapter Three for further details) and some slightly lower, more scattered data points for the granulitic impactite 79215, the scatter of the $\delta^{37}Cl$ values for the remaining five samples are very similar. Differences emerge between Cl abundance which appears to be more varied, particularly for mare basalts 14053, 15058, 15065 and 15016 and granulitic impactite 79125. The reason for this could be due to the measurement of different apatite grains within the samples (e.g. inter-grain heterogeneity) or measurement of a different point in the same apatite grain (e.g. intra-grain heterogeneity). An overall comparison shows that, whilst Cl abundance is more heterogeneous across the same samples, $\delta^{37}Cl$ for the majority of the same samples is, within statistical uncertainty, very similar.

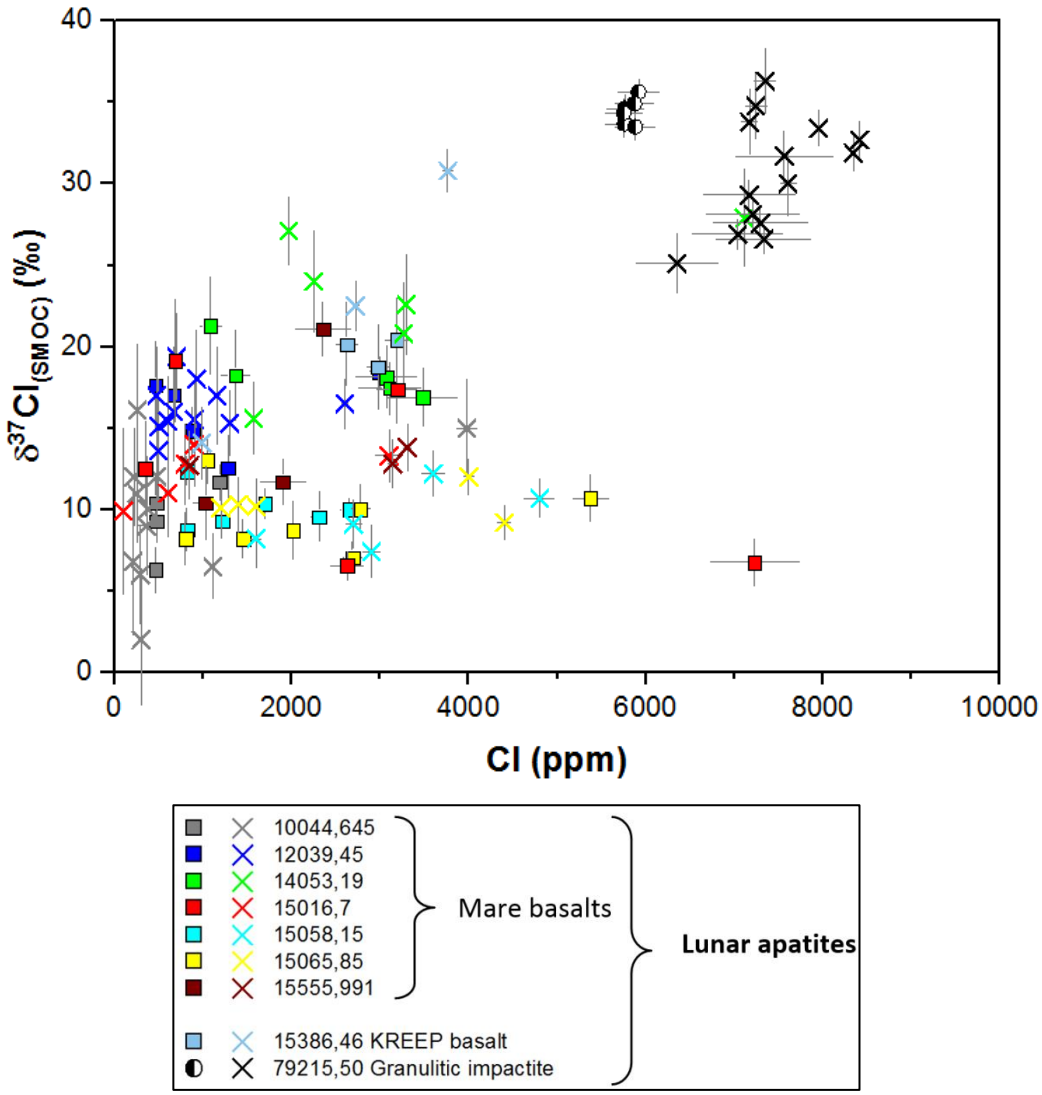

Figure 4.3. Plot of Cl isotopes ($\delta^{37}Cl_{(SMOC)}$) against Cl abundance for a selection of lunar apatites analysed both in this project and in other studies. The square symbols and circle symbol are for apatite data from this study (as shown in the previous two plots); the corresponding crosses represent apatite data from other studies for the same samples (Treiman et al., 2014; Boyce et al., 2015; Barnes et al., 2016; Potts et al., 2018; Barnes et al., 2019).

The apatites of all twelve mare basalts, KREEP basalt, granulitic impactite and impact melt breccia (lunar meteorite) analysed in this project are plotted in Figure 4.4 alongside available apatite data from the scientific literature (colour shaded regions). As a result of the S analysis, Cl isotopes and abundance of apatites in five samples (12031, 15085, 15475, 15545 and 15556) that have not previously been reported in the scientific literature were measured in this project. Low-Ti mare basalt, 12031, plots within the low-Ti yellow shaded region (also overlapped by the grey shaded high-Ti mare basalt region) in Figure 4.4, but it is clear that the individual apatite grains have fairly scattered $\delta^{37}Cl$ values and Cl abundances within the low-Ti basalt region that is characteristic of all of the mare basalt

apatites analysed in this project (e.g. there are no samples with tightly grouped/ homogeneous Cl values).

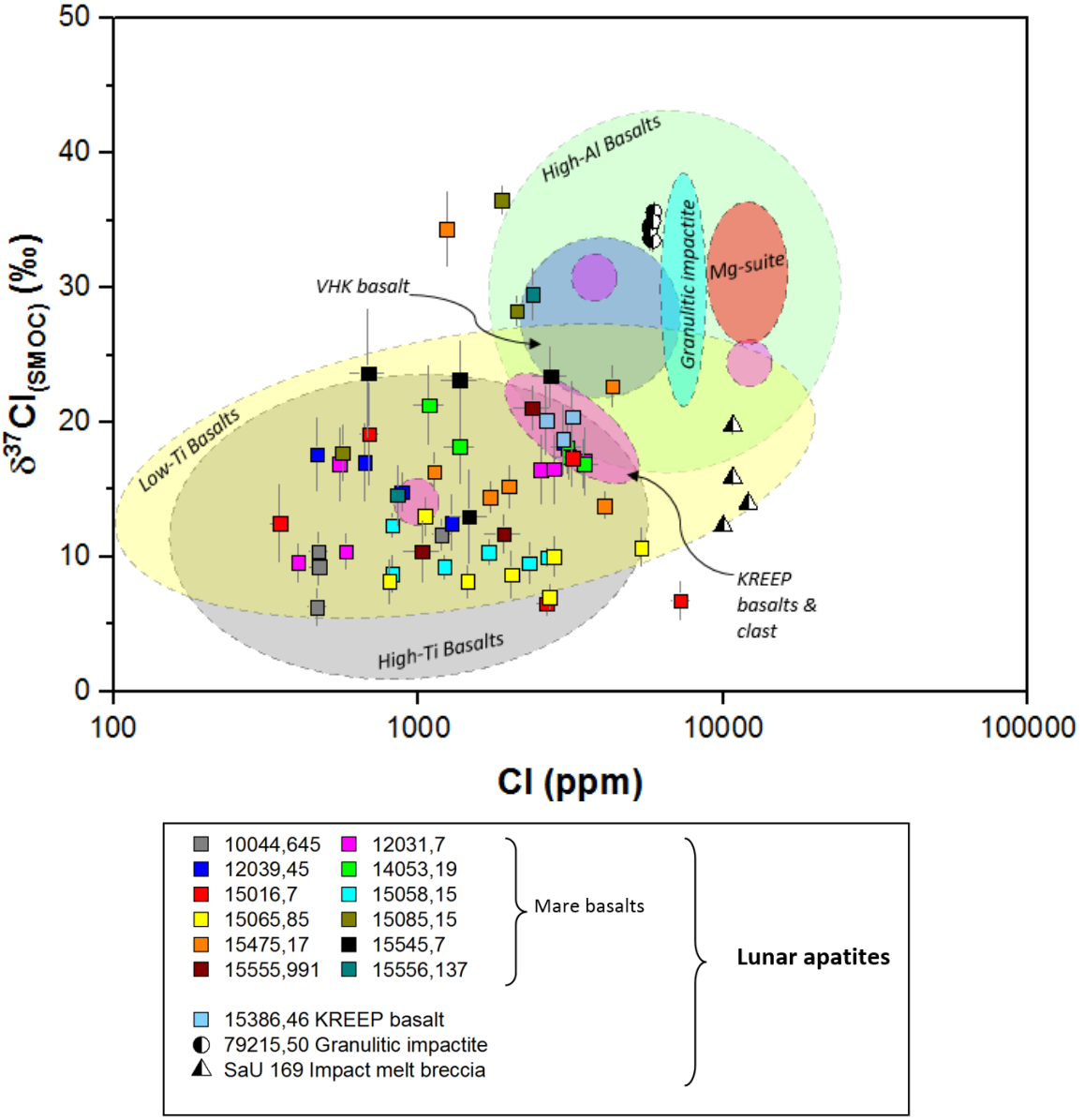

Figure 4.4. Plot of Cl isotopes ($\delta^{37}Cl_{(SMOC)}$) against Cl abundance for lunar apatites analysed in this project alongside lunar apatites reported in other studies. The symbols shown in the key at the bottom are for apatite data from this study; the individually coloured ovals and circles are labelled on the graph (where VHK = very high potassium) and represent apatite data from the scientific literature which include Apollo samples and a KREEP clast from brecciated lunar meteorite (NWA 4472) (Sharp et al., 2010; Treiman et al., 2014; Tartèse et al., 2014b; Boyce et al., 2015; Barnes et al., 2016; Potts et al., 2018; Barnes et al., 2019).

Low-Ti basalt 15085 does not plot within the low-Ti basalt region but has much heavier $\delta^{37}Cl$ values (28.3 ± 1.1‰ and 36.5 ± 1.1‰) with one apatite grain plotting in the overlap-region combining high-Al and VHK basalts and the other plotting just outside the high-Al

region. The latter data point has the highest $\delta^{37}Cl$ of all of the apatites analysed in this project (36.5 ± 1.1‰) and, save for the fractionally lower Cl abundance, is very similar to high-Al basalts. Like 15085, low-Ti basalt 15475 also has a heavy $\delta^{37}Cl$ value (34.4 ± 2.7‰) but only for one of the apatites analysed. Despite the very heterogeneous Cl abundances, the other five apatites plot within the low-Ti basalt region, albeit with one of the apatites having a relatively heavier $\delta^{37}Cl$ value (22.7 ± 1.6‰) that plots within the overlap-region combining low-Ti and high-Al basalts. One apatite of low-Ti 15556 also plots within the high-Al basalt region (slightly overlapped with the VHK basalt region) with a $\delta^{37}Cl$ value of (29.5 ± 1.9‰) but the second apatite in this sample plots firmly within the low-Ti basalt region (overlapped with the high-Ti basalt region) with a much lighter $\delta^{37}Cl$ of 14.6 ± 2.2‰ and lower Cl abundance (~853 ppm Cl compared with ~2,365 ppm Cl in the second grain).

The only newly reported sample that does not have apatites associated with the high-Al region is low-Ti 15545, where all of the four apatites plot with the low-Ti region. Three of the grains have very homogeneous $\delta^{37}Cl$ values (~23‰) that are at the top end of the low-Ti region, but one grain is much lower with 13.0 ± 3.4‰. All four grains are heterogeneous with respect to Cl abundance (ranging from ~682–2,708 ppm Cl). From a petrological point of view, the apatites analysed within 15545 were all located within mesostasis regions. However, with the exception of one apatite in 12031 that was enclosed within a pyroxene grain, it is also the case for the other four newly measured samples: they were all located within mesostasis, late-stage melt pockets. The pyroxene-enclosed grain (Ap004) of 12031 did not show any statistically significant $\delta^{37}Cl$ or Cl abundance differences when compared with the other apatites in the same sample.

What is clear from the $\delta^{37}Cl$ and Cl abundance reported here for the five samples is that there is considerable heterogeneity. Potts et al. (2018) reported very variable $\delta^{37}Cl$ values between +14.6 ± 1.6‰ and +40.0 ± 2.9‰ and Cl abundances between 580 ppm Cl and 16,149 ppm Cl for apatites of Apollo 14 high-Al samples. A positive trend was not observed between $\delta^{37}Cl$ and rare earth elements (REEs) (Barnes et al., 2016), leading Potts et al. (2018) to suggest that a secondary process, involving a combination of ^{35}Cl degassing and variable interaction between a Cl-rich vapour phase and the late-stage melt, must have caused the Cl isotopic fractionation. Such interaction required that there was wide-spread fumarolic activity on the nearside of the Moon at ~4 Ga, resulting in varying degrees of

metasomatism in the studied Apollo 14 samples. Some apatites crystallised before and some after vapour phase interaction, which gave rise to heterogeneous $\delta^{37}Cl$ values and Cl abundances. The Cl-rich vapour phase was produced either by an impact event and a corresponding ejecta blanket or by a lava flow – both of which could have heated the immediate underlying region enough to initiate release of vapours and permit interaction with the crystallising rock (Potts et al., 2018).

Similarly, to explain the heavy $\delta^{37}Cl$ value, sample 79215 was thought to have experienced metasomatism resulting from the transportation of element-carrying vapours through the crust and regolith (Treiman et al., 2014). The vapours were driven by an impact event that was ultimately responsible for producing the brecciated granulite sample. Sample 79215 is depleted in K and REEs, but otherwise has a KREEPy signature with high concentrations of P, Cl and F and a heavy $\delta^{37}Cl$ value of +32.7 ± 1.6‰. Treiman et al. (2014) suggested that the mobile vapour was initially derived from a KREEPy source but it then underwent 'elemental fractionation' whereby P, Cl and F were added to the apatite but, as the vapour moved through cracks within the original granulitic protolith, 'KREE-' was carried away from the apatite to be deposited elsewhere.

It is, therefore, possible that the five newly analysed samples in this project encountered variable mixing between the basaltic source region and urKREEP (or a KREEP component) that resulted in heavier $\delta^{37}Cl$ values for 15085, 15475, 15545 and 15475 but a relatively light $\delta^{37}Cl$ value for 12031 (e.g. Boyce et al, 2018; Barnes et al., 2019). The $\delta^{37}Cl$ and Cl abundance variabilities observed between apatite grains within the same sample could also be explained by variable interaction with a metasomatic agent (Treiman et al., 2014; Potts et al., 2018).

4.2.2. Sulfur and chlorine in lunar apatite: a comparison

At the time of writing, the measurement of S and Cl on the same spot in lunar apatites has not been reported in the literature. As stated previously (Chapter One), the reason for measuring S and Cl on the same spot within the same grains and, in some cases, measuring Cl in apatite grains from samples that have already had Cl apatite data published within the scientific literature, was to better understand the behaviour of S in the late-stage magmas through comparisons with what is already known for Cl in apatite. In particular, the

simultaneous measurement of S and Cl allows assessment of whether or not the two elements underwent the same evolutionary processes within the lunar interior, such as those detailed above and in Chapter One.

The combined S and Cl abundance results for apatites of ten mare basalts, a KREEP-basalt and a feldspathic granulitic impactite (lunar meteorite SaU 169 used for proof of concept is excluded for the S and Cl comparisons) are shown in Figure 4.5. Most notable is that S abundance in apatite is lower than Cl abundance. There is no overall significant statistical correlation between S and Cl abundance (R^2 = 0.03) for the twelve samples shown in Figure 4.5. However, there are two apparent *trends*, one with a positive trend where Cl and S abundance increase (or decrease) for apatites with relatively low S abundance (<~350 ppm S), and the other with a negative trend where Cl increases (or decreases) for apatites with relatively high S abundance (>~350 ppm S).

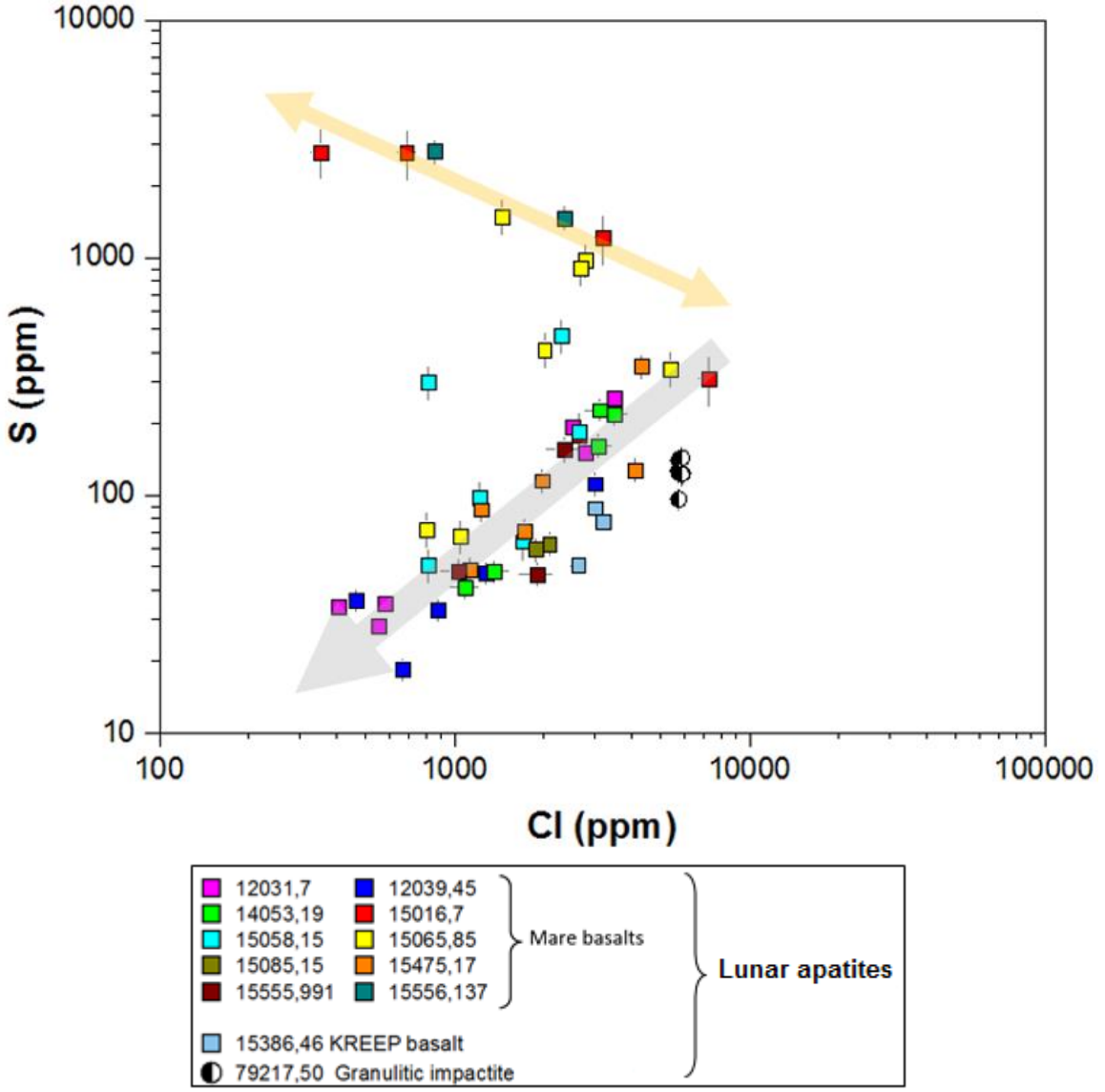

Figure 4.5. Plot of S abundance (ppm) against Cl abundance (ppm) in apatite for the analysed lunar samples. The graph shows the results of S and Cl measurements (this study) for apatites of ten Apollo mare basalts (samples 10044 and 15545 only have Cl data available (see Table 4.1)), a KREEP basalt and granulitic impactite (SaU 169 is not shown). There is no overall statistically significant correlation but a positive trend (grey arrow) and a negative trend (orange/yellow double-headed arrow) are apparent. See text for further details. The error bars are the 2σ uncertainty associated with the measurements. Note the log scale on both axes.

As detailed in the previous section, apatites of vesicular basalt 15016 has the highest S abundance but, it is apparent from Figure 4.5 that it also has both the lowest and highest Cl abundance which results in a negative correlation between S and Cl. Sample 15556, also a vesicular basalt, has the same negative trend as 15016. The trend suggests that simultaneous magma degassing, where there is loss of both S and Cl from a melt, cannot have occurred, but degassing of either S or Cl is possible. Given the vesicular nature of

these samples, it is unlikely that one or the other element was not involved in the degassing process. As an alternative, when the melt fraction reduced, the concentration of incompatible S and Cl would have increased and so there could have been an oscillatory process involving the loss of S and Cl through degassing but an increase of S and Cl as crystallisation progressed (represented by the double-headed arrow in Figure 4.5). By comparing S and Cl abundance, it is not clear which of these processes was dominant and what the impact of each process was on each element. Gabbroic basalt 15065 appears to feature in both the positive and the negative trends because it has both relatively low and relatively high S content. The trend for low S apatites could imply that S and Cl were degassing together, whereas the trend for higher S apatites could imply that Cl continued to degas independently which allowed S to increase in the melt as the melt fraction reduced in size. Like 15016 and 15556, independent S and Cl degassing and/ or crystallisation could have caused this relationship.

The remaining seven mare basalts have apatites that feature in the positive trend (grey arrow in Figure 4.5) which could indicate that, for lower S abundance samples, S and Cl are degassing simultaneously from the melt, albeit Cl is being exhausted from the melt marginally more quickly. Boyce et al. (2010) noted a positive correlation between S and Cl abundance in 14053 and suggested that it could have been caused by magmatic crystal growth and/ or post-crystallisation exchange of both elements. However, the Cl contents of apatites in mare basalt samples 10044 and 15545 are 464–1,188 ppm Cl and 682–2,708 ppm Cl, respectively (Table 4.1), but it was not possible to report the corresponding S abundance because it was below the limit of ion microprobe detection. With such Cl contents, and using the approximate positive trend in Figure 4.5, S abundance of up to ~60 ppm S and ~110 ppm S for 10044 and 15545, respectively, might have been expected. It appears that not all samples display a positive trend between S and Cl at low S abundances.

The Cl content of 79215 is very homogeneous across the six apatite grains (some data points are on top of each other) and has consistently the highest Cl content of all of the samples analysed. Likewise, KREEP basalt 15386 has homogeneous Cl abundance across the three apatites analysed but the Cl abundance falls within the average Cl for all of the samples analysed. Both samples have below average S abundance (<415 ppm S) and, whilst not significant (the S abundance of 15386 and 79215 overlap), there is a slight increase of S from the apatites in 15386 to the apatites in 79215. Otherwise, there is no

indication from the S contents to suggest that they were derived by different processes (e.g. 79215 is a granulitic impactite and 15386 has incorporated KREEP-rich components).

When S and Cl isotopes are compared (Figure 4.6), the clear lack of any statistically significant correlation demonstrates the decoupling of S and Cl. The three distinct $\delta^{34}S$ groups highlighted earlier in Figure 4.1 are still easily discernible when plotted against $\delta^{37}Cl$. When $\delta^{37}Cl$ was plotted earlier against Cl abundance in Figure 4.2, there were no clear $\delta^{37}Cl$ groups but, when plotted against $\delta^{34}S$, there is a clear difference between granulitic impactite 79215 and the majority of apatite grains in mare basalts and the KREEP basalt (dashed red rectangles in Figure 4.6 below). Less obvious are the apatites in KREEP basalt 15386 that are clustered together with a $\delta^{37}Cl$ value that is slightly higher than most of the apatites in the mare basalts. There is, therefore, a slight $\delta^{37}Cl$ trend from mare basalts, to KREEP basalt 15386, to granulitic impactite 79215. As mentioned above, mare basalts are found to have lower $\delta^{37}Cl$ values than KREEP-rich basalts which have lower $\delta^{37}Cl$ values than highlands rocks (e.g. Barnes et al., 2016). Whilst 79215 is chemically very different from the bulk of other lunar highlands breccias (see Chapter Three), it does have a heavy $\delta^{37}Cl$ that is expected of highlands samples. As a rock containing a clast of troctolite (mafic intrusive rock - associated with Mg-rich highlands rocks) that exclusively holds all of the apatites in the sample, it may not be completely unexpected that the apatites have a heavy $\delta^{37}Cl$ signature.

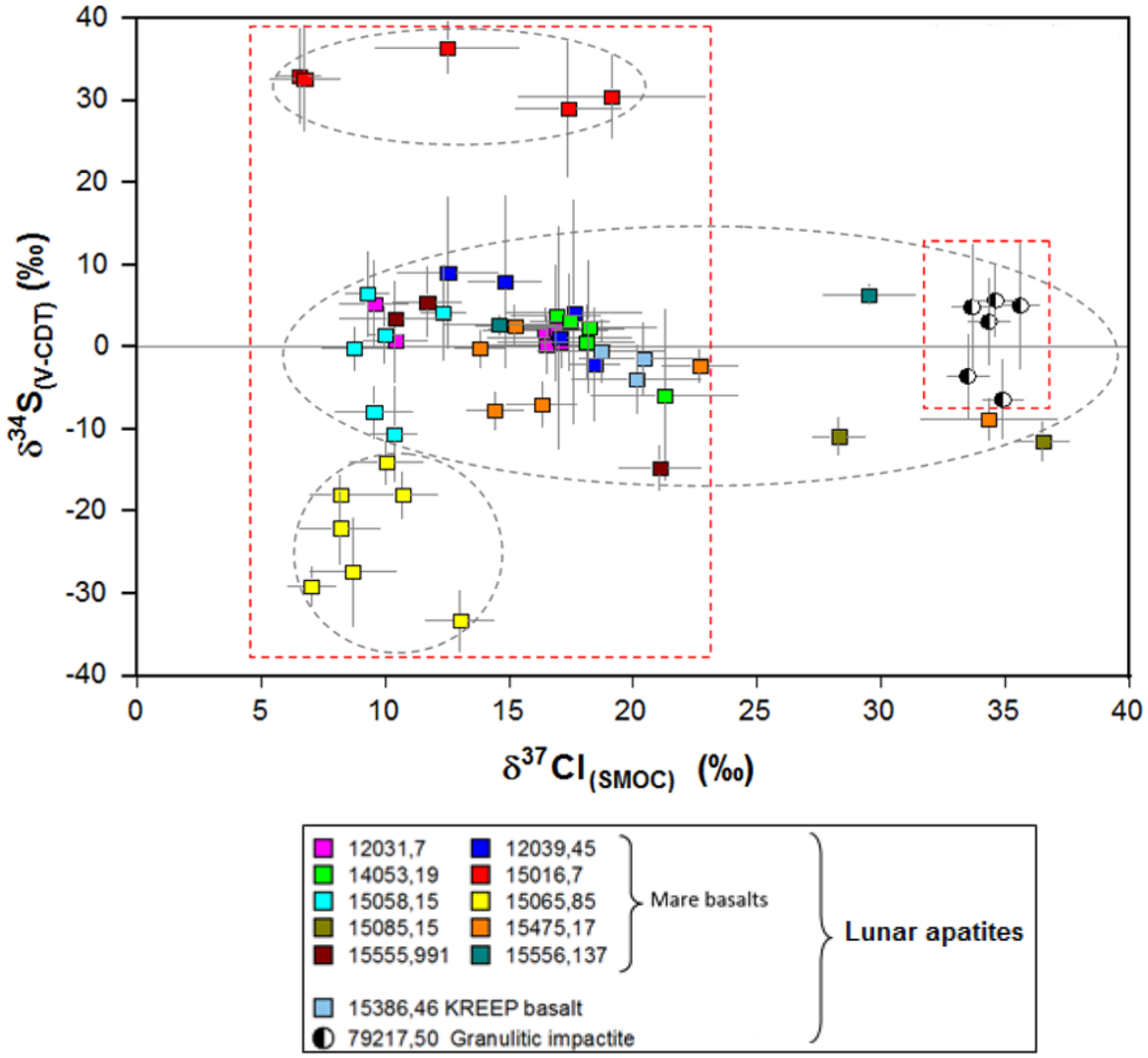

Figure 4.6. Plot of S isotopes ($\delta^{34}S_{(V\text{-}CDT)}$) against Cl isotopes ($\delta^{37}S_{(SMOC)}$) in apatite for the analysed lunar samples. There is the lack of relationship between S and Cl for apatites of ten Apollo mare basalts, a KREEP basalt and a granulitic impactite measured in this study. The three distinct isotope clusters of S (grey dashed ovals) and the largely separated chlorine isotope groups for mare basalts and the granulitic impactite sample (the larger and smaller red dashed rectangles, respectively) are discernible. The vertical and horizontal error bars are the 2σ uncertainty associated with the measurements.

The increasing $\delta^{37}Cl$ trend across different rock types is, however, not observed for $\delta^{34}S$. A similar relationship would require an increase in $\delta^{34}S$ from mare basalts through to KREEP-rich basalt 15386 through to granulitic impactite 79215. Instead, the majority of mare basalts are clustered between ~+10‰ and ~-10‰ and appear to be indistinguishable from 15386 and 79215. Gabbroic basalt 15065 has distinctly light $\delta^{34}S$ values but the $\delta^{37}Cl$ values appear to be non-distinct when compared with the other relatively light $\delta^{37}Cl$ samples. Whereas for Cl, heavy $\delta^{37}Cl$ values are expected for highlands samples, in the case of S, it is vesicular basalt 15016 that has the heaviest $\delta^{34}S$ values. The lack of mare

basalt, KREEP basalt, highlands rock (79215 in this case) trend and correlation between S and Cl isotopes is a strong piece of evidence for decoupling of S and Cl during the evolution of the lunar interior and, therefore, a separate process is required to explain the measured S isotopic fractionations.

4.3. Sulfur in lunar apatite

4.3.1. A comparison of sulfur abundance in lunar apatite

Lunar sulfur abundances reported in the scientific literature are dominated by measurements of bulk-rock samples, lunar soils, volcanic glasses and melt inclusions. As detailed in Chapter One, mare basalt bulk-rocks have been shown to contain ~550–2,130 ppm S (e.g. Thode and Rees, 1971, 1972; Rees and Thode, 1972, 1974; Gibson and Moore, 1974; Des Marais, 1983; Wing and Farquhar, 2015), whereas lunar soils contain up to ~830 ppm S (Kerridge et al., 1975a, 1975b), volcanic glasses contain ~110–580 ppm S (e.g. Ding et al., 1983; Saal et al., 2008) and melt inclusions contain ~360–1,900 ppm S (e.g. Bombardieri et al., 2005; Hauri et al., 2011; Chen et al., 2015a; Ni et al., 2019). At the time of writing and to the best of our knowledge, only three published studies (Boyce et al. 2010; Greenwood et al., 2011; Treiman et al. 2014) have measured S abundance in lunar apatite with an ion microprobe, enabling a direct comparison with the measurements carried out in this project.

The S abundance of five individual apatite grains measured in high-Al basalt 14053 are much lower (~41–229 ppm S) than that reported for a different thin section of the same sample by Boyce et al. (2010), where seven analyses on a single apatite grain gave a range of ~310–460 ppm S. Likewise, a comparison of pigeonite basalt 12039 shows that the S abundance reported by Greenwood et al. (2011) for a single apatite grain from a different thin section for the same sample ranged from below the limit of detection to <~600 ppm S which, at the upper end, is far higher than the ~20–110 ppm S measured in this study. By contrast, the abundance of 102–111 ppm S reported by Treiman et al. (2014) for three different apatite grains from feldspathic granulitic impactite 79215 is similar to the ~96–144 ppm S determined (this study) for six individual apatite grains in a different thin section from the same sample.

It is possible that the higher S abundances reported by Boyce et al. (2010) and Greenwood et al. (2011) for 14053 and 12039, respectively, are due to the authors measuring part of a single grain that is uncharacteristically S-rich. For example, it has been suggested that rims of apatites in 12039 are S- and Cl-rich, possibly due to interaction with a late-stage metasomatic S- and Cl-carrying vapour phase, transported from a deeper decompressing magma (Konecke et al., 2017b). Alternatively, the differences could be due to incorporation of S hotpots within the single apatite grains that would not be detected with EPMA or with other investigative techniques (e.g. backscatter or secondary electron images) given their very small sizes (<<1 μm). Using the NanoSIMS imaging mode, sulfur hotspots were clearly observed in 12039 and 14053 (Figure 4.7), but not in 79215, and contained far higher counts of S (up to ~300,000 counts per second) relative to the homogeneous apatite regions (rarely more than ~20,000 counts per second). The imaging mode allowed S hotspots to be avoided during analysis and any that could not be completely excluded were removed during image processing (see Chapter Two for further details).

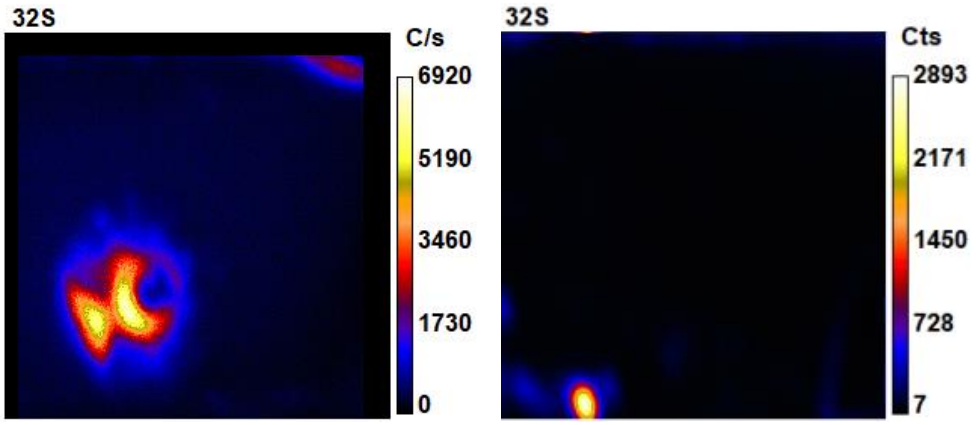

Figure 4.7. Sulfur hotspots in lunar apatite. **A)** 10 x 10 μm NanoSIMS image of an apatite in Apollo sample 14053 is shown with a sulfur (^{32}S) hotspot just towards the bottom-left of centre with up to ~6,900 counts per second. **B)** An equivalent image for Apollo sample 12039 is shown with a sulfur hotspot at the bottom left of an apatite grain with up to ~2,800 counts per second.

Other studies have used electron probe microanalysis (EPMA) to measure S abundance of lunar apatite grains within certain basalt samples studied in this project. The abundance (~51–472 ppm S) of six apatite grains in pigeonite basalt 15058 (measured with NanoSIMS in this study) encapsulates the electron probe results of ~0–300 ppm S reported by Tartèse et al. (2013) for six apatite grains in the same sample. The overall range of ~50–450 ppm S determined with EPMA for two apatites in olivine normative basalt 15555

(Tartèse et al., 2013) is quite a bit higher than found for three apatite grains in the same sample measured with NanoSIMS (~47–157 ppm S). Sample 15555 is known to have quantitative chemical differences between individual thin sections due to proportionally small size of the sub-samples allocated to investigators relative to the large size of the crystals contained within the individual samples (see Chapter Three for further details), meaning that a difference in measured S abundance is not necessarily unexpected, even if comparing between two different measurement techniques. Three apatite grains in KREEP basalt 15386 have ~51–89 ppm S (this study), whereas Tartèse et al., (2014a) reported a greater range and a higher maximum abundance at ~0–200 ppm S which may be due to the greater number (n = 13) of apatite grains measured in that study. It should be noted that sulfur abundance measurements with EPMA must be performed with caution for lunar apatites because it is not possible to detect and exclude the very small S hotpots that have been observed with the NanoSIMS imaging mode.

When compared with S in terrestrial apatites, the majority of the lunar apatite grains have a lower abundance of S. For example, eleven basalts (ten mare basalts and one KREEP basalt) have individual apatite grains containing <~300 ppm S and only three mare basalts (15016, 15065 and 15556) have apatite grains that contain >~1,000 ppm S. For terrestrial apatites, S abundance is commonly found to be >~1,000 ppm S (e.g. Streck and Dilles, 1998; Humphreys et al., 2006; Van Hoose et al., 2013; Economos et al., 2017) with values of up to ~5,860 ppm S having been reported (Humphreys et al., 2006).

4.3.2. A comparison of sulfur isotope values

As detailed in Chapter One, and similarly to S abundance measurements of lunar materials, most of the lunar S isotope studies in the scientific literature are dominated by measurements of bulk-rock samples and lunar soils (e.g. Thode and Rees, 1971, 1972; Rees and Thode, 1972, 1974; Petrowski et al., 1974; Gibson et al., 1975; Kerridge et al., 1975a, 1975b; Kaplan et al., 1976; Des Marais, 1983; Wing and Farquhar, 2015). There have been a few *in situ* S isotope investigations of lunar volcanic glasses (e.g. Ding et al., 1983) and, at the time of writing, the S isotope value of just a single lunar apatite grain in one rock sample has been published (Treiman et al., 2014).

The S isotope results of this study for sample 79215 are between –6.4 ± 4.9‰ and +5.6 ± 4.4‰ (2σ) which represents measurements on six different lunar apatite grains. Two measurements were made on a single apatite grain from a different thin section of the same sample by Treiman et al. (2014) which resulted in marginally higher values of +11.3 ± 3‰ and +9.7 ± 2.8‰ (2σ). When compared with the two points measured on the single apatite grain (Treiman et al., 2014), the $\delta^{34}S$ value of four out of the six apatite grains measured in the current study are, within statistical uncertainty, the same (Figure 4.8). As the only other study to have measured S isotopes in lunar apatite, the work of Treiman et al. (2014), therefore, confirms the reproducibility of the isotope measurements between the different laboratories and demonstrates that the S isotope protocol developed at the Open University has analytical validity. An interpretation of the ^{34}S-enrichment in lunar apatite was not provided by Treiman et al. (2014).

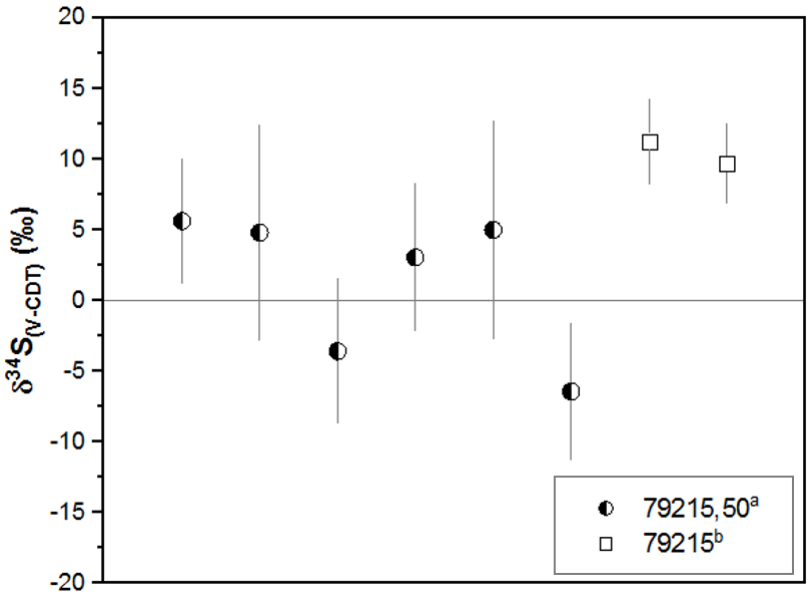

Figure 4.8. Reproducibility of S isotope measurements. The graph compares the results of S isotope measurements ($\delta^{34}S_{(V\text{-}CDT)}$ (‰)) made on six individual apatite grains in Apollo sample 79215,50 for [a] this study and two measurement points made on a single apatite grain for [b] Treiman et al. (2014) (thin section 79215,51 or 79215,56). The vertical error bars are the 2σ uncertainty associated with the measurements.

When compared with the $\delta^{34}S$ values of lunar apatite, the majority of the previous bulk-rock $\delta^{34}S$ values are much more restricted. For example, Thode and Rees (1971) and Rees and Thode (1972) measured five Apollo 12 bulk-rock mare basalts and reported a slight ^{34}S-enrichment with $\delta^{34}S$ values between +0.37‰ and +0.68‰. Rees and Thode (1972) also reported slightly higher values of +0.90‰ and +1.44‰ for an Apollo 14 breccia with basalt clasts. From the measurement of fifteen bulk-rocks including Apollo 15 and Apollo

17 samples, Gibson et al. (1975) noted $\delta^{34}S$ values spanning –1.6‰ to +0.9‰, with only three rock samples having a positive $\delta^{34}S$.

Petrowski et al. (1974) published the most negative $\delta^{34}S$ of –5.2‰ for a bulk-rock Apollo 17 anorthositic brecciated gabbro which was attributed either to the addition of fractionated S from an extra-lunar source or to indigenous S isotopes being much more heterogeneous than previously thought. Other studies have reported negative $\delta^{34}S$ values from *in situ* S isotope measurements of 'vein and replacement troilite' (FeS) from Apollo 16 lunar highlands clasts (–3.3 ± 1.6‰ to –1.0 ± 1.6‰ (2σ)) (Shearer et al., 2012) (see section 4.6.3 for more details) and of volcanic orange and black glass beads collected from the Apollo 17 landing site (down to –2.62‰) that were suggested to have been a product of lunar fire-fountaining which had undergone the preferential loss of ^{32}S to the vapour phase during extrusive volcanism (Ding et al., 1983) (see Chapter One for more details). In a recent study (Wing and Farquhar, 2015), ten lunar basalts from the Apollo 11, 12 and 17 missions were targeted for bulk-rock sulfur isotope measurements and, unlike the previous studies, were found to have very restricted, homogeneous $\delta^{34}S$ values with a mean of +0.57 ±0.07‰ (spanning +0.443‰ to +0.686‰). The bulk Moon was estimated to have a $\delta^{34}S$ value of +0.58 ± 0.05‰ (Figure 4.9) which was very similar to the individual mare basalts values.

Only a few samples that had previously had bulk-rock S isotope values reported in the scientific literature (mentioned above) could be investigated in this project (Table 4.2). This was either because the samples were not available during the course of the PhD project or because investigations (e.g. SEM) as part of the current project showed that they contained no apatite or did not contain apatite that was suitable for the analytical techniques of this project e.g. they were too small or were too cracked.

Table 4.2. A comparison of the available published bulk-rock S isotope data with the S isotope results of apatite (this study) contained within the same rock samples.

Sample	**$\delta^{34}S$ (‰) (bulk-rock)**	**$\delta^{34}S$ (‰) (apatite)**[d]
12031,17	-	+0.2 to +2.2
12039,45	-	-2.1 to +9.0
14053,19	-	-5.9 to +3.8
15016,7	+0.7 to 2.6 ± 0.3[a] -1.6[b] +0.7[c]	+28.9 to +36.4
15058,15	-0.5 to -0.6[b]	-10.5 to +6.5
15065,85	-0.9[b]	-33.3 to -14.1
15085,15	-1.3[b]	-11.4 to -10.8
15386,46	-	-3.9 to -0.4
15475,17	-	-8.8 to +2.6
15555,991	-0.3[b] +0.7[c]	-14.7 to +5.5
15556,137	+0.9[b]	+2.7 to +10.6
79215,50	-	-6.4 to +5.6

[a] Des Marais et al. (1983); [b] Gibson et al. (1975); [c] Kaplan et al. (1976); [d] This project.

At the time of writing, only one S isotope study of terrestrial apatite is known to us. When compared with lunar apatites, the $\delta^{34}S$ of the terrestrial apatite grains is exclusively positive with values of 2.6‰ to 8.5‰ and 1.0‰ to 7.2‰ reported for apatite core and rim measurements, respectively (Economos et al., 2017). The $\delta^{34}S$ variations within and between grains was attributed to the presence of multiple oxidation states of sulfur (most likely S^{6+} and S^{2-}) introduced by magma mixing. Likewise, ascent-driven degassing, whereby more reduced magmas preferentially retain ^{32}S (^{34}S is degassed) and more oxidized magmas preferentially retain ^{34}S (^{32}S is degassed), also affected the $\delta^{34}S$ value of apatite due to its preference for incorporating S^{6+} relative to S^{2-} (Economos et al., 2017).

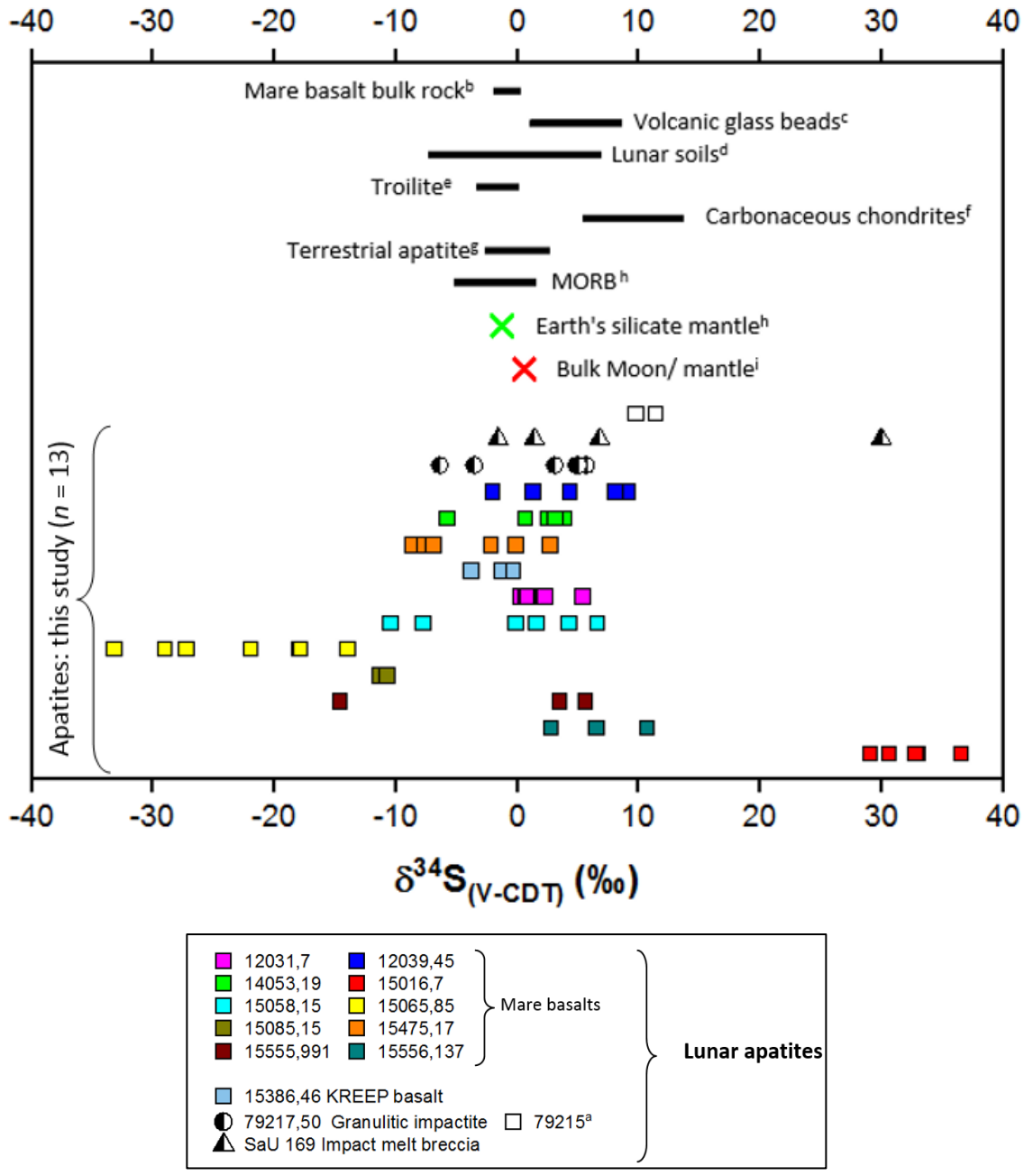

Figure 4.9. Plot of S isotopes ($\delta^{34}S_{(V\text{-}CDT)}$) for the analysed lunar apatites and other lunar and non-lunar materials from the scientific literature. The plot shows the wide range and distribution of S isotopes for apatites within ten Apollo mare basalts, a KREEP basalt, a granulitic impactite and a lunar meteorite (impact melt breccia) (n = 13) measured in this project compared with other lunar and non-lunar materials. Data from [a] Treimen et al. (2014); [b] Thode and Rees (1971), Rees and Thode (1972), Petrowski et al. (1974), Rees and Thode (1974), Gibson et al. (1975), Wing and Farquhar (2015); [c] Ding et al. (1983); [d] Thode and Rees (1971), Rees and Thode (1972, 1974), Kerridge et al. (1975a, 1975b), Kaplan et al. (1976); [e] Shearer et al. (2012); [f] Gao and Thiemens (1993), Bullock et al. (2010); [g] Economos et al. (2017); [h] Labidi et al. (2013); [i] Wing and Farquhar (2015).

4.4. Secondary processes affecting indigenous S in lunar apatite

4.4.1. Terrestrial contamination

The Apollo samples analysed within this study were collected from the surface of the Moon and were returned in collection boxes to be placed into quarantine before being examined under vacuum conditions (Allton et al., 1998). Today, the Apollo samples are housed and analysed in a dry N_2 atmosphere to prevent terrestrial contamination during sample processing (e.g. Day et al. 2018). The curation procedures, therefore, are unlikely to have introduced any significant contamination to the samples analysed in this project.

In order to limit the absorption of any contaminating terrestrial atmospheric gases, the protocol adopted for this project involved cleaning the samples with isopropanol (IPA) before baking them in a vacuum oven for several days. The samples were then baked for another couple of days (~2-3) under vacuum in the NanoSIMS airlock before being moved into the vessel chamber (maintained at higher vacuum conditions than the airlock) which facilitated further removal of any remaining surface contamination prior to moving the thin section in the analysis chamber (maintained at the highest vacuum condition at ~10^{-10} mbar) for analysis. The NanoSIMS analysis also involved 'pre-sputtering' the target sample surface prior to isotope measurement so that any residual surface contamination was eliminated (further details in Chapter Two).

Moreover, based on S combustion experiments of bulk-rocks (Des Marais, 1983), Apollo sample 15016 was reported to release S in an increasing and constant manner with increasing temperature. Any terrestrial organic S would have been volatilized between ~400–500 °C which would have caused the pattern of S release to become bimodal in nature. Terrestrial contamination of this sample was ruled out (Des Marais, 1983) and it is, therefore, highly unlikely that it contributed to the very heavy $\delta^{34}S$ values (up to +36.4‰) reported in this project for apatite.

Lunar meteorite, SaU 169 (impact melt breccia), used for proof of concept in this project, was not collected from the Moon but is a hot desert 'find', discovered in Oman. Whilst it is possible that it was exposed to terrestrial contamination, the terrestrial weathering of the meteorite has been classified as W1 (Russell et al., 2003) which means that, based on a

weathering scale introduced for ordinary chondrites, it has undergone only very minor oxidation around metal rims with the possibility of minor oxide veins being present (Wlotzka, 1993). This suggests that terrestrial alteration of a crystalline material such as apatite is unlikely or insignificant.

4.4.2. Vaporization by micrometeorite impacts

As detailed in Chapter One, lunar soils have a relatively heavy $\delta^{34}S$ (+5.3‰ to +13.5‰) when compared with bulk-rocks, which appears to be correlated with the maturity of the lunar soil (Kerridge et al., 1975a, 1975b). The heavy $\delta^{34}S$ signature is believed to have been caused by the thermal vaporization of S following bombardment of the Moon's surface by micrometeorites that interacted with the lunar regolith. So far, no mass balance solutions (i.e. materials with correspondingly light $\delta^{34}S$ values) have been discovered to account for the heavy isotope value of the lunar soil and, therefore, it has been suggested that there is a complete loss of the lighter ^{32}S isotope out into space (Clayton et al., 1974; Kerridge et al., 1975a, 1975b). This model is complicated by the fact that S abundance in lunar soils is not depleted relative to lunar rocks, whereby the lunar soil is thought to have been derived from the physical destruction of the nearby rocks. Kerridge et al. (1975b), therefore, suggested that the S abundance of lunar soils is formed from a mixture of S from indigenous rocks and an extra-lunar material of meteoritic origin (with a $\delta^{34}S$ of ~0‰) that adds S to the regolith and either cancels out the loss of S to space or, in the case of Apollo 16 soils, leaves a S-enrichment.

From the point of view of the samples studied in this project, the apatites in 15016 have the heaviest sulfur isotopes (up to +36.4‰) which might suggest fractionation was caused by a similar process to that of lunar soil or that the $\delta^{34}S$ signature of the lunar soil was assimilated into the melt that formed the 15016 apatites. However, if such processes were to have acted upon the apatites of 15016, it would be very difficult for the whole rock not to also be affected. The bulk-rock $\delta^{34}S$ value is, however, between ~+0.7‰ and +2.6‰ (Gibson et al., 1975; Kaplan et al., 1976; Des Marais et al., 1983).

4.4.3 Solar wind and cosmic ray spallation

The implantation of solar wind, whereby protons carried by the solar wind are incorporated into materials at the lunar surface, has been implicated in the formation and isotopic fractionation of hydrogen, nitrogen and carbon within lunar soils and highly altered lunar rocks exposed at the Moon's surface (e.g. Crider and Vondrak, 2002). This process is thought to affect exposed materials to a depth of ~50–100 nm (Hashizume et al., 2000). The apatites analysed within this project are located within thin sections that were cut from the inside of whole rock specimens, putting them at a depth far greater than 100 nm and away from possible direct interaction with the solar wind.

Rock sample 14053 is known to have been affected by the solar wind (Chapter Three), whereby it was altered by post-crystallisation hydrogen (H) implantation and thermal metamorphism at the lunar surface that allowed the solar wind H to enter the outer sections of the rock (Taylor et al., 2004). However, unlike H, the abundance of S carried by the solar wind is thought to be too low to make any significant contribution to either the S abundance or the S isotopes of materials exposed at the lunar surface (Moore et al. 1971; Haskin and Warren, 1991).

In contrast to the solar wind, high energy galactic cosmic rays (GCR) can penetrate materials at the lunar surface to depths of ~1 m and, via a process of cosmic ray spallation (CRS), can lead to the production of cosmogenic isotopes from target atoms (Vaniman et al., 1991). For example, CRS is known to produce the isotopes ^{33}S and ^{36}S from the target atoms ^{56}Fe or ^{40}Ca (Gao and Thiemens, 1991; Wing and Farquhar, 2015). For lunar bulk-rocks, the generation of ^{33}S and ^{36}S from CRS were found to be below the limits of detection (Thode and Rees, 1971) or were negligible, with any contributions reported to be within the estimated uncertainty of the $^{33}S/^{32}S$ and $^{36}S/^{32}S$ ratio measurements performed (Wing and Farquhar, 2015).

4.4.4. Post-crystallisation alteration of S in apatite

The introduction of non-indigenous S or the removal of indigenous S from an apatite grain after it has crystallised from a magma is limited because apatite is considered to be resistant to secondary alteration processes such as post-entrapment diffusion or

modification from, for example, weathering (Peng et al., 1997, Stock et al., 2016). It has been shown for OH, F and Cl, that post-crystallisation diffusion from apatite is possible if a parent magma undergoes prolonged cooling with rates of ~1 °C per year (Brenan, 1994). However, it is believed that lunar basalts cooled at much faster rates of ~0.1–30 °C per hour (Taylor et al. 1991) and, therefore, it is less likely that post-entrapment diffusion of volatiles was significant enough to alter the volatile composition of apatite relative to that of the magma at the time apatite crystallised (Anand et al., 2014). Sulfur diffuses more slowly when compared with OH, F and Cl (Ustunisik et al., 2015) and, therefore, it is likely that apatite also preserves the S signature of the magma at the time of apatite crystallisation.

As mentioned in section 4.2.1, brecciated granulite sample 79215 (non-basalt sample) was thought to have experienced post-crystallisation metasomatism resulting from the transportation of element-carrying vapours through the crust and regolith. The vapours were driven by an impact that was responsible for producing the brecciated nature of the sample and led to phosphate mineral merrillite being transformed to apatite (Treiman et al., 2014). Whilst the behaviour or, indeed, the presence or absence of S within the suggested mobile vapour phase was not mentioned by Treiman et al. (2014), the possibility of post-crystallisation alteration with respect to S cannot be ruled out for 79215.

4.5. Sulfur in the basaltic source region(s)

Mare basalts are thought to have formed from the partial melting of the lunar mantle at different depths and from different sources (e.g. Grove and Krawczynski, 2009; Longhi, 1992) (see Chapter Three for more details). From the analysis of olivine-hosted melt inclusions in an Apollo 17 orange soil sample (composed of glass beads), the lunar mantle was estimated to contain 193–352 ppm S (Hauri et al., 2011), which is similar to Earth's upper mantle (~250 ppm S (McDonough and Sun, 1995)) but slightly higher than the mid-ocean ridge basalt (MORB) mantle source region (~146 ppm S (Saal et al., 2002)). Hauri et al. (2011) suggested that there is a reservoir within the interior of the Moon that contains similar sulfur contents as the MORB source region and that any low abundances of all lunar volatiles (including S) reported so far are as a result of degassing having occurred in the samples measured.

However, from the analysis of olivine-hosted melt inclusions in mare basalts from multiple Apollo landing sites (Apollo 11, 12 and 15) as well as the same Apollo 17 orange soil sample (74220) studied by Hauri et al. (2011), the S abundance within the lunar mantle source region was estimated by Bombardieri et al. (2005) and Chen et al. (2015a) to be much lower at ~75 ppm S and ~70 ppm S, respectively, which is 2 to 3 times lower than Earth's upper mantle (Bombardieri et al., 2005). The S results of Chen et al. (2015a) did, however, agree with Hauri et al. (2011) and confirmed that the S abundance within melt inclusions of the orange glass beads were similar to that measured in MORB melt inclusions.

The oxygen fugacity (fO_2) of the lunar mantle is estimated to be ~1 log unit below the iron-wüstite (IW) redox buffer, with certain Apollo basalts and volcanic glasses recording an fO_2 of ~IW+0.2 to IW-1 (e.g. Sato et al., 1973; Longhi, 1992; Wadhwa, 2008). Sulfur is considered to be dissolved in reduced silicate melts as S^{2-}, with the level of S dissolved and the S oxidation state (e.g. S^{2-} or the more oxidized S^{6+}) being dictated by temperature, pressure, melt composition and oxygen fugacity (e.g. Fincham and Richardson, 1954; Carroll and Rutherford, 1988; Wallace and Carmichael, 1992; Carroll and Webster, 1994). The abundance of S in a silicate melt that is saturated with a sulfide phase is known as the sulfur concentration at sulfide saturation (SCSS). It represents the upper limit of S abundance that can occur in silicate melts at reduced oxygen fugacities (i.e. where sulfide rather than sulfate is dominant) where 'saturation' refers to the coexistence of two phases such as a melt phase saturated with a gas phase or saturated with a crystalline phase (e.g. troilite, FeS) that are in equilibrium with each other (e.g. Baker and Moretti, 2011). SCSS has been shown to increase with increasing temperature and to increase with decreasing pressure and is strongly affected by the initial abundance of S in the mantle and the magma composition (for example, different combinations of water, FeO, TiO_2, SiO_2 and Al_2O_3 within lunar magmas can act to both increase and decrease the SCSS) (e.g. O'Neill and Mavrogenes, 2002; Fortin et al., 2015; Ding et al., 2018).

The lunar basaltic source region(s) is believed to be sulfide undersaturated (e.g. Bombardieri et al., 2005) with SCSS values estimated to have been 1,400–4,800 ppm S (Ding et al., 2018) and 1,900–7,400 ppm S (Steenstra et al., 2018). Sulfide exhaustion occurs when sulfur, present as a sulfide, enters a liquid when partial melting begins and, as the melt fraction increases, is completely removed into the melt (i.e. it behaves

incompatibly). Sulfide exhaustion, therefore, depends on the degree of partial melting. Ding et al. (2018) confirmed that the estimated S abundance for the majority of near-primary magmas in the lunar basalt source region (e.g. Hauri et al., 2011; Bombardieri et al., 2005; Chen et al., 2015a) was much lower than the corresponding SCSS. Sulfide exhaustion had, therefore, occurred during partial melting, leaving the source region sulfide undersaturated.

According to Steenstra et al. (2018), sulfide exhaustion of the lunar magma source region agrees with the reported low S abundances in the lunar core (<0.16 wt.% S (Steenstra et al., 2017b)) and mantle (70–75 ppm S (e.g Chen et al., 2015a; Bombardieri et al., 2005)) and reinforces the idea of relatively minor degassing of S during the Moon-forming event (e.g. Wing and Farquhar, 2015 – see Chapter One for more details). Ding et al. (2018) concluded that the varying estimates of S contained within initial lunar magmas for different lunar materials (mare basalts, orange glasses and green glasses) were as a result of the lunar mantle source regions being heterogeneous with respect to S, which was possibly caused by crystallisation of the LMO and inefficient convection of the mantle following the lunar mantle overturn.

4.6. The behaviour of sulfur in late-stage lunar magmas

4.6.1. Sulfide separation: immiscible FeS

Whilst the basaltic source region of the lunar mantle is believed to be sulfide undersaturated (Bombardieri et al., 2005; Ding et al., 2018; Steenstra et al., 2018), late-stage lunar magmas must have become sulfide saturated as the overall melt fraction decreased and the S concentration in that residual melt increased. The evidence for this comes from the presence of troilite, in varying abundances, in every Apollo sample analysed in this project. If the silicate melt became sulfide saturated, separation of immiscible $FeS_{(liquid)}$ from the silicate melt would have formed a late-stage sulfide melt ($Fe^{2+} + S^{2-} \leftrightarrow FeS_{(liquid)}$) (e.g. Marini et al., 2011). The separation of immiscible $FeS_{(liquid)}$ from the silicate melt can reduce the $\delta^{34}S$ of the silicate melt to ~-1.9‰ from a starting value of 0‰ at 1,200 °C. Precipitation of $FeS_{(troilite)}$ would have begun after apatite crystallisation from the basaltic magma (e.g. Papike et al., 1991).

4.6.2. Sulfur degassing and isotope fractionation from silicate melts

The diffusion of S through basaltic melts is relatively very slow (10^{-11} m^2 s^{-1} at ~1,200 °C in hydrous basaltic melts). No significant differences between the diffusion rate for sulfide and sulfate have been recorded but both are dependent upon the viscosity of the magma (the higher the viscosity, the slower the diffusion rate). Diffusion is a significant process for the partitioning of volatiles into a gas phase when a magma becomes oversaturated with dissolved volatiles (Behrens and Stelling, 2011). The separation of an exsolving gas (i.e. by degassing) occurs as a magma ascends to shallower depths and undergoes decompression as a result of reducing pressure (Sparks, 2003) and can be a complicated process because the solubilities (see Chapter One for further details regarding S solubility) of different volatile components vary depending upon the melt and gas compositions, the temperature, the pressure and the oxygen fugacity (fO_2) (e.g. Wallace and Carmichael, 1992).

The S species degassed from a magma can be in the form of S_2, H_2S, SO_2, COS and SO_3, which is as a result of the multiple oxidation states of S (S^{2-}, S^0, S^{4+} and S^{6+}) (Oppenheimer et al., 2011). For more reduced magmas (below the fayalite-magnetite-quartz redox buffer (FMQ-1)), the degassed S species are usually S_2, H_2S and COS, whereas for more oxidized magmas (above FMQ), SO_2 and minor SO_3 prevail as the degassed S species (Carroll and Webster, 1994). Magmatic degassing can cause sulfur isotope fractionation via the separation of a gas phase from a melt phase, leaving the fractionated (residual) melt with a different $\delta^{34}S$ than that of the original magma source (Marini et al., 2011).

As mentioned in section 4.3.2, degassing of more reduced melts tends to involve the loss of ^{34}S due to the preferential retention of ^{32}S in the melt, whereas degassing of more oxidized melts tends to involve the loss of ^{32}S due to the preferential retention of ^{34}S in the melt (e.g. Economos et al., 2017). This is because the more oxidized S species has a stronger covalent bond with the heavier ^{34}S isotope when compared with the lighter ^{32}S isotope (de Moor et al., 2013). If a reduced (S^{2-}) melt degases, the extent of S isotope fractionation between the melt phase and gas phase is far greater when SO_2 (containing the more oxidised S^{4+}) degasses compared with when H_2S (containing S^{2-}) degasses. Likewise, if an oxidized (S^{6+}) melt degasses, the extent of S isotope fractionation between the melt phase

and gas phase is greatest when H_2S degasses compared with when SO_2 degasses (Figure 4.10) (de Moor et al., 2013). In this scenario, mass-dependent S isotope fractionation is occurring (where fractionations are governed by relative mass differences between isotope species) (Criss and Farquhar, 2008), and it depends on the sulfur speciation of the melt and the gas (e.g. Marini et al., 2011). The possible reactions that can be involved in the fractionation of S isotopes between residual melts and gases are shown in Equations 4.1 and 4.2 for H_2S or SO_2 degassing from a S^{2-} melt, respectively, and in Equations 4.3 and 4.4 for H_2S or SO_2 degassing from a SO_4^{2-} melt, respectively (e.g. Moretti et al., 2003; Marini et al., 2011).

$$S^{2-}_{(melt)} + H_2O_{(gas)} \leftrightarrow O^{2-}_{(melt)} + H_2S_{(gas)} \quad \text{Equation 4.1}$$

$$S^{2-}_{(melt)} + \frac{3}{2}O_{2(gas)} \leftrightarrow O^{2-}_{(melt)} + SO_{2(gas)} \quad \text{Equation 4.2}$$

$$SO_4^{2-}{}_{(melt)} + H_2O_{(gas)} \leftrightarrow 2O^{2-}_{(melt)} + \frac{1}{2}O_{2(gas)} + H_2S_{(gas)} \quad \text{Equation 4.3}$$

$$SO_4^{2-}{}_{(melt)} \leftrightarrow O^{2-}_{(gas)} + \frac{1}{2}O_{2(gas)} + SO_{2(gas)} \quad \text{Equation 4.4}$$

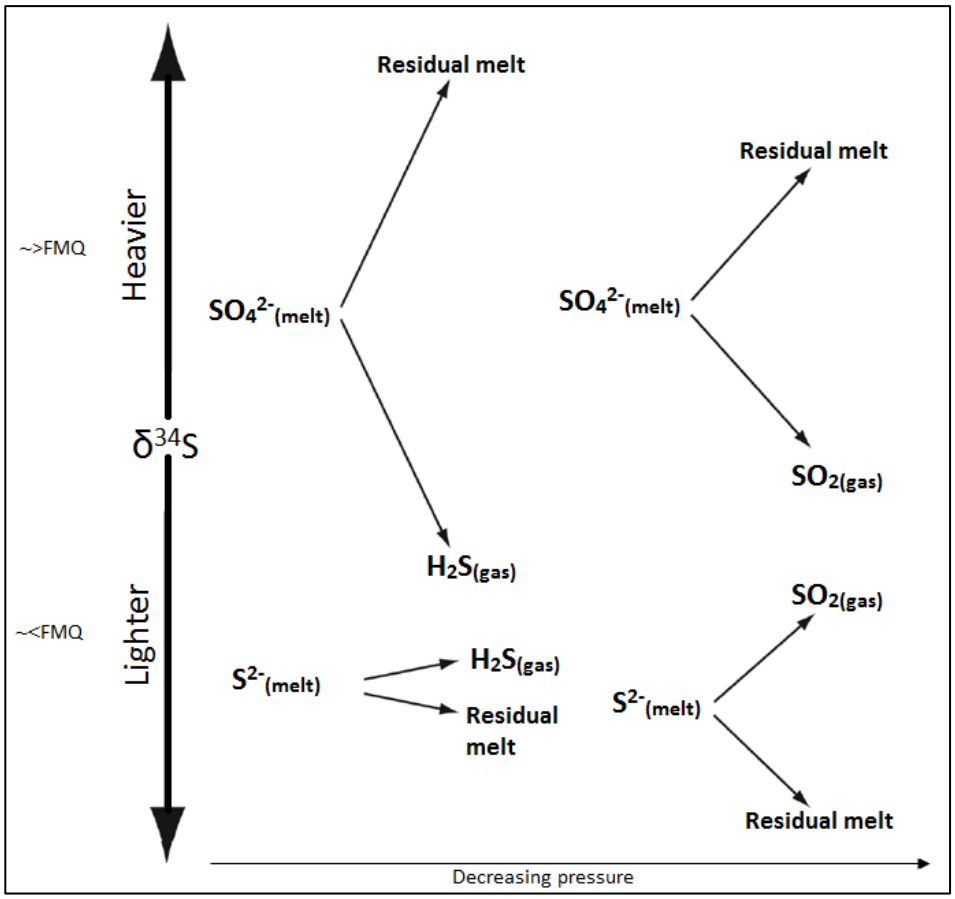

Figure 4.10. Schematic diagram illustrating the magnitude of mass-dependent S isotope fractionation. The bottom half of the diagram shows partial degassing from a more reduced (S^{2-}) melt: H_2S degassing causes very little fractionation (as indicated by the $\delta^{34}S$ scale to the left) and SO_2 degassing causes a greater degree of fractionation because the more oxidized S^{4+} (within $SO_{2(gas)}$) is enriched in ^{34}S due to the stronger covalent bonding. The top half of the diagram also shows partial degassing of H_2S and SO_2 but from a more oxidized (SO_4^{2-}) melt where, this time, the fractionations are much greater and the residual melt (S^{6+}) is left with a much heavier $\delta^{34}S$ value (adapted from de Moor et al., 2013).

4.6.3. Sulfur in lunar apatite: late-stage melts and gaseous S species

As detailed in Chapter One, apatite is a late-stage crystallising mineral in lunar basaltic magmas (Papike et al. 1991) that is capable of holding S within its crystallographic structure (Hughes and Rakovan, 2015). Therefore, by measuring the S contained in lunar apatite, petrogenetic information about the evolution of the very last stages of lunar basaltic magmatism can be obtained, as reflected by the magnitude of S isotope fractionation and the oxidation state and speciation of S in the fractionating melt and gas phases. Such knowledge is important because it adds to our understanding of the dynamic evolution of the lunar interior and, by comparison, other similar planetary bodies in the Solar System.

The bulk Moon has a $\delta^{34}S$ value of +0.58 ± 0.05‰ (Wing and Farquhar, 2015) (see section 4.3.2) and, from the reported bulk-rock $\delta^{34}S$ values of mare basalts, there is no evidence that mantle-derived magmas have a $\delta^{34}S$ value that is significantly different from ~0‰. By extension, the initial $\delta^{34}S$ value of the silicate melt crystallising apatite is assumed to be ~0.58‰. Any deviation from this initial value may be due to secondary magmatic processes, for example, magma degassing or interaction with mobile vapour phases.

Gabbroic basalt sample 15065 has the lightest $\delta^{34}S$ values recorded (-33.3 ± 3.8‰ to -14.1 ± 2.6‰) for apatites in this project. The slight positive correlation between $\delta^{34}S$ and S abundance (Figure 4.1), whereby $\delta^{34}S$ appears to decrease with decreasing S abundance, suggests that S isotopes were fractionated by the loss of ^{34}S from a reduced silicate melt (S^{2-}-rich) through a process of degassing. A reduced melt would preferentially retain the ^{32}S isotope. Likewise, the core-rim decrease of $\delta^{34}S$ (from ~-18.0‰ to ~-27.4‰) and S abundance (from ~1,501 ppm S to ~412 ppm S) in grain Ap005b is also indicative of ^{34}S loss during degassing (e.g. Saal et al., 2008).

To achieve a very light $\delta^{34}S$ value in the residual melt from which the apatites formed, a predominantly reduced silicate melt (S^{2-}) might have initially undergone $H_2{}^{34}S$ degassing (Equation 4.1), causing very little S isotope fractionation, before evolving to degas $^{34}SO_2$ at lower pressures (Equation 4.2), resulting in the largest S isotope fractionation in the residual melt (Figure 4.10). Degassing as one possible cause of isotope fractionation is in agreement with the hydrogen isotope (δD) data available for apatites in the same sample (15065). Degassing led to the loss of the lighter H isotope relative to the heavier isotope (deuterium, D) (e.g. Tartèse and Anand, 2013) and resulted in heavy δD values of ~+931‰ to ~+1,076‰ (Barnes et al., 2019). As with S, a correlation typical of degassing was observed between δD and H_2O, whereby δD increased as the lighter H isotope was degassed as H_2O. According to the degassing modelling of Tartèse et al. (2013), a residual melt with a δD value of ~+1,000‰ can result from degassing of H_2S at temperatures of ~1,100 °C.

As was detailed in Chapter One (and shown in Figure 4.9), negative $\delta^{34}S$ values of –3.3 ± 1.6‰ to –1.0 ± 1.6‰ (2σ) were reported for a secondary, vein and replacement troilite (FeS) in lunar highlands (Apollo 16) clasts by Shearer et al. (2012). Interaction between

plutonic lithologies of the shallow lunar crust and a sulfur-enriched vapour with elevated ^{32}S contents was suggested as the cause of the light $\delta^{34}S$ values. The apatites in 15065 are clearly magmatic in origin and show no signs of having been a product of secondary alteration and, for zoned apatite Ap005b, there are clear signs of crystal growth within a silicate magma. However, given the anomalously low $\delta^{34}S$ values for apatites in 15065, it is possible that a late-stage ^{32}S-rich vapour, derived from a separate degassing magmatic source (possibly at depth), interacted with the silicate melt from which apatites formed. This would have occurred prior to the main phase of ^{34}S degassing from the late-stage silicate melt, leaving the pre-degassed melt with a light $\delta^{34}S$ signature.

Marginal differences between the individual apatite $\delta^{34}S$ values may have been caused by crystallisation at slightly different degassing stages. Interestingly, with the exception of grain Ap003, all of the apatites are enclosed within pyroxene, which suggests a relatively early crystallisation when compared with Ap003 which is found within a late-stage mesostasis region. However, Ap003 has a slightly less negative $\delta^{34}S$ (-14.1 ± 2.6) (and above average (~661 ppm S) S abundance of ~978 ppm S), which might have been caused by crystallisation from an isolated late-stage melt pocket that either underwent fractionally less degassing or interacted slightly less with the late-stage ^{32}S-rich vapour when compared with the earlier crystallising apatites included within the pyroxenes.

At the other extreme, apatites in vesicular basalt 15016 have the heaviest $\delta^{34}S$ values out of all of the lunar basalt samples (+28.9 ± 8.3‰ to +36.4 ± 3.2‰). The potentially anomalous heavy $\delta^{34}S$ signature may have been acquired as a result of increased oxidation in the late-stage silicate magma at ~96–99.5% crystallisation when phosphate saturation had occurred and apatite began crystallising (e.g. Sha, 2000; Tartèse and Anand, 2013). A more oxidised late-stage silicate melt would predominantly contain S^{6+} as dissolved SO_4^{2-}. Whilst more oxidized melts are unexpected in the lunar environment, transient oxidized conditions have been suggested by Joy et al. (2015) following the discovery of an Fe-oxide (Fe^{3+}) phase (magnetite) in a clast from an Apollo 16 regolith (lunar soil) breccia. The magnetite could have been formed by the breakdown of troilite (FeS) following interaction with an oxidizing vapour phase. The vapour phase was thought to have originated from degassing of a magmatic source region and it carried H_2O (liquid or steam) and CO_2, which combined with the desulfurized Fe to form magnetite (Fe_3O_4) (Joy et al., 2015). Likewise, McCanta et al. (2017) also reported ferric iron (Fe^{3+}) to varying degrees in volcanic glass

beads discovered at several Apollo landing sites (11, 14, 15 and 17). In this case, degassing of H (predominantly as H_2) from the lunar magmas from which the glass beads were formed was considered to be driving the increase in Fe oxidation state in the magma.

The suggestion of an oxidizing vapour phase that originates from a degassing magmatic source region (e.g. Joy et al., 2015) could also be a potential means of increasing the oxidation state of the melt from which apatites formed. A late-stage, oxidized ^{34}S-rich vapour could have interacted with the silicate melt prior to the main phase of ^{32}S degassing, which would have resulted in a late-stage silicate melt with a relatively heavy $\delta^{34}S$ signature.

Apatites in 15016 are reported to have low δD values of -91 ± 109‰ to +441 ± 327‰ (2σ) (Barnes et al., 2019) and it is suggested by Tartèse et al. (2014a) that low ratios of D/H in lunar basalts represent very little to no degassing of H_2O. However, the vesicular nature of 15016 testifies to historic volatile degassing (e.g. Taylor et al, 1991), making it an exception. Likewise, the δD values of 15016 are associated with very high statistical uncertainty due to the spallation corrections (necessary because of the long cosmic ray exposure (CRE) age of up to ~422 Ma (Füri et al., 2017)) on a sample with low H_2O abundance (54–348 ppm H_2O). In addition, by measuring the isotopes of trapped nitrogen and noble gases in the vesicles of a crushed chip of 15016, Berkaert et al. (2018) concluded that the gases had a cosmic ray origin (e.g. cosmogenic ^{21}Ne, ^{38}Ar, ^{83}Kr, and ^{126}Xe were present) and/ or a solar wind origin. There were no indications that the isotope signatures from the vesicles were related to an indigenous magmatic source.

Due to the potential interactions with the solar wind and cosmic rays, the δD values and H_2O abundance of apatites in 15016 cannot reliably be interpreted in relation to the S isotope values reported here. There is less certainty about whether 15016 was derived from a relatively wet or dry melt. From a late-stage silicate melt composition dominated by SO_4^{2-}, if the melt was relatively wet, degassing of $H_2{}^{32}S$ may have occurred in the first instance (Equation 4.3) which would have created a large S isotope fractionation between the gas and residual melt (Figure 4.10). Alternatively, if the melt was relatively dry, degassing of $^{32}SO_2$ (Equation 4.4) would also have led to a large gas-melt S isotope fractionation. For both scenarios, the more oxidized (S^{6+}) melt would have preferentially

retained ^{34}S to leave the residual melt with a heavy $\delta^{34}S$ signature following the degassing of ^{32}S.

Within statistical error, the $\delta^{34}S$ values of the 15016 apatites are identical, which suggests that the main phase of ^{32}S degassing in the late-stage melt may have occurred before apatite crystallisation. Sulfur abundance and $\delta^{34}S$ are not obviously correlated. The varied S abundance between apatites could be an indication that the apatite grains crystallised at slightly different stages, i.e. the smallest fraction of melt remaining would contain the highest concentration of incompatible S. This suggestion is demonstrated by zoned apatite grain Ap42 which has a core-rim increase of S abundance (~1,212 to 2,763 ppm S) that appears to coincide with crystal growth in the melt. With the exception of Ap42 which is enclosed within a pyroxene, all of the apatites formed in mesostasis regions. However, there is no significant $\delta^{34}S$ difference between the mesostasis apatites and Ap42, and the S abundance of Ap42 is similar to that of apatite grain Ap6 (~2,797 ppm S).

Like 15016, apatites in vesicular basalt 15556 have exclusively positive $\delta^{34}S$ values (+2.7 ± 1.2‰ to +10.6 ± 3.2‰). It is highly likely that, as a vesicular basalt, 15556 underwent volatile degassing from the magma from which it was formed. There is a perfect negative correlation (-1.0) between $\delta^{34}S$ and S abundance with $\delta^{34}S$ increasing as S abundance reduces. This is a clear indication of ^{32}S loss through degassing from a late-stage melt dominated by SO_4^{2-}. At the time of writing, D/H data for 15556 are not available, which means that the degassed S species may or may not have involved H_2. However, given the greater magnitude of S fractionation between gas and melt when H_2 is involved (Figure 4.10), the predominant degassing S species is more likely to have been $^{32}SO_2$ (Equation 4.4) to leave a relatively positive $\delta^{34}S$ in the residual melt. All three apatite grains analysed were located within mesostasis regions.

In contrast, both apatites in pigeonite basalt 15085 have exclusively negative $\delta^{34}S$ values (-10.8 ± 2.4‰ and -11.4 ± 2.4‰), making 15085 similar to 15065. Interestingly, both of these apatites are enclosed within pyroxenes which was also observed for five of the six apatites in 15065. A degassing trend cannot be established for 15085 because, within statistical uncertainty, the $\delta^{34}S$ values and S abundances (59 ± 7 ppm S and 63 ± 7 ppm S) are identical. Unfortunately, the low S abundance within this sample prohibited measurement of further apatite grains that had otherwise been identified as suitable. The

negative $\delta^{34}S$ values do, however, point towards a process of late-stage degassing from a predominantly reduced silicate melt, similar to 15065. The D/H data for 15085 is also currently not available, which means that the involvement of H_2 cannot be stated with confidence. However, the degassed S species is likely to have involved $^{34}SO_2$ from the reduced melt to leave a relatively negative $\delta^{34}S$ in the residual melt.

Three of the six apatites analysed in pigeonite 15475 have $\delta^{34}S$ values that are very close to ~0‰ (+2.6 ± 2.5‰, -0.2 ± 2.3‰ and -2.3 ± 2.0‰). This could indicate that those three formed before the main S degassing phase in the late-stage silicate melt and, therefore, preserved a bulk Moon S isotope signature (e.g. Wing and Farquhar, 2015). Alternatively, the two marginally negative $\delta^{34}S$ apatites might be as a result of S isotope fractionation caused by immiscible $FeS_{(liquid)}$ separation from the silicate melt – large grains of troilite are abundant in 15475. The S isotopes of the remaining three apatites have been fractionated to leave relatively negative and restricted $\delta^{34}S$ values (-7.0 ± 2.8‰, -7.8 ± 2.4‰ and -8.8 ± 2.5‰), suggestive of crystallisation after late-stage S degassing from a predominantly reduced silicate melt. The melt would have preferentially retained ^{32}S by undergoing late-stage degassing of $H_2{}^{34}S$ and/ or $^{34}SO_2$ to leave the residual melt with a lighter $\delta^{34}S$ value. These three low $\delta^{34}S$ apatites contain less S when compared with the other three apatites (with a value of ~0‰), which may also be evidence of S degassing from the silicate melt. Sample 15475 also does not currently have D/H data available and so the involvement of H_2 in the degassing process cannot be confirmed at this stage. All six apatites are located within the mesostasis regions of the sample.

Pigeonite basalts 12031 and 12039 and high-Al basalt 14053 have $\delta^{34}S$ values that straddle ~0‰ from -5.9 ± 10.5‰ up to +9.0 ± 9.2‰. The large statistical uncertainties resulting from relatively low S abundance in the majority of the apatites makes it impossible to say with confidence what the S species in the silicate melt might have been at the time of apatite crystallisation and whether there was little or no late-stage degassing of S from the silicate melt. Sample 12031 does not currently have reported D/H data which, if available might confirm whether the S degassing species did involve H_2S (e.g. Tartèse et al., 2013). One of the apatites in 12031 was enclosed within a pyroxene, whereas the other five apatites were located within the mesostasis region, but no significant $\delta^{34}S$ or S abundance differences were observed between the two different locations. As with 15475, sample 12031 contains abundant and large (>100 μm) troilite grains which means that S isotope

fractionation caused by immiscible $FeS_{(liquid)}$ separation from the silicate melt may have occurred in addition to possible (varying) degrees of ^{32}S degassing in the melt, to leave three of the six apatite grains with a marginally positive $\delta^{34}S$ values.

The D/H data does, however, exist for sample 12039 which has reported δD values between ~+472‰ and ~+1,010‰ (e.g. Greenwood et al., 2011; Tartèse et al., 2013; Boyce et al., 2015). The values were found to be more restricted by Tartèse et al. (2013) who reported an average of +873 ± 65‰. Whilst this demonstrates that H_2O was degassed from the late-stage melt, at a temperature of ~1,100 °C, degassing of H_2 was slightly more dominant than H_2S (Tartèse et al., 2013). Coupled with the $\delta^{34}S$ values that, within statistical uncertainty, are ~0‰, the apatites in 12039 may be virtually un-degassed with respect to S and represent the bulk Moon $\delta^{34}S$ signature. All of the analysed apatites were located within the same mesostasis region.

The low average δD value of ~-190.8‰ reported for 14053 (Greenwood et al., 2011) suggests little to no degassing of H_2O from the late-stage melt (Tartèse et al., 2014a), which means that, as with 12039, if S did degas from the late-stage melt, it was unlikely to have been alongside H_2O. As mentioned in Section 4.2.1, vapour phase metasomatism has also been reported for 14053 from the view point of Cl (Potts et al., 2018). It is, therefore, not impossible that such a mechanism may have altered the S isotopes and S content of 14053, however, no distinct S isotope signatures (like those of 15065 or 15016) have been identified to confirm whether this might have been the case. All five of the analysed apatites were located within mesostasis regions.

One of the six apatite grains analysed in pigeonite basalt 15058 has a $\delta^{34}S$ value of ~0‰, which suggests that it might have formed prior to late-stage S degassing. Of the other five apatites, three have slightly positive $\delta^{34}S$ values (+1.5 ± 3.5‰ to +6.5 ± 5.2‰) and two have more negative $\delta^{34}S$ values (-10.5 ± 5.9‰ and -7.9 ± 3.2‰). The apatites with positive $\delta^{34}S$ values are negatively correlated with S abundance, which is suggestive of ^{32}S loss by degassing from a silicate melt. In contrast, the apatites with negative $\delta^{34}S$ values are positively correlated with S abundance, indicating that ^{34}S was lost by degassing. This could be evidence for a late-stage melt that contained varying amounts of S^{6+} and S^{2-} (e.g. Economos et al., 2017) from which ^{32}S and ^{34}S were degassed to different degrees. Alternatively, if the two negative $\delta^{34}S$ apatites crystallised fractionally earlier than the

other four apatites, the silicate melt may have evolved from being more reduced to more oxidized resulting in a change from more negative to more positive $\delta^{34}S$ values in the residual melt. Interestingly, the apatites with the negative $\delta^{34}S$ values are enclosed within pyroxene grains, whereas the other apatites are within late-stage mesostasis regions, which means that the former did indeed crystallise slightly earlier. Within each group (negative or positive $\delta^{34}S$), $\delta^{34}S$ values are relatively restricted, therefore, S degassing from the late-stage melt might have occurred prior to apatite crystallisation. The average δD value of apatites in 15058 is +581 ± 62‰, which is associated with degassing at a higher temperature of ~1,300 °C where HCl is the dominant gas species degassing H_2O (Tartèse et al., 2013). It is, therefore, likely that only very minor H_2S was degassed from either a multi-valent or an evolving (reduced to oxidized) late-stage melt which was otherwise dominated by degassing of variable amounts of $^{34}SO_2$ and $^{32}SO_2$ species (c.f. Figure 4.10).

Only three analyses of apatite in olivine normative basalt 15555 were possible due to very low S abundance in some grains. The unusually large $\delta^{34}S$ spread (~20.2‰) in which two grains show positive values (+3.4 ± 4.6‰ and +5.5 ± 4.2‰) and one grain shows a negative value (-14.7 ± 2.8‰) could be symptomatic of different late-stage S degassing histories, as per 15058 above. However, unlike 15058, all three apatite grains were located within the mesostasis regions suggesting that they all crystallised at a very late stage. Within statistical uncertainty, 15555 has an identical δD value (+597 ± 99‰) (Tartèse et al., 2013) to that of 15058 which suggests a similar degassing history to 15058 in relation to H_2O.

As the only KREEP basalt, three apatites in 15386 have marginally negative $\delta^{34}S$ values but, within statistical uncertainty, all values straddle ~0‰ which is characteristic of the bulk Moon S isotope composition. This suggests that there was little or no degassing of S from the late-stage melt from which the apatites crystallised. Sample 15386 has very low S abundance (51–89 ppm S) which may be representative of a low-S basalt source region. All three grains were located within late-stage mesostasis regions. The δD values of apatites in 15386 range from +89 ± 99‰ to +778 ± 123‰ and are negatively correlated with OH contents, leading Tartèse et al. (2014a) to conclude that OH degassing from the melt had led to the increasing δD values. For the heavier δD values of 15386, H_2S and H_2 degassing from the melt at a higher temperature of ~1,300 °C could be the cause of H

isotope fractionation (Tartèse et al., 2013) but, based upon the $\delta^{34}S$ reported here, H_2 is more probable.

Sample 79215 is the only non-basalt sample, being an altered feldspathic granulitic impactite. Mare basalts represent partial melting of the lunar mantle and can, therefore, provide information about the interior of the Moon (see Chapter Three for more details). The S isotope fractionation process for apatites of altered 79215 is, therefore, likely to have been different than for the apatites of mare basalts (and KREEP basalt) which underwent degassing in lunar basaltic magmas. Whilst four of the six apatites in this sample have marginally positive $\delta^{34}S$ values (+3.1 ± 5.2‰ to +5.6 ± 4.4‰), with the other two apatites being marginally negative (-3.6 ± 5.1‰ to 6.4 ± 4.9‰), the relatively large corresponding statistical uncertainty precludes any reliable interpretation of the S isotope fractionation in this sample. As stated in Section 4.2.1, a vapour phase carrying Cl and H_2O, driven by an impact event, interacted with 79215 (Treiman et al., 2014). If there were post-crystallisation alteration of S via the same vapour phase (something not suggested by Treiman et al. (2014)) then the S isotopes may well have been fractionated.

4.6.4. Late-stage degassing effect on troilite (FeS)

As previously mentioned (Chapter One), the primary phase of lunar sulfur in mare basalt rocks is the mineral troilite (FeS) (Haskin and Warren, 1991), where troilite forms just after apatite in the late-stage magma (e.g. Papike et al., 1991). The S isotope values of bulk-rock samples, therefore, predominantly reflect the S isotope values of the primary S phase (troilite). As was shown in Table 4.2 above, bulk-rock samples that contain apatite have $\delta^{34}S$ values between ~–1.3‰ and ~+2.6‰, whereas the apatites within those rocks have $\delta^{34}S$ values between ~–33.3‰ and ~+36.4‰. Likewise, bulk-rock samples which were investigated in this study and found not to contain apatite (and were, therefore, not analysed, e.g. Apollo samples 10049 and 10057), have bulk-rock $\delta^{34}S$ values of ~+0.4‰ to ~+0.7‰ (Wing and Farquhar, 2015), which suggests that the presence or absence of apatite within the rock samples has essentially no effect on the bulk-rock $\delta^{34}S$ value. Given the dominance of troilite within mare basalts, it is likely that the more restricted S isotope values reported for bulk-rocks (i.e. troilite) are masking the far greater $\delta^{34}S$ range (~–33.3‰ to +36.4‰) measured *in situ* in the minor S constituent apatite phase.

The degassing models of Marini et al. (2011) show that very little melt-gas S isotope fractionation occurs when H_2S is degassed from a sulfide melt at 1,200 °C (~0.2‰ fractionation between S-bearing melt and gas) (see also Figure 4.10). This means that if, like the late-stage silicate melt, the sulfide melt is degassing H_2S then the large S isotope fractionations seen for apatite are not expected for troilite. Whilst 'desulfurization' of troilite has been suggested as a S removal mechanism as S_2 to account for a negative Fe and S correlation in Apollo 15 and 17 basalts (Gibson and Moore, 1974), it is unlikely that this process was operating in the late-stage melt of the samples studied in this project because loss of S from troilite would have led to the growth of Fe grains around the rims of troilite (e.g. Skinner, 1970), which was not observed. Therefore, limited S isotope fractionation during S degassing from a sulfide melt might explain why the mare basalt bulk-rock $\delta^{34}S$ values are so much more restricted than those reported in this project for lunar apatite.

Chapter Five:

The oxidation state of sulfur in lunar apatite

This chapter details the analytical process involved in measuring the oxidation state of sulfur in lunar apatite with X-ray absorption near-edge structure (XANES) spectroscopy. A description of the analytical methods and techniques employed in this study is documented in the first part of the chapter. The data reduction process and reproducibility related to the analytical technique is recorded alongside the S-XANES results in the sections that follow. The final sections of the chapter provide an evaluation of the S-XANES results alongside the S isotope and abundance results from Chapter Four. A discussion is also formed concerning the use of S in apatite as an indicator of the oxygen fugacity of lunar late-stage silicate melts.

5.1 Introduction

Experiments on a terrestrial apatite (Durango) and experimentally crystallised apatites with micro-X-ray absorption near-edge structure (μ-XANES) spectroscopy at the S K-edge have shown that sulfate (S^{6+}), sulfite (S^{4+}) and sulfide (S^{2-}) can exist together, to varying degrees, in the apatite crystallographic structure at oxygen fugacities of FMQ+3 (fayalite-magnetite-quartz redox buffer) down to FMQ-1 (Konecke et al., 2017a; 2019). Mare basalts and, therefore, the lunar apatites that crystallised within the rocks, are believed to have formed under reducing conditions in a low oxygen fugacity environment (IW-1 (e.g. Sato et al., 1973; Longhi, 1992; Wadhwa, 2008). It is expected that the reduced form of sulfur, S^{2-}, should exist under such conditions (e.g. Fincham and Richardson, 1954; Carroll and Rutherford, 1985; Wallace and Carmichael, 1992; Wilke et al., 2008) but the substitution reactions known to be associated with the accommodation of S into terrestrial apatite involves the more oxidized S^{6+} ($S^{6+} + Si^{4+} \leftrightarrow 2P^{5+}$ and $S^{6+} + Na^{+} \leftrightarrow P^{5+} + Ca^{2+}$) (e.g. Peng et al., 1997).

The results of very recent S-XANES spectroscopy of apatites in two Apollo basalt samples (10044,33 and 12039,4) have been interpreted as evidence for the dominance of S^{2-}, where more than half of measurements had a ratio of S^{6+} to total sulfur ($S^{6+}/\Sigma S_{tot}$) of <3%. It was suggested that the presence of S^{2-}-only apatites was indicative of apatite crystallisation from a relatively low oxygen fugacity (fO_2) lunar magma (Brounce et al., 2019).

Based on the lunar apatite S abundance and isotope results detailed in Chapter Four, it is suggested that apatites had crystallised from late-stage silicate melts that were composed of reduced (S^{2-}), oxidized (SO_4^{2-}) or a combination of both S^{2-} and SO_4^{2-} species. This interpretation means that multiple oxidation states of S (e.g. S^{6+}, S^{2-}) existed within lunar late-stage silicate melts that were driven by variations in magma fO_2; a similar argument has been made recently for terrestrial melts crystallising apatite (Economos et al., 2017). If true, the existence of multiple oxidation states of S in lunar melts, therefore, has significant implications for the S isotopic fractionation processes (e.g. de Moor et al., 2013) of apatites because of their ability to incorporate multiple oxidation states of S.

In order to further constrain which species of S existed or was a dominant component (reduced and/ or oxidized) within late-stage silicate melts and to better understand the late-

stage behaviour of S in lunar magmas, the oxidation state of S in lunar apatite was determined with μ-XANES spectroscopy at the S K-edge (to be referred to as S-XANES) at Diamond Light Source, the national synchrotron science facility in the UK.

5.1.1 Sample and standard selection

All of the lunar samples selected for S-XANES (Table 5.1) had been investigated with optical and scanning electron microscopy (SEM) (including cathodoluminescence) in preparation for nano-scale secondary ion mass spectrometry (NanoSIMS), as detailed in Chapter Two. With the exception of Apollo sample 10044 (for which only chlorine isotopes were measured), sulfur isotopes of all the samples selected for S-XANES had been measured by NanoSIMS (see Chapter Four for details). No new lunar samples were introduced for S-XANES spectroscopy, therefore, all of the descriptions for the Apollo samples analysed in this chapter are contained within Chapter Three.

Initially, the crucial factor for selecting suitable Apollo samples for S-XANES was that apatite grains contain levels of S that would be detectable during analysis. Beamline I18 at Diamond Light Source had a lower detection limit of ~100 ppm S (Fred Mosselmans, *pers. comm.*). Based on NanoSIMS work (Chapter Four), three Apollo 15 samples were selected with apatites that mostly contain >100 ppm S for S-XANES. In addition, Apollo samples 10044 and 12039, which contain lower S levels, were included because, just before the allotted beam time, a study of the oxidation state of S in lunar apatite was published (Brounce et al., 2019) that analysed these two samples and, therefore, presented an opportunity to check for measurement reproducibility and make inter-laboratory comparisons.

By the May 2019 session, further Apollo 15 samples had been analysed with NanoSIMS and were found to contain sufficient abundances of S for S-XANES. Based on the January 2019 session, the need for a relatively larger beam size became apparent (see section 5.2.3.2. for details) and, therefore, samples with larger apatite grains were necessary, even if they did not contain the highest levels of S (albeit the S content was above the limit of S-XANES detection).

A total of seven different Apollo samples were analysed in both the January and May 2019 sessions (Table 5.1). In addition, surrounding mineral phases including troilite, pyroxene and glass as well as the epoxy that was used to mount the Apollo samples onto the thin section glass slides were analysed. This was to assess any possible interaction with or, in the case of the epoxy, contamination from these materials and the lunar apatite grains. Lunar meteorite SaU 169 (impact melt breccia) was also analysed so that the optimal energy settings for the measurements (see section 5.2.3.2.) could be established before analysing the precious Apollo samples.

Table 5.1. Lunar samples analysed with S-XANES spectroscopy.

Session	Sample I.D.	Sample type	Number of apatite grains analysed
Jan 19	10044,645*	Ilmenite basalt	2
Jan 19	12039,45	Pigeonite basalt	2
Jan 19	15016,7	Olivine basalt	2
Jan 19	15058,15	Pigeonite basalt	3†
Jan 19	15065,85	Gabbroic basalt	4
Jan 19	SaU 169	Impact melt breccia (lunar meteorite).	3
Jan 19	15058,15	Symplectite glass	N/A
Jan 19	15058,15	Epoxy	N/A
Jan 19	15058,15	Pyroxene	N/A
May 19	10044,669*	Ilmenite basalt	4
May 19	12039,5*	Pigeonite basalt	2
May 19	15085,15*	Pigeonite basalt	2
May 19	15085,19*	Pigeonite basalt	4
May 19	15065,85	Gabbroic basalt	4#
May 19	15475,127	Porphyritic pigeonite basalt	3

* S-XANES spectroscopy was carried out on apatites in the samples but the results are not reported in this chapter because the counts of S were too low. † The results of one of the grains is not reported because of the close proximity of apatite to troilite (FeS). # The results of three of the grains are not reported because the counts of S were too low.

The use of reference materials with known S oxidation states was necessary for defining the peak energy positions of S^{6+}, S^{4+} and S^{2-} (see section 5.3.1.), as well as the features associated with the peaks, that might have existed in the lunar apatites (Table 5.2).

Table 5.2. Reference standard material used for S-XANES spectroscopy.

Reference standard	Known sulfur oxidation state*	Location/ source
Troilite (FeS)	2-	Contained within Apollo sample 15058 and lunar meteorite SaU 169.
Elemental S	0	Supplied by I18 beamline scientist.
Sodium-sulfite (Na_2SO_3) (anhydrous)	4+	Purchased from Fisher Scientific.
Terrestrial apatite (Durango)	6+	Durango, Mexico. Supplied by Excalibur Mineral Corp, USA.
Rose gypsum (anhydrite: $CaSO_4$)	6+	Courtesy of Peter Landsberg, The Open University

* Jugo et al. (2010); Konecke et al. (2017a); The European Synchrotron Radiation Facility (ESRF) (2006).

5.2. Micro-X-ray absorption near-edge structure spectroscopy

5.2.1. Fundamental principles

Micro-X-ray absorption near-edge structure (μ-XANES) spectroscopy is a virtually non-destructive technique which can acquire characteristic elemental spectra from a polished thin section (e.g. Mosselmans et al., 2008; Schofield et al., 2010). The fundamental principle of μ-XANES is the absorption of incident X-ray photons by excitation of an inner core-level electron in an absorbing atom that results in an electronic transition of the electron to an unoccupied higher energy level. Each core shell has a different binding energy and an absorption 'edge' results when a core electron absorbs X-ray energy which causes an electronic transition to a higher energy state. Absorption edges are identified by the shell from which the core electron originates. For example, μ-XANES at the sulfur (S) 'K-edge' (at 2472 eV) involves a 1s level electron that is excited to the lowest unoccupied 3p energy level (Wilke et al., 2011). When the incident X-ray energy is greater than that of the absorption edge, the excited electron is ejected from the atom as a photoelectron, leaving the atom in an excited state with an empty electronic level (a core hole) (Figure 5.1). Once the excited core hole has relaxed back to ground state, an electron from a higher

energy state drops down to fill the hole which leads to energy release with a fluorescent X-ray (or auger electron) being emitted (Jalilehvand, 2006).

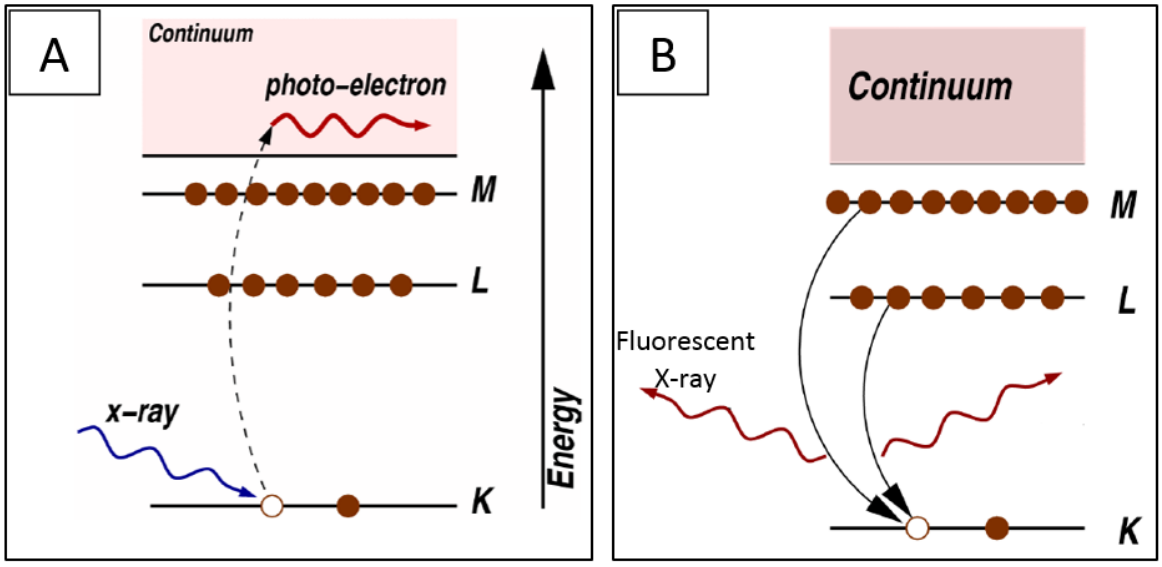

Figure 5.1. Incident X-ray interaction with an atom. **A)** Absorption of incident X-ray photons excites an inner core-level electron (here a K level electron) in an absorbing atom that results in the electron exiting the atom as a photoelectron. A core hole is left in the electronic level. **B)** A higher level electron relaxes back down (shown here from the M or L shell) to fill the core hole and a fluorescent X-ray is emitted (adapted from Newville, 2004).

A XANES spectrum is shown in Figure 5.2 and is comprised of the fine structure just below the absorption edge (the pre-edge region), the absorption edge itself and the near-edge region (the XANES region) that typically continues for up to ~40 eV beyond the absorption edge. The absorption edge inflection point can be used to estimate the core binding energy at E0 (see section 5.3.1.). The absorption edge energy is sensitive to the oxidation state of an absorbing atom, whereby a higher edge energy results from a higher oxidation state (Jalilehvand, 2006). For example, at the sulfur K-edge, energy increases from ~2470 eV to ~2483 eV as the S oxidation state changes from S^{2-} to S^{6+} (Jugo et al., 2010).

Beyond the XANES spectrum region is the extended X-ray absorption fine structure (EXAFS) which begins at ~100 eV and continues to ~1,000 eV above the absorption edge (Figure 5.2) (Wilke et al., 2011). The oscillatory EXAFS region can provide structural information such as the type and number of neighbouring atoms relative to a target atom and their interatomic distances (Jalilehvand, 2006).

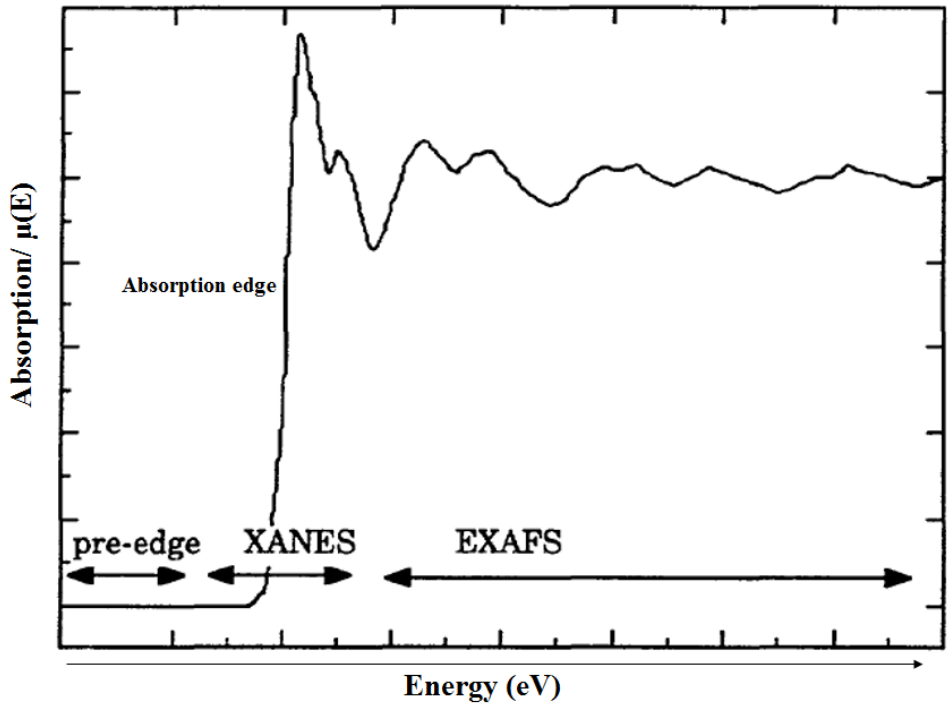

Figure 5.2. A typical X-ray absorption structure (XAS) spectrum. The schematic shows absorption (absorption coefficient μ(E)) as a function of energy (eV) for three regions of an XAS spectrum with the pre-edge, the XANES region (with the absorption edge labelled) where more X-ray photon absorption occurs at a lower energy level and the oscillatory EXAFS region. See text for more details. (Adapted from Alp et al., 1990).

Whilst historical S oxidation studies have employed electron probe microanalysis (EPMA), prolonged exposure with EPMA can lead to photo-reduction or oxidation of S (e.g. $S^{6+} \rightarrow S^{4+}$ and $S^{2-} \rightarrow S^{6+}$), resulting in erroneous calculations of $S^{6+}/\Sigma S_{tot}$ (Métrich et al., 2009; Wilke et al., 2008). When compared with EPMA, which uses S*K*α peak wavelength-shifts and assumes only S^{6+} and S^{2-} are present, XANES spectroscopy achieves a superior spatial resolution by determining the oxidation state of S directly from working on the principle of a 1s→3p electronic transition, which makes the technique very sensitive to S oxidation state (Wilke et al., 2008).

5.2.2. Analytical methods

5.2.2.1. Sample and standard preparation

All of the selected lunar samples that were to be analysed with S-XANES were carefully inspected with optical microscopy and cleaned thoroughly subsequent to NanoSIMS analysis in order to remove the gold coats that had been previously applied to the thin

section sample surfaces for conductivity during the analysis. Comparable with the sample preparation methods of Chapter Two, the sample surfaces were polished gently (to prevent plucking out or rounding off some of the grains from the thin section) with a 0.25 μm diamond paste and corresponding polishing Alpha Cloth. Any residual gold coating and diamond paste was removed by putting the samples in a beaker of isopropanol (IPA) which was placed in an ultrasonic bath (Bandelin SONOREX Digital DK 255 P) for 10 minutes at 60% vibrational power (at room temperature). The samples were dried thoroughly with an air hose before being baked in a vacuum oven at ~55° C for ~2-3 days in order to limit the absorption of any contaminating atmospheric gases prior to analysis.

The troilite (FeS) reference standards used to represent the S^{2-} energy peak were located within the bulk-rock thin sections of Apollo sample 15058 and lunar meteorite SaU 169. The preparation of troilite was, therefore, as detailed for the lunar thin section samples above. The rose gypsum and sodium-sulfite standards, used to identify the S^{6+} and S^{4+} energy peaks, respectively, and the elemental sulfur (S^0) were separately hand-crushed to a fine powder with a pestle and mortar. The terrestrial (Durango) apatite was analysed as both a loose, intact, small crystal and a hand-crushed, powered form.

Once prepared, the thin section samples and the loose crystals were separately affixed to a small strip (~10 cm in length) of Kapton tape which was attached to the centre of a magnet film holder (Figure 5.3). Separately, the powered reference standards were very thinly spread (a single layer) onto the same quantity of Kapton tape before being attached to a magnet film holder.

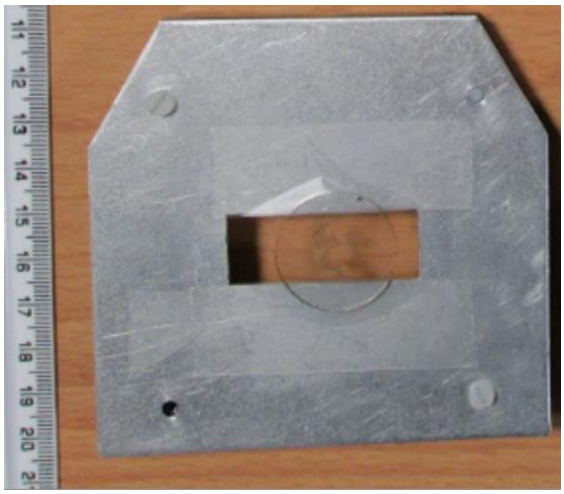

Figure 5.3. A magnet film holder. The image shows thin section Apollo sample 15016 attached to a magnet film holder with the sample at the centre of the holder for analysis.

5.2.3. Analytical techniques

5.2.3.1. Beamline I18

The microfocus spectroscopy beamline, I18 (Figure 5.4), at Diamond Light Source (DLS), Harwell Science and Innovation Campus, UK, was used in this study to collect XANES spectra at the S K-edge from lunar apatite samples. The design of beamline I18 includes an in-vacuum undulator X-ray source, three mirrors (Figure 5.5) and a liquid nitrogen cooled double crystal monochromator. The water-cooled apertures and primary slits act to minimise and guide the beam from the source. The water-cooled toroidal mirror (having a bent cylindrical surface) focusses the beam of X-rays into the monochromator which has a tunable Si (111) crystal with an angular range covering photon energies of between 2.0 keV and 20.7 keV. The harmonic rejection (HR) mirror (used when collecting XANES at low energies e.g. S-XANES (see section 5.2.3.2.)) is fitted with Si and Rh stripes for S spectroscopy and the Kirkpatrick-Baez (KB) mirrors focus the beam onto the sample with a spatial resolution of 2 μm x 2 μm (Mosselmans et al., 2009). A custom-made optical microscope with an attached camera permitted easy navigation across the samples (to locate previously selected apatite grains (Chapter Two)) and reference materials.

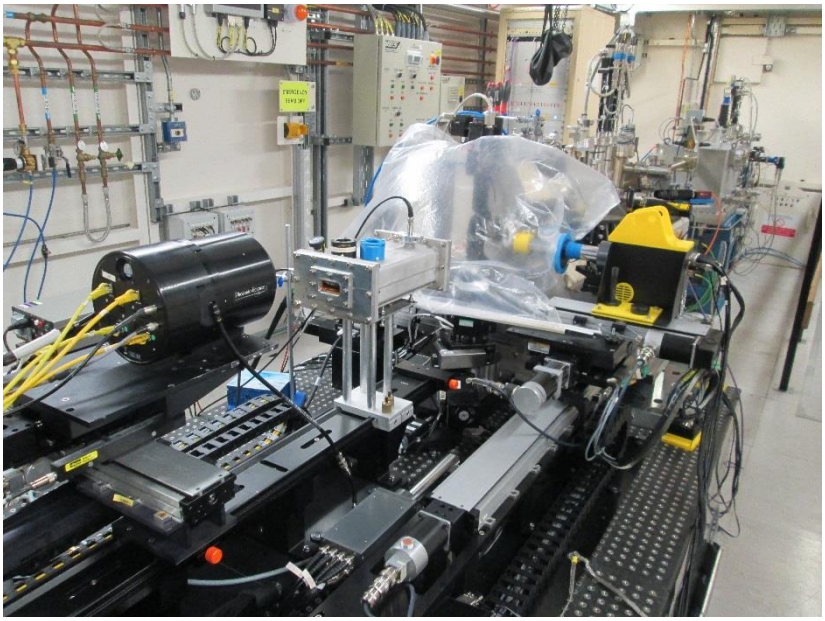

Figure 5.4. Photograph of beamline I18, Diamond Light Source. The image shows the interior of the experimental hutch of beamline I18, where sample analysis occurs behind a secure door (no individual is allowed inside once the experiments start due to harmful X-ray exposure). At the centre of the image is a large helium-filled bag (see text) that surrounds the sample and the detector.

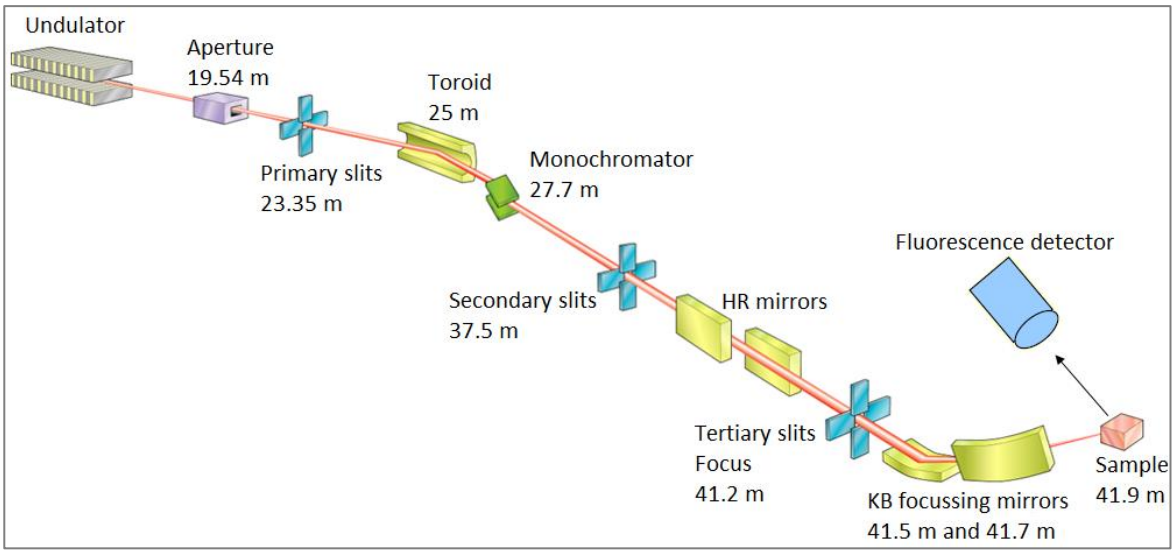

Figure 5.5. A schematic showing the optics of beamline I18. The undulator X-ray source is shown at the top left of the diagram from which the X-ray beam (pink) can be traced through an aperture, slits and mirrors to the sample. The X-ray fluorescence signal is recorded by the fluorescence detector. The numbers beneath the labels represent the distance from the X-ray source (the sample is an incredible ~42 m away from the source) (adapted from Diamond Light Source, 2019).

5.2.3.2. Sulfur X-ray absorption near-edge structure (XANES) spectroscopy: sulfur protocol

S-XANES spectra was collected in fluorescence mode for both analytical sessions (January and May 2019) with a four-element Vortex Silicon Drift X-ray detector. In order to confirm internal reproducibility, both analytical sessions began with S-XANES analysis of the sulfur reference standards (Table 5.2) in order to check the sulfate (S^{6+}), sulfite (S^{4+}) and sulfide (S^{2-}) peak energy positions of the standards against the corresponding known peak energy positions (~2483 eV, ~2478 eV and ~2470, respectively) (The European Synchrotron Radiation Facility (ESRF), 2006). The Si (111) double crystal monochromator was used for all S-XANES spectroscopy.

For the S-XANES analysis, the samples, standards and the detector were positioned within a helium environment to minimize absorption of the X-ray fluorescence signal into the surrounding atmosphere. A single magnet film holder (containing either the samples or standards (Figure 5.3)) was placed in front of the detector, the latter of which was positioned at 45° to the X-ray beam. Kapton tape (~13 µm) was placed in front of the detector for both analytical sessions in order to dampen the high phosphorous signal given off by the apatites.

For the lunar samples, X-ray fluorescence (XRF) element maps of the apatite regions of interest (ROI) were acquired, which involved the continuous scanning of the beam over the ROI (typically 100 μm x 100 μm in size, depending on the apatite grain size) and recording fluorescence at 2500 eV with a dwell time of ~0.5 s per spot. The elements collected were P, S, Si and Cl (with K-alpha X-ray absorption energies of ~2013 eV, ~2306 eV, ~1740 eV and ~2620 eV, respectively). The acquired XRF element maps were used during S-XANES analyses to ensure that the beam was correctly positioned on the lunar apatite grain of interest (using both P and Cl alongside previously acquired backscattered electron (BSE) images (see Chapter Three for more details) to confirm the identity of apatite grains. S-XANES data analysis points were positioned across the apatite grains with use of the maps, which also meant that cracks in the grains and any adjacent areas containing sulfides could be avoided. S-XANES data was not collected for some grains due to the close proximity to troilite (FeS^{2-}). XRF mapping was not necessary for the S reference materials or for the epoxy, symplectite glass and pyroxene grain because the fluorescing beam could be easily seen on the surface of these materials.

For the January 2019 session (five full days: 120 hours), a beam size of ~2 μm x 2 μm and an incident beam intensity (flux) at the S K-edge of ~1 x 10^{10} photons/s was used for reference standard and sample S-XANES data collection. Initially, XANES spectra at the S K-edge were collected to include the EXAFS region by scanning the incident beam from 2430 eV to 2600 eV, with energy step sizes of between 1 eV and 5 eV in the (extended) pre- and post-edge regions and 0.2–0.5 eV between 2465 eV and 2507 eV (which included the S K-edge region of ~2465–2484 eV) with scan durations of 1 s per energy step.

It became apparent that some S in lunar apatites was being oxidized due to the long scanning range used for S-XANES. This was detected by monitoring the S^{6+} peak relative to the S^{2-} peak when making repeat measurements on the same spot on an apatite grain. To address the possibility of beam damage (and S oxidation) from longer scanning durations, the energy range was restricted to exclude the extended region. Accordingly, S-XANES spectra were collected by scanning the incident beam from 2465 eV to 2494 eV with energy steps of 0.5 eV and 1 s per energy step.

The May 2019 analytical session was a full two day (48 hours) 'rapid access' continuation of the five day January 2019 session. New thin section samples had been requested and were supplied by NASA's Curation and Analysis Planning Team for Extraterrestrial Materials (CAPTEM) for the May analysis session to ensure that the samples had not previously been exposed to other X-ray measurement techniques (e.g. EPMA or XANES) that might have caused beam damage (and potential oxidation of S). Following on from the January session, and in order to address further the possibility of beam damage during S-XANES analyses, the X-ray beam was defocussed to give a larger beam size of ~20 x 20 µm. This required apatite grains to be larger than those analysed in the January session and meant that only Apollo samples containing apatites of >~50 µm in the longest dimension were included for S-XANES analysis. The incident flux at the S K-edge was the same as January (~1 x 10^{10} photons/s) except, vanadium foils were placed in front of the beam (between the beam and sample) to reduce the intensity/ flux of the beam by allowing only ~20% of the beam through to the sample. Compared with the January analytical session, the S-XANES spectra collection range was 2450 eV – 2550 eV with steps of 0.5 eV and 1 s per energy point.

The larger apatite grains analysed in May have relatively low S abundances when compared with the apatites studied in January and, with the above instrument setup, no S signal reached the detector. Phosphorous was also swamping any low S signals that may have been present. Therefore, in order to increase the S signal, the beam size was reduced to ~>10 x 10 µm and the vanadium foils were removed. To maintain a low P signal, the Kapton tape in front of the beam was increased to ~25 µm (from ~13 µm) and the detector was positioned further away from the sample during analysis. This improved the S signal, to the extent that S spectra were collected from the apatites, albeit with only very low levels of S being detected (the signal to noise (S/N) ratio was very low).

5.3. Data reduction

5.3.1. Quantification of standards

The peak energy positions of each of the reference materials (Table 5.2) were defined by S-XANES spectroscopy following the S protocol described in the previous section. The raw S spectra were edge-step normalized in the X-ray absorption spectroscopy (XAS) data

processing software Athena (Ravel and Newville, 2005). Normalization involved regressing a line both to the pre-edge and to the post edge region (the data beyond the edge) of a spectrum and extrapolating both lines back to the absorption edge (known as E0) of the spectrum (Figure 5.2). The pre-edge line was subtracted from the post-edge line at the point where both lines passed through E0 to give the 'edge-step' parameter. The subtracted data was then divided by the edge-step value which flattened the pre- and post-edge regions and assigned values of 0 and 1, respectively.

Figure 5.6 shows the normalized S-XANES spectra of the reference materials used to define the peak energy positions of S oxidation states that could be contained in apatite. Anhydrite and terrestrial apatite (Durango) define the S^{6+} peak at an energy of ~2483 eV. The Durango also has another peak at ~2478 eV which is thought to represent the presence of S^{4+} and, therefore, multiple S oxidation states in terrestrial apatite (e.g. Konecke et al., 2017a). The Durango apatite was used to confirm the external reproducibility of our analyses (section 5.5). Troilite (FeS) from two different lunar samples (Apollo 15058 and lunar meteorite SaU 169) show a sharp peak at ~2471 eV that represents S^{2-}. It is reported that a broad peak also exists for S^{2-} at ~2476.8 eV (e.g. Jugo et al., 2010). Troilite does show a broad peak in Figure 5.6 at ~2477 eV and both the sharp and the broad peaks were used in this study to identify S^{2-} in lunar apatite samples. Sodium sulfite appears to have two prominent peaks in Figure 5.6, with one at ~2478 eV and the other at ~2483 eV. Whilst anhydrous (used in this study) is more stable than hydrous sodium sulfite, it can become oxidized to sodium sulfate if it is not kept completely dry (Kastle and Elvove, 1909) and it is likely that the second peak (~2483 eV) represents partial oxidation (Jugo et al., 2010). Therefore, only the first peak (~2478 eV) was used to identify S^{4+} in lunar apatites in this study. The energy peak for elemental sulfur (S^0) is positioned at ~2473 eV.

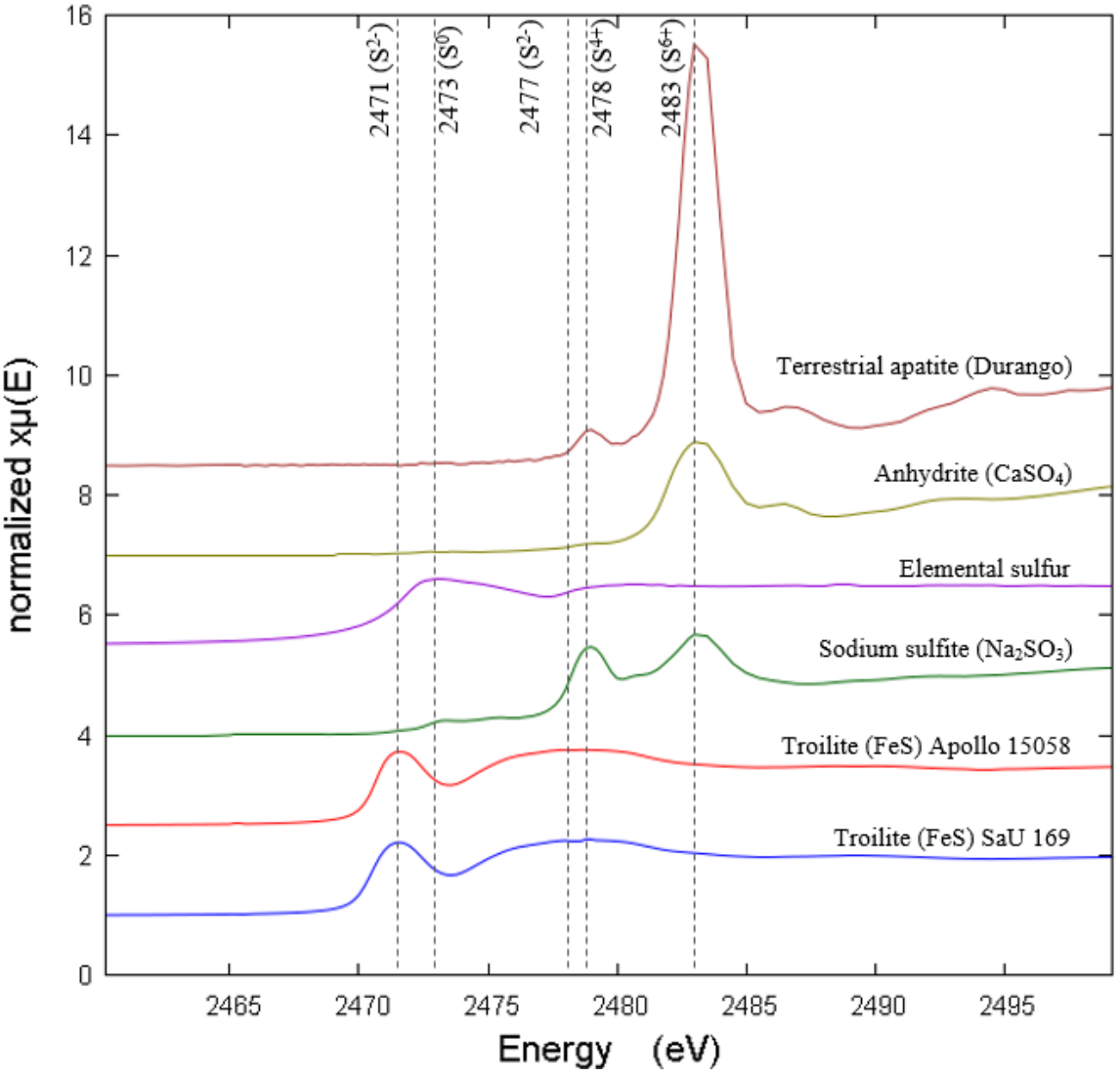

Figure 5.6. Edge-step normalized XANES spectra at the S K-edge of S reference materials. Individual spectra are offset vertically for clarity. See text for details.

5.3.2. Lunar apatite samples: peak area integration analysis

The Athena software (Ravel and Newville, 2005) was used to edge-step normalize each of the S-XANES spectra collected from the lunar apatite samples (Apollo and lunar meteorite) following the same method outlined above for the S reference materials. The normalized data was exported from Athena and loaded into the non-linear curve fitting software Fityk (version 1.3.1) (Wojdyr, 2010) in order to carry out peak area integration analysis of the acquired S-XANES spectra. To define an area under a peak with the software, the peak is divided into many (dependent upon the area of the peak) rectangles which are added together to give an estimated total area under the peak.

5.3.2.1. Background removal, peak fitting and S peak area ratio

Each S-XANES spectrum has an associated background signal which, using a similar method to Koneceke (2017a), was removed with an exponentially modified Gaussian (EMG) function in Fityk. For all spectra, the pre- and post-edges of the EMG function were set to 0 and 1, respectively, with the EMG function inflection point set to ~2479 eV (Figure 5.7). The peak fitting method with background removal is reported to be a semi-quantitative method, whereby the derived peak area ratios are proportional to the abundance of each S oxidation state in an apatite grain (Konecke et al., 2017a).

With use of the known peak energy positions of S^{6+} (~2483 eV), S^{4+} (~2478 eV) and S^{2-} (~2471 eV and ~2477), individual Gaussian curves were positioned onto the background-subtracted S-XANES spectrum in Fityk so that the highest point (the peak) of the Gaussian curve was positioned at a known absorption energy. For example, when adding a Gaussian curve in the S^{6+} region, the highest point of the curve was positioned as close to 2483 eV as possible. Peak fitting of each spectrum was performed with the Gaussian area (Gaussian-A) function in Fityk. The peak area fitting energy range was truncated so that only S-XANES data between ~2465 eV and ~2485 eV (the S K-edge) were included within the peak fitting (Figure 5.7).

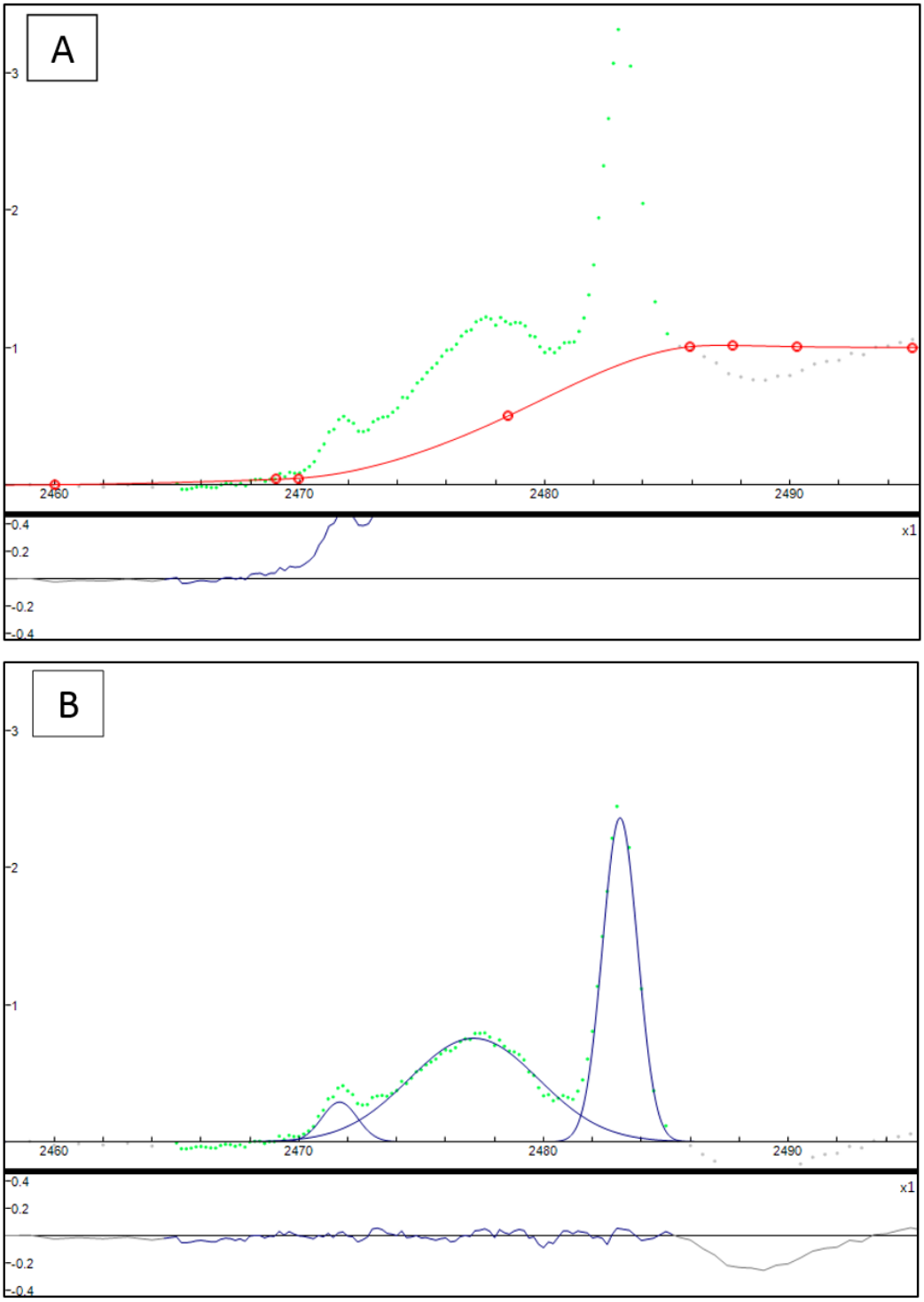

Figure 5.7. An example of background removal and peak fitting of S-XANES in Fityk. The normalized S-XANES spectrum of data collected from a single point on an apatite within Apollo sample 15065 is shown in **A)** where the green dotted line is the spectrum and the red line is the EMG function (fitted background) before subtraction. The y-axis is the absorption intensity. Visible grey dots represent data that was excluded from the fit (in the pre- and post-edge regions). **B)** The same spectrum is shown but the background has been subtracted and the Gaussian-A functions (added peaks, in blue) have been fitted. The lower panel of **B)** shows the peak fitting residual, which represents the difference between the best-fitting model and the data points, and is based on weighted sum of squared residuals (WSSR) (chi-square) (Wojdyr, 2010). The grey lines represent data that was excluded from the fitting.

The peak fitting process determined the individual area values of peaks representing S^{6+}, S^{4+} and S^{2-} (where present) and the corresponding residual standard deviation for all of the fitted spectra. To calculate the S^{6+} content of a lunar apatite sample, the peak area value of S^{6+} was divided by the sum of the peak area values of all sulfur (e.g. $S^{6+} + S^{4+} + S^{2-}$) to give a peak area ratio of 'S^{6+} to total sulfur': $S^{6+}/\Sigma S_{tot}$.

S-XANES scans that appeared to be oxidized were not included. For example, from repeat measurements of the same spot, if the energy peak representing S^{6+} was observed to increase in height as the measurements progressed but the rest of spectrum did not appear to increase, then beam damage was suspected and the scan(s) were excluded from data processing.

5.4. S-XANES results

The full S-XANES spectroscopy results for apatites in five different Apollo samples and a lunar meteorite are shown in Appendix B Table B.5 along with a terrestrial apatite (Durango) and non-apatite materials contained within one Apollo sample. Table 5.3 shows a summary of the results for each sample by taking the average $S^{6+}/\Sigma S_{tot}$ value of the S-XANES scans. An image of each individual Apollo apatite grain refered to in Table 5.3 is shown in Appendix C, Figure C.1 All of the S-XANES spectra reported in this study have $S^{6+}/\Sigma S_{tot}$ ratios of >0. Whilst S^{4+} was observed in the terrestrial apatite and in lunar meteorite SaU 169, it was not detected in any of the Apollo samples.

Not all of the apatites analysed for S abundance and isotopes by NanoSIMS (Chapter Four) could be analysed with S-XANES due to the limited beam time available at the synchrotron facility, low levels of S, small grain size and the proximity of FeS to some of the apatite. The number of S-XANES scans carried out on each apatite grain varied depending on practical considerations such as the size of the apatite and the need to avoid cracks where present.

Table 5.3. A summary of the S-XANES results. The average $S^{6+}/\Sigma S_{tot}$ ratio of the measurements made for individual apatite grains is recorded in the table. The corresponding S isotope values and S abundances determined in this study with NanoSIMS (see Chapter Four) are shown. The individual S-XANES scan results are shown in Appendix B Table B.5.

Session	Sample type	Sample I.D.	Analysis I.D.	Avg. $S^{6+}/\Sigma S_{tot}$	$\delta^{34}S$ (‰)	2σ (‰)	S (ppm)	2σ (ppm)
January 2019	Olivine basalt	15016,7	Ap42	0.55	29.7 *	6.7	1,987 *	464
	Gabbroic basalt	15065,85	Ap007	0.27	-29.1	2.4	903	146
			Ap005b	0.29	-22.7 *	4.5	957 *	155
			Ap001b	0.25	-18.0	2.8	341	55
			Ap003	0.36	-14.1	2.6	978	158
	Pigeonite basalt	15058,15	Ap012a	0.34	-7.9	3.2	472	76
			Ap016	0.30	-0.2	2.7	301	49
	Pigeonite basalt	12039,45	Ap001_a	0.23	9.0	9.2	47	5
			Ap001_f	0.39	-2.1	7.0	112	12
	Symplectite glass	15058,15	-	0.12	N/A	N/A	N/A	N/A
	Epoxy	15058,15	-	b.d.	N/A	N/A	N/A	N/A
	Pyroxene	15058,15	-	0.06	N/A	N/A	N/A	N/A
	Impact melt breccia (lunar meteorite)	SaU 169	SOI 7	0.86	1.4	4.2	245	19
			SOI 14	1.00	6.8	3.6	340	26
			SOI 15	1.00	29.9	3.5	477	37
	Terrestrial apatite	Durango	-	0.95	-	-	-	-
May 2019	Gabbroic basalt	15065,85	Ap007	0.19	-29.1	2.4	903	146
	Porphyritic pigeonite basalt	15475,127	Ap002	0.05	-8.8 to 2.6 †	-	49 to 348 †	-
			Ap003a	0.12	-8.8 to 2.6 †	-	49 to 348 †	-
			Ap003b	0.09	-8.8 to 2.6 †	-	49 to 348 †	-

b.d. = below level of detection. * Average of the core and rim S isotope and S contents values for the zoned grain. † 15475,127 is a different thin section to that studied in Chapter Four (15475,17) so only a range of S content and isotopes that were derived in this study are shown in the table.

It was only possible to analyse one lunar apatite grain in sample 15016 due to the close proximity of large troilite (FeS) grains to the other four apatite grains previously measured in this project (Chapter Four). The troilite might have affected the $S^{6+}/\Sigma S_{tot}$ results by, for example, giving a falsely low $S^{6+}/\Sigma S_{tot}$ value due to the exclusive presence of S^{2-} in the mineral phase. The minimum $S^{6+}/\Sigma S_{tot}$ value acquired for Ap42 is 0.31 and the maximum is 0.79 (Figure 5.8 and Appendix B Table B.5). Sample 15016 has the highest $S^{6+}/\Sigma S_{tot}$ ratio of all of the samples analysed with an average $S^{6+}/\Sigma S_{tot}$ value for grain Ap42 of 0.55 (Table 5.3) where ~ ⅔ of the measurements have a $S^{6+}/\Sigma S_{tot}$ value of >0.5. The random distribution of the scan results for Ap42 demonstrates that beam damage did not occur as the scans progressed, i.e. there is not a continuous increase or decrease of $S^{6+}/\Sigma S_{tot}$ (Figure 5.8).

The individual S-XANES scan results for sample 15065 are shown in Figure 5.9. Four apatite grains with the highest S contents (see Chapter Four) were selected for analysis. Grain Ap007 was studied in both the January and May 2019 sessions, albeit more scans were possible in January due to the superior S/N ratio. The results of the few scans that were possible in May 2019 are within the range of those from January 2019 where the former has a minimum and maximum $S^{6+}/\Sigma S_{tot}$ value of 0.17 and 0.22, respectively, and the latter has a minimum and maximum of 0.09 and 0.35, respectively. The average $S^{6+}/\Sigma S_{tot}$ value for Ap007 is 0.27 for the January data and 0.19 for the May data.

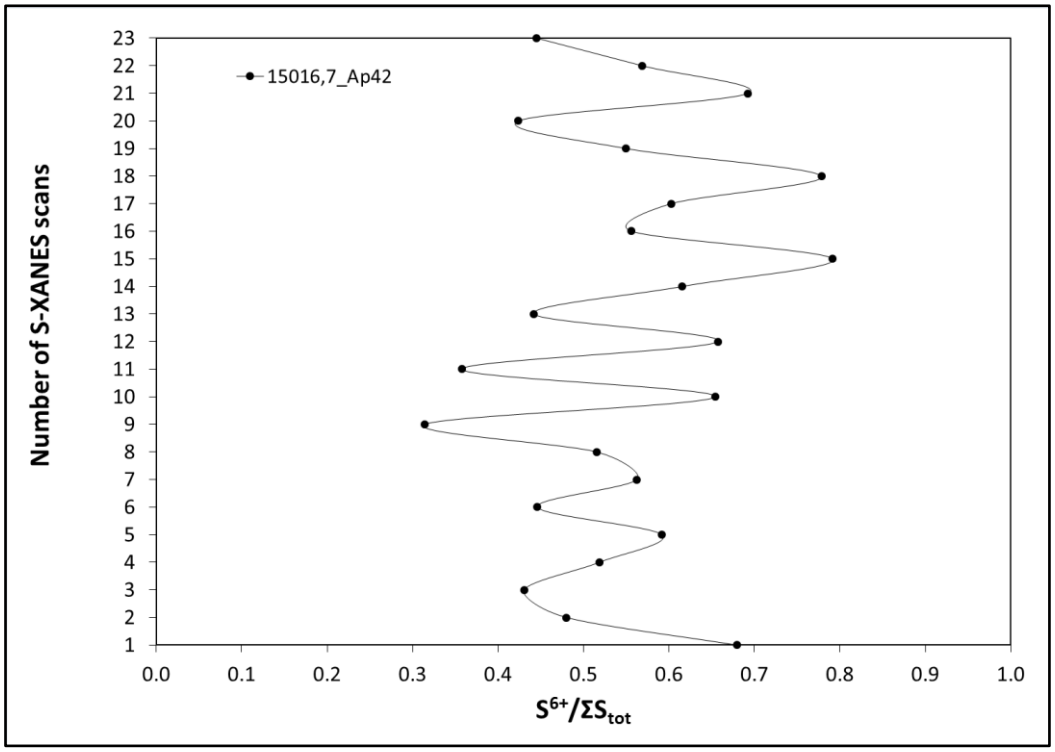

Figure 5.8. Individual S-XANES scans of Apollo sample 15016,7. The plot shows the $S^{6+}/\Sigma S_{tot}$ ratio results of twenty-three S-XANES scans that were acquired from apatite grain Ap42 by profiling across the apatite grain. See text for details.

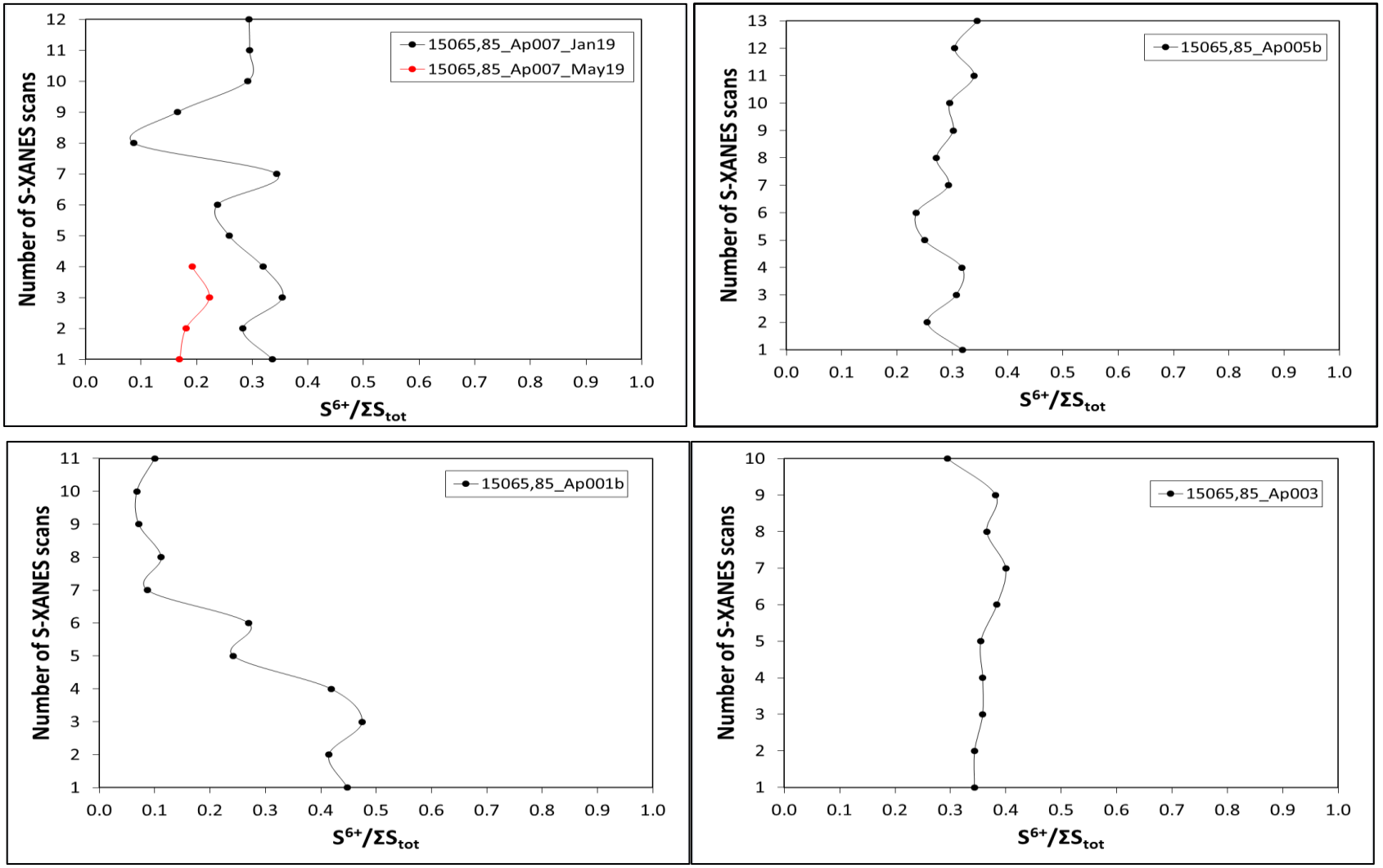

Figure 5.9. Individual S-XANES scans of Apollo sample 15065,85. The plots shows the $S^{6+}/\Sigma S_{tot}$ ratio results of four different apatite grains that were acquired by profiling across the apatite grains. See text for details.

When compared with the May data for Ap007, apatite grain Ap005b has a more restricted $S^{6+}/\Sigma S_{tot}$ range between 0.25 and 0.34 and a fractionally higher average value (0.29) for the whole apatite grain. Apatite Ap001b has the lowest recorded $S^{6+}/\Sigma S_{tot}$ value of sample 15065 at 0.07 but it also has the highest at 0.47. Figure 5.9 appears to show a decrease of $S^{6+}/\Sigma S_{tot}$ as the scans numbers progress. The average for the whole grain is also the lowest of all apatites analysed in 15065 at 0.25. The most restricted $S^{6+}/\Sigma S_{tot}$ values are from Ap003 which show very little variation across the grain (Figure 5.9) with a minimum and maximum $S^{6+}/\Sigma S_{tot}$ value of 0.29 and 0.40, respectively. Ap003 has the highest $S^{6+}/\Sigma S_{tot}$ average for the whole grain at 0.36. The average $S^{6+}/\Sigma S_{tot}$ for all of the apatites analysed in sample 15065 is 0.29.

As mentioned in section 5.2.3.2., different beam settings were used to address any possible beam damage that might have been caused by collecting spectra from a larger energy range. As a consequence, sample 15065 experienced both the longer and shorter scan times. Negligible differences were observed between the different length scans. For example, the average $S^{6+}/\Sigma S_{tot}$ value of the longer scans for apatite Ap005b was 0.28, whereas the average $S^{6+}/\Sigma S_{tot}$ value for the shorter scan times was 0.32, which is opposite to the result expected if beam damage (and oxidation) were occurring.

The individual S-XANES scan results for two apatites in sample 15058 are shown in Figure 5.10. Sulfur abundance and isotope analyses had been carried out on six apatites (Chapter Four) but only three of those grains were selected for S-XANES analysis because their S contents is >100 ppm S. The S-XANES results of the third apatite that was adjacent to a large troilite grain cannot be reported with confidence and are excluded here. For grain Ap012a, the minimum and maximum $S^{6+}/\Sigma S_{tot}$ value is 0.25 and 0.43, respectively, giving it an average $S^{6+}/\Sigma S_{tot}$ of 0.32. The $S^{6+}/\Sigma S_{tot}$ average for grain Ap016 is similar to Ap012a with a value of 0.30 and minimum and maximum values of 0.21 and 0.39, respectively, albeit only four scans were deemed reliable for this apatite due to low S/N ratios.

Additionally, S-XANES analyses of a symplectite glass and a pyroxene grain in close proximity to grain Ap016 (from sample 15058) (Table 5.3 and Appendix B Table B.5) were carried out and show no spectral similarities with the apatite (Figure 5.11). The epoxy of sample 15058 was also analysed but, because the S content was below the level of S-

XANES detection, no S spectra could be acquired which suggests that S signals from the epoxy are unlikely to have affected apatite S-XANES measurements.

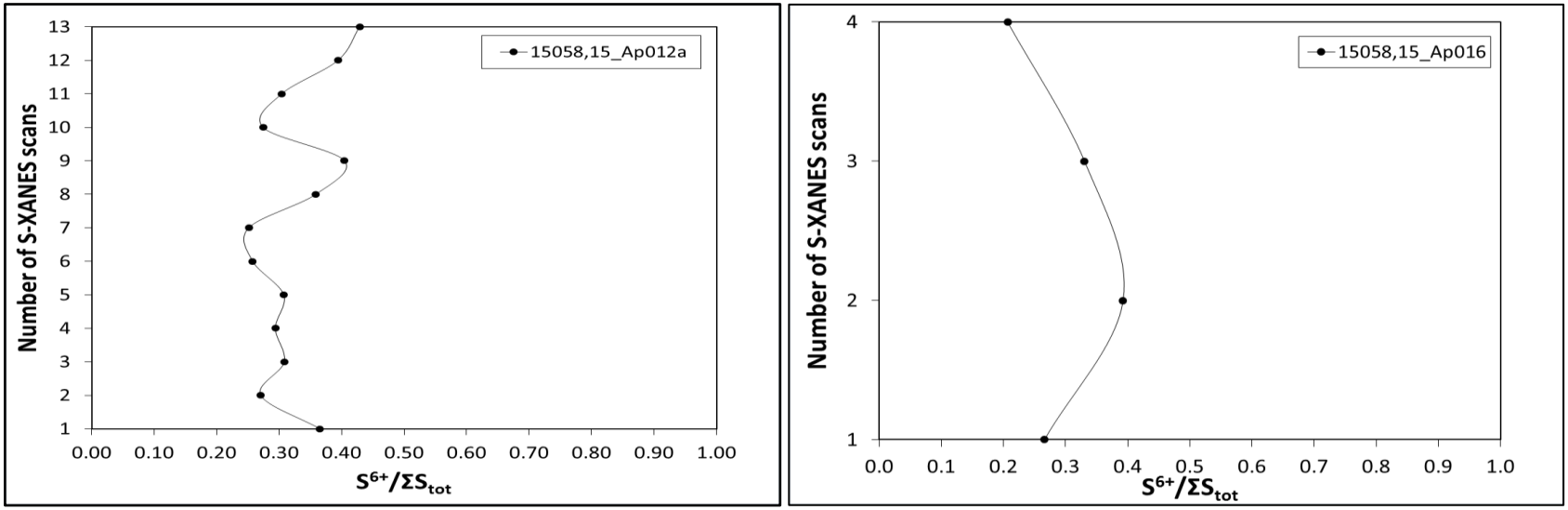

Figure 5.10. Individual S-XANES scans of Apollo sample 15058,15. The plots show the $S^{6+}/\Sigma S_{tot}$ ratio results of two different apatite grains that were acquired by profiling across the apatite grains. See text for details.

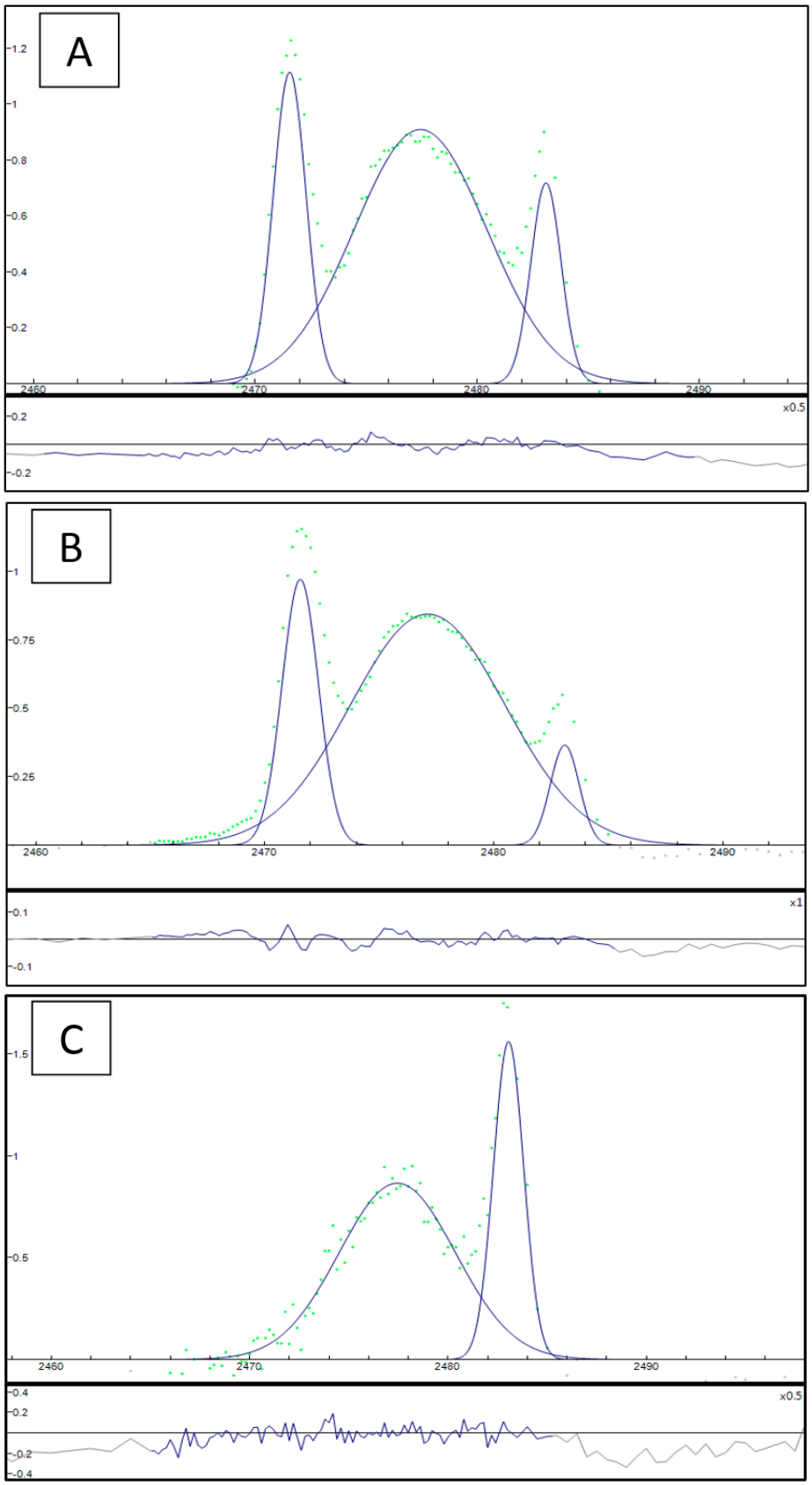

Figure 5.11. Fitted S-XANES spectra of **A)** symplectite glass in Apollo sample 15058, **B)** a pyroxene grain in 15058 and **C)** apatite Ap016 of from 15058. Both the glass and the pyroxene contain three peaks representing S^{2-} (~2471 eV and ~2477 eV) and S^{6+} (~2483 eV). The apatite in **C)** lacks the sharp S^{2-} peak at 2471 eV.

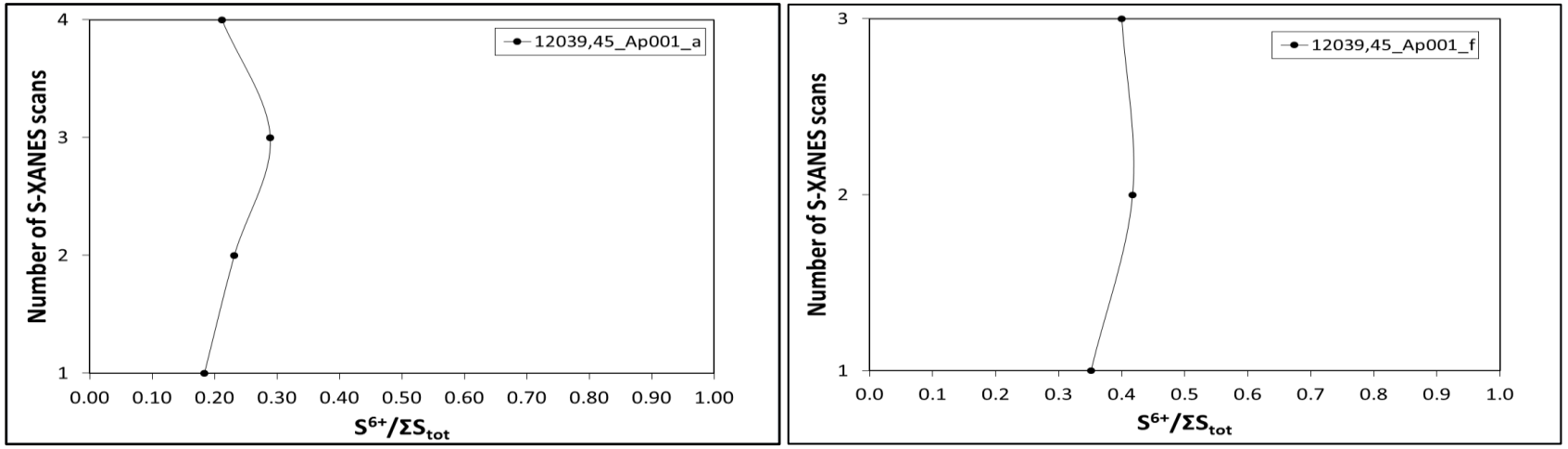

Figure 5.12. Individual S-XANES scans of Apollo sample 12039,45. The plots show the $S^{6+}/\Sigma S_{tot}$ ratio results of two different apatite grains that were acquired by profiling across the apatite grain. See text for details.

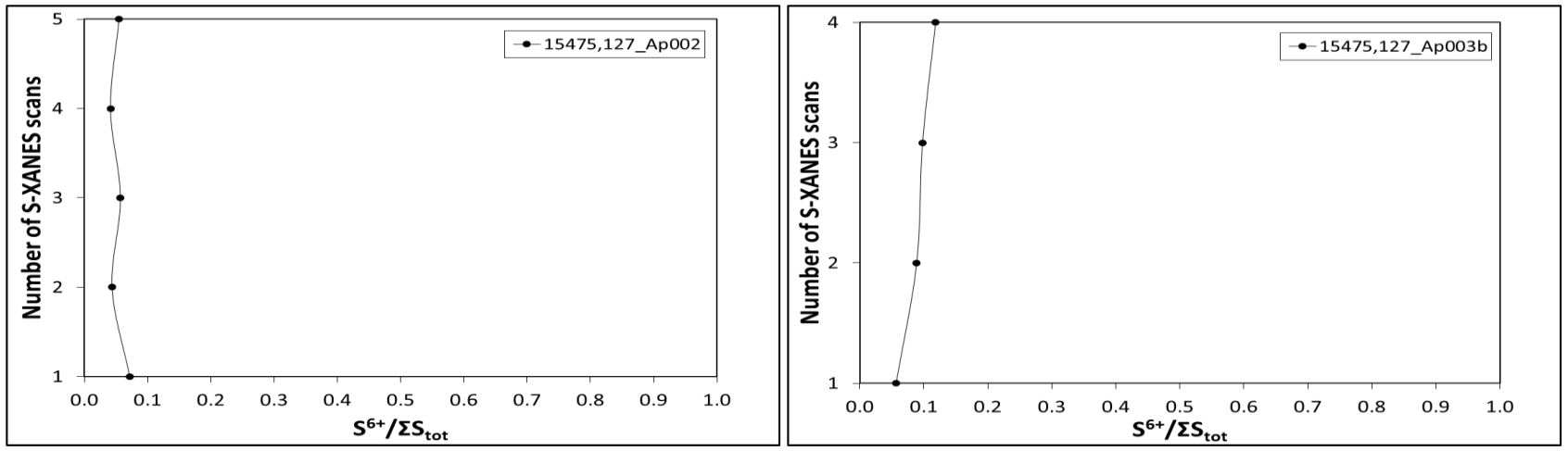

Figure 5.13. Individual S-XANES scans of Apollo sample 15475,127. The plots show the $S^{6+}/\Sigma S_{tot}$ ratio results of two different apatite grains that were acquired by profiling across the apatite grain. See text for details.

It was only possible to analyse two apatite grains in sample 12039 due to the very low S contents (<40 ppm S in the excluded grains). The S/N ratio was very low for analysed grain Ap001_a due to the low S content in the grain (47 ppm S) which means that only 4 of the scans are included in the final results (Figure 5.12). The $S^{6+}/\Sigma S_{tot}$ ratio for Ap001_a ranged from 0.18 to 0.29 with an average value for the grain of 0.23. Similarly, only 3 scans could be included for grain Ap001_f due to the low S contents (112 ppm S) and the resulting low S/N ratio of many of the excluded scans. The $S^{6+}/\Sigma S_{tot}$ values are higher than Ap001_a with a minimum and a maximum of 0.35 and 0.40, respectively, and an average of 0.39.

It was possible to analyse three apatites in sample 15475 but only a handful of the scan results can be reported due to the very low S contents in the apatites and, therefore, either the absence of S signal or a very low S/N ratio. Only the results of two of the apatites are shown in Figure 5.13 because just one measurement for the third apatite (Ap003a) could be fully processed (due to low S) which has a $S^{6+}/\Sigma S_{tot}$ value of 0.12 (Table 5.3). The minimum and maximum $S^{6+}/\Sigma S_{tot}$ values of grain Ap002 are 0.04 and 0.07, respectively, with an average of 0.05. Whereas, the minimum and maximum $S^{6+}/\Sigma S_{tot}$ values of grain Ap003b are 0.06 and 0.12, respectively, with an average of 0.09. With an average of 0.08 for ten measurements across all three apatite grains, sample 15475 has the lowest $S^{6+}/\Sigma S_{tot}$ ratios measured in this project.

Lunar meteorite, SaU 169 (impact melt breccia), used for proof of concept (Appendix A) in this project, was a hot desert 'find', discovered in Oman. The terrestrial weathering of the meteorite has been classified as W1 (Russell et al., 2003), meaning that it has undergone only very minor oxidation around metal rims with the possibility of minor oxide veins being present (Wlotzka, 1993). Whilst this suggests that terrestrial alteration of a crystalline material such as apatite is unlikely or insignificant, the S-XANES results (Table 5.3 and Appendix B Table B.5) show that it contains almost exclusively S^{6+} ($S^{6+}/\Sigma S_{tot}$ values of 0.85 to 1.0). By way of comparison, the Durango terrestrial apatite has a $S^{6+}/\Sigma S_{tot}$ average value of 0.95 (Table 5.3). This might imply that the S in the apatites was oxidized during the meteorite's time on Earth in the desert environment.

5.5. Reproducibility

In order to confirm the reproducibility of the S-XANES measurements (and the data reduction technique) performed in this study, repeated S-XANES measurements of the Durango apatite were performed during the January 2019 analytical session (Figure 5.14). The integrated $S^{6+}/\Sigma S_{tot}$ peak area ratio of Durango apatite has been previously reported by Konecke et al. (2017a) as 0.956 ± 0.002 (2 sigma (2σ)) based on an average of twenty S-XANES scans. The error attributed to $S^{6+}/\Sigma S_{tot}$ values in Figure 5.14 is the residual standard deviation (reported in the Fityk software) associated with each fitted spectrum. The precision of the measurements made by this study is ~0.02 (2σ), which was calculated by taking the standard deviation (2σ) of the average $S^{6+}/\Sigma S_{tot}$ ratios (n = 5) derived for the Durango apatite. Figure 5.14 shows that, within error, the measurements performed were also accurate based on the external value (0.956) reported by Konecke et al. (2017a).

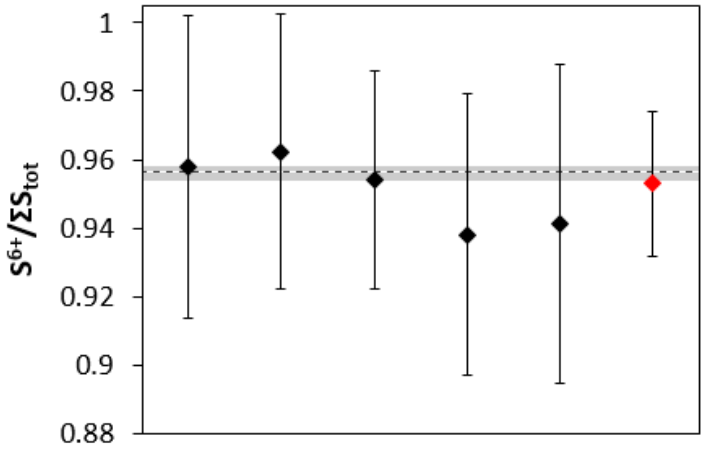

Figure 5.14. The precision and accuracy of S-XANES analyses. Five individual S-XANES data collection scans of Durango apatite are plotted as the integrated peak area ratios ($S^{6+}/\Sigma S_{tot}$) (black diamonds) from the January 2019 analytical session. The dashed line at 0.956 represents the average $S^{6+}/\Sigma S_{tot}$ (n = 20) of Durango apatite, derived independently by Konecke et al. (2017a), where the grey band denotes the reported 2σ uncertainty (0.002). The red diamond is the average of the measurements (n = 5) made in this study. The error bars associated with each of the measurement points represent the residual standard deviation (see text for details).

5.6. The sulfur oxidation state in lunar apatite

5.6.1. A comparison of S-XANES and S isotopes

Five Apollo samples that were analysed with S-XANES were also investigated with NanoSIMS (Chapter Four) to determine their S abundances and associated isotopic composition (Table 5.3). The combined S-XANES and S isotope results of these Apollo samples is shown in Figure 5.15. Lunar meteorite SaU 169 will not be considered further in this section because it was used as a proof of concept for S isotope and S-XANES analyses. Figure 5.15 shows a positive trend between $\delta^{34}S$ and $S^{6+}/\Sigma S_{tot}$ for all but one of the apatites for which both S-XANES and S isotope data exists for the exact same grain. The following pages in this section will discuss the relationship between the S-XANES and S isotope results.

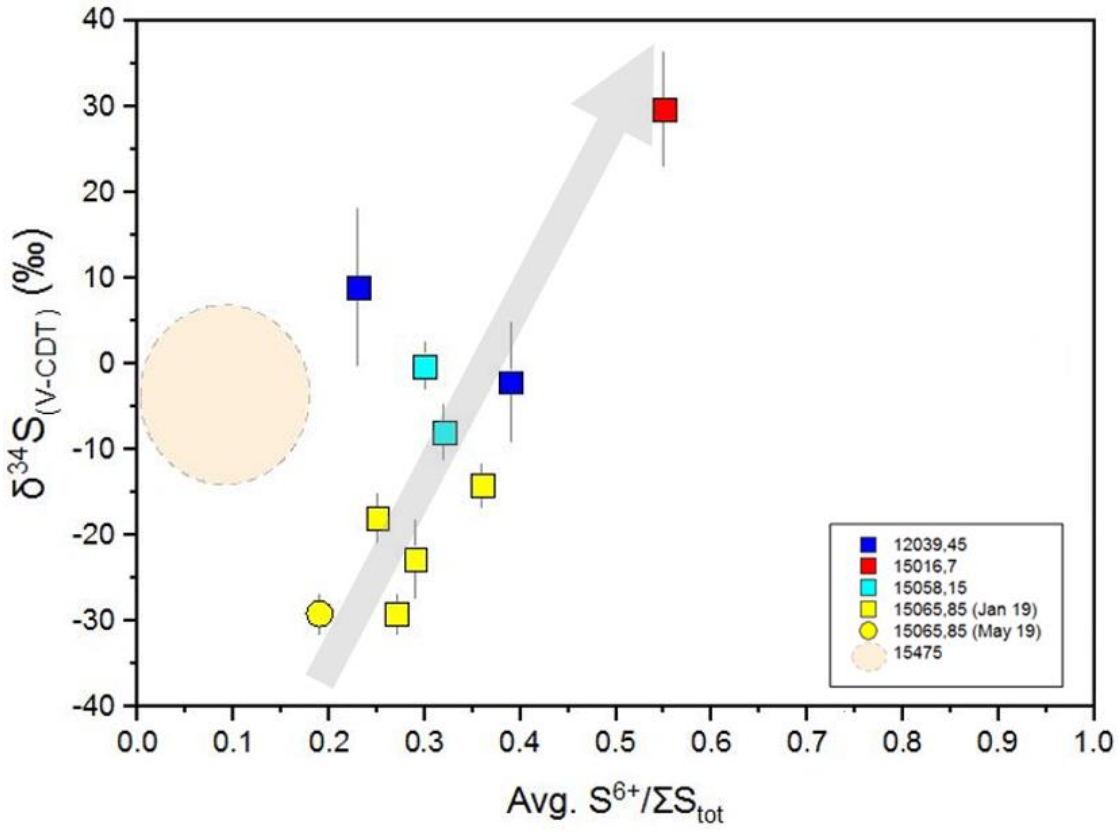

Figure 5.15. Plot of S isotopes ($\delta^{34}S_{(V\text{-}CDT)}$) against the average ratio of S^{6+} to total sulfur ($S^{6+}/\Sigma S_{tot}$) for lunar apatites. The individual data points represent the average value of the scans collected for each apatite within a specific sample (see key at bottom right). The S isotope error bars represent the standard deviation (2σ) of the measurements made (Chapter Four). The pale orange shaded region represents Apollo sample 15475 for which both S-XANES and S isotope data does not exist for the exact same apatite grains – see text for further details. The plot is based on the results in Table 5.3.

In Chapter Four, it was suggested that sample 15016, with the heaviest $\delta^{34}S$ values (+28.9 ± 8.3‰ to +36.4 ± 3.2‰) recorded for apatites in this project, may have acquired its potentially anomalous heavy $\delta^{34}S$ signature as a result of increased oxidation in the late-stage silicate melt (at ~96–99.5% crystallisation (e.g. Sha, 2000; Tartèse and Anand, 2013)). A more oxidised late-stage silicate melt would be dominated by S^{6+} relative to S^{2-}, with a corresponding melt composition of SO_4^{2-}. With an average $S^{6+}/\Sigma S_{tot}$ value of 0.55 (where >65% of the measurement scans have a $S^{6+}/\Sigma S_{tot}$ value of >0.5), the S-XANES data for grain Ap42 provide additional evidence for a more oxidized late-stage silicate magma from which apatites of 15016 crystallised. As discussed in Chapter Four, degassing of ^{32}S from the oxidized late-stage silicate melt (as SO_2 and possibly H_2S) would have contributed to driving the $\delta^{34}S$ signature to a more positive value with ^{34}S preferentially retained by a more oxidized melt due to the most oxidized form of S bonding more strongly with ^{34}S.

At the other extreme, apatites in sample 15065 have the lightest $\delta^{34}S$ values recorded in this project (-33.3 ± 3.8‰ to -14.1 ± 2.6‰). The light S isotope values are consistent with loss of ^{34}S from a reduced (S^{2-}) silicate melt (Chapter Four) which means that, compared with 15016, apatites within sample 15065 should contain S with a lower oxidation state. The average $S^{6+}/\Sigma S_{tot}$ values for the four apatites (0.19 to 0.36) does provide evidence for a melt richer in S^{2-} relative to S^{6+} and confirms that the melt was more reduced than that from which 15016 formed. With the least negative $\delta^{34}S$ value (-14.1 ± 2.6‰) of the four apatite grains analysed in 15065, it was suggested (Chapter Four) that grain Ap003 might have either crystallised from an isolated late-stage melt pocket or interacted slightly less with a late-stage ^{32}S-rich vapour when compared with the other three earlier crystallising apatites (those enclosed in pyroxene grains). The S-XANES results for Ap003 reveal that the S in the grain is less reduced than the other three apatites, with an average $S^{6+}/\Sigma S_{tot}$ value of 0.36 (average values are 0.19 to 0.29 for the other three grains) (Figure 5.15).

The average $S^{6+}/\Sigma S_{tot}$ difference of 0.08 (0.27 – 0.19) between the measurements made in January 2019 and May 2019 for grain Ap007 can be explained by only a limited number of scans (four) being able to be reported (due to low S signals reaching the detector) and averaged from the May results. The results of the individual scans for Ap007 from May

(with $S^{6+}/\Sigma S_{tot}$ values of 0.17 to 0.22) are otherwise within the boundary of results of the individual scans performed in January (with $S^{6+}/\Sigma S_{tot}$ values of 0.09 to 0.35).

Sample 15058 has both light and heavy $\delta^{34}S$ values from -10.5 ± 5.9‰ to +6.5 ± 5.2‰ across six apatite grains, leading to the suggestion that apatites might have crystallised from a late-stage silicate melt that may have evolved from being more reduced to more oxidized (Chapter Four). S-XANES data for only two of the six apatite grains are reported here (section 5.4.) and both of those have negative S isotope values which means that it is expected that the S should be relatively reduced for these grains. With $\delta^{34}S$ values of -0.2 ± 2.7‰ and -7.9 ± 3.2‰ for grain Ap016 and Ap012a, respectively, both apatites contain more S^{2-} relative to S^{6+} based on an average $S^{6+}/\Sigma S_{tot}$ values of 0.30 and 0.32, respectively. Both apatites therefore, crystallised from a S^{2-}-rich magma, which agrees with the negative S isotope interpretations of Chapter Four.

The $\delta^{34}S$ values reported for five apatites in sample 12039 in Chapter Four are between -1.2 ± 7.0‰ and +9.0 ± 9.2‰ and it was concluded that, due to the high levels of statistical uncertainty related to the NanoSIMS measurements, it was not possible to confidently determine which S species (S^{2-} or SO_4^{2-}) existed within the late-stage silicate melt at the time of apatite crystallisation. However, based on previous hydrogen isotope analyses (Tartèse et al., 2013) which showed that degassing of H_2S might have been limited (degassing of H_2 was slightly more dominant), it was suggested that apatites in 12039 may be un-degassed with respect to S and represent the reduced bulk Moon signature. The two apatites analysed with S-XANES do have a higher proportion of reduced S (average $S^{6+}/\Sigma S_{tot}$ of 0.23 and 0.39), suggesting that the dominant S content in the late-stage silicate magma was S^{2-}. Grain Ap001_a, with the most reduced S (average $S^{6+}/\Sigma S_{tot}$ 0.23) also has the highest statistical uncertainty associated with the S isotope measurement (+9.0 ± 9.2‰). Given that the $\delta^{34}S$ value cannot be reported with absolute confidence, it is not unexpected that the apatite plots to the top left of the trend line in Figure 5.15.

S-XANES spectroscopy of a different thin section of sample 12039 was performed by Brounce et al. (2019) and, using a linear combination fitting (LCF) method, was reported to have $S^{6+}/\Sigma S_{tot}$ values of between 0 and 0.45 across six lunar apatite grains. It was suggested that analyses that resulted in a $S^{6+}/\Sigma S_{tot}$ value of >0.03 were due to the presence of fractures and/ or pits within the apatite grain. There was a possibility, therefore, that

measurements in these regions may not represent the primary S of the apatite but a secondary alteration that caused an oxidation from sulfide to sulfate (Brounce et al., 2019). However, the present study shows that only one of the eight measurements made in apatite of 12039 had a $S^{6+}/\Sigma S_{tot}$ value of <0.03, with the other seven grains having $S^{6+}/\Sigma S_{tot}$ values between 0.18 and 0.42 (Appendix B Table B.5). A cathodoluminescence image is shown in Figure 5.16 of the two apatites analysed in this study which highlights that there is only one prominent crack in Ap001_f that was easily avoidable with use of the acquired XRF element maps. The three individual X-SANES scans of Ap001_f (with S contents of 112 ppm) had $S^{6+}/\Sigma S_{tot}$ values of >0.35.

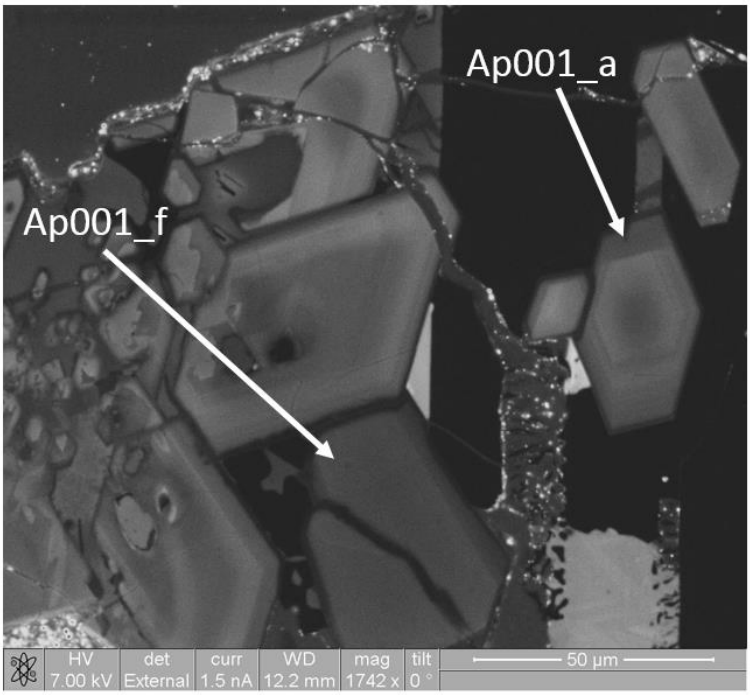

Figure 5.16. Apatite grains analysed in sample 12039,45. The cathodoluminescence (CL) image shows the two grains analysed with S-XANES (Ap001_a and Ap001_f). No cracks can be seen in the concentrically zoned apatite Ap001_a. In Ap001_f, a prominent crack can be seen cutting diagonally from top left to bottom right but no other cracks are visible.

The thin section sample 15475,127 was different from that used in the NanoSIMS work (15475,17) and, therefore, without the S isotope measurements for the exact apatite grains, the S-XANES relative to the S isotope results can only be plotted as a shaded (pale orange) region in Figure 5.15. The $\delta^{34}S$ values of six apatites in 15475 cover a relatively wide range from -8.8 ± 2.5‰ to 2.6 ± 2.5‰, with only one apatite having a positive value (Chapter Four). It is expected, therefore, that the $S^{6+}/\Sigma S_{tot}$ values for 15475 should be

relatively low, with S^{2-} being dominant and this is what is found for the three apatites analysed with S-XANES.

5.6.2. A comparison of S-XANES and S abundance

Terrestrial apatite experiments (Parat et al., 2011) have shown that high S abundances are positively correlated with high oxygen fugacity (fO_2), and that the traditional S substitution reactions related to apatite ($S^{6+} + Si^{4+} \leftrightarrow 2P^{5+}$ and $S^{6+} + Na^{+} \leftrightarrow P^{5+} + Ca^{2+}$) (Peng et al., 1997) at the tetrahedral (*T*) cation site (Hughes and Rakovan, 2015) (Chapter One) occur under more oxidising conditions where SO_3 contents are relatively high (Peng et al., 1997). However, with the exception of 15016, a correlation between S abundance and S oxidation state ($S^{6+}/\Sigma S_{tot}$) was not observed for the apatites studied with S-XANES in this project. For example, the apatites of samples 15016 and 15065 both contain high levels of S (Table 5.3) and yet 15016 has an average $S^{6+}/\Sigma S_{tot}$ value of 0.55, whereas 15065 has average $S^{6+}/\Sigma S_{tot}$ values of 0.25 to 0.36.

For lunar apatite within Apollo samples, it was speculated that there might be an alternative mechanism operating, whereby the *X*-site (the anion column) of apatite is capable of holding S, probably as S^{2-} (Boyce et al., 2010), but this has so far only been seen in synthesized experimental charges and not in nature (Henning et al., 2000; Kim et al., 2017). When recent S-XANES analyses on a natural terrestrial apatite and an experimentally crystallised apatite were compared with their corresponding electron backscatter diffraction (EBSD) patterns (Konecke et al., 2017a), the S oxidation state as a function of crystallographic orientation was found to vary. It was concluded that this might be evidence for the simultaneous incorporation of S^{6+} and S^{2-} at different crystallographic sites within the apatite (*T*-site and *X*-site, respectively). Thermodynamic modelling has also shown that S^{2-} might be stable in the *X*-site, with a prediction that S^{2-} resides closest to Cl^{-} in natural apatite (Kim et al., 2017). For the incorporation of S^{2-}, the coupled substitution of two anions within the *X*-site of the apatite structure was proposed: $2(F,Cl,OH)^{-} \leftrightarrow S^{2-}$ (Kim et al., 2017).

An explanation for the high S abundances, the lack of positive correlation with fO_2 and the dominance of S^{2-} (with the exception of sample 15016) for lunar apatites studied in this project, might be that S is situated within both the crystallographic *T*- and *X*-sites of

apatite. Sample 15016 has high S contents and a higher S oxidation state which might suggest that S is predominantly situated within the *T*-site.

5.6.3. S in apatite as an oxybarometer

In terrestrial apatite, S exists in multiple oxidation states (S^{6+}, S^{4+} and S^{2-}) (Konecke et al., 2017a). The current study has shown that S^{4+} is not present in the particular Apollo samples investigated, but that both S^{6+} and S^{2-} can exist simultaneously in late-stage lunar silicate melts. A relatively oxidized magma containing S^{6+} is something not expected in the reducing lunar environment. It has very recently been suggested by Konecke et al. (2019) that S^{6+} could be present at very low levels (currently undetectable) in a reduced (≤FMQ redox buffer) silicate melt. Apatite will preferentially incorporate the more oxidized S^{6+} relative to S^{2-} into its crystallographic structure (the *T*-site) (Peng et al., 1997; Parat et al., 2011, Konecke et al., 2019) which means that even if S^{6+} is not abundant enough to be measured in a reduced silicate melt, it can be preferentially sequestered and, therefore, more easily detected in apatite (Konecke et al., 2019).

The results of this chapter have demonstrated that S-XANES analysis is capable of providing a way of determining the S oxidation state of lunar apatite. All of the apatite S-XANES results reported in this study have $S^{6+}/\Sigma S_{tot}$ ratios of >0 which means that the oxidation state of S in lunar apatite can provide an indication of the oxygen fugacity (fO_2) of a late-stage silicate melt and can, therefore, act as an oxybarometer (e.g. Konecke et al., 2017a, 2019). The $S^{6+}/\Sigma S_{tot}$ value can also provide insight into the evolution of the fO_2 of the silicate melt. For example, the inter-grain $S^{6+}/\Sigma S_{tot}$ ratio was seen to increase as apatite crystallisation progressed in sample 15065 (0.27 to 0.29 for apatites enclosed within pyroxene and 0.36 for an apatite in the mesostasis region, respectively) which indicates that the fO_2 of the silicate melt also increased with crystallisation. Likewise, the intra-grain $S^{6+}/\Sigma S_{tot}$ variations seen across all of the apatites (Figures 5.8 to 5.13 (excluding 5.11)) analysed with S-XANES are likely to reflect slight changes in the S oxidation state of the late-stage silicate melt during apatite crystal growth. This is particularly noticeable in apatite Ap001b of sample 15065 where a decrease of $S^{6+}/\Sigma S_{tot}$ (and, therefore, an increase of S^{2-}) across the apatite grain suggests that the late-stage silicate melt became more reduced as the apatite crystallised.

The results of Chapter Four suggest that the majority of apatites crystallised after the main phase of S degassing, therefore, the estimated fO_2 of the silicate melt would represent the time at which apatites crystallised, rather than the fO_2 of the silicate melt prior to degassing. This finding agrees with Konecke et al. (2017a) and Kim et al. (2017) who both confirmed that the oxidation state of S in apatite records the fO_2 of the silicate melt at the time of apatite crystallisation, assuming that the apatite has not been subsequently altered.

5.7. Future work

As a S oxidation measurement technique, S-XANES is advantageous in that very little sample preparation is required and, once the optimal measurement settings have been applied, the XRF mapping and S-XANES scanning process is relatively straightforward. The main challenges surrounding the measurement of S oxidation state in lunar apatite are related to the low S contents contained within the apatites and the relatively small size of the apatite grains (most <~30 μm). The two issues did not always go together. For example, smaller apatites often contained S content that was comfortably above the S-XANES limit of detection, whereas larger apatites (>~50 μm) tended to have S content below the limit of detection. Whilst the former had S that was above the limit of detection, problems arose if small apatites were adjacent to large troilite (FeS) grains which might have affected the measurement of the apatite. The latter issue (large apatite grains) meant that the S being measured could confidently be assigned to apatite but the S signal was too weak to provide reliable results.

As a result of the small sample sizes, beam-induced oxidation was a risk throughout the S-XANES analyses because, for small apatites, a smaller, more intense beam was necessary in order to avoid adjacent (non-apatite) grains. The second session (May 2019) at Diamond Light Source sought to reduce this risk by analysing larger apatites with a less focussed beam alongside a dampened beam intensity/ flux (through use of vanadium foils).

The findings of this chapter are based on apatites in five mare basalt samples that represent two Apollo landing sites. It is important that further suitable apatite samples that both contain high S contents and are ~>50 μm in size are identified in order to confirm whether this trend is typical of wider lunar magmatism. This will require further sample

characterisations and S analyses (using scanning electron microscopy and NanoSIMS), along with gaining regular access to a synchrotron facility to carry S-XANES.

However, the results from the S-XANES analyses reported in this chapter are promising. All of the analysed apatites contain a mixture of both S^{6+} and S^{2-} with the dominance of each oxidation state of S varying between apatite grains. There appears to be a positive trend between $S^{6+}/\Sigma S_{tot}$ and $\delta^{34}S$ for lunar apatite. Bringing these two data sets together for lunar apatite has not previously been undertaken and it provides new insight into the behaviour of S in the late-stage lunar silicate magma.

Chapter Six:

Conclusions and future work

6.1. Summary of work

The aim of this research project was to develop an understanding of the behaviour of S in the late-stage lunar silicate melt. To achieve this, Nano-scale secondary ion mass spectrometry (NanoSIMS) was used to measure the abundances and isotopic compositions of S and Cl in lunar apatite. Performed here for the first time, the simultaneous measurement of both S and Cl was possible for apatites in twelve Apollo samples (ten mare basalts, one KREEP basalt and a feldspathic granulitic impactite) and a lunar meteorite. This is the first study to report S isotopic composition of apatites from mare basalts and a KREEP basalt. The Cl abundance and isotope results from measurements of apatites in two further mare basalts are also reported, with the results for a total of five mare basalts presented in this study that have not previously been reported in the scientific literature. The samples analysed with NanoSIMS represent five different Apollo landing sites (11, 12, 14, 15 and 17). Sulfur X-ray absorption near-edge structure (S-XANES) spectroscopy was used to measure the oxidation state of S in lunar apatite. The analyses involved five mare basalts (representing two Apollo landing sites: 12 and 15), with the results of apatites in four of the mare basalts reported for the first time.

6.2. Main findings and interpretations

6.2.1. Sulfur and chlorine in lunar apatite

For the five previously unreported mare basalt samples analysed with NanoSIMS, it was shown that δ^{37}Cl and Cl abundances of apatite are considerably heterogeneous. The Cl abundance varies by an order of magnitude from ~400 ppm to ~4,320 ppm, whilst the δ^{37}Cl ranges from +9.6 ± 1.4‰ to 36.5 ± 1.1‰ (2σ) in the apatites across the five samples. The inter-sample heterogeneity in Cl isotopic composition in lunar apatite might be reflecting the effects of magma degassing (preferential loss of ^{35}Cl) during mare volcanism (e.g. Barnes et al., 2016) and/ or interactions between mare magmas, derived from isotopically light and Cl-poor mantle source regions, with differing quantities of the Cl-rich and isotopically heavy urKREEP/ KREEP component (e.g. Boyce et al, 2018; Barnes et al., 2019). The observed intra-sample variations in isotopic compositions might have been caused by a combination of relatively local events such as late-stage magma degassing and/ or variable interactions with a Cl-rich metasomatic agent, such as a vapour

phase (e.g. Treiman et al., 2014; Potts et al., 2018). Crystallisation of apatites potentially occurred both before and after vapour phase interactions resulting in heterogeneous $\delta^{37}Cl$ values and Cl abundances (e.g. Potts et al., 2018).

From the simultaneous measurement of S and Cl abundances and isotopes on the same spot in apatites of twelve Apollo samples, this study has demonstrated that, for apatites containing relatively high S abundances (>~450 ppm), degassing of S and Cl is unlikely to have been the only process operating in the late-stage silicate melt. Evidence for this comes from a comparison of the abundances of S and Cl, which display a negative trend, whereby S increases as Cl decreases and vice-versa. It is possible to explain the trend by a separate oscillatory process involving the loss of S and Cl from the melt by degassing on the one hand and, on the other, an increase of the S and Cl concentrations (both incompatible elements) in the melt as crystallisation of the melt progressed. What is not clear is which of these two processes (loss through degassing or an increase through crystallisation) was dominant and what the impact/ extent of each process was on each element. For relatively low S abundances (<~450 ppm) in apatite, a positive trend between S and Cl abundance suggests that simultaneous degassing of S and Cl from the late-stage silicate melt might have occurred, with the rate of degassing marginally greater for Cl. The lack of any statistically significant correlation between $\delta^{34}S$ and $\delta^{37}Cl$, however, demonstrates the decoupling of S and Cl during the evolution of the lunar interior because the trend of increasing $\delta^{37}Cl$ from mare basalts to KREEP basalts to highlands rocks that tells a story of the evolution of Cl in the lunar interior, is not shown by the $\delta^{34}S$ dataset.

6.2.2. Sulfur in lunar apatite

From the S analyses performed with NanoSIMS for twelve Apollo samples, a minimum and maximum content of ~20 ppm and ~2,800 ppm, respectively, highlights the heterogeneous distribution of S within lunar apatites, with two orders of magnitude difference between the lowest and the highest S abundance. The heterogeneity is also present within the same samples with, for example values of ~180 ppm S and ~2,760 S ppm recorded in the apatites of sample 15016. Heterogeneity also exists for the S isotope values of apatite, where a range of ~70‰ separates the minimum and maximum S isotope values of -33.3 ± 3.8‰ and +36.4 ± 3.2‰ (2σ), respectively. There is a lack of inter-sample systematic positive or negative correlation between S abundances and S isotope

values of apatite but there are three notable groupings in terms of S isotopic compositions, one with heavy $\delta^{34}S$ values, one with light $\delta^{34}S$ values and one that includes $\delta^{34}S$ values that straddle ~0‰ and cover a region of ~+10‰ to ~-10‰. There is, however, intra-sample positive or negative correlation between the S content and $\delta^{34}S$ for the majority of apatites.

The $\delta^{34}S$ values of lunar apatites analysed in this project have a far greater spread when compared with previously reported mare basalt bulk-rock values of between –5.2‰ and +1.44‰ (e.g. Thode and Rees, 1971, 1972; Rees and Thode, 1972, 1974; Petrowski et al., 1974; Gibson et al., 1975; Kaplan et al., 1976; Wing and Farquhar, 2015). Some of the previous bulk-rock S isotope measurements are of mare basalts for which the apatites were analysed in this project. On comparison, the differences between the bulk-rock and apatite $\delta^{34}S$ still existed. Given that the primary S-bearing mineral phase in mare basalts is troilite (FeS) which exists, in varying abundances, in every Apollo sample analysed in this project, it is possible that the more restricted $\delta^{34}S$ bulk-rock value predominantly reflects the $\delta^{34}S$ value of troilite, which masks the S contribution from the apatite. Troilite crystallised from the sulfide melt, which experienced limited S isotope fractionation during H_2S degassing (Marini et al., 2011), unlike the late-stage silicate melt from which apatite crystallised.

The bulk Moon is reported to have a $\delta^{34}S$ value of +0.58 ± 0.05‰ (Wing and Farquhar, 2015) and, for the current study, it is assumed that the initial $\delta^{34}S$ value of the silicate melt crystallising apatite is also ~0.58‰. To explain the deviations from this $\delta^{34}S$ value, and the three distinct S isotope groups that are seen in apatite, a process of S degassing from the late-stage silicate melt, with or without variable interaction between vapour phases and the melt, is likely to have been responsible. For samples with apatites that show, within statistical uncertainty, little to no deviation from the bulk Moon $\delta^{34}S$ value, it is likely that late-stage S degassing would have been very limited.

This study has demonstrated a link between S and H_2O degassing where, for example, hydrogen data exists in the scientific literature (Tartèse et al., 2013; Barnes et al., 2019) for apatites in the same samples studied in this project. Where the $\delta^{34}S$ values suggest very little degassing of H_2S (e.g. ~0‰) or a greater extent of H_2S degassing from the late-stage silicate melt (e.g. ~+30‰) (this study), the hydrogen data suggests that H_2 was the dominant degassing species or H_2S was the dominant degassing species, respectively.

Sulfur degassing is postulated because of the intra-sample correlations between $\delta^{34}S$ and S abundance in apatite. The direction of the correlations (positive or negative) is dependent upon the S species within the late-stage silicate melt. Where S^{2-} was the dominant species in the silicate melt, ^{34}S was degassed in the form of either $H_2{}^{34}S$ or $^{34}SO_2$ which, through isotopic fractionation, left the residual silicate melt enriched in ^{32}S and thus exhibiting a negative $\delta^{34}S$ value. The extent of S isotope fractionation in the residual late-stage silicate melt is greatest when $^{34}SO_2$ is degassed. If SO_4^{2-} was the dominant S species in the silicate melt, ^{34}S would have been preferentially retained due to the strong covalent bond between the more oxidized S species and the ^{34}S isotope. Consequently, degassing resulted in the loss of ^{32}S from the melt as either $H_2{}^{32}S$ or $^{32}SO_2$, which led to the fractionation of S isotopes and a residual melt enriched in ^{34}S with a positive $\delta^{34}S$ value (Figure 6.1). Contrary to a silicate melt dominated by S^{2-}, degassing of $H_2{}^{32}S$ from a silicate melt dominated by SO_4^{2-} results in a larger S isotopic fractionation than when $^{32}SO_2$ degasses. For the late-stage silicate melts that experienced S degassing and, therefore, underwent S isotope fractionation, crystallisation of apatites occurred *after* the main S degassing phase in order to preserve the $\delta^{34}S$ signature in apatite.

The S species in the late-stage silicate melt and, therefore, the S species that was degassed was dictated by the S oxidation state of the melt. A melt dominated by S^{2-} contains the reduced form of S, whereas a melt dominated by SO_4^{2-} contains the oxidized form of sulfur, S^{6+}. The three distinct S isotope groups can, therefore, be partially explained by variable levels of S degassing from reduced, oxidized or a combination of both reduced and oxidized late-stage silicate melts. For mare basalt sample 15065 which contains apatites with anomalously light $\delta^{34}S$ values (-33.3 ± 3.8‰ to -14.1 ± 2.6‰), in addition to ^{34}S degassing, the silicate melt (from which apatites crystallised) appears to have interacted with a late-stage ^{32}S-rich vapour phase that originated from a separate, nearby degassing magmatic source (possibly at depth) (Figure 6.1). The timing of interaction would have been prior to the main phase of ^{34}S degassing from the late-stage silicate melt, thereby the pre-degassed melt would have had an initially light $\delta^{34}S$ signature.

At the other extreme is sample 15016 which contains apatites with anomalously heavy $\delta^{34}S$ values (+28.9 ± 8.3‰ to +36.4 ± 3.2‰). Degassing of ^{32}S from the late-stage silicate melt drove the isotopic fractionation of S but, additionally, interaction with an oxidizing vapour

phase that originated from a degassing magmatic source region (e.g. Joy et al., 2015), enriched the silicate melt from which apatites formed with ^{34}S (Figure 6.1). The interaction would have occurred prior to the main phase of ^{32}S degassing from the late-stage silicate melt.

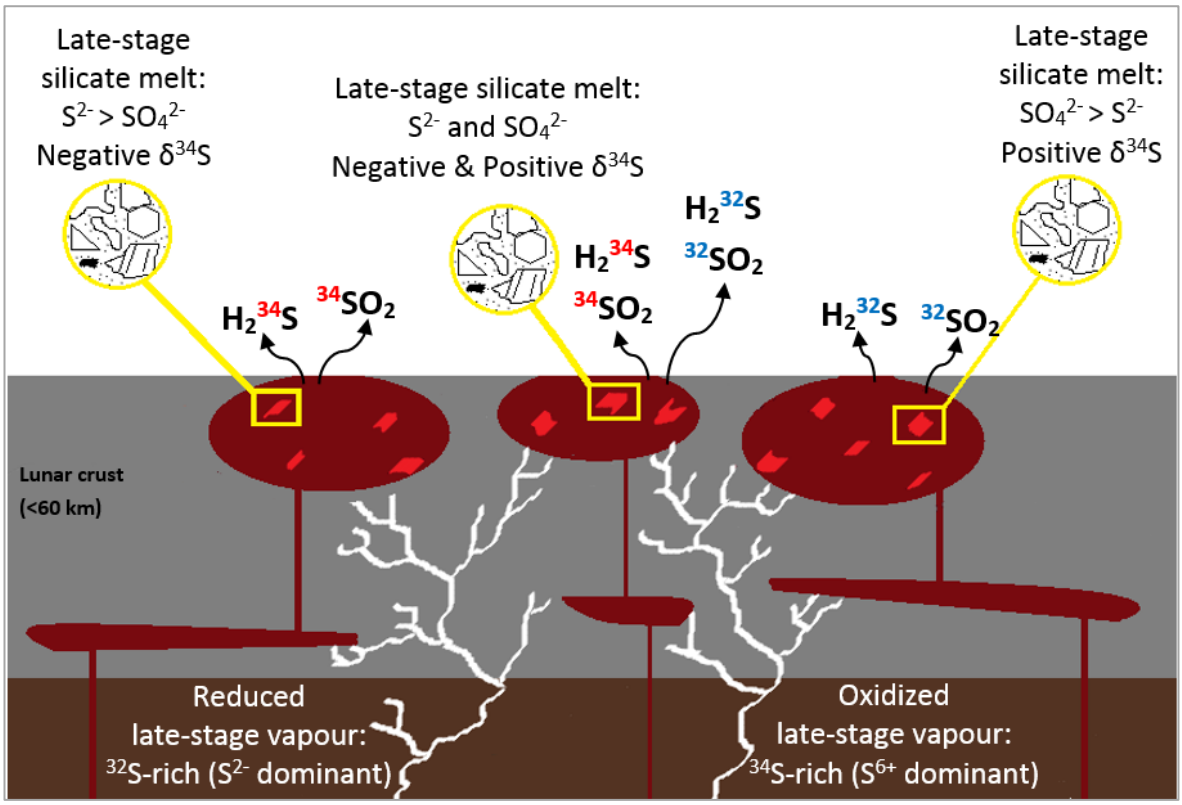

Figure 6.1. The late-stage silicate melt prior to apatite crystallisation. The schematic shows three different scenarios that are explained in the main text. The first is a reduced ($S^{2-} > SO_4^{2-}$) late-stage silicate melt (left side of figure) that has interacted with a reduced (^{32}S-rich) late-stage vapour phase (white veins on the left-hand-side) and is degassing ^{34}S (as H_2S and SO_2) to leave the residual melt ^{32}S-rich (e.g. as seen for sample 15065). The right side of the figure shows an oxidized late-stage melt ($SO_4^{2-} > S^{2-}$) that has interacted with a late-stage oxidized (^{34}S-rich) vapour phase (white veins on the right-hand-side) and is degassing ^{32}S (as H_2S and SO_2) to leave the residual melt ^{34}S-rich (e.g. as seen for sample 15016). Samples that contain apatites with both negative and positive $\delta^{34}S$ (e.g. 15058) would have crystallised from the late-stage silicate melt shown at the centre of the figure, which has a mixed silicate melt containing varying quantities of S^{2-} and SO_4^{2-}, following interaction with reduced and oxidized late-stage vapour-phases. For this last scenario, both ^{32}S and ^{34}S are degassed as H_2S and SO_2.

Oxidized melts are not expected because mare basalts and, therefore, the apatites crystallised within the rocks, are believed to have formed under reducing conditions in a low oxygen fugacity environment (IW-1 (e.g. Sato et al., 1973; Longhi, 1992; Wadhwa, 2008). The reduced form of sulfur, S^{2-}, is expected to be the only oxidation state of sulfur

to exist under such conditions (e.g. Fincham and Richardson, 1954; Carroll and Rutherford, 1985; Wallace and Carmichael, 1992; Wilke et al., 2008). However, the S-XANES results in this study have shown that the more oxidized state of S (S^{6+}) is present in every lunar apatite analysed, with the S-XANES spectra for all of the apatites in five different mare basalts having $S^{6+}/\Sigma S_{tot}$ ratios of >0. The average $S^{6+}/\Sigma S_{tot}$ ratio of the analysed apatites varies from 0.05 to 0.55 which reflected the oxidation state of the silicate melt at the time of apatite crystallisation (e.g. Konecke et al., 2017a; Kim et al., 2017). The current study has not detected S^{4+} (sulfite) in the particular Apollo samples investigated.

The S-XANES analyses has complemented the NanoSIMS work by providing further evidence of which S species resided in the late-stage silicate melt from which apatite crystallised. Of the five mare basalts studied with S-XANES, four of them contain apatites with exclusively negative $\delta^{34}S$ values and are, therefore, expected to have formed from a reduced silicate melt that was dominated by S^{2-}. With average $S^{6+}/\Sigma S_{tot}$ values of between 0.05 and 0.39, the S-XANES results confirm that S^{2-} was the dominant oxidation state of sulfur at the time of apatite crystallisation. Sample 15016 was the only mare basalt analysed with S-XANES to contain apatites with positive $\delta^{34}S$ values, whereby the melt from which the apatites formed was expected to have been oxidized and dominated by S^{6+}. The individual S-XANES spectra for the apatites of 15016 had $S^{6+}/\Sigma S_{tot}$ values that ranged from 0.31 up to 0.79, with ~ ⅔ of the measurements having a $S^{6+}/\Sigma S_{tot}$ value of >0.5. The S-XANES results, therefore, provide additional corroborative evidence for the late-stage oxidation of the silicate melt from which the apatites of this sample crystallised.

Overall, a positive trend between sulfur isotopes and the oxidation state of sulfur in lunar apatite ($\delta^{34}S$ and $S^{6+}/\Sigma S_{tot}$) has been highlighted by this research. With the exception of 15016, a correlation between S abundance and S oxidation state of lunar apatite was not observed for the apatites studied with S-XANES. This might be due to the suggested simultaneous incorporation of S^{6+} and S^{2-} at different crystallographic sites within apatite, where the oxidized S^{6+} resides in the *T*-site (via possible substitution reactions of $S^{6+} + Si^{4+} \leftrightarrow 2P^{5+}$ and $S^{6+} + Na^{+} \leftrightarrow P^{5+} + Ca^{2+}$) and the reduced S^{2-} is situated in the *X*-site (the anion column – with a possible substitution reaction of $2(F,Cl,OH)^{-} \leftrightarrow S^{2-}$) (Boyce et al., 2010; Kim et al., 2017). With high S contents and the dominance of S^{6+}, the S content of apatites in sample 15016 might predominantly be situated within the *T*-site.

Apatite is sensitive to S oxidation state changes in the melt and will preferentially incorporate S^{6+}, if it is present in the late-stage silicate melt, into its crystallographic structure (*T*-site) (Peng et al., 1997; Parat et al., 2011, Konecke et al., 2019). This means that very low quantities of S^{6+} present in a reduced silicate melt that are currently undetectable in the melt, can be detected in apatite (Konecke et al., 2019). Accordingly, S in lunar apatite could be used to gauge the oxygen fugacity (fO_2) of the late-stage silicate melt from which it crystallised and, therefore, act as an oxybarometer (e.g. Konecke et al., 2017a, 2019).

When used in conjunction, this study highlights the remarkable potential of combining NanoSIMS and S-XANES datasets to understand the late-stage behaviour of S within lunar magmas. By combining the S and Cl abundance and isotope data with the S oxidation state data of lunar apatite, four significant questions can be addressed:

1. Does any evolutionary relationship exist between S and urKREEP
2. What was the nature of the S species in the late-stage silicate melt
3. What was the nature of the degassing S species and
4. What was the oxidation state of S in the late-stage silicate melt at the time of apatite crystallisation

This information will contribute to improving our understanding of the evolution of volatiles in the lunar interior.

6.3. Future work

The combined NanoSIMS and S-XANES work presented in this research project is the first of its kind. The S and Cl abundance and isotope results are, however, restricted to lunar apatites contained within Apollo samples that were returned from four Apollo landing sites. Whereas, the S-XANES results represent just two different Apollo landing sites. For the latter, it is important that further suitable samples collected from additional Apollo landing sites are identified for measurement with S-XANES. In particular, where suitable samples have already been analysed with NanoSIMS in this project, more beamline time needs to be secured at a synchrotron facility in order to acquire the corresponding S-XANES data to further test the findings and interpretations of this research project.

At the time of writing, two types of lunar samples are available for analysis. Those that were returned from the lunar missions (Apollo and Luna) and those that have been found on Earth: lunar meteorites. Relative to the total surface of the Moon (~3.8 x 10^7 km^2 (NASA, 2020)), the Apollo and Luna missions sampled only a very small area of the Moon's surface. As a result, and from the point of view of the current project, the samples that are available for analysis also represent just a small part of the Moon and may not tell the full lunar magmatic story. Whilst lunar meteorites might offer a more diverse sampling area of the Moon, the lunar meteorite used in this project as a proof of concept was suspected to have been oxidized whilst on the Earth's surface (based on the S-XANES results). For S-XANES work, pristine, unaltered (i.e. not oxidized by a non-lunar secondary process) samples are essential.

In November 2019, NASA's Lunar Sample Laboratory Facility scientists opened, for the first time since its return from the Apollo 17 mission, a two-foot long drive tube containing lunar rocks and soil (NASA, 2019). Whilst still only representing one small region of the Moon, the contents is yet to be analysed which presents new opportunities to further understand the evolution of the lunar interior. The ideal scenario would be for new sample return missions to collect and bring back to Earth additional rock samples from different locations on the Moon. Missions have been designed for this very purpose (e.g. 'Chang'e-5' and 'Chang'e-6' sample return missions - Chinese National Space Administration (CNSA)) but, from the perspective of wanting to discover and learn more about how the Moon formed and the interior evolved, it is important not to just focus on areas thought to be rich in lunar volatiles, such as the South Pole Aitken (SPA) basin. To further the research of the present study, many more missions to the lunar maria are necessary (e.g. Chang'e-5).

The work carried out in this study would benefit from further hydrogen (abundance and isotopes) analyses to fully complement the samples which now have S isotope and abundance data. Four of the basalt samples studied in this project (12031, 15085, 15475 and 15556) do not have associated hydrogen data reported for the apatites contained within them. For the remaining six basalts that do have available hydrogen data, being able to compare the hydrogen degassing history of the late-stage silicate melt with the S isotope and abundance results reported in this project provided additional evidence for the type of S species degassing from the late-stage silicate melt.

In situ S isotope studies of troilite (FeS) in lunar basalts are currently very limited (e.g. Shearer et al., 2012) and, at the time of writing, there are no published S isotope studies of melt inclusions (MIs) in lunar basalts. It is suggested in this project that mare basalt bulk-rock $\delta^{34}S$ values predominantly represent the troilite phase within the rock. To test this theory further, S isotope measurements of apatite, troilite and MIs of mare basalt rocks for which the bulk-rock $\delta^{34}S$ value already exists would provide a complete insight into the behaviour of S within mare basalts, where MIs represent the pre-eruptive, relatively un-degassed portion of the melt's history. Once a comprehensive dataset has been acquired, S analyses could be expanded to included non-mare lithologies through the study of S-bearing phases (apatite, troilite and MIs) in lunar highlands samples.

References

Akram, W. and Schönbächler, M. (2016) 'Zirconium isotope constraints on the composition of Theia and current Moon-forming theories', *Earth and Planetary Science Letters*, vol. 449, pp. 302-310.

Albarède, F. (2009) 'Volatile accretion history of the terrestrial planets and dynamic implications', *Nature*, vol. 461, no. 7268, pp. 1227-1233.

Albarède, F., Ballhaus, C., Blichert-Toft, J., Lee, C.-T., Marty, B., Moynier, F., Yin, Q.-Z. (2013) 'Asteroidal impacts and the origin of terrestrial and lunar volatiles', *Icarus*, vol. 222, no. 1, pp. 44-52.

Albarède, F., Albalat, E., Lee, C.-T. A. (2015) 'An intrinsic volatility scale relevant to the Earth and Moon and the status of water in the Moon', *Meteoritics & Planetary Science*, vol. 50, no. 4, pp. 568-577.

Allton, J. H., Bagby J. R. Jr., Stabekis P. D. (1998) 'Lessons learned during Apollo lunar sample quarantine and sample curation', Advances in Space Research, vol. 22, no. 3, pp. 373–382.

Alp, E. E., Mini, S. M., Ramanathan, M. (1990) *X-Ray Absorption Spectroscopy: EXAFS and XANES - A Versatile Tool to Study the Atomic and Electronic Structure of Materials*. Synchrotron X-ray sources and new opportunities in the soil and environmental sciences: Workshop Report, Argonne National Laboratory, vol. 22, pp.25-36.

Anand, M. (2014) 'Analyzing moon rocks', *Science*, vol. 344, no. 6182, pp. 365-366.

Anand, M., Tartèse, R., Barnes, J. J. (2014) 'Understanding the origin and evolution of water in the Moon through lunar sample studies', *Philosophical Transactions of the Royal Society A: Mathematical, Physical and Engineering Sciences*, vol. 372, no. 2024, pp. 1-33.

Andersen, D. J. and Lindsley, D. H. (1979) 'The olivine-ilmenite thermometer', *Proceedings of the 10th Lunar and Planetary Science Conference*. Houston, March 19-23, pp. 493-507.

Antonangeli, D., Morard, G., Schmerr, N. C., Komabayashi, T., Krisch, M., Fiquet, G., Fei, Y. (2015) 'Towards a mineral physics reference model for the Moon's core', *Proceedings of the National Academy of Sciences*, vol. 112, no. 13, pp. 3916–3919.

Armytage, R. M. G., Georg, R. B., Williams, H. M., Halliday, A. N. (2012) 'Silicon isotopes in lunar rocks: Implications for the Moon's formation and the early history of the Earth', *Geochimica et Cosmochimica Acta*, vol. 77, pp. 504-514.

Baker, D. R. and Moretti, R. (2011) 'Modelling the solubility of sulfur in magmas: A 50-year old geochemical challenge', in Behrens, H., Webster, J. D. (ed[s]) *Reviews in Mineralogy and Geochemistry: Sulfur in Magmas and Melts: Its Importance for Natural and Technical Processes,* Virginia, The Mineralogical Society of America, vol. 73, pp. 167-213.

Barnes, J. D., Sharp, Z. D., Fischer, T. P. (2008) 'Chlorine isotope variations across the Izu-Bonin-Mariana arc', *Geology*, vol. 36, no. 11, pp. 883-886.

Barnes, J. D., Sharp, Z. D., Fischer, T. P., Hilton, D. R., Carr, M. J. (2009) 'Chlorine isotope variations along the Central American volcanic front and back arc', *Geochemistry, Geophysics, Geosystems,* vol. 10, no. 11, pp. 1-17.

Barnes, J. J., Franchi, I. A., Anand, M., Tartèse, R., Starkey, N. A., Koike, M., Sano, Y., Russell, S. S. (2013) 'Accurate and precise measurements of the D/H ratio and hydroxyl content in lunar apatites using NanoSIMS', *Chemical Geology,* vol. 337-338, pp. 48-55.

Barnes, J. J. (2014) *Water in the Moon: A Geochemical Approach*, unpublished PhD thesis, Milton Keynes, The Open University.

Barnes, J. J., Tartèse, R., Anand, M., McCubbin, F. M., Franchi, I. A., Starkey, N. A., Russell, S. S. (2014) 'The origin of water in the primitive Moon as revealed by the lunar highlands samples', *Earth and Planetary Science Letters,* vol. 390, pp. 244-252.

Barnes, J. J., Tartèse, R., Anand, M., McCubbin, F. M., Neal, C. R., Franchi, I. A. (2016) 'Early degassing of lunar urKREEP by crust-breaching impact(s)', *Earth and Planetary Science Letters,* vol. 447, pp. 84-94.

Barnes, J. J., Franchi, I., McCubbin, F. M., Anand, M (2019) 'Multiple reservoirs of volatiles in the Moon revealed by the isotopic composition of chlorine in lunar basalts', *Geochimica et Cosmochimica Acta,* vol. 266, pp. 144-162.

Barrett, T. J., Barnes, J. J., Tartèse, R., Anand, M., Franchi, I. A., Greenwood, R. C., Charlier, B. L. A., Grady, M. M. (2016) 'The abundance and isotopic composition of water in eucrites', *Meteoritics & Planetary Science,* vol. 51, no. 6, pp. 1110-1124.

Bass, M. N. (1971) 'Sample descriptions', in Butler, P. (ed[s]) *Lunar Sample Information Catalog: Apollo 15*, Houston, Texas, NASA, pp. 47-292.

Beaty, D. W. and Albee, A. L. (1978) 'Comparative petrology and possible genetic relations among the Apollo 11 basalts', *Proceedings of the 9th Lunar Science Conference*. Houston, March 13-17, vol. 1, pp. 359-463.

Beaty, D. W., Hill, S. M. R., Albee, A. L., Baldridge, W. S. (1979) 'Apollo 12 feldspathic basalts 12031, 12038 and 12072 - Petrology, comparison and interpretations', *Proceedings of the 10th Lunar and Planetary Science Conference*. Houston, March 19-23, vol. 1, pp. 115-139.

Behrens, H. and Stelling, J. (2011) 'Diffusion and redox reactions of sulfur in silicate melts', in Behrens, H., Webster, J. D. (ed[s]) *Reviews in Mineralogy and Geochemistry: Sulfur in Magmas and Melts: Its Importance for Natural and Technical Processes*, Virginia, The Mineralogical Society of America, vol. 73, pp. 79-111.

Bekaert, D. V., Avice, G., Marty, B. (2018) 'Origin and significance of cosmogenic signatures in vesicles of lunar basalt 15016', *Meteoritics & Planetary Science*, vol. 53, no. 6, pp. 1–14.

Bence, A. E. and Papike, J. J. (1972) 'Pyroxenes as recorders of lunar basalt petrogenesis: chemical trends due to crystal-liquid interaction', *Proceedings of the 3rd Lunar and Planetary Science Conference*. Houston, January 10-13, vol. 1, pp. 431-469.

Best, M. G. (2003) *Igneous and Metamorphic Petrology*, 2nd edn, Malden, USA, Blackwell Science Ltd.

Bianco, A. S. and Taylor, L. A. (1977) 'Applications of dynamic crystallisation studies: lunar olivine-normative basalts', *Proceedings of the 8th Lunar and Planetary Science Conference*. Houston, March 14-18, pp.1583-1610.

Bickel, C. E., Warner, J. L., Phinney, W. C. (1976) 'Petrology of 79215: Brecciation of a lunar cumulate', *Proceedings of the 7th Lunar and Planetary Science Conference*. Houston, March 15-19, pp. 1793–1819.

Birck, J. L., Fourcade, S., Allegre, C. J. (1975) '^{87}Rb-^{86}Sr age of rocks from the Apollo 15 landing site and significance of internal isochrons', Earth and Planetary Science Letters, vol. 26, no. 1, pp. 29-35.

Boggs, S. and Krinsley, D. (2006) *Application of Cathodoluminescence Imaging to the Study of Sedimentary Rocks*, Cambridge University Press, Cambridge.

Bombardieri, D. J., Norman, M. D., Kamenetsky, V. S., Danyushevsky, L. V. (2005) 'Major element and primary sulfur concentrations in Apollo 12 mare basalts: The view from melt inclusions', *Meteoritics & Planetary Science*, vol. 40, no. 5, pp. 679-693.

Bonnand, P., Parkinson, I. J., Anand, M. (2016) 'Mass dependent fractionation of stable chromium isotopes in mare basalts: implications for the formation and the differentiation of the Moon', *Geochimica et Cosmochimica Acta*, vol. 175, pp. 208-221.

Bottke, W. F., Walker, R. J., Day, J. M. D., Nesvorny, D., Elkins-Tanton, L. (2010) 'Stochastic late accretion to Earth, the Moon, and Mars', *Science*, vol. 330, no. 6010, pp. 1527-1530.

Boyce, J. W., Liu, Y., Rossman, G. R., Guan, Y., Eiler, J. M., Stolper, E. M., Taylor, L. A. (2010) 'Lunar apatite with terrestrial volatile abundances', *Nature*, vol. 466, no. 7305, pp. 466-469.

Boyce, J. W., Tomlinson, S. M., McCubbin, F. M., Greenwood, J. P., Treiman, A. H. (2014) 'The lunar apatite paradox', *Science*, vol. 344, no. 6182, pp. 400-402.

Boyce, J. W., Treiman, A. H., Guan, Y., Ma, C., Eiler, J. M., Gross, J., Greenwood, J. P., Stolper, E. M. (2015) 'The chlorine isotope fingerprint of the lunar magma ocean', *Science Advances*, vol. 1, no. 8.

Boyce, J. W., Kanee, S. A., McCubbin, F. M., Barnes, J. J., Bricker, H., Treiman, A. H. (2018) 'Early loss, fractionation, and redistribution of chlorine in the Moon as revealed by the low-Ti lunar mare basalt suite', *Earth and Planetary Science Letters*, vol. 500, pp. 205–214.

Boyet, M. and Carlson, R. W. (2005) '^{142}Nd Evidence for Early (>4.53 Ga) Global Differentiation of the Silicate Earth', *Science*, vol. 309, no. 5734, pp. 576-581.

Brenan, J. (1994) 'Kinetics of fluorine, chlorine and hydroxyl exchange in fluorapatite'. *Chemical Geology*, vol. 110, no. 1-3, pp. 195–210.

Brounce, M., Boyce, J., McCubbin, F. M., Humphreys, J., Reppart, J., Stopler, E., Eiler, J. (2019) 'The oxidation state of sulfur in lunar apatite', *American Mineralogist*, vol. 104, pp. 307–312.

Brown, G. M., Emeleus, J. G., Holland, J. G., Peckett, A., Phillips, R. (1972) 'Mineral-chemical variations in Apollo 14 and Apollo 15 basalts and granitic fractions', *Proceedings of the 3rd Lunar and Planetary Science Conference*. Houston, January 10-13, vol. 1, pp. 141-157.

Bullock, E. S., McKeegan, K. D., Gounelle, M., Grady, M. M., Russell, S. S. (2010) 'Sulfur isotopic composition of Fe-Ni sulfide grains in CI and CM carbonaceous chondrites', *Meteoritics & Planetary Science*, vol. 45, no. 5, p. 885-898.

Bunch, T. E., Keil, K., Prinz, M. (1972) 'Mineralogy, petrology and chemistry of lunar rock 12039', *Meteoritics & Planetary Science*, vol. 7, no. 3, pp. 245-255.

Butler, P. (1971) '15016', in Butler, P. (ed[s]) *Lunar Sample Information Catalog: Apollo 15*, Houston, Texas, NASA, pp. 51-53.

Cameron, A. G. W. and Ward, W. R. (1976) 'The origin of the Moon', *Proceedings of the 7th Lunar Science Conference*. Houston, March 15-19, no. 1041, pp. 120-122.

Canup, R. M. and Asphaug, E. (2001) 'Origin of the Moon in a giant impact near the end of the Earth's formation', *Nature,* vol. 412, no. 6848, pp. 708-712.

Canup, R. M. (2004) 'Simulations of a late lunar-forming impact', *Icarus,* vol. 168, no. 2, pp. 433-456.

Canup, R. M. (2008) 'Lunar-forming collisions with pre-impact rotation', *Icarus,* vol. 196, no. 2, pp. 518-538.

Carroll, M. R., Rutherford, M. J. (1985) 'Sulfide and sulfate saturation in hydrous silicate melts', *Journal of Geophysical Research: Solid Earth*, vol. 90, no. S02, pp. C601–C612.

Carroll, M. R., Rutherford, M. J. (1988) 'Sulfur speciation in hydrous experimental glasses of varying oxidation state: Results from measured wavelength shifts of sulfur X-rays', *American Mineralogist,* vol. 73, pp. 845-849.

Carroll, M. R. and Webster, J. D. (1994) 'Solubilities of Sulfur, Noble Gases, Nitrogen, Chlorine, and Fluorine in Magmas', in Carroll, M. R. and Holloway, J. R. (ed[s]) *Volatiles in Magmas*, Virginia, The Mineralogical Society of America, vol. 30, pp. 231-279.

CCWJ (2012) *Microscopy* [Online]. Available at https://sites.ualberta.ca/~ccwj/teaching/microscopy/ (Accessed 5th January 2018).

Černok, A., White, L. F., Darling, J., Dunlop, J., Anand, M. (2019) 'Shock-induced microtextures in lunar apatite and merrillite', *Meteoritics & Planetary Science*, vol. 54, no. 6, pp. 1262-1282.

Chappell, B. W., Compston, W., Green, D. H., Ware, N. G. (1972) 'Chemistry, geochronology and petrogenesis of lunar sample 15555', *Science*, vol. 175, no. 4020, pp. 415-416.

Chen, Y., Zhang, Y., Liu, Y., Guan, Y., Eiler, J., Stolper, E. M. (2015a) 'Water, fluorine, and sulfur concentrations in the lunar mantle', *Earth and Planetary Science Letters,* vol. 427, pp. 37-46.

Chen, L., Xu, J., Chen, J. (2015b) 'Applications of scanning electron microscopy in earth sciences', *Science China Earth Sciences,* vol. 58, no. 10, pp. 1768-1778.

Clayton, R. N., Mayeda, T. K., Hurd, J. M. (1974) 'Loss of oxygen, silicon, sulfur and potassium for the lunar regolith', *Proceedings of the 5th Lunar and Planetary Science Conference.* Houston, March 18-22, vol. 2, pp. 1801-1809.

Crider, D. H. and Vondrak, R. R. (2002) 'Hydrogen migration to the lunar poles by solar wind bombardment of the moon', *Advances in Space Research,* vol. 30, no. 8, pp. 1869-1874.

Criss, R. E. and Farquhar, J. (2008), 'Abundance, notation, and fractionation of light stable isotopes', *Reviews in Mineralogy & Geochemistry,* vol. 68, pp. 15-30.

Ćuk, M. and Stewart, S. T. (2012) 'Making the moon from a fast-spinning earth: A giant impact followed by resonant despinning', *Science,* vol. 338, no. 6110, pp. 1047-1052.

Cushing, J. A., Taylor, G. J., Norman, M. D., Keil, K. (1999) 'The granulitic impactite suite: Impact melts and metamorphic breccias of the early lunar crust', *Meteoritics & Planetary Science,* vol. 34, no. 2, pp. 185-195.

Cuttita, R., Rose, H. J., Annell, C. S., Carron, M. K., Christian, R. P., Ligon, D. T., Dwornik, E. J., Wright, T. L. , Greenland, L. P. (1973) 'Chemistry of twenty-one igneous rocks and soils returned by the Apollo 15 mission', *Proceedings of the 4th Lunar and Planetary Science Conference.* Houston, March 5-8, vol. 2, pp. 1081-1096.

Dalton, J. and Hollister, L. S. (1974) 'Spinel-silicate co-crystallization relations in sample 15555', *Proceedings of the 5th Lunar and Planetary Science Conference.* Houston, March 18-22, vol. 2, pp. 421-429.

Darwin, G. H. (1879) 'A tidal theory of the evolution of satellites', *The Observatory,* vol. 3, no. 27, pp. 79-84.

Dauphas, N., Burkhardt, C., Warren, P. H., Teng, F.-Z. (2014) 'Geochemical arguments for an Earth-like Moon-forming impactor', *Philosophical Transactions of the Royal Society A: Mathematical, Physical and Engineering Sciences,* vol. 372, no. 2024.

Day, J. M. D. and Moynier, F. (2014) 'Evaporative fractionation of volatile stable isotopes and their bearing on the origin of the Moon', *Philosophical Transactions of the Royal Society A: Mathematical, Physical and Engineering Sciences,* vol. 372, no. 2024.

Day, J. M. D., Pearson, D. G., Taylor, L.A. (2007) 'Highly siderophile element constraints on accretion and differentiation of the earth-moon system', *Science,* vol. 315, no. 5809, pp. 217-219.

Day, J. M. D., Maria-Benavides, J., McCubbin, F. M., Zeigler, R. A. (2018) 'The potential for metal contamination during Apollo lunar sample curation', *Meteoritics & Planetary Science,* vol. 53, no. 6, pp. 1283-1291.

Deer, W. A., Howie, R. A., Zussman, J. (2013) *An Introduction to the Rock- Forming Minerals (3rd edition),* The Mineralogical Society, London.

Delano, J. W. (1986) 'Pristine lunar glasses: Criteria, data, and implications', *Journal of Geophysical Research Solid Earth*, vol. 91, no. B4, pp. 201-213.

de Meijer, R. J., Anisichkin, V. F., van Westrenen, W. (2013) 'Forming the Moon from terrestrial silicate-rich material', *Chemical Geology*, vol. 345, pp. 40-49.

de Moor, J. M., Fischer, T. P., Sharp, Z. D., King, P. L., Wilke, M., Botcharnikov, R. E., Cottrell, E., Zelenski, M., Marty, B., Klimm, K., Rivard, C., Ayalew, D., Ramirez, C., Kelley, K. A. (2013) 'Sulfur degassing at Erta Ale (Ethiopia) and Masaya (Nicaragua) volcanoes: Implications for degassing processes and oxygen fugacities of basaltic systems', *Geochemistry, Geophysics, Geosystems*, vol. 14, no. 10, pp. 4076-4108.

Des Marais, D. J. D. (1983) 'Light element geochemistry and spallogenesis in lunar rocks', *Geochimica et Cosmochimica Acta*, vol. 47, no. 10, pp. 1769-1781.

Diamond Light Source (2019) *Beamline schematic* [Online]. Available at https://www.diamond.ac.uk/Instruments/Spectroscopy/I18/Specification.html (Accessed 14th April 2019).

Ding, S., Hough, T., Dasgupta, R. (2018) 'New high pressure experiments on sulfide saturation of high-FeO* basalts with variable TiO_2 contents – Implications for the sulfur inventory of the lunar interior', *Geochimica et Cosmochimica Acta*, vol. 222, pp. 319–339.

Ding, T. P., Thode, H. G., Rees, C. E. (1983) 'Sulphur content and sulphur isotope composition of orange and black glasses in Apollo 17 drive tube 74002/1', *Geochimica et Cosmochimica Acta*, vol. 47, no. 3, pp. 491-496.

Ding, T., Valkiers, S., Kipphardt, H., De Biévre, P., Taylor, P. D. P., Gonfiantini, R., Krouse, R. (2001) 'Calibrated sulfur isotope abundance ratios of three IAEA sulfur isotope reference materials and V-CDT with a reassessment of the atomic weight of sulfur', *Geochimica and Cosmochimica Acta*, vol. 65, no. 15, pp. 2433–2437.

Drozd, R. J., Hohenberg C. M., Morgan C. J., Ralston C. E. (1974) 'Cosmic-ray exposure history at the Apollo 16 and other lunar sites: lunar surface dynamics', *Geochimica et Cosmochimica Acta*, vol. 38, no. 10, pp. 1625-1642.

Economos, R., Boehnke, P., Burgisser, A. (2017) 'Sulfur isotopic zoning in apatite crystals: A new record of dynamic sulfur behavior in magmas', *Geochimica et Cosmochimica Acta*, vol. 215, pp. 387-403.

Elkins-Tanton, L. T., Van Orman, J. A., Hager, B. H., Grove, T. L. (2002) 'Re-examination of the lunar magma ocean cumulate overturn hypothesis: melting or mixing is required', *Earth and Planetary Science Letters*, vol. 196, no. 3-4, pp. 239-249.

Elkins-Tanton, L.T., Chatterjee, N., Grove, T. L. (2003) 'Magmatic processes that produced lunar fire fountains', *Geophysical Research Letters,* vol. 30, no. 10, pp. 20-1.

Elkins-Tanton, L. T. and Grove, T. L. (2011) 'Water (hydrogen) in the lunar mantle: Results from petrology and magma ocean modeling', *Earth and Planetary Science Letters,* vol. 307, no. 1-2, pp. 173-179.

Epstein, S., Taylor H. P. Jr. (1970) 'The concentration and isotopic composition of hydrogen, carbon and silicon in Apollo 11 lunar rocks and minerals' *Proceedings of the Apollo 11 Lunar Science Conference*. Houston, January 5-8, vol. 2, pp. 1085–1096.

Epstein, S. and Taylor, H. P. (1971) 'O^{18}/O^{16}, Si^{30}/Si^{28}, D/H and C^{13}/C^{12} ratios in lunar samples'. *Proceedings of the 2nd Lunar Science Conference.* Houston, January 11-14, pp. 1421-1441.

Epstein, S. and Taylor, H. P. (1972) 'O^{18}/O^{16}, Si^{30}/Si^{28}, C^{13}/C^{12} and D/H studies of Apollo 14 and 15 samples'. Lunar Planet. *Proceedings of 3rd Lunar Science Conference*. Houston, January 10-13, pp. 236-238.

Epstein, S., Taylor, H. P. Jr. (1973) 'The isotopic composition and concentration of water, hydrogen, and carbon in some Apollo 15 and 16 soils and in the Apollo 17 orange soil', *Proceedings of the 4th Lunar Science Conference*. Houston, March 5-8, vol. 2, pp. 1559–1575.

Eugster, O., Eberhardt, P., Geiss, J., Grogler, N., Jungck, M., Meier, F., Morgell, M., Niederer, F. (1984) 'Cosmic ray exposure histories of Apollo 14, Apollo 15 and Apollo 16 rocks', *Proceedings of the 14th Lunar and Planetary Science Conference. Part 2 Journal of Geophysical Research*, vol. 89, pp. B498-B512.

Evensen, N. M., Murthy V. R., Coscio M. R. (1973) 'Rb-Sr ages of some mare basalts and the isotopic and trace element systematics in lunar fines', *Proceedings of the 4th Lunar and Planetary Science Conference*. Houston, March 5-8, vol. 4, pp. 1707-1724.

Fincham, C. J. B. and Richardson, F. D. (1954) 'The behaviour of sulphur in silicate and aluminate melts', *Proceedings of the Royal Society A: Mathematical, Physical and Engineering Sciences*, vol. 223, no. 1152, pp. 40-62.

Fischer-Gödde, M. and Becker, H. (2012) 'Osmium isotope and highly siderophile element constraints on ages and nature of meteoritic components in ancient lunar impact rocks', *Geochimica et Cosmochimica Acta,* vol. 77, pp. 135-156.

Fortin, M-A., Riddle, J., Desjardins-Langlais, Y., Baker, D. R. (2015) 'The effect of water on the sulfur concentration at sulfide saturation (SCSS) in natural melts', *Geochimica et Cosmochimica Acta,* vol. 160, pp. 100–116.

Friedman, I., O'Neill, J. R., Adami, L. H., Gleason, J. D., Hardcastle, K. (1970) 'Water, Hydrogen, Deuterium, Carbon, Carbon-13, and Oxygen-18 content of selected lunar material', *Science*, vol. 167, no. 3918, pp. 538-540.

Friedman, I., O'Neill, J. R., Gleason, J. D., Hardcastle, K. (1971) 'The carbon and hydrogen content and isotopic composition of some Apollo 12 materials', *Proceedings 2nd Lunar Science Conference*. Houston, January 11-14, pp. 1407-1415.

Füri, E., Deloule, E., Gurenko, A., Marty, B. (2014) 'New evidence for chondritic lunar water from combined D/H and noble gas analyses of single Apollo 17 volcanic glasses', *Icarus*, vol. 229, pp. 109-120.

Füri, E., Deloule, E., Trappitsch, R. (2017) 'The production rate of cosmogenic deuterium at the Moon's surface', *Earth and Planetary Science Letters*, vol. 474, pp. 76-82.

Gao, X., Thiemens, M. (1993) 'Isotopic composition and concentration of sulfur in carbonaceous chondrites', *Geochimica et Cosmochimica Acta*, vol. 57, pp. 3159-3169.

Garvin J. B., Head J. W. and Wilson L. (1982) 'Magma vesiculation in Apollo 15 mare basalts: Observations and theory', *Proceedings of the 8th Lunar and Planetary Science Conference*. Houston, March 14-18, pp. 255-256.

Gerstenkorn, H. (1955) 'Über Gezeitenreibung beim Zweikörperproblem', *Zeitschrift für Astrophysik*, vol. 36, pp. 245-274.

Gibson, E. K. Jr. and Moore, G. W. (1974) 'Sulfur abundances and distributions in the valley of Taurus-Littrow: Evidence of mixing', *Proceedings of the 5th Lunar Science Conference*. Houston, March 18-22, vol. 2, pp. 1823–1837.

Gibson, E. K. Jr., Chang, S., Lennon, K., Moore, G. W., Pearce, G. W. (1975) 'Sulfur abundances and distributions in mare basalts and their source magmas', *Proceedings of* the *6th Lunar Science Conference*. Houston, March 17-21, pp. 1287-1301.

Gnos, E., Hofmann, B. A., Al-Kathiri, A., Lorenzetti, S., Eugster, O., Whitehouse, M. J., Villa, I. M., Jull, A. J. T., Eikenberg, J., Spettel, B., Krähenbühl, U., Franchi, I. A., Greenwood, R. C. (2004) 'Pinpointing the source of a lunar meteorite: Implications for the evolution of the moon', *Science*, vol. 305, pp. 657–659.

Goldoff, B., Webster, J. D., Harlov, D. E. (2012) 'Characterization of fluor-chlorapatites by electron probe microanalysis with a focus on time-dependent intensity variation of halogens', *American Mineralogist*, vol. 97, no. 7, pp. 1103-1115.

Götze, J. and Kempe, U. (2008) 'A comparison of optical microscope- and scanning electron microscope-based cathodoluminescence (CL) imaging and spectroscopy applied to geosciences', *Mineralogical Magazine*, vol. 72, no. 4, pp.909–924.

Götze, J. (2009) ‘Cathodoluminescence microscopy and spectroscopy of lunar rocks and minerals’, in Gucsik, A. (ed[s]) *Cathodoluminescence and its Application in the Planetary Sciences*, Berlin, Springer-Verlag, pp. 87–110.

Götze, J. and Kempe, U. (2009) ‘Physical Principles of Cathodoluminescence (CL) and its Applications in Geosciences’, in Gucsik, A. (ed[s]) *Cathodoluminescence and its Application in the Planetary Sciences*, Berlin, Springer-Verlag, pp.1-17.

Götze, J. (2012) ‘Application of Cathodoluminescence Microscopy and Spectroscopy in Geosciences’, *Microscopy and Microanalysis*, vol. 18, no. 6, pp. 1270-1284.

Greenwood, J. P., Itoh, S., Sakamoto, N., Warren, P., Taylor, L., Yurimoto, H. (2011) ‘Hydrogen isotope ratios in lunar rocks indicate delivery of cometary water to the Moon’, *Nature Geoscience*, vol. 4, no. 2, pp. 79-82.

Grove, T. L. and Krawczynski, M. J. (2009) ‘Lunar mare volcanism: where did the magmas come from?’, *Elements Magazine*, vol. 5, pp. 29-34.

Grove, T. L. and Walker, D. (1977) ‘Cooling histories of Apollo 15 quartz-normative basalts’, *Proceedings of the 8th Lunar and Planetary Science Conference*. Houston, March 14-18, pp. 1501-1520.

Hallis, L. J., Anand, M., Greenwood, R. C., Miller, M. F., Franchi, I. A., Russell, S. S. (2010) ‘The oxygen isotope composition, petrology and geochemistry of mare basalts: Evidence for large-scale compositional variation in the lunar mantle’, *Geochimica et Cosmochimica Acta*, vol. 74, no. 23, pp. 6885-6899.

Hallis, L. J., Anand, M., Strekopytov, S. (2014) ‘Trace-element modelling of mare basalt parental melts: Implications for a heterogeneous lunar mantle’, *Geochimica et Cosmochimica Acta*, vol. 134, pp. 289-316.

Hamers, M. F. and Drury, M. R. (2011) ‘Scanning electron microscope-cathodoluminescence (SEM-CL) imaging of planar deformation features and tectonic deformation lamellae in quartz’, *Meteoritics & Planetary Science*, vol. 46, no. 12, pp. 1814-1834.

Hammond, C. (2009) *The Basics of Crystallography and Diffraction*, 3rd edn, Oxford, Oxford University Press.

Hartmann, W. K. and Davis, D. R. (1975) ‘Satellite-sized planetesimals and lunar origin’, *Icarus*, vol. 24, no. 4, pp. 504-515.

Hashizume, K., Chaussidon, M., Marty, M., Robert, F. (2000) 'Solar Wind Record on the Moon: Deciphering Presolar from Planetary Nitrogen', *Science*, vol. 290, no. 5494, pp. 1142-1145.

Haskin, L. A. and Warren, P. H. (1991) 'Lunar Chemistry', in Heiken, G., Vaniman, D. T., French, B. M. (ed[s]) *Lunar Sourcebook: A user's guide to the Moon*, New York, Cambridge University Press, pp. 357–474.

Hauri, E., Wang, J., Dixon, J. E., King, P. L., Mandeville, C., Newman, S. (2002) 'SIMS analysis of volatiles in silicate glasses 1. Calibration, matrix effects and comparisons with FTIR', *Chemical Geology*, vol. 183, no. 1-4, pp. 99-114.

Hauri, E. H., Weinreich, T., Saal, A. E., Rutherford, M. C., Van Orman, J. A. (2011) 'High pre-eruptive water contents preserved in lunar melt inclusions', *Science*, vol. 333, no. 6039, pp. 213-215.

Hauri, E. H., Saal, A. E., Rutherford, M. J., Van Orman, J. A. (2015) 'Water in the moon's interior: Truth and consequences', *Earth and Planetary Science Letters*, vol. 409, pp. 252-264.

Hauri, E. H., Papineau, D., Wang, J., Hillion, F. (2016) 'High-precision analysis of multiple sulfur isotopes using NanoSIMS', Chemical Geology, vol. 420, pp. 148-161.

Henning, P. A., Adolfsson, E., Grins J. (2000) 'The chalcogenide phosphate apatites $Ca_{10}(PO_4)_6S$, $Sr_{10}(PO_4)_6S$, $Ba_{10}(PO_4)_6S$ and $Ca_{10}(PO_4)_6Se$', *Zeitschrift für Kristallographie*, vol. 215, no.4, pp. 226-230.

Herwartz, D., Pack, A., Friedrichs, B., Bischoff, A. (2014) 'Identification of the giant impactor Theia in lunar rocks', *Science*, vol. 344, no. 6188, pp. 1146-1150.

Hess, P. C. and Parmentier, E. M. (1995) 'A model for the thermal and chemical evolution of the Moon's interior: implications for the onset of mare volcanism', *Earth and Planetary Science Letters*, vol. 134, no. 3-4, pp. 501-514.

Hiesinger, H., Jaumann, R. (2014) 'The Moon', in Spohn, T., Breuer, D., Johnson, T. V. (ed[s]) *Encyclopedia of the Solar System*, Amsterdam, Elsevier, vol. 3, pp. 493-538.

Hohenberg, C. M., Davis, P. K., Kaiser, W. A., Lewis, R. S., Reynolds, J. H. (1970) 'Trapped and cosmogenic rare gases from stepwise heating of Apollo 11 samples', *Geochimica et Cosmochimica Acta Supplement*, vol. 1, pp. 1283-1309.

Hoppe, P., Cohen, S., Meibom, A. (2013) 'NanoSIMS: Technical Aspects and Applications in Cosmochemistry and Biological Geochemistry', *Geostandards and Geoanalytical Research*, vol. 37, no. 2, pp. 111-154.

Höschen, C., Höschen, T., Mueller, C.W., Lugmeier J., Elgeti, S., Rennert, T., Kögel-Knabner, I. (2015) 'Novel sample preparation technique to improve spectromicroscopic analyses of micrometer-sized particles', *Environmental Science and Technology*, vol. 49, no. 16, pp. 9874-9880.

Hudgins, J. A., Spray, J. G., Kelley, S. P., Korotev, R. L., Sherlock, S. C. (2008) 'A laser probe40Ar/39Ar and INAA investigation of four Apollo granulitic breccias', *Geochimica et Cosmochimica Acta*, vol. 72, no. 23, pp. 5781-5798.

Hughes, J. M., Cameron, M., Crowley, K. D. (1990) 'Crystal structures of natural ternary apatites; solid solution in the Ca5 (PO4)3 X (X= F, OH, Cl) system', *American Mineralogist*, vol. 75, no. 3-4, pp. 295-304.

Hughes, J. M. and Rakovan, J. F. (2015) 'Structurally robust, chemically diverse: Apatite and apatite supergroup minerals', *Elements*, vol. 11, no. 3, pp. 165-170.

Hui, H., Peslier, A. H., Zhang, Y., Neal, C. R. (2013) 'Water in lunar anorthosites and evidence for a wet early Moon', *Nature Geoscience*, vol. 6, no. 3, pp. 177-180.

Humphreys, J., Rohrer, G. S., Rollett, A. (2017) *Recrystallization and related annealing phenomena*, Oxford, Elsevier.

Humphreys, M. C. S., Blundy, J. D., Sparks, R. S. J. (2006) 'Magma Evolution and Open-System Processes at Shiveluch Volcano: Insights from Phenocryst Zoning', *Journal of Petrology*, vol. 47, no. 12, pp. 2303–2334.

Husain, L. (1974) '^{40}Ar-^{39}Ar chronology and cosmic ray exposure ages of the Apollo 15 samples', *Journal of Geophysical Research*, vol. 79, no. 17, pp. 2588-2606.

Iowa State University (2017) *Backscattered Electrons* [Online]. Available at http://www.mse.iastate.edu/research/laboratories/sem/microscopy/how-does-the-sem-work/high-school/how-the-sem-works/backscattered-electrons/ (Accessed 24th July 2017).

Jakes, D. (1971) 'Sample descriptions', in Butler, P. (ed[s]) *Lunar Sample Information Catalog: Apollo 15*, Houston, Texas, NASA, pp. 47-292.

Jalilehvand, F. (2006) 'Sulfur: Not a "silent" element any more', *Chemical Society Reviews*, vol. 35, no. 12, pp. 1256-1268.

Jana, D. and Walker, D. (1997) 'The influence of sulfur on partitioning of siderophile elements', *Geochimica et Cosmochimica Acta*, vol. 61, no. 24, pp. 5255-5277.

Joy, K. H., Zolensky, M. E., Nagashima, K., Huss, G. R., Ross, D. K., McKay, D. S., Kring, D. A. (2012) 'Direct detection of projectile relics from the end of the lunar basin–forming epoch', *Science*, vol. 336, no. 6087, pp. 1426-1429.

Joy, K. H., Visscher, C., Zolensky, M. E., Mikouchi, T., Hagiya, K., Ohsumi, K., Kring, D. (2015) 'Identification of magnetite in lunar regolith breccia 60016: Evidence for oxidized conditions at the lunar surface', *Meteoritics & Planetary Science*, vol. 50, no. 7, pp. 1157–1172.

Jugo, P. J., Wilke, M., Botcharnikov, R. E. (2010) 'Sulfur K-edge XANES analysis of natural and synthetic basaltic glasses: Implications for S speciation and S content as function of oxygen fugacity', *Geochimica et Cosmochimica Acta*, vol. 74, pp. 5926–5938.

Kaplan, I. R., Kerridge, J. F., Petrowski, C. (1976) 'Light element geochemistry of the Apollo 15 site', *Proceedings of the 7th Lunar and Planetary Science Conference*. Houston, March 15-19, vol. 1, pp. 481-492.

Kastle, J. H. and Elvove, E. (1909) 'On the use of Anhydrous Sodium Sulphite in the preparation of Endo's Medium, together with a note on the preparation of Anhydrous Sodium Sulphite and its stability under ordinary conditions', *The Journal of Infectious Diseases*, vol. 6, no. 5, pp. 619-629.

Keil, K., Prinz, M., Bunch, T. E. (1971) 'Mineralogy, petrology, and chemistry of some Apollo 12 samples', *Proceedings of the 2nd Lunar Science Conference*. Houston, January 11-14, pp. 319-341.

Kerridge, J. F., Kaplan, I. R., Petrowski, C. (1975a) 'Light element geochemistry of the Apollo 16 site', *Geochimica et Cosmochimica Acta*, vol. 39, pp. 137-162.

Kerridge, J. F., Kaplan, I. R., Petrowski, C. (1975b) 'Evidence for meteoritic sulfur in the lunar regolith', *Proceedings of the 6th Lunar Science Conference.* Houston, March 17-21, vol. 2, pp. 2151-2162.

Kesson, S. E. (1975) 'Mare basalts: Melting experiments and petrogenetic interpretations', *Proceedings of the 6th Lunar and Planetary Science Conference*. Houston, March 17-21, vol. 1, pp. 921-944.

Kesson, S. E. (1977) 'Mare Basalt Petrogenesis', in (ed[s]) *Philosophical Transactions of the Royal Society of London. Series A, Mathematical and Physical Sciences, The Moon: A New Appraisal from Space Missionsand Laboratory Analyses*, vol. 285, no. 1327, pp. 159-167.

Kilburn, M. R. and Wacey, D. (2015) 'Nanoscale Secondary Ion Mass Spectrometry (NanoSIMS) as an analytical tool in the geosciences' in Grice, K. (ed[s]) *Principles and Practice of Analytical Techniques in Geosciences*, Cambridge, Royal Society of Chemistry, 1–34.

Kim, Y., Konecke B., Fiege, A., Simon, A., Becker, U. (2017) 'An ab-initio study of the energetics and geometry of sulfide, sulfite, and sulfate incorporation into apatite: The thermodynamic basis for using this system as an oxybarometer', *American Mineralogist*, vol. 102, no. 8, pp. 1646-1656.

Kirsten T., Deubner J., Horn P., Kaneoka I., Kiko J., Schaeffer O.A., Thio S. K. (1972) 'The rare gas record of Apollo 14 and 15 samples', *Proceedings of the 3rd Lunar and Planetary Science Conference*. Houston, January 10-13, vol. 1, pp. 1865-1889.

Kirsten T., Horn P., Kiko J. (1973) '^{39}Ar-^{40}Ar dating and rare gas analysis of Apollo 16 rocks and soils', *Proceedings of the 4th Lunar and Planetary Science Conference*. Houston, March 5-8, vol. 4, pp. 1757-1784.

Konecke, B. A., Fiege, A., Simon, A. C., Parat, F., Stechern, A. (2017a) 'Co-variability of S^{6+}, S^{4+}, and S^{2-} in apatite as a function of oxidation state: Implications for a new oxybarometer', *American Mineralogist,* vol. 102, no. 3, pp. 548–557.

Konecke, B. A., Fiege, A., Simon, A. C., Holtz, F. (2017b) 'Cryptic metasomatism during late-stage lunar magmatism implicated by sulfur in apatite, *Geology*, vol. 45, no. 8, pp. 739-742.

Konecke, B. A., Fiege, A., Simon, Linsler, S., Holtz, F. (2019) 'An experimental calibration of a sulfur-in-apatite oxybarometer for mafic systems', *Geochimica et Cosmochimica Acta*, vol. 265, pp. 242-258.

Korotev, R. L., Zeigler R. A., Jolliff B. L., Irving A. J., Bunch T. E. (2009) 'Brecciated lunar meteorites of intermediate iron concentration', *Meteoritics & Planetary Science*, vol. 44, no. 9, pp. 1287–1322.

Kring, D. A. and Cohen, B. A. (2002) 'Cataclysmic bombardment throughout the inner solar system 3.9–4.0 Ga', *Journal of Geophysical Research*, vol. 107, No. E2, pp. 4-1–4-6.

Kruijer, T. S., Kleine, T., Fischer-Gödde, M., Sprung, P., (2015) 'Lunar tungsten isotopic evidence for the late veneer', *Nature*, vol. 520, pp. 534-537.

Kruijer, T. S. and Kleine, T. (2017) 'Tungsten isotopes and the origin of the Moon', *Earth and Planetary Science Letters*, vol. 475, pp. 15–24.

Labidi, J., Cartigny, P., Birck, J. L., Assayag, N., Bourrand, J. J. (2012) 'Determination of multiple sulfur isotopes in glasses: A reappraisal of the MORB $\delta^{34}S$', *Chemical Geology*, vol. 334, pp. 189-198.

Labidi, J., Cartigny, P., Moreira, M. (2013) 'Non-chondritic sulphur isotope composition of the terrestrial mantle', Nature, vol. 501, no. 7466, pp. 208-211.

Labidi, J., Cartigny, P., Hamelin, C., Moreira, M., Dosso, L. (2014) 'Sulfur isotope budget (^{32}S, ^{33}S, ^{34}S and ^{36}S) in Pacific–Antarctic ridge basalts: A record of mantle source heterogeneity and hydrothermal sulfide assimilation', *Geochimica et Cosmochimica Acta*, vol. 133, pp. 47–67.

Labidi, J. and Cartigny, P. (2016) 'Negligible sulfur isotope fractionation during partial melting: Evidence from Garrett transform fault basalts, implications for the late-veneer and the hadean matte', *Earth and Planetary Science Letters*, vol. 451, pp. 196–207.

Labidi, J., Farquhar, J., Alexander, C. M. O. D., Eldridge, D. L., Oduro, H. (2017) 'Mass independent sulfur isotope signatures in CMs: Implications for sulfur chemistry in the early solar system', *Geochimica et Cosmochimica Acta,* vol. 196, pp. 326-350.

Lin, Y., Tronche, E. J., Steenstra, E. S., van Westrenen, W. (2017) 'Evidence for an early wet Moon from experimental crystallization of the lunar magma ocean', *Nature Geoscience,* vol. 10, pp. 14-18.

Liu, Y., Mosenfelder, J. L., Guan, Y., Rossman, G. R., Eiler, J. M., Taylor, L. A. (2012a) 'SIMS analysis of water abundance in nominally anhydrous minerals in lunar basalts', *Proceedings of the 43rd Lunar and Planetary Science Conference*. Houston, March 19-23, no. 1866.

Liu, Y., Guan, Y., Zhang, Y., Rossman, G. R., Eiler, J. M., Taylor, L. A. (2012b) 'Direct measurement of hydroxyl in the lunar regolith and the origin of lunar surface water', *Nature Geoscience,* vol. 5, no. 11, pp. 779-782.

Lodders, K. (2003) 'Solar System Abundances and Condensation Temperatures of the Elements', *Astrophysical Journal Letters,* vol. 591, no. 2, pp. 1220-1247.

Longhi, J. (1992) 'Experimental petrology and petrogenesis of mare volcanics', *Geochimica et Cosmochimica Acta*, vol. 56, no. 6, pp. 2235-2251.

Lunar and Planetary Laboratory (2007) *The Michael J. Drake Electron Microprobe Laboratory University of Arizona* [Online]. Available at http://pirlwww.lpl.arizona.edu/~domanik/UA_Microprobe/Intro.html (Accessed 14th December 2017).

Lunar and Planetary Institute (2018a) *Apollo Missions* [Online]. Available at https://www.lpi.usra.edu/lunar/missions/apollo/ (Accessed 15th February 2018).

Lunar and Planetary Institute (2018b) *Apollo 15 Mission* [Online]. Available at https://www.lpi.usra.edu/lunar/missions/apollo/apollo_15/ (Accessed 19th April 2018).

Lunar and Planetary Institute (2018c) *Apollo 17 Mission* [Online]. Available at https://www.lpi.usra.edu/lunar/missions/apollo/apollo_17/overview/ (Accessed 1st March 2018).

LSPET (Lunar Sample Preliminary Examination Team) (1972) *Apollo 15 Preliminary Science Report*, Washington D.C., NASA, SP-289, pp. 5-1 – 6-1.

LSPET (Lunar Sample Preliminary Examination Team) (1970) Preliminary Examination of Lunar Samples from Apollo 12, *Science*, vol. *167*, no. 3923, pp. 1325-1339.

Marini, L., Moretti, R., Accornero, M (2011) 'Sulfur isotopes in magmatic-hydrothermal systems, melts, and magmas', in Behrens, H., Webster, J. D. (ed[s]) *Reviews in Mineralogy and Geochemistry: Sulfur in Magmas and Melts: Its Importance for Natural and Technical Processes,* Virginia, The Mineralogical Society of America, vol. 73, pp. 423-292.

Marti, K. and Lightner, B. D. (1972) 'Rare gas record in the largest Apollo 15 rock', *Science*, vol. 175, no. 4020, pp. 421-422.

Mason, B., Jarosewich, E., Melson, W. G. (1972) 'Mineralogy, petrology, and chemical composition of lunar samples 15085, 15256, 15271, 15471, 15475, 15476, 15535, 15555, and 15556', *Proceedings of the 3rd Lunar Science Conference*. Houston, January 10-13, vol. 3, pp.785-796.

Mason, R. (2014) 'The physics and chemistry of cathodoluminescence', in Coulson, I. M. (ed[s]) *Cathodoluminescence and its Application to Geoscience*, Mineralogical Association of Canada, vol. 45, pp. 1-10.

McCanta, M. C., Dyar, M. D., Rutherford, M. J., Lanzirotti, A., Sutton, S. R., Thomson, B. J. (2017) '*In situ* measurement of ferric iron in lunar glass beads using Fe-XAS', *Icarus*, vol. 285, pp. 95-102.

McCubbin, F. M., Steele, A., Nekvasil, H., Schnieders, A., Rose, T., Fries, M., Carpenter, P. K., Jolliff, B. L. (2010a) 'Detection of structurally bound hydroxyl in fluorapatite from Apollo Mare basalt 15058,128 using TOF-SIMS', *American Mineralogist,* vol. 95, no. 8-9, pp. 1141-1150.

McCubbin, F. M., Steele, A., Hauri, E. H., Nekvasil, H., Yamashita, S., Hemley, R. J. (2010b) 'Nominally hydrous magmatism on the Moon', *Proceedings of the National Academy of Sciences of the United States of America,* vol. 107, no. 25, pp. 11223-11228.

McCubbin, F. M., Jolliff, B. L., Nekvasil, H., Carpenter, P. K., Zeigler, R. A., Steele, A. b, Elardo, S. M., Lindsley, D. H. (2011) 'Fluorine and chlorine abundances in lunar apatite: Implications for heterogeneous distributions of magmatic volatiles in the lunar interior', *Geochimica et Cosmochimica Acta*, vol. 75, no. 17, pp. 5073-5093.

McCubbin, F. M., Kaaden, K. E. V., Tartèse, R., Klima, R. L., Liu, Y., Mortimer, J., Barnes, J. J., Shearer, C. K., Treiman, A. H., Lawrence, D. J., Elardo, S. M., Hurley, D. M., Boyce, J. W., Anand, M. (2015) 'Magmatic volatiles (H, C, N, F, S, Cl) in the lunar mantle, crust, and regolith: Abundances, distributions, processes, and reservoirs', *American Mineralogist*, vol. 100, no. 8-9, pp. 1668-1707.

McDonough, W. F. and Sun, S.-. (1995) 'The composition of the Earth', *Chemical Geology*, vol. 120, no. 3-4, pp. 223-253.

McGee, P., Warner, J., Simonds, C. (1977) *Introduction to the Apollo collections. Part 1: Lunar igneous rocks*. Houston, NASA STI/Recon, Technical Report No. 77: 22034.

McGee, J. J., Bence, A. E., Eichhorn, G., Schaeffer, O. A. (1978) 'Feldspathic granulite 79215: Limitations on *T*-fO_2 conditions and time of metamorphism', *Proceedings of the 9th Lunar Science Conference*. Houston, March 13-17, pp. 743–772.

McKay, D. S., Heiken, G., Basu, A., Blanford, G., Simon, S., Reedy, R., French, B. M., Papike, J. (1991) 'The lunar regolith', in Heiken, G., Vaniman, D. T., French, B. M. (ed[s]) *Lunar Sourcebook: A user's guide to the Moon*, New York, Cambridge University Press, pp. 285-356.

Merlivat, L., Nief, G., Roth, E. (1974a) 'Deuterium content of lunar material', *Proceedings of 3rd Lunar Science Conference*. Houston, January 10-13, pp. 1473-1477.

Merlivat, L., Lelu, M., Nief, G., Roth, E. (1974b) 'Deuterium, hydrogen, and water content of lunar material', *Proceedings of 5th Lunar Science Conference*. Houston, March 18-22, pp. 1885-1895.

Merlivat, L., Lelu, M., Nief, G., Roth, E. (1976) 'Spallation deuterium in rock 70215', *Proceedings of 7th Lunar Science Conference*. Houston, March 15-19, vol. 2, pp. 649-658.

Métrich, N. and Clocchiatti, R. (1996) 'Sulfur abundance and its speciation in oxidized alkaline melts', *Geochimica et Cosmochimica Acta*, vol. 60, no. 21, pp. 4151-4160.

Métrich, N., Berry, A. J., O'Neill, H. S. C., Susini, J. (2009) 'The oxidation state of sulfur in synthetic and natural glasses determined by X-ray absorption spectroscopy', *Geochimica et Cosmochimica Acta*, vol. 73, no. 8, pp. 2382-2399.

Meyer, C. (2010) *Lunar Sample Compendium*, Astromaterials Research & Exploration Science (ARES), NASA Johnson Space Centre, Houston [Online]. Available at https://curator.jsc.nasa.gov/lunar/lsc/index.cfm (Accessed 19th April 2018).

Mills, R. D., Simon, J. I., Alexander, C. M. O'D, Wang, J., Hauri, E. H. (2016) 'Water in alkali feldspar: The effect of rhyolite generation on the lunar hydrogen budget', *Geochemical Perspectives Letters*, vol. 3, pp. 115-123.

Mitchell, R. H., Xiong, J., Mariano, A. N., Fleet, M. E. (1997) 'Rare-earth-element-activated cathodoluminescence in apatite', *The Canadian Mineralogist*, vol. 35, no. 4, pp. 979-998.

Mitchell, R. (2014) 'Cathodoluminescence of apatite', in Coulson, I. M. (ed[s]) *Cathodoluminescence and its Application to Geoscience*, Mineralogical Association of Canada, vol. 45, pp. 143-168.

Moore, C. B., Lewis, C. F., Larimer, J. W., Delles, F. M., Gooley, R. C., Nichiporuk, W. (1971) 'Total carbon and nitrogen abundances in Apollo 12 lunar samples', *Proceedings of the 2nd Lunar Science Conference*. Houston, January 11-14, pp. 1343-1350.

Morbidelli, A., Marchi, S., Bottke, W. F., Kring, D. A. (2012) 'A sawtooth-like timeline for the first billion years of lunar bombardment', *Earth and Planetary Science Letters*, vol. 355-356, pp. 144-151.

Morbidelli, A., Nesvorny, D., Laurenz, V., Marchi, S., Rubie, D. C., Elkins-Tanton, L., Wieczorek, M., Jacobson, S. (2018) 'The timeline of the lunar bombardment: Revisited', *Icarus*, vol. 305, pp.262-276.

Moretti, R., Papale, P., Ottonello, G. (2003) 'A model for the saturation of C-H-O-S fluids in silicate melts', in Oppenheimer, C., Pyle, D. M., Barclay, J. (ed[s]) *Volcanic Degassing*, London, The Geological Society, Special Publication 213, pp. 81-101.

Morrison, D. A. and Silver, L. T. (1971) 'Sample descriptions', in Butler, P. (ed[s]) *Lunar Sample Information Catalog: Apollo 15*, Houston, Texas, NASA, pp. 47-292.

Mosenfelder, J. L., Le Voyer, M., Rossman, G. R., Guan, Y., Bell, D. R., Eiler, J. M., Asimow, P. D. (2011) 'Analysis of hydrogen in olivine by SIMS: Evaluation of standards and protocol', *American Mineralogist*, vol. 96, no. 11-12, pp. 1725–1741.

Mosselmans, J. F. W., Quinn, P. D., Rosell, J. R., Atkinson, K. D., Dent, A. J., Cavill, S. I., Hodson, M. E., Kirk, C. A., Schofield, P. F. (2008) 'The first environmental science experiments on the new microfocus spectroscopy beamline at Diamond', *Mineralogical Magazine*, vol. 72, no. 1, pp. 197-200.

Mosselmans, J. F. W., Quinn, P. D., Dent, A. J., Cavill, S. A., Diaz Moreno, S., Peach, A., Leicester, P. J., Keylock, S. J., Gregory, S. R., Atkinson, K. D., Roque Rosell, J. (2009) 'I18 – the microfocus spectroscopy beamline at the Diamond Light Source', *Journal of Synchrotron Radiation,* vol. 16, pp. 818-824.

Muehlberger, W. R., Batson, R. M., Cernan, E. A., Freeman, V. L., Hait, M. H., Holt, H. E., Howard, K. A., Jackson, E. D., Larson, K. B., Reed, V. S., Rennilson, J. J., Schmitt, H. H., Scott, D. H., Sutton, R. L., Stuart-Alexander, D., Swann, G. A., Trask, N. J., Ulrich, G. E., Wilshire, H. G., Wolfe, E. W. (1973) *Preliminary geologic investigation of the Apollo 17 landing site,* Washington, D.C., U.S., in Apollo 17 Preliminary Science Report: NASA Special Paper no. 330, pp. 6-1–6-71.

Mukhopadhyay, S. (2012) 'Early differentiation and volatile accretion recorded in deep-mantle neon and xenon', *Nature,* vol. 486, no. 7401, pp. 101-104.

Nakamura, N., Unruh, D. M., Gensho, R., Tatsumoto, M. (1977) 'Evolution history of lunar mare basalts: Apollo 15 samples revisited', *Proceedings of the 8th Lunar and Planetary Science Conference.* Houston, March 14-18, pp. 712-714.

NASA (2005) *Soviet Lunar Missions* [Online]. Available at https://nssdc.gsfc.nasa.gov/planetary/lunar/lunarussr.html (Accessed 9th August 2018).

NASA (2016) *Lunar Rocks and Soils from Apollo Missions* [Online]. Available at https://curator.jsc.nasa.gov/lunar/index.cfm# (Accessed 15th February 2018).

NASA (2019) *NASA Opens Previously Unopened Apollo Sample Ahead of Artemis Missions* [Online]. Available at https://www.nasa.gov/feature/nasa-opens-previously-unopened-apollo-sample-ahead-of-artemis-missions (Accessed 19th January 2020).

NASA (2020) *Earth's Moon* [Online]. Available at https://solarsystem.nasa.gov/moons/earths-moon/by-the-numbers/ (Accessed 19th January 2020).

Nava, D. F. (1974) 'Chemical compositions of some soils and rock types from the Apollo 15, 16 and 17 lunar sites', *Proceedings of the 5th Lunar and Planetary Science Conference.* Houston, March 18-22, vol. 2, pp. 1087-1096.

Neal, C. R., Hacker, M. D., Snyder, G. A., Taylor, L. A., Liu, Y.-G., Schmitt, R. A (1994) 'Basalt generation at the Apollo 12 site, Part 1: New data, classification, and re-evaluation', *Meteoritics and Planetary Science,* vol. 29, no. 3, pp. 334-348.

Newcombe, M. E., Brett, A., Beckett, J. R., Baker, M. B., Newman, S., Guan, Y., Eiler, J. M., Stolper, E. M. (2017) 'Solubility of water in lunar basalt at low pH_2O', *Geochimica et Cosmochimica Acta,* vol. 200, pp. 330-352.

Newville, M. (2004) *Fundamentals of X-ray Absorption Fine Structure* [Online]. Available at http://web.mit.edu/course/5/5.062/oldwww/Fall04/XAS%20Fundamentals.pdf (Accessed 15th January 2019).

Ni, P., Zhang, Y., Chen, S., Gagnon, J. (2019) 'A melt inclusion study on volatile abundances in the lunar mantle', *Geochimica et Cosmochimica Acta*, vol. 249, pp. 17–41.

Nord, G. L., Lally, J. S., Heuer, A. H., Christie, J. M., Radcliffe, S. V., Griggs, D. T., Fisher, R. M. (1973) 'Petrologic study of igneous and metaigneous rocks from Apollo 15 and 16 using high voltage transmission electron microscopy', *Proceedings of the 4th Lunar and Planetary Science Conference.* Houston, March, vol. 1, pp. 953-970.

Norman, M. D. (2009) 'The lunar cataclysm: Reality or "mythconception"?', *Elements Magazine*, vol. 5, pp. 23-28.

Nyquist, L. D., Hubbard, N. J., Gast P. W., Bansal, B. M., Wiesmann, H., Jahn, B. (1973) 'Rb-Sr systematics for chemically defined Apollo 15 and 16 materials', *Proceedings of the 4th Lunar and Planetary Science Conference*. Houston, March 5-8, vol. 2, pp. 1823-1846.

Nyquist, L. E., Bansal, B. M., Wooden, J., Wiesmann, H. (1977) 'Sr-isotopic constraints on the peterogenesis of Apollo 12 mare basalts', *Proceedings of the 8th Lunar and Planetary Science Conference.* Houston, March 14-18, pp. 1383–1415.

Nyquist, L. E., Shih C.-Y., Wooden, J. L., Bansal, B. M., Wiesmann H. (1979) 'The Sr and Nd isotopic record of Apollo 12 basalts: Implications for lunar geochemical evolution', *Proceedings of the 10th Lunar and Planetary Science Conference.* Houston, March 19-23, pp. 77-114.

Nyquist, L. E., Bogard, D. D., Garrison, D. H., Bansal, B. M., Wiesmann H., Shih C-Y. (1991) 'Thermal resetting of radiometric ages. I: Experimental Investigations', *Proceedings of the 22nd Lunar and Planetary Science Conference*. Houston, March 18-22, pp. 985-986.

Oberli, F., Huneke, J. C., Wasserburg, G. J. (1979) 'U-Pb and K-Ar Systematics of Cataclysm and Precataclysm Lunar Impactites', *Proceedings of the 10th Lunar and Planetary Science Conference.* Houston, March 19-23, pp.940-942.

O'Neill, H. St. C. and Mavrogenes, J. A. (2002) 'The sulfide capacity and the sulphur content at sulfide saturation of silicate melts at 1400 °C and 1 bar', *Journal of Petrology*, vol. 43, no. 6, pp. 1049-1087.

Oppenheimer, C., Scaillet, B., Martin, R. S. (2011) 'Sulfur degassing from volcanoes: Source conditions, surveillance, plume chemistry and Earth system impacts', in Behrens, H., Webster, J. D. (ed[s]) *Reviews in Mineralogy and Geochemistry: Sulfur in Magmas and Melts: Its Importance for Natural and Technical Processes,* Virginia, The Mineralogical Society of America, vol. 73, pp. 363-421.

Oxford Instruments (2017) *EDS for SEM and FIB* [Online]. Available at https://www.oxford-instruments.com/products/microanalysis/energy-dispersive-x-ray-systems-eds-edx/eds-for-sem (Accessed 25th September 2017).

Pahlevan, K. and Stevenson, D. J. (2007) 'Equilibration in the aftermath of the lunar-forming giant impact', *Earth and Planetary Science Letters,* vol. 262, no. 3-4, pp. 438-449.

Paniello, R. C., Day, J. M. D., Moynier, F. (2012) 'Zinc isotopic evidence for the origin of the Moon', *Nature,* vol. 490, no. 7420, pp. 376-379.

Papanastassiou, D. A. and Wasserburg, G. J. (1971) 'Rb-Sr ages of igneous rocks from the Apollo 14 mission and the age of the Fra Mauro formation', *Earth and Planetary Science Letters,* vol. 12, no. 1, pp. 36-48.

Papanastassiou, D. A. and Wasserburg, G. J. (1973) 'Rb-Sr ages and initial strontium in basalts from Apollo 15', *Earth Planetary Science Letters,* vol. 17, no. 2, pp. 324-337.

Papike, J. J., Hodges, F. N., Bence, A. E., Cameron, N., Rhodes, J. M. (1976) 'Mare basalts: Crystal chemistry, mineralogy, and petrology', *Reviews of Geophysics and Space Physics,* vol. 14, no. 4, pp. 475-540.

Papike, J. J., Ryder, G., Shearer, C. K. (1998) 'Lunar Samples', in Papike, J. J. (ed[s]) *Reviews in Mineralogy: Planetary Materials,* vol. 36, pp. 5-1–5-234.

Papike, J., Taylor, L., Simon, S. (1991) 'Lunar Minerals', in Heiken, G., Vaniman, D. T., French, B. M. (ed[s]) *Lunar Sourcebook: A user's guide to the Moon*, New York, Cambridge University Press, pp. 121-181.

Papike, J. J., Ryder, G., Shearer, C. K. (1999) 'Lunar samples', in Papike, J. J. (ed[s]) *Reviews in Mineralogy: Planetary Materials,* Virginia, The Mineralogical Society of America, vol. 60, pp. 1-234.

Parat, F. and Holtz, F. (2004) 'Sulfur partitioning between apatite and melt and effect of sulfur on apatite solubility at oxidizing conditions', *Contributions to Mineralogy and Petrology,* vol. 147, no. 2, pp. 201-212.

Parat, F., Holtz, F., Streck, M. J. (2011) 'Sulfur-bearing Magmatic Accessory Minerals', in Behrens, H., Webster, J. D. (ed[s]) *Reviews in Mineralogy and Geochemistry: Sulfur in Magmas and Melts: Its Importance for Natural and Technical Processes*, Virginia, The Mineralogical Society of America, vol. 73, pp. 285-314.

Pendred, B. W. and Williams, I. P. (1968) 'The formation of the planets', *Icarus*, vol. 8, no. 1-3, pp. 129-137.

Peng, G., Luhr, J. F., McGee, J. J. (1997) 'Factors controlling sulfur concentrations in volcanic apatite' *American Mineralogist*, vol. 82, pp. 1210–1224.

Pepin, R. O., Basford J. R., Dragon J. C., Johnson N. L., Coscio M. R., Murthy V. R. (1974) 'Rare gases and trace elements in Apollo 15 drill fines: Depositional chronologies and K- Ar ages and production rates of spallation-porduced ^{3}He, ^{22}Ne and ^{38}Ar vrs depth', *Proceedings of the 5th Lunar and Planetary Science Conference*. Houston, March 18-22, pp. 2149-2184.

Peters, M., Strauss, H., Farquhar, J., Ockert, C., Eickmann, B., Jost, C. L. (2010) 'Sulfur cycling at the Mid-Atlantic Ridge: A multiple sulfur isotope approach', *Chemical Geology*, vol. 269, no. 3-4, pp. 180-196.

Petrowski, C., Kerridge, J. F., Kaplan, I. R. (1974) 'Light element geochemistry of the Apollo 17 site', *Proceedings of the 5th Lunar Science Conference.* Houston, March 18-22. M. I. T. Press, vol. 2, pp. 1939-1948.

Potts, N. J., Barnes, J. J., Tartèse, R., Franchi, I. A., Anand, M. (2018) 'Chlorine isotopic compositions of apatite in Apollo 14 rocks: Evidence for widespread vapor-phase metasomatism on the lunar nearside ~4 billion years ago', *Geochimica et Cosmochimica Acta*, vol. 230, pp. 46–59.

Pyle, J. M., Spear, F. S., Wark, D. A. (2002) 'Electron Microprobe Analysis of REE in Apatite, Monazite and Xenotime: Protocols and Pitfalls', in Kohn, M. J., Rakovan, J. Hughes, J. M. (ed[s]) *Reviews in Mineralogy and Geochemistry: Phosphates: Geochemical, Geobiological, and Materials Importance*, vol. 48, no. 1, pp. 337-362.

Ravel, B. and Newville, M. (2005) 'ATHENA, ARTEMIS, HEPHAESTUS: data analysis for X-ray absorption spectroscopy using IFEFFIT', *Journal of Synchrotron Radiation*, vol. 12, pp. 537-541.

Reed, S. J. B. (2005) *Electron microprobe analysis and scanning electron microscopy in geology*, Cambridge, Cambridge University Press.

Rees, C. E. and Thode, H. G. (1972) 'Sulphur concentrations and isotope ratios in lunar samples', *Proceedings of the 3rd Lunar Science Conference*. Houston, January 10-13. M. I. T. Press, vol. 2, pp. 1479-1485.

Rees, C. E. and Thode, H. G. (1974) 'Sulphur concentrations and isotope ratios in Apollo 16 and 17 samples', *Proceedings of the 5th Lunar Science Conference*. Houston, March 18-22. M. I. T. Press, vol. 2, pp. 1963-1973.

Reid, A. M., Brett, P. R. (1971) 'Sample descriptions', in Butler, P. (ed[s]) *Lunar Sample Information Catalog: Apollo 15*, Houston, Texas, NASA, pp. 47-292.

Reimer, L. (1998) *Scanning Electron Microscopy: Physics of Image Formation and Microanalysis*, Germany, Springer-Verlag.

Rhodes, J. M. and Hubbard, N. J. (1973) 'Chemistry, classification, and petrogenesis of Apollo 15 mare basalts', *Proceedings of the 4th Lunar and Planetary Science Conference*. Houston, March 5-8, vol. 2, pp. 1127-1148.

Rhodes, J. M., Blanchard D. P., Dungan M. A., Brannon J. C., Rodgers K.V. (1977) 'Chemistry of Apollo 12 mare basalts: Magma types and fractionation processes' *Proceedings of the 8th Lunar and Planetary Science Conference*. Houston, March 14-18, pp. 1305-1338.

Ridley, W. I. and Bass, M. N. (1971) 'Sample descriptions', in Butler, P. (ed[s]) *Lunar Sample Information Catalog: Apollo 15*, Houston, Texas, NASA, pp. 47-292.

Ringwood, A. E. and Kesson, S. E. (1976) 'A dynamic model for mare basalt petrogenesis', *Proceedings of the 7th Lunar and Planetary Science Conference*. Houston, March 15-19, vol. 2, pp. 1697-1722.

Ripley, E. M., Li, C., Moore, C. H., Elswick, E. R., Maynard, J. B., Paul, R. L., Sylvester, P., Seo, J. H., Shimizu, N. (2011) 'Analytical Methods for Sulfur Determination in Glasses, Rocks, Minerals and Fluid Inclusions', in Behrens, H., Webster, J. D. (ed[s]) *Reviews in Mineralogy and Geochemistry: Sulfur in Magmas and Melts: Its Importance for Natural and Technical Processes*, Virginia, The Mineralogical Society of America, vol. 73, pp. 9-39.

Robertson, M. and Gibson, S. (2014) 'The calibration, optimization and avoidance of artefacts of a cathodoluminescence system', in Coulson, I. M. (ed[s]) *Cathodoluminescence and its Application to Geoscience*, Mineralogical Association of Canada, vol. 45, pp. 11-28.

Robinson, K. L., Barnes, J. J., Nagashima, K., Thomen, A., Franchi, I. A. (2016) 'Water in evolved lunar rocks: evidence for multiple reservoirs', *Geochimica et Cosmochimica Acta*, vol. 188, pp. 244–60.

Rufu, R., Aharonson, O., Perets, H. B. (2017) 'A multiple-impact origin for the Moon', *Nature Geoscience*, vol. 10, no. 2, pp.89–94.

Russell, S. S., Zipfel, J., Folco, L., Jones, R., Grady, M. M., McCoy, T., Grossman, J. N. (2003) 'The Meteoritical Bulletin, No. 87, 2003 July', *Meteoritics & Planetary Science*, vol. 38, no. 7, pp. A189-A248.

Ryder, G. (1985a) *Catalog of Apollo 15 Rocks*, Part 1, NASA, Curatorial Branch Publication 72, JSC no. 20787, pp. 1-338.

Ryder, G. (1985b) *Catalog of Apollo 15 Rocks*, Part 3, NASA, Curatorial Branch Publication 72, JSC no. 20787, pp. 779-1296.

Ryder, G. (1985c) *Catalog of Apollo 15 Rocks*, Part 2, NASA, Curatorial Branch Publication 72, JSC no. 20787, pp. 339-778.

Saal, A. E., Hauri, E. H., Langmuir, C. H., Perfit, M. R. (2002) 'Vapour undersaturation in primitive mid-ocean-ridge basalt and the volatile content of earth's upper mantle', *Nature*, vol. 419, no. 6906, pp. 451-455.

Saal, A. E., Hauri, E. H., Cascio, M. L., Van Orman, J. A., Rutherford, M. C., Cooper, R. F. (2008) 'Volatile content of lunar volcanic glasses and the presence of water in the Moon's interior', *Nature*, vol. 454, no. 7201, pp. 192-195.

Saal, A. E., Hauri, E. H., Van Orman, J. A., Rutherford, M. J. (2013) 'Hydrogen isotopes in lunar volcanic glasses and melt inclusions reveal a carbonaceous chondrite heritage', *Science*, vol. 340, no. 6138, pp. 1317-1320.

Sarafian, A. R., Nielsen, S. G., Marschall, H. R., McCubbin, F. M., Monteleone, B. D. (2014) 'Early accretion of water in the inner solar system from a carbonaceous chondrite-like source', *Science*, vol. 346, no. 6209, pp. 623-626.

Sato, M., Hickling N. L., McLane J. E. (1973) 'Oxygen fugacity values of Apollo 12, 14, and 15 lunar samples and reduced state of lunar magmas', *Proceedings of the 4th Lunar and Planetary Science Conference.* Houston, March 5-8, vol. 4, pp. 1061-1079.

Schnare, D. W., Day, J. M. D., Norman, M. D., Lui, Y., Taylor, L. A. (2008) 'A laser-ablation ICP-MS study of Apollo 15 low-titanium olivine-normative and quartz-normative mare basalts', *Geochimica et Cosmochimica Acta*, vol. 72, no. 10, pp. 2556-2572.

Schofield, P. F., Smith, A. D., Mosselmans, J. F. W., Ohldag, H., Scholl, A., Raoux, S., Cressey, G., Cressey, B. A., Quinn, P. D., Kirk, C. A., Hogg, S. C. (2010) 'X-ray Spectromicroscopy of Mineral Intergrowths in the Santa Catharina Meteorite', *Geostandards and Geoanalytical Research*, vol. 34, no. 2, pp. 145-159.

Sha, L. K. (2000) 'Whitlockite solubility in silicate melts: some insights into lunar and planetary evolution', *Geochimica et Cosmochimica Acta*, vol. 64, no. 18, pp. 3217–3236.

Sharp, Z. D., Barnes, J. D., Brearley, A. J., Chaussidon, M., Fischer, T. P., Kamenetsky, V. S. (2007) 'Chlorine isotope homogeneity of the mantle, crust and carbonaceous chondrites', *Nature,* vol. 446, no. 7139, pp. 1062-1065.

Sharp, Z. D., Shearer, C. K., McKeegan, K. D., Barnes, J. D., Wang, Y. Q. (2010a) 'The chlorine isotope composition of the moon and implications for an anhydrous mantle', *Science,* vol. 329, no. 5995, pp. 1050-1053.

Sharp, Z. D., Barnes, J. D., Fischer, T. P., Halick, M. (2010b) 'An experimental determination of chlorine isotope fractionation in acid systems and applications to volcanic fumaroles', *Geochimica et Cosmochimica Acta,* vol. 74, no. 1, pp. 264-273.

Sharp, Z. D., Mercer, J. A., Jones, R. H., Brearley, A. J., Selverstone, J., Bekker, A., Stachel, T. (2013a) 'The chlorine isotope composition of chondrites and Earth', *Geochimica et Cosmochimica Acta,* vol. 107, pp. 189-204.

Sharp, Z., Williams, J., Shearer, C., Agee, C., McKeegan, K. (2016) 'The chlorine isotope composition of Martian meteorites 2. Implications for the early solar system and the formation of Mars', *Meteoritics & Planetary Science,* vol. 51, no. 11, pp. 2111-2126.

Shearer, C. K. and Papike, J. J. (2005) 'Early crustal building processes on the moon: Models for the petrogenesis of the magnesium suite', *Geochimica et Cosmochimica Acta,* vol. 69, no. 13, pp. 3445–3461.

Shearer, C. K., Burger, P. V., Guan, Y., Papike, J. J., Sutton, S. R., Atudorei, N.-V. (2012) 'Origin of sulfide replacement textures in lunar breccias. Implications for vapor element transport in the lunar crust', *Geochimica et Cosmochimica Acta,* vol. 83, pp. 138–158.

Silver, L. T. and Brett, P. R. (1971) 'Sample descriptions', in Butler, P. (ed[s]) *Lunar Sample Information Catalog: Apollo 15*, Houston, Texas, NASA, pp. 47-292.

Skinner, B. (1970) 'High Crystallization Temperatures Indicated for Igneous Rocks from Tranquillity Base', *Science,* vol. 167, no. 3918, pp. 652-654.

Smith, J. V., Anderson, A. T., Newton, R. C., Olsen, E. J., Crewe, A. V., Isaacson, M. S., Johnson, D., Wyllie, P. J. (1970) 'Petrologic history of the moon inferred from petrography, mineralogy and petrogenesis of Apollo 11 rocks', *Geochimica et Cosmochimica Acta Supplement* 1: pp. 897-925.

Snape, J. F., Nemchin, A. A., Bellucci, J. J., Whitehouse, M. J., Tartèse, R., Barnes, J. J., Anand, M., Crawford, I. A., Joy, K. H. (2016) 'Lunar basalt chronology, mantle differentiation and implications for determining the age of the Moon', *Earth and Planetary Science Letters,* vol. 451, pp. 149-158.

Snyder, G. A., Borg, L. E., Lee, D. C., Taylor, L. A., Nyquist, L. E., Halliday, A. N. (1997) 'Nd-Sr-Hf isotopic and geochronologic studies of Apollo 15 basalts', *Proceedings of the 28th Lunar and Planetary Science Conference*. Houston, March 17-21, pp. 1347-1348.

Sparks, R. S. J. (2003) 'Dynamics of magma degassing', in Oppenheimer, C., Pyle, D. M., Barclay, J. (ed[s]) *Volcanic Degassing*, London, The Geological Society, Special Publication 213, pp. 5–22.

Steenstra, E. S., Lin, Y., Dankers, D., Rai, N., Berndt, J., Matveev, S., van Westrenen, W. (2017a) 'The lunar core can be a major reservoir for volatile elements S, Se, Te and Sb', *Scientific Reports*, vol. 7, no. 14552, pp. 1-8.

Steenstra, E. S., Lin, Y., Rai, N., Jansen, M., van Westrenen, W. (2017b) 'Carbon as the dominant light element in the lunar core', *American Mineralogist*, vol. 102, no. 1, pp. 92-97.

Steenstra, E. S, Seegers, A. X., Eising, J., Tomassen, B. G. J., Webers, F. P. F., Berndt, J., Klemme, S., Matveev, S., van Westrenen, W. (2018) 'Evidence for a sulfur-undersaturated lunar interior from the solubility of sulfur in lunar melts and sulfide-silicate partitioning of siderophile elements', *Geochimica et Cosmochimica Acta*, vol. 231, pp. 130-156.

Stephant, A., Anand, M., Zhao, X., Chan, Q. H. S., Bonifacie, M., Franchi, I. A. (2019) 'The chlorine isotopic composition of the Moon: Insights from melt inclusions', *Earth and Planetary Science Letters*, vol. 523, pp. 1-12.

Stern, R. A. (2009) 'An introduction to secondary ion mass spectrometry (SIMS) in geology', in Fayek, M. (ed[s]) *Secondary Ion Mass Spectrometry in the Earth Sciences*, Mineralogical Association of Canada, Québec, vol. 41, pp. 1-18.

Stock, M. J., Humphreys, M. C. S., Smith, V. C., Johnson, R. D., Pyle, D. M. (2015) 'New constraints on electron-beam induced halogen migration in apatite', *American Mineralogist*, vol. 100, no. 1, pp. 281-293.

Stock, M. J., Humphreys, M. C. S., Smith, V. C., Isaia, R., Pyle, D. M. (2016) 'Late-stage volatile saturation as a potential trigger for explosive volcanic eruptions', *Nature Geoscience*, vol. 9, pp. 249–254.

Stormer Jr, J. C., Pierson, M. L., Tacker, R. C. (1993) 'Variation of F and Cl X-ray intensity due to anisotropic diffusion in apatite during electron microprobe analysis', *American Mineralogist*, vol. 78, no. 5-6, pp. 641-648.

Streck, M. J. and Dilles, J. H. (1998) 'Sulfur evolution of oxidized arc magmas as recorded in apatite from a porphyry copper batholith', *Geology*, vol. 26; no. 6, pp. 523–526.

Swann, G. A., Trask, N. J., Hait, M. H., Sutton, R. L. (1971a) 'Geologic setting of the Apollo 14 samples', *Science*, vol. 173, no. 3998, pp. 716-719.

Swann, G. A., Hait M. H., Schaber G. C., Freeman V. L., Ulrich G. E., Wolfe E. W., Reed V. S., Sutton R. L. (1971b) 'Preliminary description of Apollo 15 sample environments', U.S.G.S. Interagency Report: 36, pp. 19-216.

Tartèse, R. and Anand, M. (2013) 'Late delivery of chondritic hydrogen into the lunar mantle: Insights from mare basalts', *Earth and Planetary Science Letters*, vol. 361, pp. 480-486.

Tartèse, R., Anand, M., Barnes, J. J., Starkey, N. A., Franchi, I. A., Sano, Y. (2013) 'The abundance, distribution, and isotopic composition of Hydrogen in the Moon as revealed by basaltic lunar samples: Implications for the volatile inventory of the Moon', *Geochimica et Cosmochimica Acta*, vol. 122, pp. 58-74.

Tartèse, R., Anand, M., McCubbin, F. M., Elardo, S. M., Shearer, C. K., Franchi, I. A. (2014a) 'Apatites in lunar KREEP basalts: The missing link to understanding the H isotope systematics of the Moon', *Geology*, vol. 42, no. 4, pp. 363-366.

Tartèse, R., Anand, M., Joy, K. H., Franchi, I. A. (2014b) 'H and Cl isotope systematics of apatite in brecciated lunar meteorites Northwest Africa 4472, Northwest Africa 773, Sayh al Uhaymir 169, and Kalahari 009', *Meteoritics & Planetary Science*, vol. 49, no. 12, pp. 2266-2289.

Taylor, G. J., Warren, P., Ryder, G., Delano, J., Pieters, C., Lofgren, G. (1991) 'Lunar Rocks', in Heiken, G., Vaniman, D. T., French, B. M. (ed[s]) *Lunar Sourcebook: A user's guide to the Moon*, New York, Cambridge University Press, pp. 183-284.

Taylor, L. A. and McCallister, R. H. (1972) 'An experimental investigation of the significance of zirconium partioning in lunar ilmenite and ulvöspinel, *Earth and Planetary Science Letters*, vol. 17, no. 1, pp. 105-109.

Taylor, L. A., Onorato P. I. K., Uhlmann D. R. (1977) 'Cooling rate estimations based on kinetic modeling of Fe-Mg diffusion in olivine', *Proceedings of the 8th Lunar Science Conference*. Houston, March 14-18, vol. 2, pp. 1581-1592.

Taylor, L. A., Patchen, A., Mayne, R. G., Taylor, D.-H. (2004) 'The most reduced rock from the moon, Apollo 14 basalt 14053: Its unique features and their origin', *American Mineralogist*, vol. 89, no. 11-12, pp. 1617-1624.

Taylor, S. R., Pieters, C. M., MacPherson, G. J. (2006) 'Earth-moon system, planetary science, and lessons learned', in Jolliff, B. L., Wieczorek, M. A., Shearer, C. K., Neal, C. R. (ed[s]) *Reviews in Mineralogy and Geochemistry: New Views of the Moon*, Virginia, The Mineralogical Society of America, vol. 60, pp. 657–704.

Taylor, S. R. (2007) ‘The Moon’, in McFadden, L. A., Johnson, T. V., Weissman, P. R. (ed[s]) *Encyclopedia of the Solar System*, Amsterdam, Elsevier, vol. 2, pp. 227-250.

Tera, F., Papanastassiou, D. A., Wasserburg, G. J. (1974) Isotopic evidence for a terminal lunar cataclysm, *Earth and Planetary Science Letters*, vol. 22, pp. 1-21.

Terada, K., Anand, M., Sokol, A. K., Bischoff, A., Sano, Y. (2007) ‘Cryptomare magmatism 4.35 Gyr ago recorded in lunar meteorite Kalahari 009’, *Nature*, vol. 450, pp. 849-852.

The European Synchrotron Radiation Facility (2006) *Database Inorganic Sulfur Compounds* [Online]. Available at https://www.esrf.eu/home/UsersAndScience/Experiments/XNP/ID21/php/Database-SCompounds.html (Accessed 7th December 2018).

Thode, H. G and Rees, C. E. (1971) ‘Measurement of sulphur concentrations and the isotope ratios $^{33}S/^{32}S$, $^{34}S/^{32}S$ and $^{36}S/^{32}S$ in Apollo 12 samples’, *Earth and Planetary Science Letters*, vol. 12, no. 4, pp. 434-438.

Thode, H. G and Rees, C. E. (1972) ‘Sulphur concentrations and isotope ratios in Apollo 14 and 15 Samples’, in Chamberlain, J. W. and Watkins, C. (ed[s]) *The Apollo 15 Lunar Samples*, Houston, The Lunar Science Institute, pp. 402–403.

Touboul, M., Kleine, T., Bourdon, B., Palme, H., Wieler, R. (2007) ‘Late formation and prolonged differentiation of the moon inferred from W isotopes in lunar metals’, *Nature*, vol. 450, pp. 1206-1209.

Touboul, M., Puchtel, I. S., Walker, R. J. (2012) ‘^{182}W evidence for long-term preservation of early mantle differentiation products’, *Science*, vol. 335, no. 6072, pp. 1065-1069.

Touboul, M., Puchtel, I. S., Walker, R. J. (2015) ‘Tungsten isotopic evidence for disproportionate late accretion to the Earth and Moon’, *Nature*, vol. 520, pp. 530-533.

Treiman, A. H., Boyce, J. W., Gross, J., Guan, Y., Eiler, J. M., Stolper, E. M. (2014) ‘Phosphate-halogen metasomatism of lunar granulite 79215: Impact-induced fractionation of volatiles and incompatible elements’, *American Mineralogist*, vol. 99, no. 10, pp. 1860-1870.

Ustunisik, G., Nekvasil, H., Lindsley, D. H., McCubbin, F. M. (2015) ‘Degassing pathways of Cl-, F-, H-, and S-bearing magmas near the lunar surface: Implications for the composition and Cl isotopic values of lunar apatite’, *American Mineralogist*, vol. 100, no. 8-9, pp. 1717-1727.

van der Heide, P. (2014) *Secondary Ion Mass Spectrometry : An Introduction to Principles and Practices*, New Jersey, John Wiley & Sons Incorporated.

Van Hoose, A. E., Streck, M. J., Pallister, J. S., Wälle, M. (2013) 'Sulfur evolution of the 1991 Pinatubo magmas based on apatite', *Journal of Volcanology and Geothermal Research*, vol. 257, pp. 72–89.

Vaniman, D., Dietrich, J., Taylor, G. J., Heiken, G. (1991) 'Exploration, samples, and recent concepts of the Moon', in Heiken, G., Vaniman, D. T., French, B. M. (ed[s]) *Lunar Sourcebook: A user's guide to the Moon*, New York, Cambridge University Press, pp. 6-26.

Wadhwa, M. (2008) 'Redox Conditions on Small Bodies, the Moon and Mars', in MacPherson, G. J. (ed[s]) *Reviews in Mineralogy and Geochemistry: Oxygen in the Solar System*, Virginia, The Mineralogical Society of America, vol. 68, no. 1, pp. 493-510.

Walker, D., Longhi, J., Lasaga, A. C., Stolper, E. M., Grove, T. L., Hays, J. F. (1977) 'Slowly cooled microgabbros 15555 and 15065', *Proceedings of the 8th Lunar Science Conference*. Houston, March 14-18, vol. 2, pp. 1521-1547.

Wallace, P. and Carmichael, I. S. E. (1992) 'Sulfur in basaltic magmas', *Geochimica et Cosmochimica Acta*, vol. 56, pp. 1863-1874.

Wang, K. and Jacobsen, S. B. (2016) 'Potassium isotopic evidence for a high-energy giant impact origin of the Moon', *Nature*, vol. 538, no. 7626, pp. 487-490.

Wang, Y., Hsu, W., Guan, Y. (2019) 'An extremely heavy chlorine reservoir in the Moon: Insights from the apatite in lunar meteorites', *Scientific Reports*, vol. 9, no. 5727, pp. 1-8.

Warner, J. L., Phinney, W. C., Bickel, C. E., Simonds, C. H. (1977) 'Feldspathic granulitic impactites and pre-final bombardment lunar evolution', *Proceedings of the 8th Lunar Science Conference*. Houston, March 14-18, vol. 2, pp. 2051-2066.

Warren, P. H., Wasson, J. T. (1979) 'The origin of KREEP', *Reviews of Geophysics*, vol. 17, no. 1, pp.73-88.

Warren, P. H. (1993) 'A concise compilation of petrologic information on possibly pristine nonmare Moon rocks', *American Mineralogist*, vol. 78, pp. 360-376.

Wasserburg, G. J. and Papanastassiou, D. A. (1971) 'Age of an Apollo 15 mare basalt: lunar crust and mantle evolution', *Earth and Planetary Science Letters*, vol. 13, no. 1, pp. 97-104.

Weber, R. C., Lin, P–Y., Garnero, E. J., Williams, Q., Lognonné, P. (2011) 'Seismic Detection of the Lunar Core', *Science*, vol. 331, no. 6015, pp. 309–312.

White, William M. (2013) *Geochemistry*, Oxford, John Wiley & Sons, Ltd.

Wiechert, U., Halliday, A. N., Lee, D. C., Snyder, G. A., Taylor, L. A., Rumble, D. (2001) 'Oxygen isotopes and the Moon-forming Giant Impact', *Science*, vol. 294, no. 5541, pp. 345-348.

Wieczorek, M. A., Jolliff, B. L., Khan, A., Prithchard, M. E., Weiss, B. P., Williams, J. G., Hood, L. L., Righter, K., Neal, C. R., Shearer, C. K., McCallum, I. S., Tompkins, S., Hawke, B. R., Peterson, C., Gillis, J., Bussey, D. B. (2006) 'The constitution and structure of the lunar interior', in Jolliff, B. L., Wieczorek, M. A., Shearer, C. K., Neal, C. R. (ed[s]) *Reviews in Mineralogy and Geochemistry: New Views of the Moon*, Virginia, The Mineralogical Society of America, vol. 60, pp. 221-364.

Wiggins, S. E., Johnson, B. C., Bowling, T. J., Melosh, H. J., Silber, E. A. (2019) 'Impact Fragmentation and the Development of the Deep Lunar Megaregolith', *Journal of Geophysical Research: Planets*, vol. 124, no. 4, pp. 941-957.

Wilke, M., Jugo, P. J., Klimm, K., Susini, J., Botcharnikov, R., Kohn, S. C., Janousch, M. (2008) 'The origin of S^{4+} detected in silicate glasses by XANES', *American Mineralogist*, vol. 93, no. 1, pp. 235-240.

Wilke, M., Klimm, K., Kohn, S. C. (2011) 'Spectroscopic studies on the sulfur speciation in synthetic and natural glasses', in Behrens, H., Webster, J. D. (ed[s]) *Reviews in Mineralogy and Geochemistry: Sulfur in Magmas and Melts: Its Importance for Natural and Technical Processes*, Virginia, The Mineralogical Society of America, vol. 73, pp. 41-78.

Williams, J. T., Shearer, C. K., Sharp, Z. D., Burger, P. V., McCubbin, F. M., Santos, A. R., Agee, C. B., McKeegan, K. D. (2016) 'The chlorine isotopic composition of Martian meteorites 1: Chlorine isotope composition of Martian mantle and crustal reservoirs and their interactions', *Meteoritics & Planetary Science,* vol. 51, no. 11, pp. 2092-2110.

Wilshire, H. G. and Brett, P. R. (1971) 'Sample descriptions', in Butler, P. (ed[s]) *Lunar Sample Information Catalog: Apollo 15*, Houston, Texas, NASA, pp. 47-292.

Wing, B. A. and Farquhar, J. (2015) 'Sulfur isotope homogeneity of lunar mare basalts', *Geochimica et Cosmochimica Acta,* vol. 170, pp. 266-280.

Wlotzka, F. (1993) 'A weathering scale for the ordinary chondrites'. *Meteoritics,* vol. 28, no. 3, pp. 460-460.

Wojdyr, M. (2010) Fityk: A general-purpose peak fitting program, *Journal of Applied Crystallography*, vol. 43, pp. 1126–1128.

Wood, J. A., Dickey, J. S., Marvin, U. B., Powell, B. N. (1970) 'Lunar anorthosites and a geophysical model of the moon', *Geochimica et Cosmochimica Acta Supple*ment, vol. 1, pp. 965–968.

Wood, J. A. (1986) 'Moon over Mauna Loa: A review of hypotheses of formation of Earth's moon', in Hartmann, W. K., Phillips, R. J., Taylor, G. J. (ed[s]) *Origin of the Moon*, Houston, Lunar and Planetary Institute, pp. 17-55.

Yang, W., Hu, S., Zhang, J. C., Hao, J. L., Lin, Y. T. (2015) 'NanoSIMS analytical technique and its applications in earth sciences', *Science China Earth Sciences*, vol. 58, no. 10, pp. 1758-1767.

Yokoyama, Y., Reyss J. L., Guichard F. (1974) '^{22}Na-^{26}Al chronology of lunar surface processes', *Proceedings of the 5th Lunar and Planetary Science Conference.* Houston, March 18-22, vol. 2, pp. 2231-2247.

Young, E. D., Kohl, I. E., Warren, P. H., Rubie, D. C., Jacobson, S. A., Morbidelli, A. (2016) 'Oxygen isotopic evidence for vigorous mixing during the Moon-forming giant impact', *Science*, vol. 351, no. 6272, pp. 493-496.

Zhang, J., Dauphas, N., Davis, A. M., Leya, I., Fedkin, A. (2012) 'The proto-Earth as a significant source of lunar material', *Nature Geoscience*, vol. 5, pp. 251-255.

Zhang, J., Lin, Y., Yang, W., Shen, W., Hao, J., Hu, S., Cao, M. (2014) 'Improved precision and spatial resolution of sulfur isotope analysis using NanoSIMS', *Journal of Analytical Atomic Spectrometry*, vol. 29, no. 10, pp. 1934-1943.

Zhou, W. and Wang, Z. L. (2006) *Scanning Microscopy for Nanotechnology: Techniques and Applications*, New York, Springer.

Appendix A

A.1. Proof of concept: lunar meteorite SaU 169

In preparation for S and Cl analyses of lunar apatites in Apollo samples, apatites in a thin section sample of lunar meteorite SaU 169 (courtesy of Mahesh Anand, The Open University) were used as a proof of concept for the development of the two new S protocols and a Cl protocol. This included devising a new S and Cl isotope measurement method for lunar apatite with nano-scale secondary ion mass spectrometry (NanoSIMS (Cameca 50L ion microprobe)) that had been modified from an existing Cl isotope protocol (Tartèse et al., 2014b; Barnes et al., 2016) (see Chapter Two, sections 2.4.3.1 and 2.4.3.2). A new protocol was also developed to measure the oxidation state of S in lunar apatite with X-ray absorption near-edge structure (XANES) spectroscopy at the S K-edge at Diamond Light Source (using beamline I18) (see Chapter Five, section 5.2.3.2). This was to ensure that the S and Cl protocols developed for this project were feasible and would result in worthwhile results with levels of precision similar to those reported in the scientific literature.

A.1.1. Brief sample description: Sayh al Uhaymir 169 – Impact melt breccia

Sayh al Uhaymir (SaU) 169 is a lunar meteorite sample that was not collected from the Moon but is a hot desert 'find', discovered in Oman. The terrestrial weathering of the meteorite has been classified as W1 (Russell et al., 2003) which means that, based on a weathering scale introduced for ordinary chondrites, it has undergone only very minor oxidation around metal rims with the possibility of minor oxide veins being present (Wlotzka, 1993). The sample has both the highest abundance of incompatible elements (300 to 1,000 times that of CI chondrites) and is the most rare earth element-rich of all meteorites studied to date (Korotev et al, 2009).

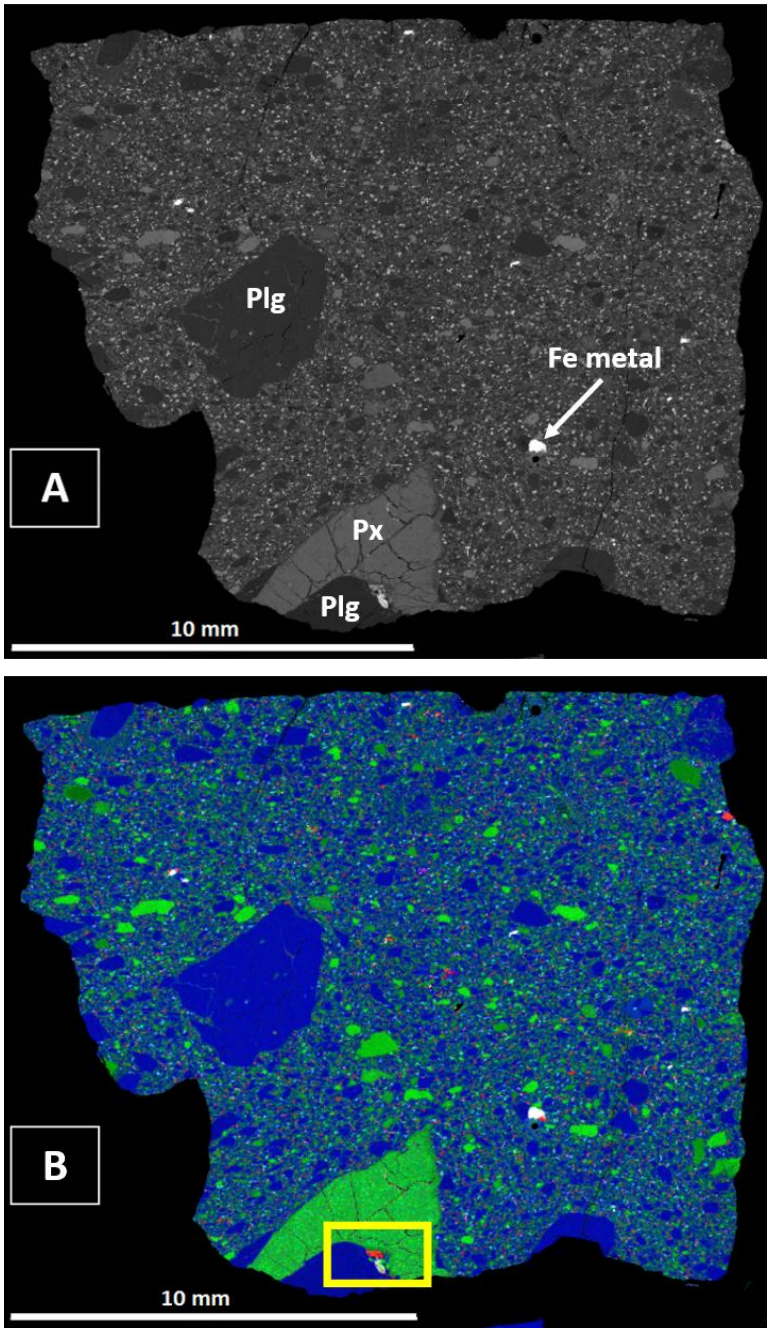

Figure A.1. Lunar meteorite sample SaU 169. **A)** Backscatter electron (BSE) montage map. Where Plg is plagioclase and Px is pyroxene. **B)** False colour image, where blue is Al, green is Mg, red is P and white is Fe-metal. The yellow box in **B)** highlights the location of the apatite shown in Figure A.2. (Images courtesy of Romain Tartèse).

The meteorite is comprised of two principal lithological fragments, including an impact melt breccia and a regolith breccia that are of different chemical compositions (Gnos et al., 2004). The thin section analysed in this study is the impact melt breccia (IMB) fragment. The IMB is composed of pyroxene, plagioclase, ilmenite, very high potassium (VHK) clasts, large Fe-metal clasts, minor apatite and merrillite and trace amounts of troilite

(Figure A.1). For the purpose of this project, the apatite grains of SaU 169 were the central focus for S and Cl measurement feasibility. The apatites are large (up to 200 µm in the longest dimension), always anhedral and contain many large cracks and fractures.

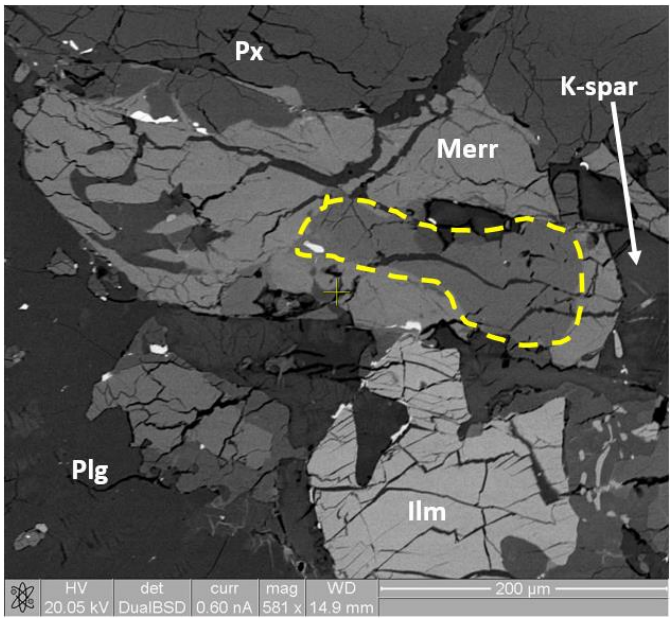

Figure A.2. Apatite in Lunar meteorite SaU 169. The backscatter electron image shows a large apatite grain highlighted by the dashed yellow line that is surrounded by merrillite (Merr), potassium feldspar (K-spar), ilmenite (Ilmenite), plagioclase (Plg) and pyroxene (Px). (Image courtesy of Romain Tartèse).

A.1.2. S and Cl NanoSIMS and S-XANES results for SaU 169

The results of the S and Cl abundance and isotope measurements and the oxidation state of S measurements in lunar apatite are shown in Table A.1. The S abundance of four different apatite grains is between ~240 ppm and ~480 ppm. The $\delta^{34}S$ values vary from -1.6 ± 3.3‰ to +29.9 ± 3.5‰. The Cl abundance of the same four apatite grains (measured on the same position (spot) of the grain as the S measurements) is between ~9,980 ppm Cl and ~12,060 ppm, whereas the $\delta^{37}Cl$ value is between 12.3 ± 0.4‰ and 19.8 ± 0.6‰.

Table A.1. NanoSIMS data for sulfur and chlorine abundances and isotopes and S-XANES data for the oxidation state of S in lunar apatite of SaU 169. $\delta^{34}S$ is calculated from the measurement of $^{34}S/^{32}S$ ratios and $\delta^{37}Cl$ is calculated from the measurement of $^{37}Cl/^{35}Cl$ ratios, where $\delta^{34}S$ is relative to V-CDT and $\delta^{37}Cl$ is relative to SMOC. Sulfur and chlorine abundances are calculated relative to apatite standards with known values. The last column of the table shows the S-XANES data, where avg. $S^{6+}/\Sigma S_{tot}$ is the average S^{6+} to total S content of many scans across an apatite grain.

Analysis I.D.	$\delta^{34}S_{(V\text{-}CDT)}$ (‰)	2σ (‰)	S (ppm)	2σ (ppm)	$\delta^{37}Cl_{(SMOC)}$ (‰)	2σ (‰)	Cl (ppm)	2σ (ppm)	Avg. $S^{6+}/\Sigma S_{tot}$
SaU 169 Ap7	1.4	4.2	245	19	12.3	0.4	9978	444	0.86
SaU 169 Ap14	6.8	3.6	340	26	14.0	0.4	12063	537	1.00
SaU 169 Ap15	29.9	3.5	477	37	15.9	0.5	10741	478	1.00
SaU 169 Ap20	-1.6	3.3	241	19	19.8	0.6	10751	478	-

A.1.3. Assessment of the S and Cl measurement methods

Previous Cl analyses of apatite in SaU 169 have been carried out by Tartèse et al. (2014b). Chlorine abundance was reported to be between ~6,270 ppm Cl and ~10,050 ppm Cl, with $\delta^{37}Cl$ values between 5.3 ± 2.2‰ and 11.5 ± 2.3‰ across three different apatite grains. This compares well with the Cl results of the new Cl measurement protocol of this study where measurements were made at different spots on different apatite grains of the same sample. The uncertainty (see Chapter Two, section 2.4.4.3 for derivation) of the Cl isotope measurements made in this study (average of ~0.5‰) is a slight improvement on that recorded by Tartèse et al. (2014b) (average of ~2.4‰).

Tartèse et al. (2014b) also measured the S contents of certain apatite grains in SaU 169 with electron probe microanalysis (EPMA) and reported levels that were barely detectable. With NanoSIMS, which is capable of detection on the parts per billion level, the current project was able to record relatively low contents of S (241–477 ppm S) with a percentage uncertainty of <8%. The sulfur isotopes of apatites within SaU 169 have not previously been measured, therefore, a direct sulfur isotope comparison is not possible. However, when compared with the Cl isotope results, the uncertainty associated with the S isotope measurements is higher. This is not entirely unexpected because the Cl isotopes were measured on apatites containing up to ~12,060 ppm Cl, whereas S isotopes were measured on apatite S contents of up to ~50 times lower than that value (~240 ppm S). The poorer

counting statistics on low S abundance samples is, therefore, the reason for the higher uncertainties associated with the S isotope measurements.

For S-XANES, sample SaU 169 was also analysed before the Apollo samples in order to avoid prolonged-exposure of the beam whilst, for example, achieving an appropriate resolution for the XRF element maps, reducing the intensity of the phosphorous signal that reached the detector and setting up an appropriate beam size and energy range for collecting spectra (see Chapter Five, section 5.2.3.2.). The S-XANES results for the apatites of SaU 169 show that S^{6+} is dominant ($S^{6+}/\Sigma S_{tot}$ ratio of 0.86–1.00) (Table A.1), suggesting that S oxidation might have occurred under terrestrial conditions as the meteorite lay in the hot desert.

The measurement of apatites in SaU 169 for both NanoSIMS and S-XANES analyses demonstrate that the newly developed S and Cl protocols are feasible. The accuracy of the Cl measurements (i.e. when compared with Tartèse et al. (2014b)) provide quantitative reassurance that the NanoSIMS measurement methods for both Cl and S are reliable and reproducible. Likewise, the precision attainable on Cl and S (with lower abundances) is considered to be acceptable given the levels of precision reported for other Cl analyses (e.g. Tartèse et al., 2014b; Barnes et al., 2016, 2019, Potts et al., 2018). Whilst S-XANES has not previously been performed on apatites of SaU 169, and so a direct comparison with another study is not possible, the measurements demonstrated that S contents of <~250 ppm could be detected with an acceptable signal to noise (S/N) ratio. Both analytical protocols were deemed suitable to be performed on the precious Apollo samples.

Appendix B

Table B.1. The 13 anion method used for calculating the stoichiometry of an apatite mineral for data acquired from EPMA. This example shows the EPMA data reduction for Apollo sample 79215,50.

Oxide	Wt.%	Molecular wt.	Wt.% / Molecular wt.	Moles of oxygen	Normalized to oxygen	Multiply by cations
P_2O_5	42.77	141.94	0.30	1.51	7.51	3.00
SiO_2	0.15	60.09	0.00	0.00	0.02	0.01
La_2O_3	0.00	325.82	0.00	0.00	0.00	0.00
Ce_2O_3	0.03	328.20	0.00	0.00	0.00	0.00
Nd_2O_3	0.10	336.48	0.00	0.00	0.00	0.00
Y_2O_3	0.06	225.82	0.00	0.00	0.00	0.00
FeO	0.15	71.85	0.00	0.00	0.01	0.01
MnO	0.02	70.94	0.00	0.00	0.00	0.00
MgO	0.14	40.31	0.00	0.00	0.02	0.02
CaO	55.37	56.00	0.99	0.99	4.93	4.93
Na_2O	0.00	62.00	0.00	0.00	0.00	0.00
SO_2	0.04	64.07	0.00	0.00	0.01	0.00
F	2.09	19.00	0.11	0.11	0.55	0.55
Cl	0.76	35.47	0.02	0.02	0.11	0.11
Total	101.68		**Total O moles**	2.51	**Sum of cations**	7.98
O=F+Cl	1.05				**Sum of anions**	0.65
Total	100.63		**Normalization factor based on 13 anions**	4.98	**Estimated OH***	0.35

*Assumes that F+Cl+OH equals 1 apfu.

Table B.2. Electron microprobe analyses results (wt.%) of apatites analysed in lunar meteorite SaU 169 and feldspathic granulitic impactite Apollo sample 79215,50. The data reduction process involved normalising the acquired data to a total of 13 anions and assumes F + Cl + OH = 1 apfu.

Sample	**SaU 169**	**79215,50**					
Analysis	**Ap15**	**Ap002**	**Ap001a**	**Ap004**	**Ap005**	**Ap009**	**Ap010**
P_2O_5	41.55	32.92	42.19	43.30	42.36	43.31	42.77
SiO_2	0.51	0.16	0.19	0.12	42.36	0.19	0.15
La_2O_3	0.05	0.03	0.04	0.00	0.05	0.03	0.00
Ce_2O_3	0.21	0.02	0.05	0.02	0.03	0.05	0.03
Nd_2O_3	0.06	0.01	0.03	0.00	0.00	0.00	0.10
Y_2O_3	0.15	0.03	0.06	0.05	0.06	0.08	0.06
FeO	0.28	0.22	0.42	0.18	0.35	0.26	0.15
MnO	0.04	0.03	0.02	0.02	0.01	0.03	0.02
MgO	0.19	0.10	0.16	0.20	0.14	0.16	0.14
CaO	53.76	50.80	54.43	55.30	55.16	54.74	55.37
Na_2O	0.05	0.00	0.00	0.00	0.00	0.00	0.00
SO_2	0.12	0.01	0.04	0.02	0.04	0.03	0.04
F	2.88	3.39	3.74	3.70	3.77	3.64	2.09
Cl	1.45	0.49	0.71	0.70	0.73	0.65	0.76
Total	101.27	88.21	102.08	103.61	145.06	103.17	101.68
O=F+Cl	1.54	1.54	1.73	1.72	1.75	1.68	1.05
Total	99.73	86.67	100.35	101.89	143.31	101.49	100.63
Structural formulae based on 13 anions							
P	2.98	2.79	3.00	3.02	1.91	3.03	3.00
Si	0.04	0.02	0.02	0.01	2.26	0.02	0.01
La	0.00	0.00	0.00	0.00	0.00	0.00	0.00
Ce	0.00	0.00	0.00	0.00	0.00	0.00	0.00
Nd	0.00	0.00	0.00	0.00	0.00	0.00	0.00
Y	0.01	0.00	0.00	0.00	0.00	0.00	0.00
Fe	0.02	0.02	0.03	0.01	0.02	0.02	0.01
Mn	0.00	0.00	0.00	0.00	0.00	0.00	0.00
Mg	0.02	0.01	0.02	0.02	0.01	0.02	0.02
Ca	4.88	5.45	4.90	4.89	3.16	4.85	4.93
Na	0.01	0.00	0.00	0.00	0.00	0.00	0.00
S	0.01	0.00	0.00	0.00	0.00	0.00	0.00
Total cations	7.98	8.30	7.98	7.96	7.37	7.94	7.97
F	0.77	1.07	0.99	0.96	0.64	0.95	0.55
Cl	0.21	0.08	0.10	0.10	0.07	0.09	0.11
Total anions	0.98	1.16	1.09	1.06	0.70	1.04	0.66
OH	0.02	0.00	0.00	0.00	0.00	0.00	0.35

Table B.3. Apatite reference standard (Francis McCubbin, Johnson Space Centre, *pers. comm.*) calibration data used for calculating S abundance within lunar apatite samples.

Date	Apatite standard	$^{32}S/^{18}O$	S (ppm)	2σ (S ppm)
Jan-18	Ap005	0.356	392	100
	Ap005	0.360	392	100
	Ap005	0.403	392	100
	Ap005	0.417	392	100
	Ap005	0.417	392	100
	Ap005	0.346	392	100
	Ap005	0.326	392	100
	Ap005	0.422	392	100
	Ap005	0.403	392	100
	Ap004	1.219	1627	243
	Ap018	4.602	3827	250
Jun-18	Ap005	0.335	392	100
	Ap005	0.326	392	100
	Ap005	0.345	392	100
	Ap005	0.334	392	100
	Ap005	0.329	392	100
	Ap004	1.221	1627	243
	Ap018	4.454	3827	250
Aug-18	Ap005	0.328	392	100
	Ap005	0.279	392	100
	Ap005	0.285	392	100
	Ap005	0.311	392	100
	Ap005	0.305	392	100
	Ap005	0.312	392	100
	Ap005	0.314	392	100
	Ap005	0.339	392	100
	Ap005	0.362	392	100
	Ap005	0.376	392	100
	Ap005	0.391	392	100
	Ap005	0.386	392	100
	Ap005	0.402	392	100
	Ap005	0.412	392	100
	Ap005	0.409	392	100
	Ap005	0.368	392	100
	Ap005	0.355	392	100
	Ap004	1.151	1627	243
	Ap018	4.241	3827	250
Dec-18	Ap005	0.421	392	100
	Ap005	0.452	392	100
	Ap004	1.358	1627	100
	Ap004	1.354	1627	243
	Ap018	4.485	3827	250
Mar-19	Ap005	0.420	392	100
	Ap005	0.420	392	100
	Ap005	0.383	392	100

Table B.3. Continued				
Mar-19	Ap005	0.368	392	100
	Ap005	0.385	392	100
	Ap005	0.405	392	100
	Ap005	0.398	392	100
	Ap005	0.392	392	100
	Ap005	0.411	392	100
	Ap005	0.379	392	100
	Ap004	1.570	1627	243
	Ap018	5.739	3827	250
	Ap003	1.608	1457	258
	Ap003	1.747	1457	258

Table B.4. Apatite reference standard (Francis McCubbin, Johnson Space Centre, *pers. comm*.) calibration data used for calculating Cl abundance within lunar apatite samples.

Date	**Apatite standard**	**$^{35}Cl/^{18}O$**	**Cl (ppm)**	**2σ (Cl ppm)**
Jan-18	Ap004	3.036	3182	351
	Ap004	2.943	3182	351
	Ap004	2.936	3182	351
	Ap004	2.966	3182	351
	Ap004	2.932	3182	351
	Ap004	2.372	3182	351
	Ap005	8.512	9044	1306
	Ap018	0.685	1497	306
May-18	Ap004	2.793	3182	351
	Ap004	2.554	3182	351
	Ap004	2.443	3182	351
	Ap004	2.260	3182	351
	Ap004	2.433	3182	351
	Ap004	2.544	3182	351
	Ap004	2.690	3182	351
	Ap004	2.637	3182	351
	Ap004	2.537	3182	351
	Ap004	2.607	3182	351
	Ap004	2.677	3182	351
	Ap004	2.617	3182	351
	Ap004	2.376	3182	351
	Ap004	2.495	3182	351
	Ap004	2.461	3182	351
	Ap004	2.386	3182	351
	Ap005	5.504	9044	1306
	Ap018	0.908	1497	306
Aug-18	Ap004	2.685	3182	351
	Ap004	2.685	3182	351
	Ap004	2.650	3182	351
	Ap004	2.635	3182	351
	Ap004	2.670	3182	351
	Ap004	2.410	3182	351

Table B.4. Continued

Aug-18	Ap004	2.681	3182	351
	Ap004	2.596	3182	351
	Ap004	2.779	3182	351
	Ap004	2.734	3182	351
	Ap005	6.075	9044	1306
	Ap018	0.965	1497	306
Oct-18	Ap004	2.377	3182	351
	Ap004	2.378	3182	351
	Ap004	2.336	3182	351
	Ap004	2.430	3182	351
	Ap004	2.488	3182	351
	Ap004	2.459	3182	351
	Ap004	2.440	3182	351
	Ap005	6.285	9044	1306
	Ap018	0.661	1497	306
Dec-18	Ap004	2.394	3182	351
	Ap004	2.465	3182	351
	Ap004	2.452	3182	351
	Ap004	2.697	3182	351
	Ap005	6.656	9044	1306
	Ap018	0.667	1497	306
Mar-19	Ap004	2.684	3182	351
	Ap004	2.775	3182	351
	Ap004	2.438	3182	351
	Ap004	2.707	3182	351
	Ap004	2.532	3182	351
	Ap004	2.684	3182	351
	Ap005	6.686	9044	1306
	Ap018	1.129	1497	306

Table B.5. S-XANES results for lunar materials from the January and May 2019 analytical sessions.

	Scan no.	Sample	Grain	S^{6+} 2483 eV	S^{4+} 2478.9 eV	S^{2-} Broad ~2477 eV	S^{2-} Sharp 2471 eV	$S^{6+}/\Sigma S_{tot}$
January 2019	135499	15016	Ap42	6.77	0.00	2.51	0.69	**0.68**
	135500	15016	Ap42	4.70	0.00	4.22	0.87	**0.48**
	135502	15016	Ap42	4.40	0.00	4.63	1.19	**0.43**
	135504	15016	Ap42	4.68	0.00	3.07	1.28	**0.52**
	135505	15016	Ap42	5.68	0.00	0.51	3.41	**0.59**
	135506	15016	Ap42	4.66	0.00	4.97	0.82	**0.45**
	135508	15016	Ap42	7.93	0.00	5.95	0.22	**0.56**
	135509	15016	Ap42	4.48	0.00	2.93	1.28	**0.52**
	135510	15016	Ap42	3.13	0.00	5.61	1.21	**0.31**
	135512	15016	Ap42	5.94	0.00	3.14	0.00	**0.65**
	135513	15016	Ap42	3.24	0.00	4.52	1.29	**0.36**
	135515	15016	Ap42	6.45	0.00	3.36	0.00	**0.66**
	135516	15016	Ap42	3.92	0.00	4.15	0.81	**0.44**
	135518	15016	Ap42	6.94	0.00	4.13	0.21	**0.62**
	135519	15016	Ap42	6.68	0.00	0.63	1.13	**0.79**
	135520	15016	Ap42	5.47	0.00	4.36	0.00	**0.56**
	135521	15016	Ap42	6.81	0.00	4.49	0.00	**0.60**
	135522	15016	Ap42	6.55	0.00	1.87	0.00	**0.78**
	135523	15016	Ap42	5.24	0.00	2.82	1.47	**0.55**
	135524	15016	Ap42	4.34	0.00	4.68	1.22	**0.42**
	135525	15016	Ap42	6.68	0.00	1.83	1.13	**0.69**
	135526	15016	Ap42	5.26	0.00	2.77	1.21	**0.57**
	135527	15016	Ap42	4.62	0.00	4.45	1.30	**0.45**
	135634	15065	Ap007	3.30	0.00	4.83	1.68	**0.34**
	135635	15065	Ap007	3.04	0.00	6.89	0.83	**0.28**
	135636	15065	Ap007	3.78	0.00	5.87	1.01	**0.35**

Table B.5. Continued								
January 2019	136022	15065	Ap007	4.30	0.00	7.68	1.47	**0.32**
	136023	15065	Ap007	3.29	0.00	7.90	1.55	**0.26**
	136024	15065	Ap007	2.68	0.00	6.86	1.78	**0.24**
	136025	15065	Ap007	5.37	0.00	8.79	1.45	**0.34**
	136027	15065	Ap007	0.72	0.00	5.40	2.16	**0.09**
	136028	15065	Ap007	1.33	0.00	4.85	1.87	**0.16**
	136029	15065	Ap007	3.96	0.00	7.76	1.86	**0.29**
	136030	15065	Ap007	5.17	0.00	11.00	1.36	**0.30**
	136031	15065	Ap007	5.26	0.00	11.46	1.16	**0.29**
	135558	15065	Ap005b	3.45	0.00	7.40	0.00	**0.32**
	135573	15065	Ap005b	2.63	0.00	1.28	6.42	**0.25**
	135576	15065	Ap005b	2.97	0.00	3.15	3.57	**0.31**
	135578	15065	Ap005b	2.91	0.00	5.00	1.27	**0.32**
	135583	15065	Ap005b	2.44	0.00	6.59	0.76	**0.25**
	135586	15065	Ap005b	2.25	0.00	1.21	6.13	**0.23**
	135588	15065	Ap005b	2.82	0.00	6.11	0.72	**0.29**
	135589	15065	Ap005b	2.63	0.00	5.75	1.33	**0.27**
	135590	15065	Ap005b	2.87	0.00	5.88	0.77	**0.30**
	135977	15065	Ap005b	5.19	0.00	11.47	0.92	**0.30**
	135978	15065	Ap005b	7.05	0.00	12.91	0.83	**0.34**
	135980	15065	Ap005b	6.17	0.00	13.09	1.01	**0.30**
	135981	15065	Ap005b	4.39	0.00	6.78	1.56	**0.34**
	135640	15065	Ap001b	4.84	0.00	1.52	4.44	**0.45**
	135641	15065	Ap001b	4.51	0.00	6.25	0.11	**0.41**
	135643	15065	Ap001b	4.87	0.00	3.28	2.10	**0.47**
	135644	15065	Ap001b	3.94	0.00	4.71	0.77	**0.42**
	135645	15065	Ap001b	2.39	0.00	6.22	1.26	**0.24**
	135646	15065	Ap001b	2.80	0.00	6.38	1.22	**0.27**
	136007	15065	Ap001b	0.85	0.00	6.16	2.78	**0.09**

Table B.5. Continued

January 2019	136008	15065	Ap001b	1.32	0.00	7.64	2.83	**0.11**
	136009	15065	Ap001b	0.68	0.00	6.36	2.51	**0.07**
	136010	15065	Ap001b	0.41	0.00	3.17	2.47	**0.07**
	136019	15065	Ap001b	0.73	0.00	4.27	2.28	**0.10**
	135594	15065	Ap003	3.34	0.00	4.87	1.51	**0.34**
	135596	15065	Ap003	3.32	0.00	3.14	3.20	**0.34**
	135600	15065	Ap003	3.46	0.00	5.24	0.96	**0.36**
	135604	15065	Ap003	3.28	0.00	5.04	0.85	**0.36**
	135608	15065	Ap003	3.41	0.00	5.41	0.79	**0.35**
	135612	15065	Ap003	3.61	0.00	5.29	0.51	**0.38**
	135616	15065	Ap003	3.95	0.00	3.85	2.09	**0.40**
	135620	15065	Ap003	3.36	0.00	5.07	0.77	**0.37**
	135624	15065	Ap003	3.49	0.00	4.65	1.00	**0.38**
	135626	15065	Ap003	2.75	0.00	5.58	1.02	**0.29**
	135664	15058	Ap012a	3.64	0.00	6.32	0.00	**0.37**
	135666	15058	Ap012a	3.00	0.00	8.08	0.00	**0.27**
	135667	15058	Ap012a	2.99	0.00	6.72	0.00	**0.31**
	135668	15058	Ap012a	2.85	0.00	6.84	0.00	**0.29**
	135670	15058	Ap012a	3.02	0.00	6.79	0.00	**0.31**
	135671	15058	Ap012a	2.90	0.00	7.52	0.84	**0.26**
	135672	15058	Ap012a	2.56	0.00	6.54	1.09	**0.25**
	135674	15058	Ap012a	4.12	0.00	6.87	0.50	**0.36**
	135676	15058	Ap012a	3.86	0.00	3.89	1.79	**0.40**
	135677	15058	Ap012a	2.82	0.00	7.46	0.00	**0.27**
	135678	15058	Ap012a	3.02	0.00	5.53	1.38	**0.30**
	135680	15058	Ap012a	4.60	0.00	6.33	0.75	**0.39**
	135682	15058	Ap012a	4.96	0.00	6.36	0.25	**0.43**
	135686	15058	Ap016	2.42	0.00	6.68	0.00	**0.27**
	135687	15058	Ap016	4.15	0.00	6.42	0.00	**0.39**

Table B.5. Continued								
January 2019	135688	15058	Ap016	4.49	0.00	9.10	0.00	**0.33**
	135692	15058	Ap016	2.22	0.00	8.55	0.00	**0.21**
	135928	12039	Ap001_a	1.57	0.00	5.05	1.91	**0.18**
	135929	12039	Ap001_a	2.33	0.00	6.67	1.05	**0.23**
	135931	12039	Ap001_a	2.41	0.00	4.26	1.66	**0.29**
	135932	12039	Ap001_a	1.97	0.00	5.58	1.74	**0.21**
	135945	12039	Ap001_f	3.84	0.00	5.10	1.99	**0.35**
	135946	12039	Ap001_f	4.31	0.00	4.06	1.95	**0.42**
	135947	12039	Ap001_f	4.32	0.00	4.63	1.84	**0.40**
	135788	SaU 169	SOI 7	6.25	0.00	0.29	0.75	**0.86**
	135789	SaU 169	SOI 7	4.72	0.78	0.00	0.00	**0.86**
	135791	SaU 169	SOI 7	10.50	0.00	0.00	1.85	**0.85**
	135829	SaU 169	SOI 14	7.28	0.00	0.00	0.00	**1.00**
	135832	SaU 169	SOI 14	7.87	0.00	0.00	0.00	**1.00**
	135835	SaU 169	SOI 14	10.44	0.00	0.00	0.00	**1.00**
	135838	SaU 169	SOI 14	11.45	0.00	0.00	0.00	**1.00**
	135841	SaU 169	SOI 14	12.07	0.00	0.00	0.00	**1.00**
	135850	SaU 169	SOI 15	12.24	0.00	0.00	0.00	**1.00**
	135851	SaU 169	SOI 15	11.31	0.00	0.00	0.00	**1.00**
	135852	SaU 169	SOI 15	12.06	0.00	0.00	0.00	**1.00**
	135853	SaU 169	SOI 15	10.98	0.00	0.00	0.00	**1.00**
	135854	SaU 169	SOI 15	9.13	0.00	0.00	0.00	**1.00**
	135770	Symp glass	15058	0.90	0.00	7.17	2.08	**0.09**
	135771	Symp glass	15058	1.35	0.00	6.79	2.03	**0.13**
	135772	Symp glass	15058	1.26	0.00	6.74	2.04	**0.13**
	135756	Epoxy	15058	b.d.	b.d.	b.d.	b.d.	-
	135758	Epoxy	15058	b.d.	b.d.	b.d.	b.d.	-
	135741	Pyroxene	15058	0.80	0.00	7.11	2.29	**0.08**
	135742	Pyroxene	15058	0.29	0.00	7.23	2.21	**0.03**

Table B.5. Continued								
January 2019	135743	Pyroxene	15058	1.20	0.00	6.75	2.42	**0.12**
	135744	Pyroxene	15058	0.00	0.00	8.57	1.91	**0.00**
	135745	Pyroxene	15058	0.58	0.00	7.15	1.93	**0.06**
	135746	Pyroxene	15058	1.00	0.00	6.53	1.89	**0.11**
	135687	Durango	In epoxy	11.93	0.53	0.00	0.00	**0.96**
	135871	Durango	Out of epoxy	11.23	0.44	0.00	0.00	**0.96**
	135873	Durango	Out of epoxy	12.11	0.58	0.00	0.00	**0.95**
	135874	Durango	Out of epoxy	11.42	0.75	0.00	0.00	**0.94**
	135878	Durango	Out of epoxy	12.42	0.78	0.00	0.00	**0.94**
May 2019	145295	15065	Ap007	1.69	0.00	6.11	2.18	**0.17**
	145296	15065	Ap007	1.93	0.00	6.51	2.26	**0.18**
	145297	15065	Ap007	2.35	0.00	5.87	2.35	**0.22**
	145298	15065	Ap007	2.23	0.00	7.25	2.16	**0.19**
	145491	15475,127	Ap002	0.74	0.00	7.53	2.06	**0.07**
	145492	15475,127	Ap002	0.44	0.00	7.50	2.21	**0.04**
	145493	15475,127	Ap002	0.60	0.00	7.73	2.21	**0.06**
	145494	15475,127	Ap002	0.41	0.00	7.38	2.21	**0.04**
	145495	15475,127	Ap002	0.56	0.00	7.46	2.17	**0.05**
	145480	15475,127	Ap003a	1.90	0.00	12.47	1.33	**0.12**
	145485	15475,127	Ap003b	0.68	0.00	9.74	1.61	**0.06**
	145486	15475,127	Ap003b	1.22	0.00	10.85	1.66	**0.09**
	145487	15475,127	Ap003b	1.25	0.00	9.85	1.69	**0.10**
	145488	15475,127	Ap003b	1.59	0.00	10.19	1.66	**0.12**

Appendix C

C.1. Lunar apatite images

Figure C.1. Backscatter electron (BSE) images of each Apollo apatite grain analysed in this research project. There are 67 apatites from a total of 14 Apollo samples (including two different thin sections of Apollo sample 15475 (17 and 127)). The apatites are identified by a label on each image which states the Apollo sample number and the individual apatite grain name as assigned and discussed in the text of this thesis. The identification corresponds with 'sample I.D.' and 'analysis I.D.', as listed in Tables 4.1 and 5.3. Where Ap = apatite, which pinpoints the analysed apatite grain on the image. Image 14053,19_Ap005 is a secondary electron image. The apatite images of Apollo sample 10044 and images of Ap6 and Ap1 of Apollo sample 15386 are courtesy of Jessica Barnes, The Open University.

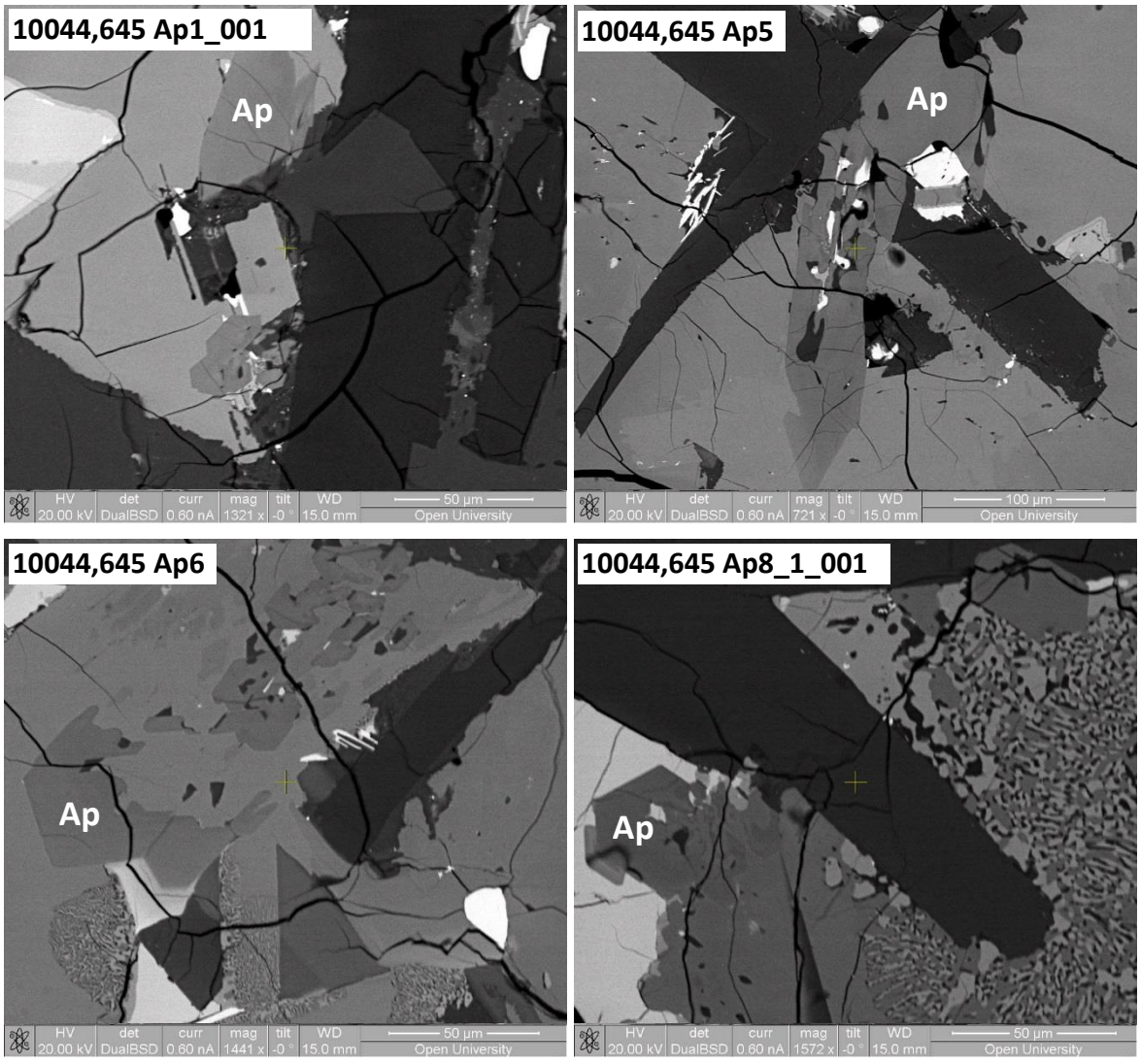

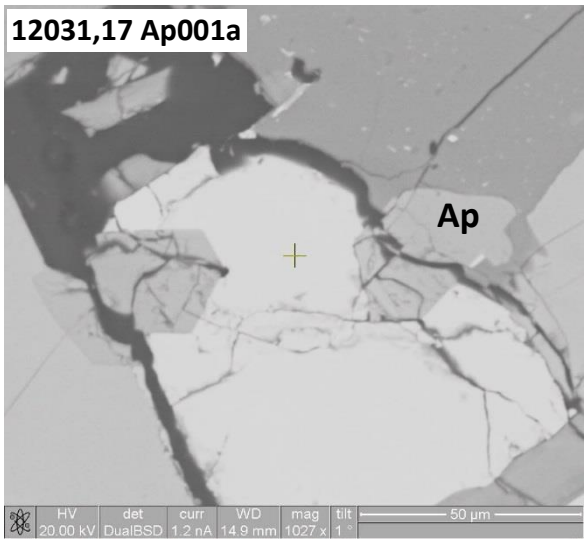
12031,17 Ap001a
Ap
HV 20.00 kV
det DualBSD
curr 1.2 nA
WD 14.9 mm
mag 1027 x
tilt 1 °
50 µm

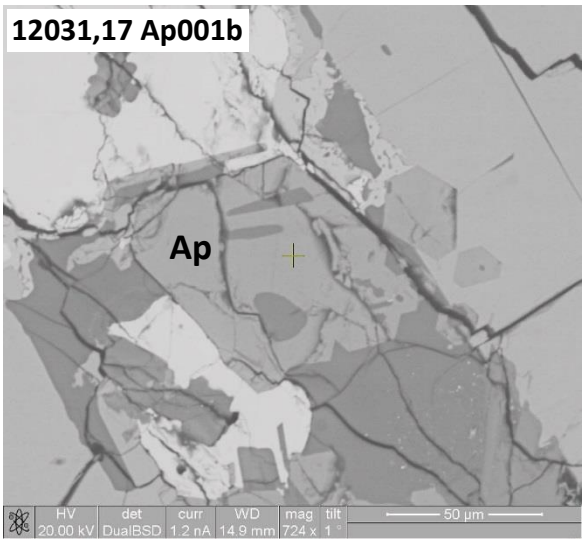
12031,17 Ap001b
Ap
HV 20.00 kV
det DualBSD
curr 1.2 nA
WD 14.9 mm
mag 724 x
tilt 1 °
50 µm

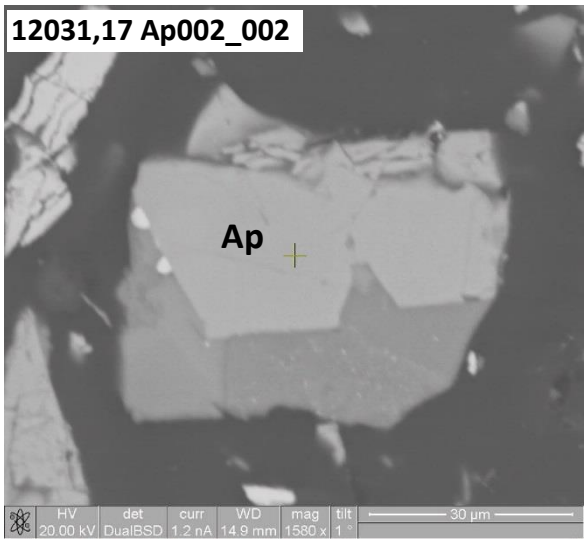
12031,17 Ap002_002
Ap
HV 20.00 kV
det DualBSD
curr 1.2 nA
WD 14.9 mm
mag 1580 x
tilt 1 °
30 µm

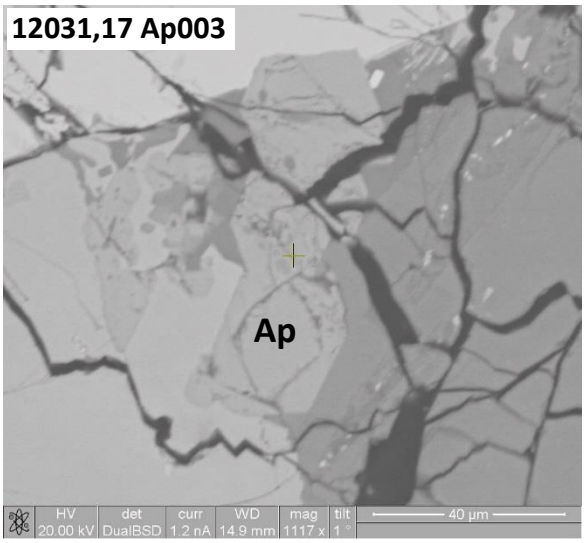
12031,17 Ap003
Ap
HV 20.00 kV
det DualBSD
curr 1.2 nA
WD 14.9 mm
mag 1117 x
tilt 1 °
40 µm

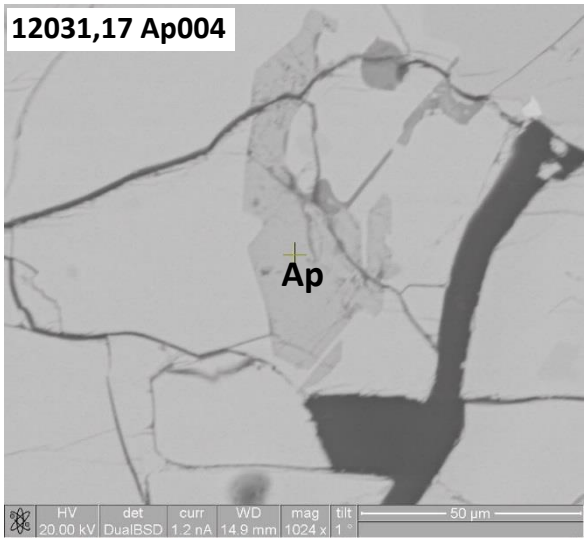
12031,17 Ap004
Ap
HV 20.00 kV
det DualBSD
curr 1.2 nA
WD 14.9 mm
mag 1024 x
tilt 1 °
50 µm

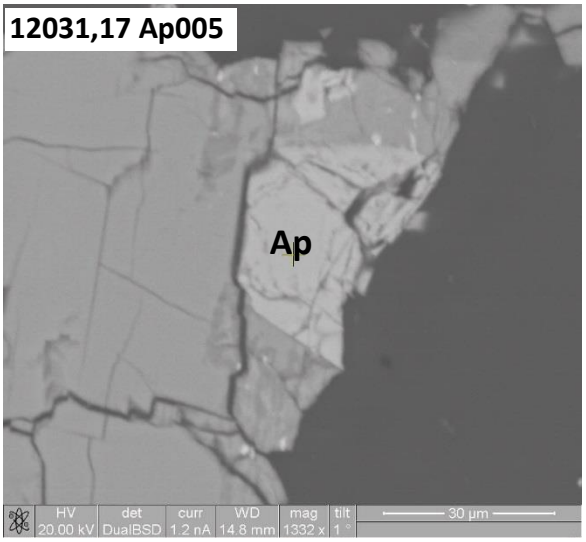
12031,17 Ap005
Ap
HV 20.00 kV
det DualBSD
curr 1.2 nA
WD 14.8 mm
mag 1332 x
tilt 1 °
30 µm

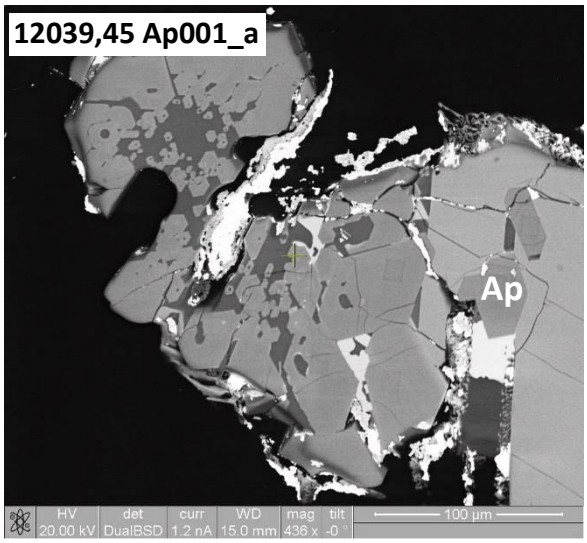
12039,45 Ap001_a
Ap
HV 20.00 kV
det DualBSD
curr 1.2 nA
WD 15.0 mm
mag 436 x
tilt -0 °
100 µm

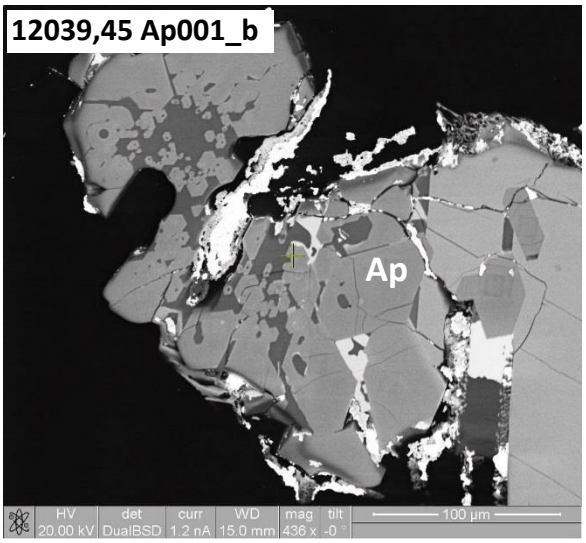
12039,45 Ap001_b
Ap
HV 20.00 kV
det DualBSD
curr 1.2 nA
WD 15.0 mm
mag 436 x
tilt -0 °
100 µm

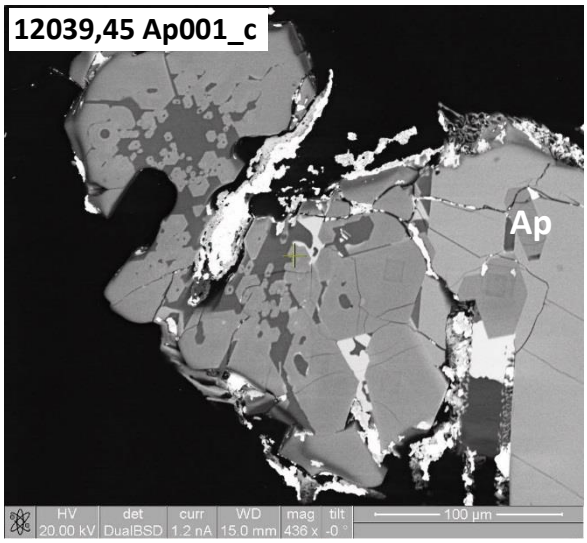
12039,45 Ap001_c
Ap
HV 20.00 kV
det DualBSD
curr 1.2 nA
WD 15.0 mm
mag 436 x
tilt -0 °
100 µm

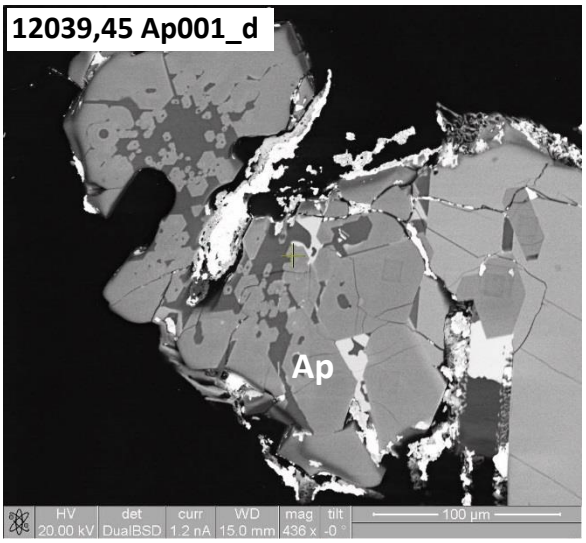
12039,45 Ap001_d
Ap
HV 20.00 kV
det DualBSD
curr 1.2 nA
WD 15.0 mm
mag 436 x
tilt -0 °
100 µm

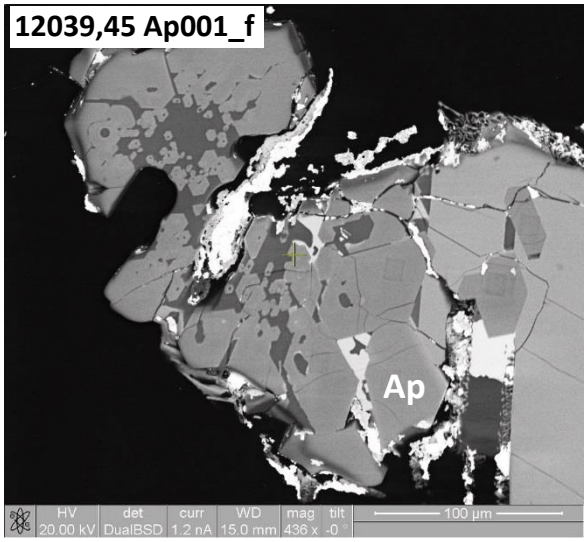
12039,45 Ap001_f
Ap
HV 20.00 kV
det DualBSD
curr 1.2 nA
WD 15.0 mm
mag 436 x
tilt -0 °
100 µm

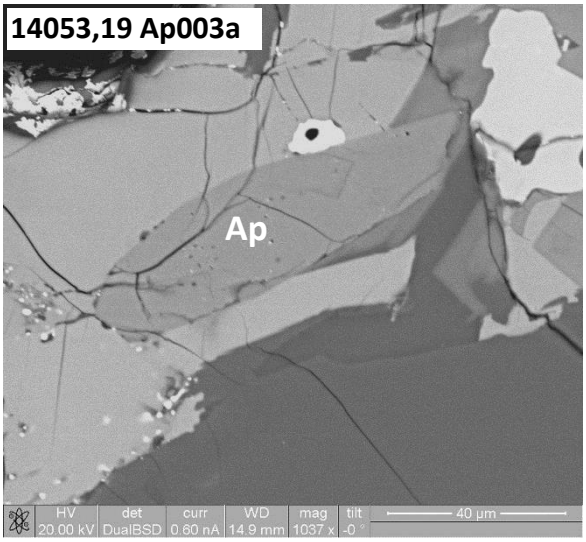
14053,19 Ap003a
Ap
HV 20.00 kV
det DualBSD
curr 0.60 nA
WD 14.9 mm
mag 1037 x
tilt -0 °
40 µm

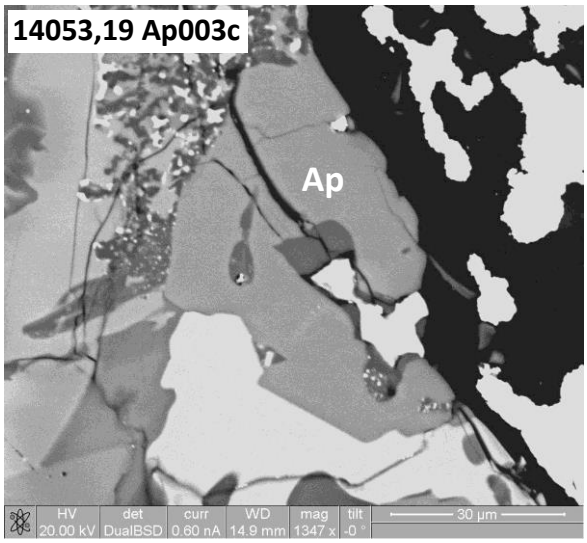
14053,19 Ap003c
Ap
HV 20.00 kV
det DualBSD
curr 0.60 nA
WD 14.9 mm
mag 1347 x
tilt -0 °
30 µm

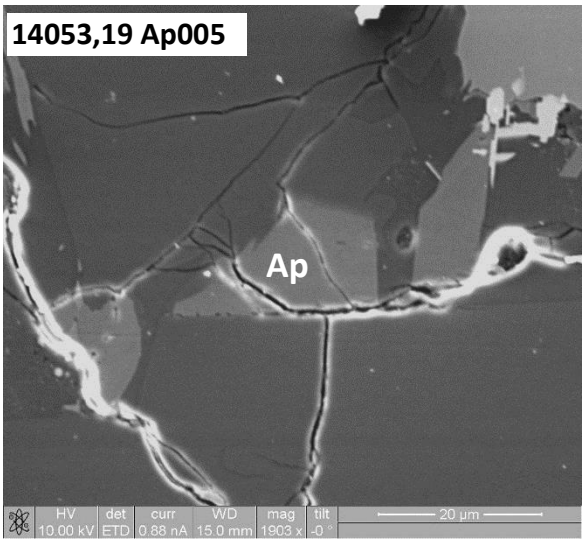
14053,19 Ap005
Ap
HV 10.00 kV
det ETD
curr 0.88 nA
WD 15.0 mm
mag 1903 x
tilt -0 °
20 µm

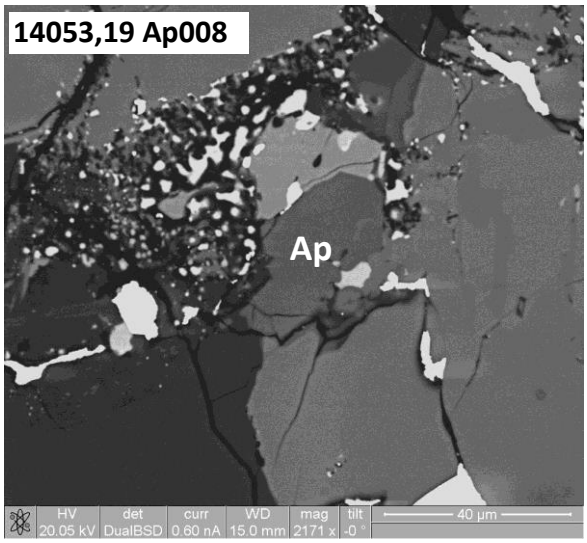
14053,19 Ap008
Ap
HV 20.05 kV
det DualBSD
curr 0.60 nA
WD 15.0 mm
mag 2171 x
tilt -0 °
40 µm

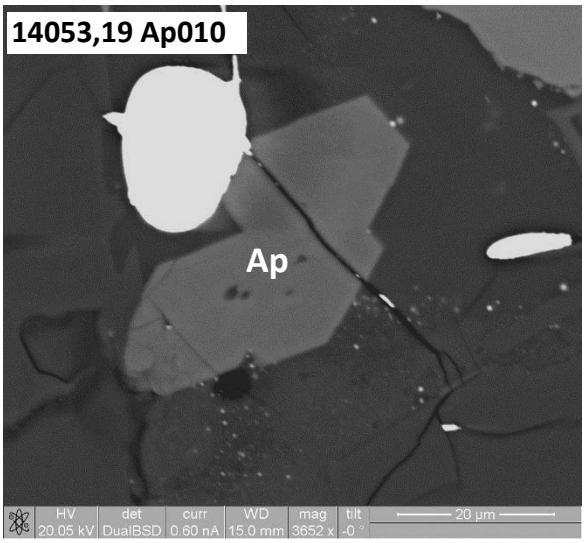
14053,19 Ap010
Ap
HV 20.05 kV
det DualBSD
curr 0.60 nA
WD 15.0 mm
mag 3652 x
tilt -0 °
20 µm

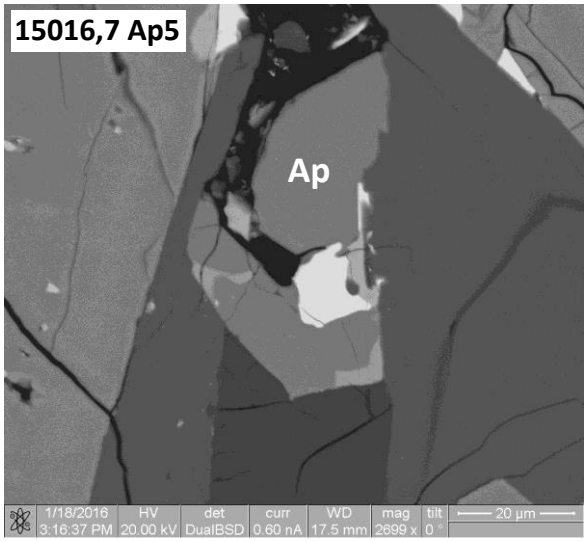
15016,7 Ap5
Ap
1/18/2016 3:16:37 PM
HV 20.00 kV
det DualBSD
curr 0.60 nA
WD 17.5 mm
mag 2699 x
tilt 0 °
20 µm

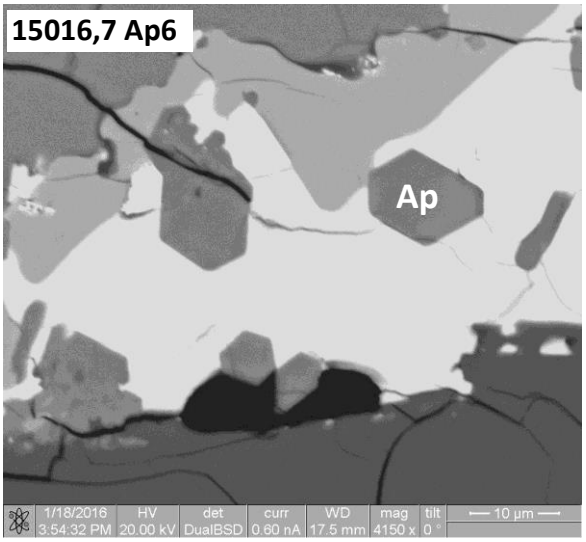
15016,7 Ap6
Ap
1/18/2016 3:54:32 PM
HV 20.00 kV
det DualBSD
curr 0.60 nA
WD 17.5 mm
mag 4150 x
tilt 0 °
10 µm

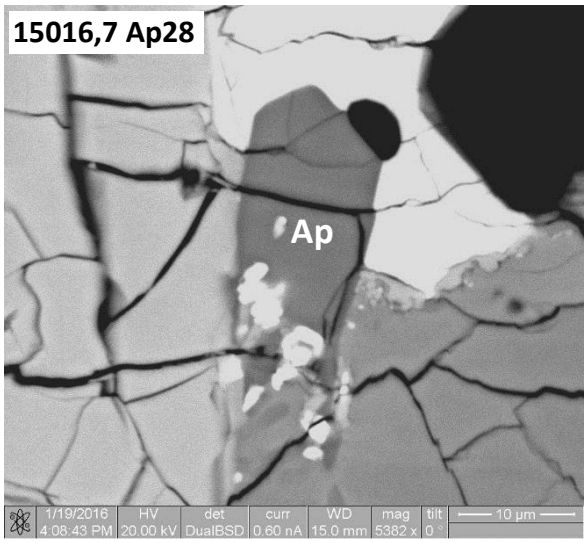
15016,7 Ap28
Ap
1/19/2016 4:08:43 PM
HV 20.00 kV
det DualBSD
curr 0.60 nA
WD 15.0 mm
mag 5382 x
tilt 0 °
10 µm

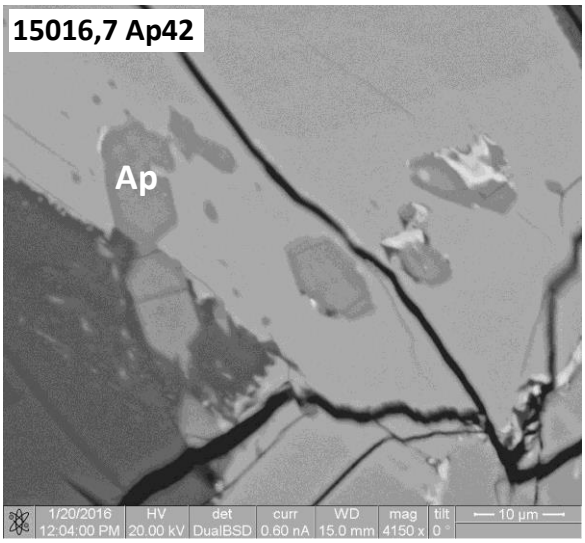
15016,7 Ap42
Ap
1/20/2016 12:04:00 PM
HV 20.00 kV
det DualBSD
curr 0.60 nA
WD 15.0 mm
mag 4150 x
tilt 0 °
10 µm

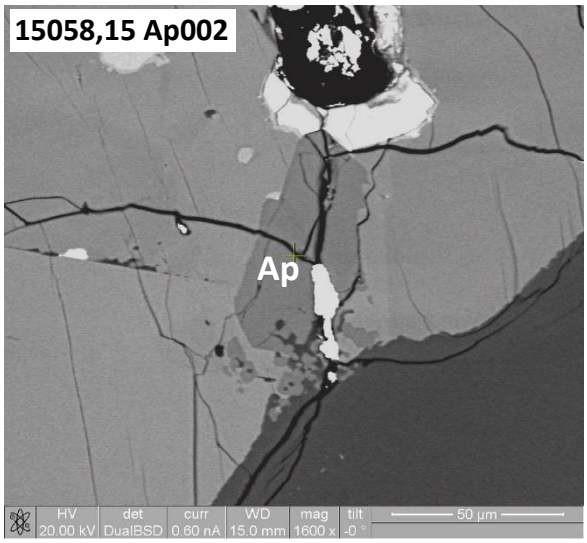
15058,15 Ap002
Ap
HV 20.00 kV
det DualBSD
curr 0.60 nA
WD 15.0 mm
mag 1600 x
tilt -0 °
50 µm

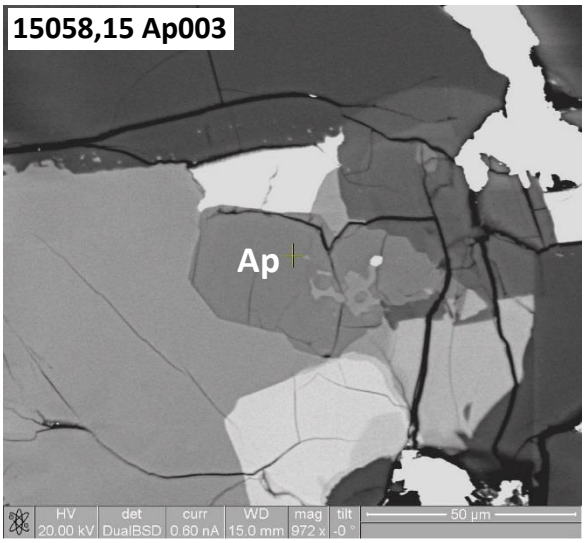
15058,15 Ap003
Ap
HV 20.00 kV
det DualBSD
curr 0.60 nA
WD 15.0 mm
mag 972 x
tilt -0 °
50 µm


15058,15 Ap007
Ap
HV 20.00 kV
det DualBSD
curr 0.60 nA
WD 15.1 mm
mag 486 x
tilt -0 °
100 µm

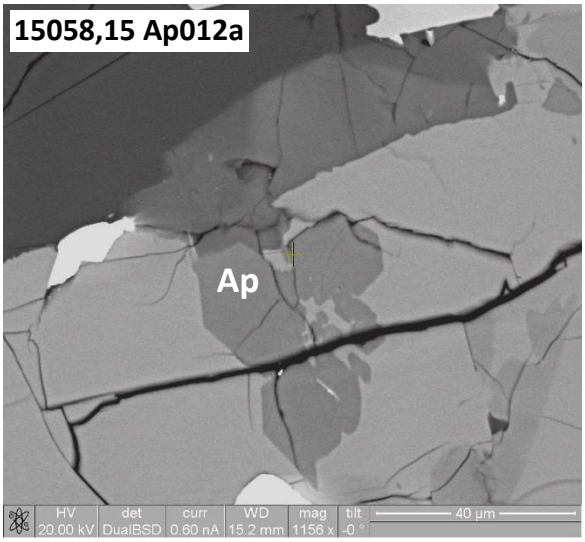
15058,15 Ap012a
Ap
HV 20.00 kV
det DualBSD
curr 0.60 nA
WD 15.2 mm
mag 1156 x
tilt -0 °
40 µm

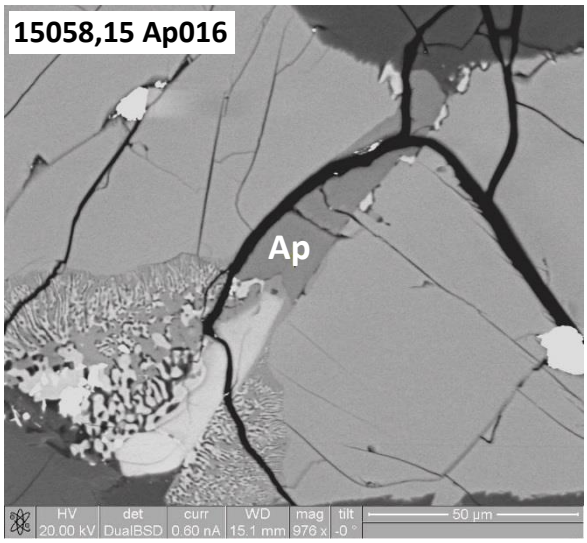
15058,15 Ap016
Ap
HV 20.00 kV
det DualBSD
curr 0.60 nA
WD 15.1 mm
mag 976 x
tilt -0 °
50 µm

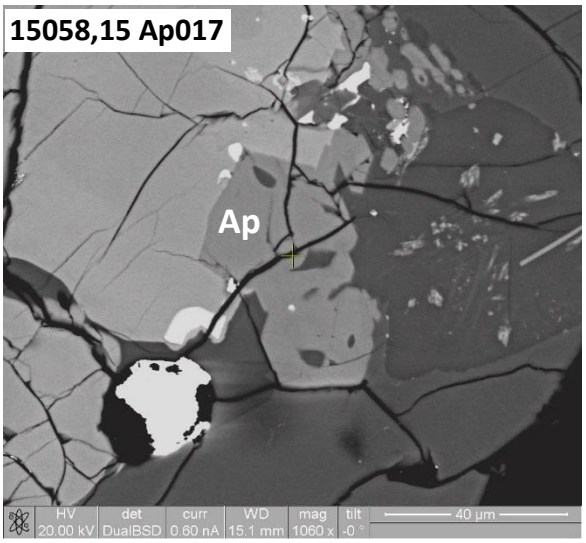
15058,15 Ap017
Ap
HV 20.00 kV
det DualBSD
curr 0.60 nA
WD 15.1 mm
mag 1060 x
tilt -0 °
40 µm

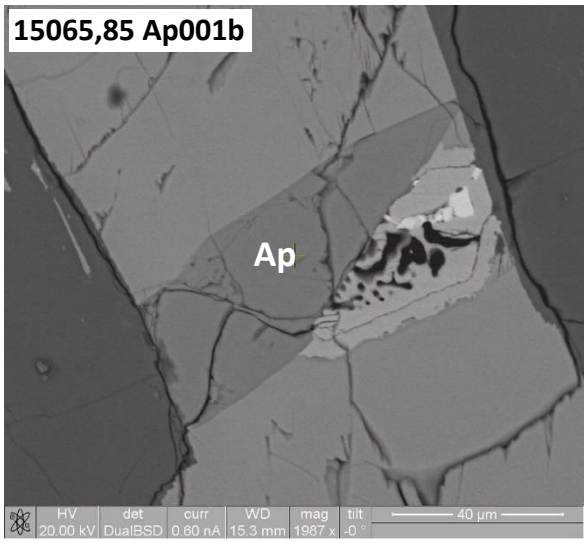
15065,85 Ap001b
Ap
HV 20.00 kV
det DualBSD
curr 0.60 nA
WD 15.3 mm
mag 1987 x
tilt -0 °
40 µm

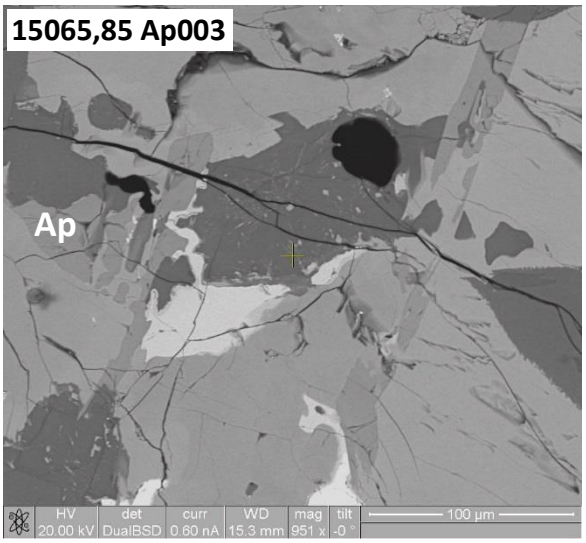
15065,85 Ap003
Ap
HV 20.00 kV
det DualBSD
curr 0.60 nA
WD 15.3 mm
mag 951 x
tilt -0 °
100 µm

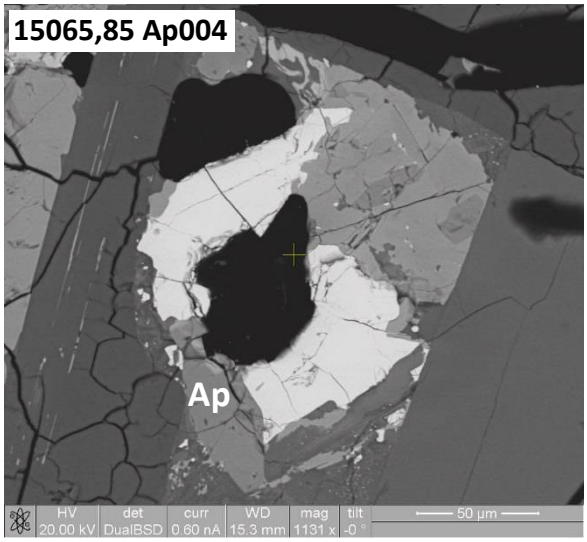
15065,85 Ap004
Ap
HV 20.00 kV
det DualBSD
curr 0.60 nA
WD 15.3 mm
mag 1131 x
tilt -0 °
50 µm

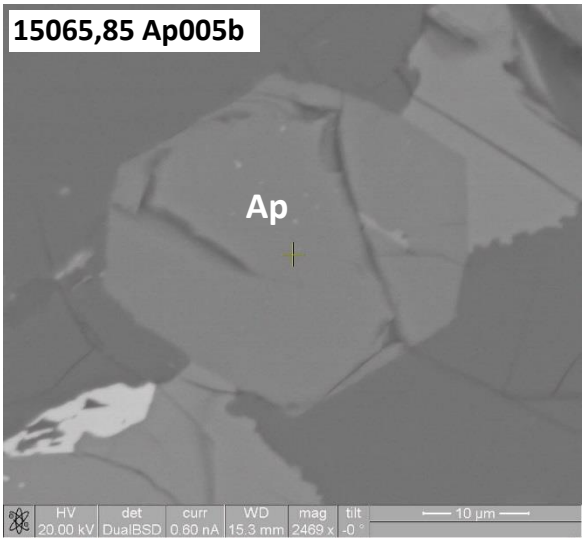
15065,85 Ap005b
Ap
HV 20.00 kV
det DualBSD
curr 0.60 nA
WD 15.3 mm
mag 2469 x
tilt -0 °
10 µm

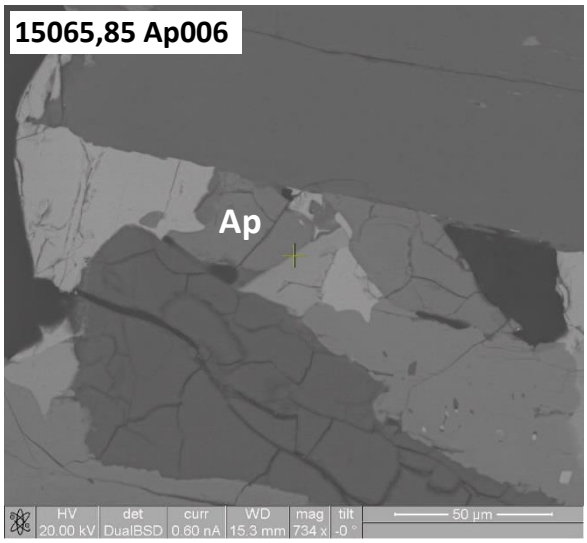
15065,85 Ap006
Ap
HV 20.00 kV
det DualBSD
curr 0.60 nA
WD 15.3 mm
mag 734 x
tilt -0 °
50 µm

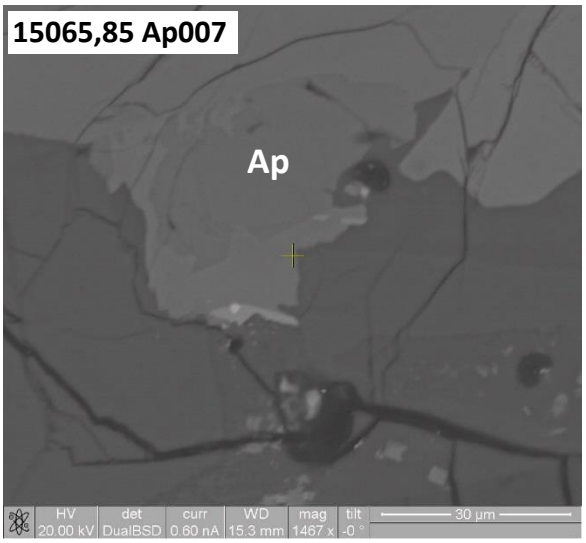
15065,85 Ap007
Ap
HV 20.00 kV
det DualBSD
curr 0.60 nA
WD 15.3 mm
mag 1467 x
tilt -0 °
30 µm

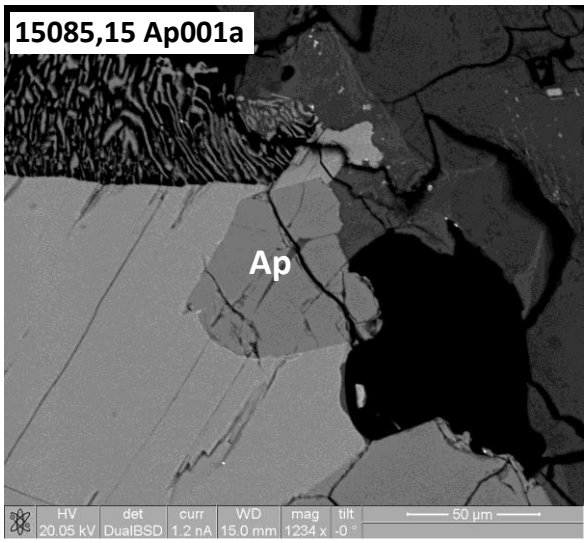
15085,15 Ap001a
Ap
HV 20.05 kV
det DualBSD
curr 1.2 nA
WD 15.0 mm
mag 1234 x
tilt -0 °
50 µm

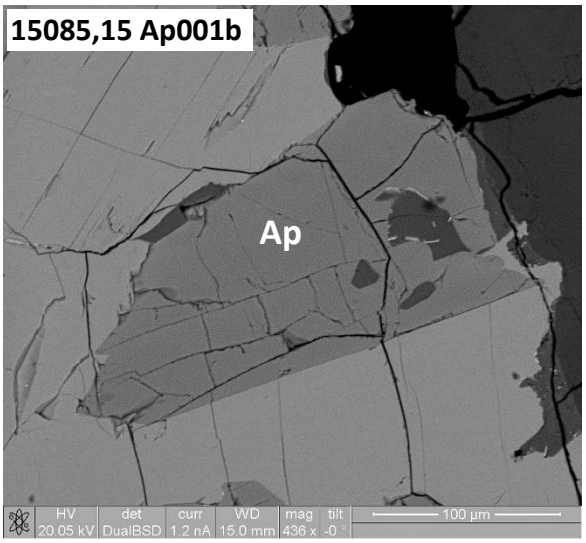
15085,15 Ap001b
Ap
HV 20.05 kV
det DualBSD
curr 1.2 nA
WD 15.0 mm
mag 436 x
tilt -0 °
100 µm

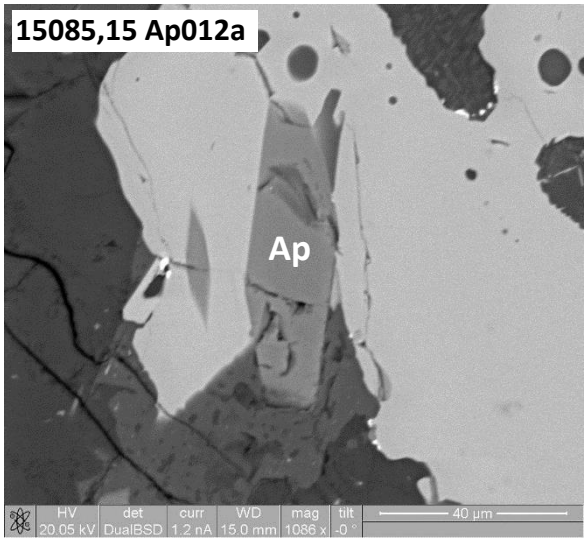
15085,15 Ap012a
Ap
HV 20.05 kV
det DualBSD
curr 1.2 nA
WD 15.0 mm
mag 1086 x
tilt -0 °
40 µm

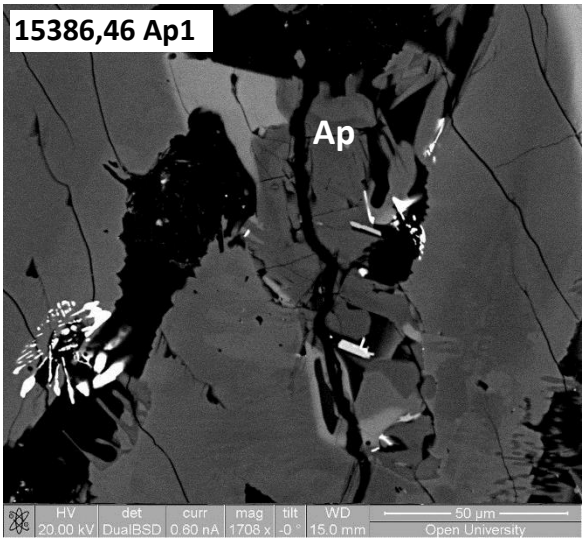
15386,46 Ap1
Ap
HV 20.00 kV
det DualBSD
curr 0.60 nA
mag 1708 x
tilt -0 °
WD 15.0 mm
50 µm
Open University

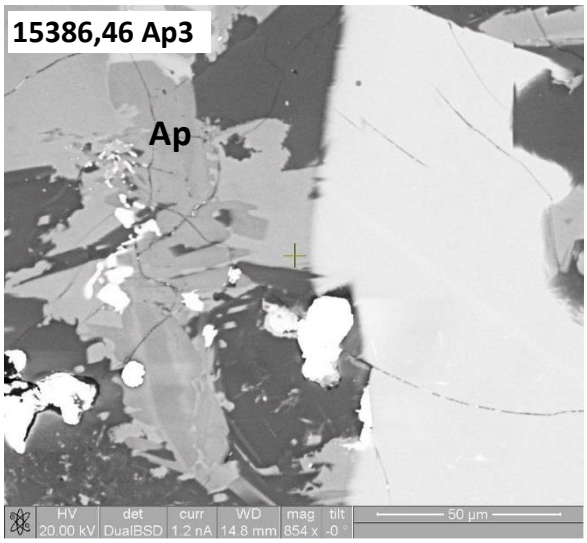
15386,46 Ap3
Ap
HV 20.00 kV
det DualBSD
curr 1.2 nA
WD 14.8 mm
mag 854 x
tilt -0 °
50 µm

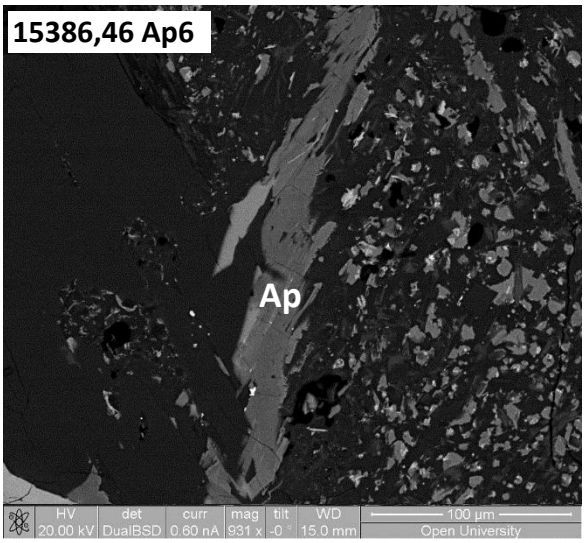
15386,46 Ap6
Ap
HV 20.00 kV
det DualBSD
curr 0.60 nA
mag 931 x
tilt -0 °
WD 15.0 mm
100 µm
Open University

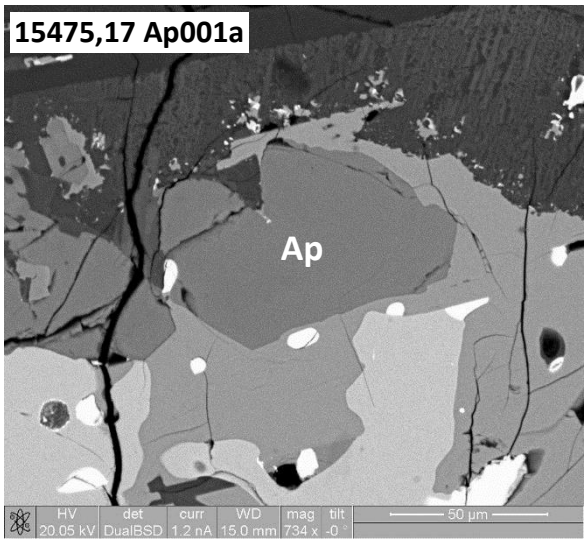
15475,17 Ap001a
Ap
HV 20.05 kV
det DualBSD
curr 1.2 nA
WD 15.0 mm
mag 734 x
tilt -0 °
50 µm

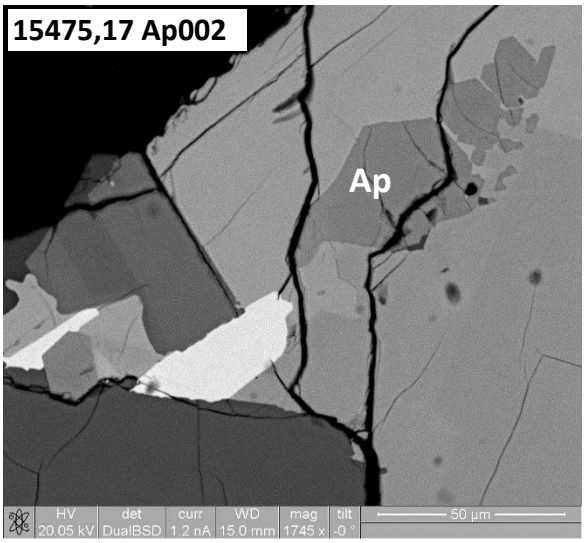
15475,17 Ap002
Ap
HV 20.05 kV
det DualBSD
curr 1.2 nA
WD 15.0 mm
mag 1745 x
tilt -0 °
50 µm

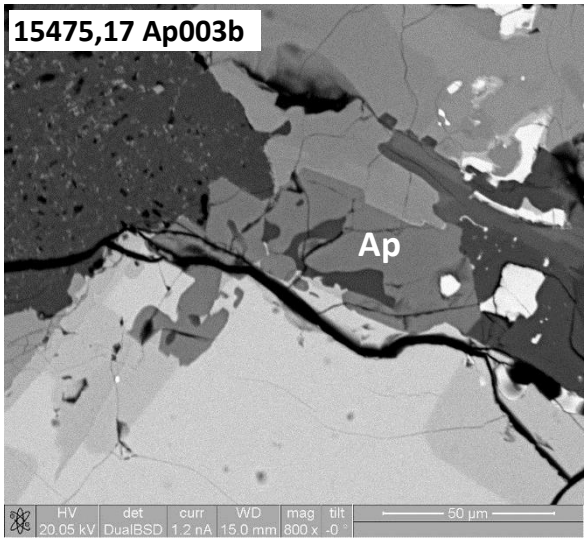
15475,17 Ap003b
Ap
HV 20.05 kV
det DualBSD
curr 1.2 nA
WD 15.0 mm
mag 800 x
tilt -0 °
50 µm

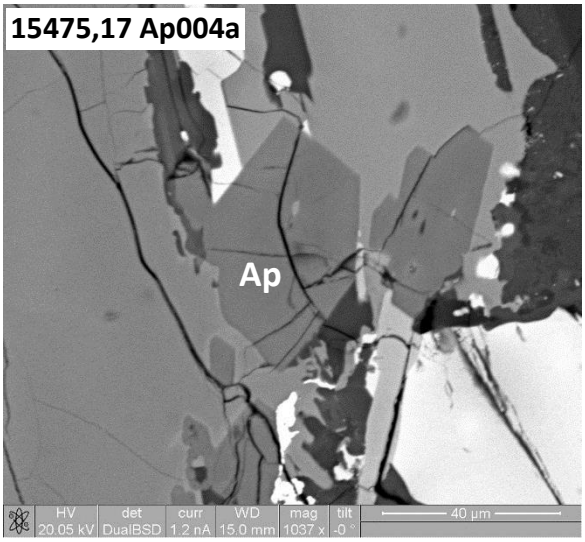
15475,17 Ap004a
Ap
HV 20.05 kV
det DualBSD
curr 1.2 nA
WD 15.0 mm
mag 1037 x
tilt -0 °
40 µm

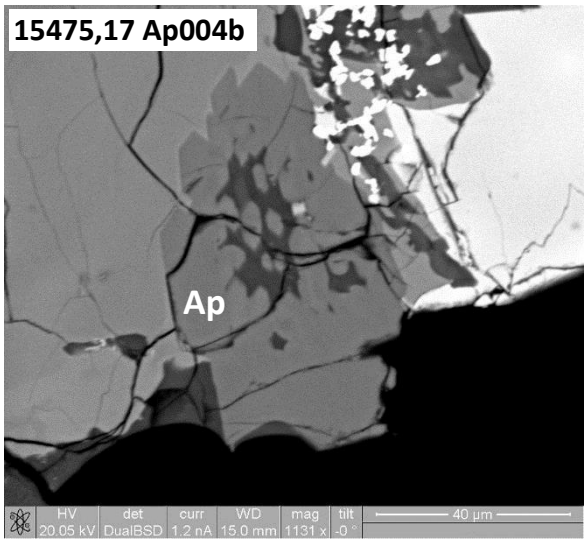
15475,17 Ap004b
Ap
HV 20.05 kV
det DualBSD
curr 1.2 nA
WD 15.0 mm
mag 1131 x
tilt -0 °
40 µm

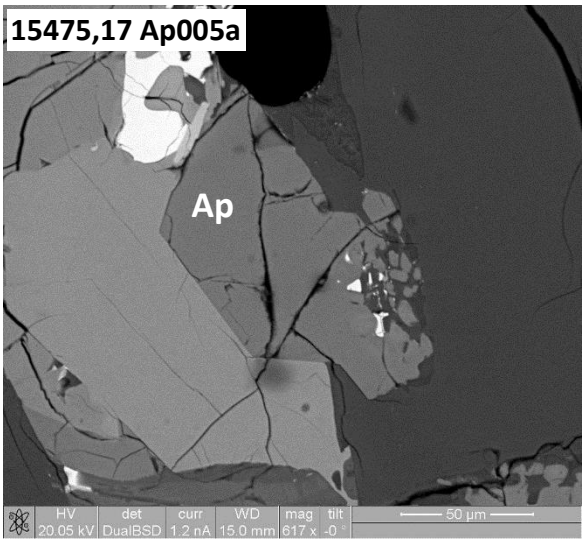
15475,17 Ap005a
Ap
HV 20.05 kV
det DualBSD
curr 1.2 nA
WD 15.0 mm
mag 617 x
tilt -0 °
50 µm

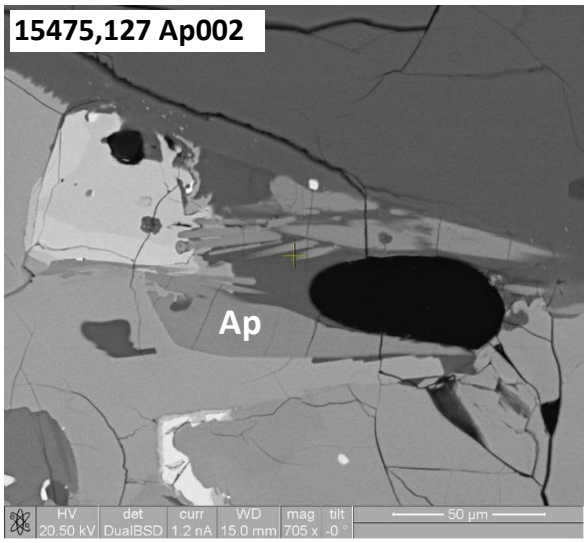
15475,127 Ap002
Ap
HV 20.50 kV
det DualBSD
curr 1.2 nA
WD 15.0 mm
mag 705 x
tilt -0 °
50 µm

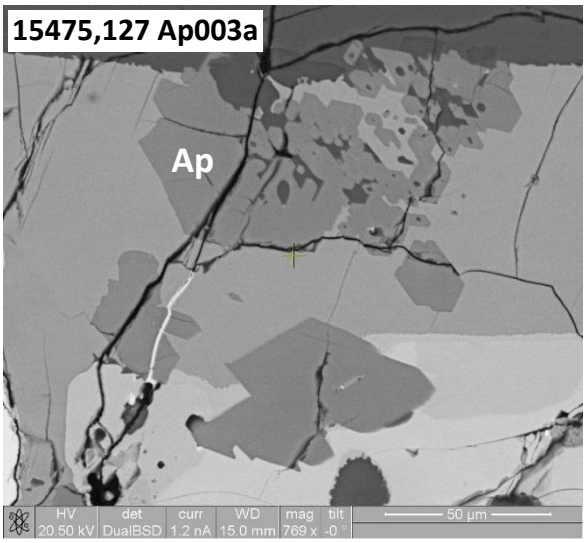
15475,127 Ap003a
Ap
HV 20.50 kV
det DualBSD
curr 1.2 nA
WD 15.0 mm
mag 769 x
tilt -0 °
50 µm

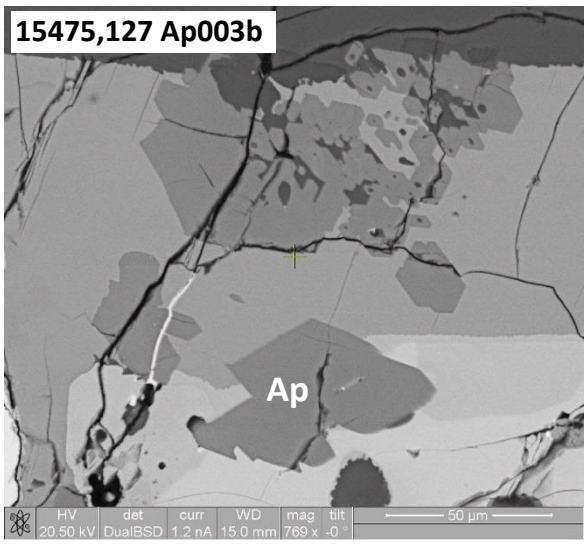
15475,127 Ap003b
Ap
HV 20.50 kV
det DualBSD
curr 1.2 nA
WD 15.0 mm
mag 769 x
tilt -0 °
50 µm

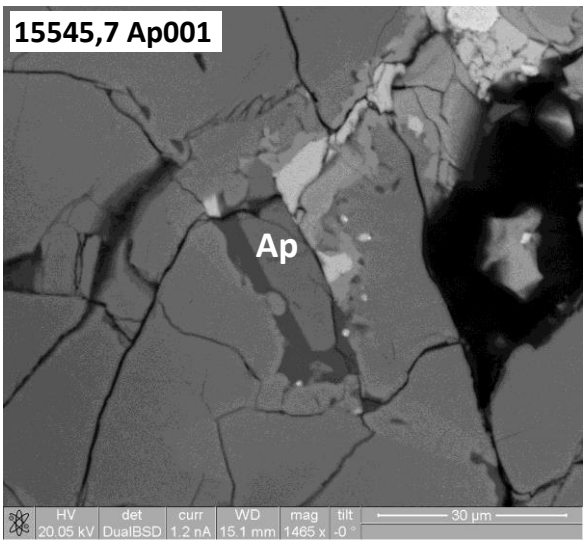
15545,7 Ap001
Ap
HV 20.05 kV
det DualBSD
curr 1.2 nA
WD 15.1 mm
mag 1465 x
tilt -0 °
30 µm

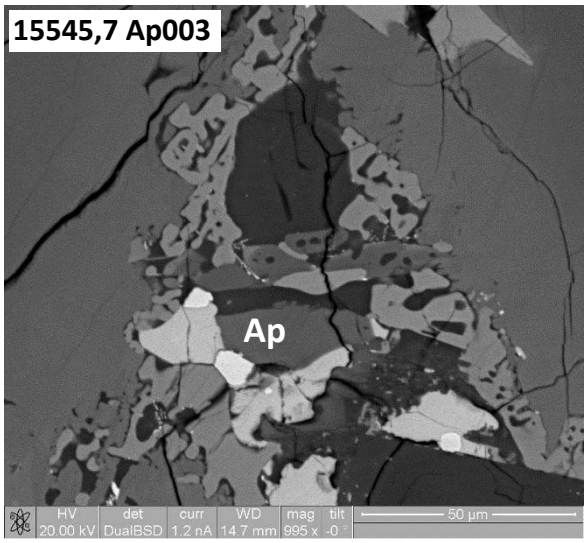
15545,7 Ap003
Ap
HV 20.00 kV
det DualBSD
curr 1.2 nA
WD 14.7 mm
mag 995 x
tilt -0 °
50 µm

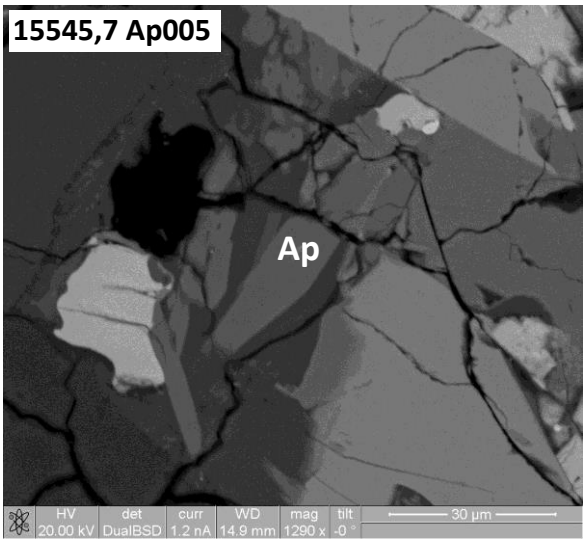
15545,7 Ap005
Ap
HV 20.00 kV
det DualBSD
curr 1.2 nA
WD 14.9 mm
mag 1290 x
tilt -0 °
30 µm

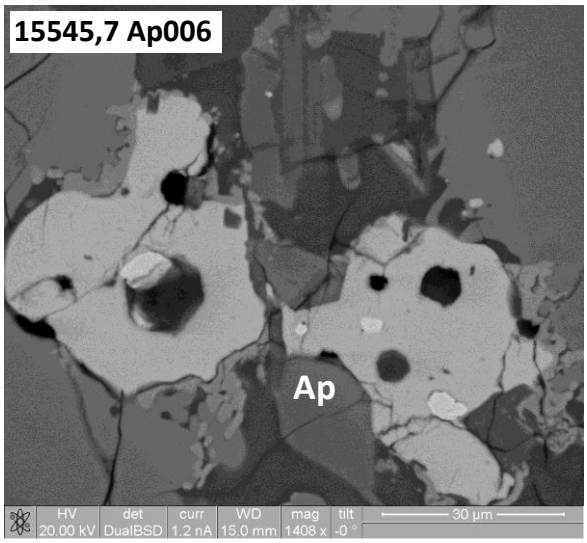
15545,7 Ap006
Ap
HV 20.00 kV
det DualBSD
curr 1.2 nA
WD 15.0 mm
mag 1408 x
tilt -0 °
30 µm

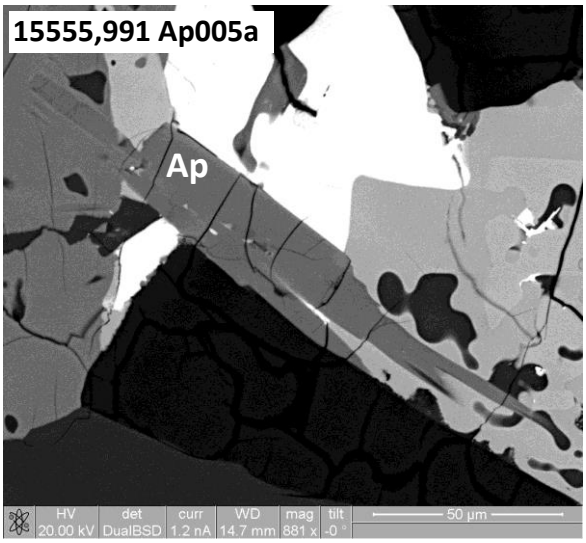
15555,991 Ap005a
Ap
HV 20.00 kV
det DualBSD
curr 1.2 nA
WD 14.7 mm
mag 881 x
tilt -0 °
50 µm

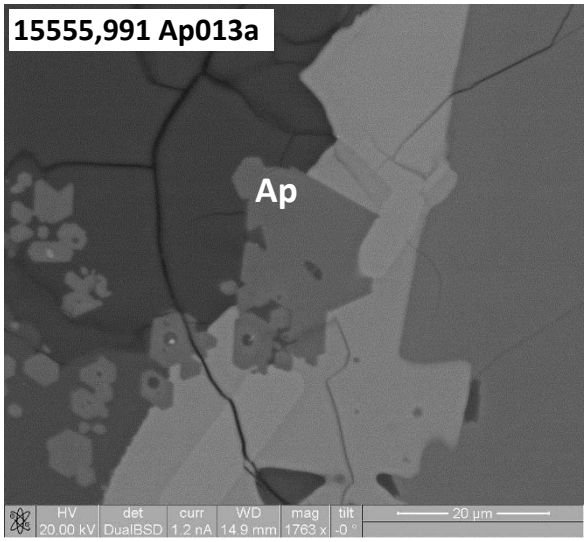
15555,991 Ap013a
Ap
HV 20.00 kV
det DualBSD
curr 1.2 nA
WD 14.9 mm
mag 1763 x
tilt -0 °
20 µm

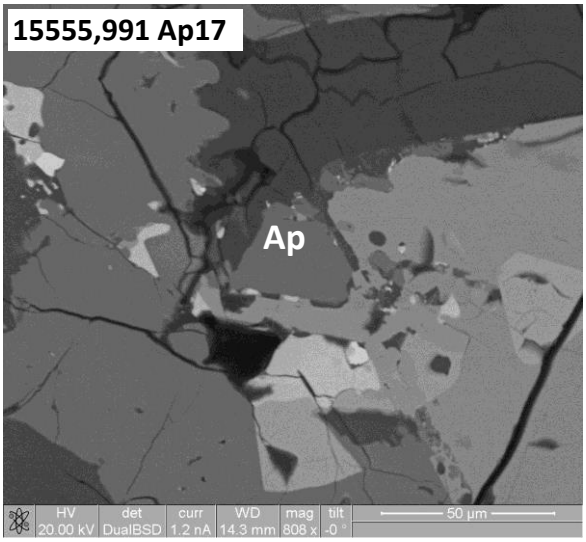
15555,991 Ap17
Ap
HV 20.00 kV
det DualBSD
curr 1.2 nA
WD 14.3 mm
mag 808 x
tilt -0 °
50 µm

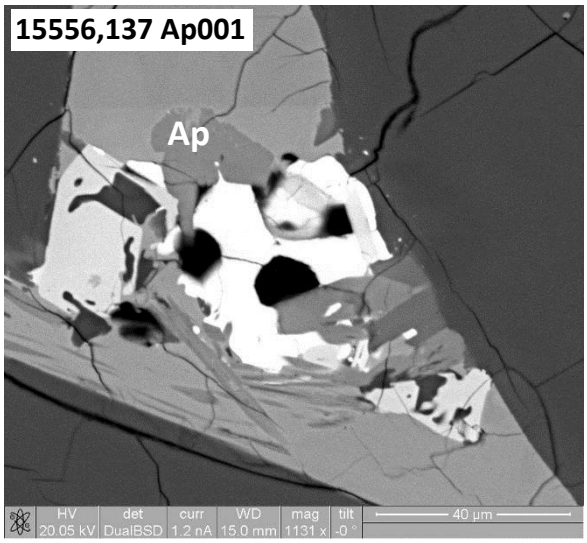
15556,137 Ap001
Ap
HV 20.05 kV
det DualBSD
curr 1.2 nA
WD 15.0 mm
mag 1131 x
tilt -0 °
40 µm

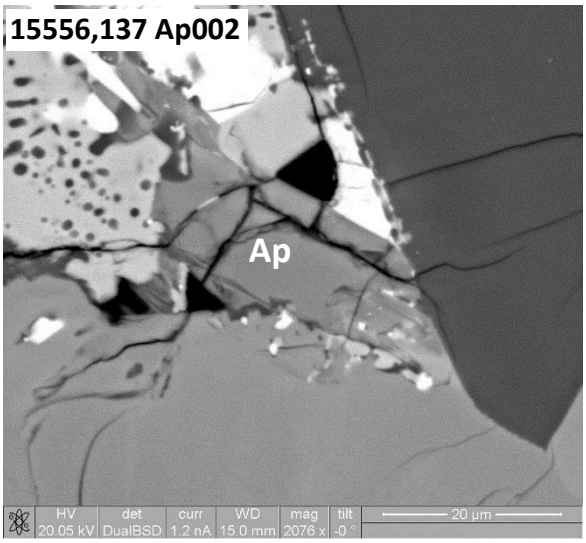
15556,137 Ap002
Ap
HV 20.05 kV
det DualBSD
curr 1.2 nA
WD 15.0 mm
mag 2076 x
tilt -0 °
20 µm

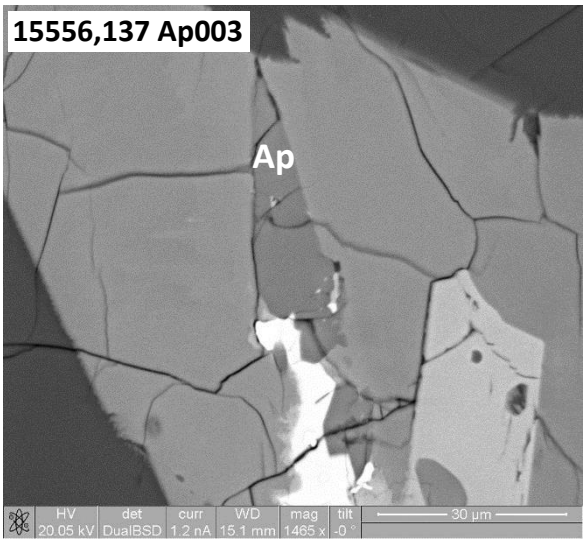
15556,137 Ap003
Ap
HV 20.05 kV
det DualBSD
curr 1.2 nA
WD 15.1 mm
mag 1465 x
tilt -0 °
30 µm

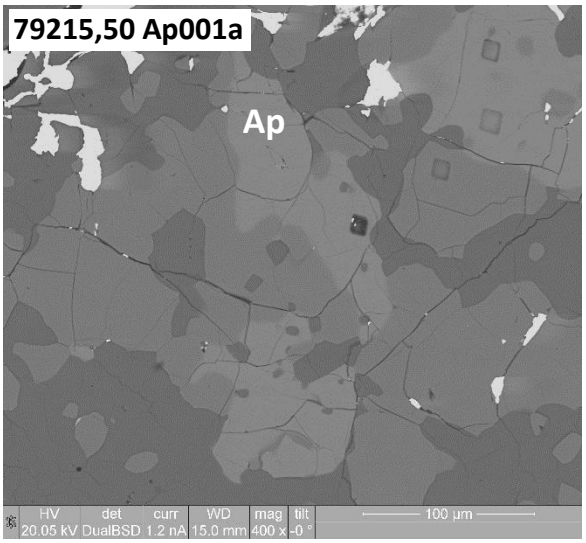
79215,50 Ap001a
Ap
HV 20.05 kV
det DualBSD
curr 1.2 nA
WD 15.0 mm
mag 400 x
tilt -0 °
100 µm

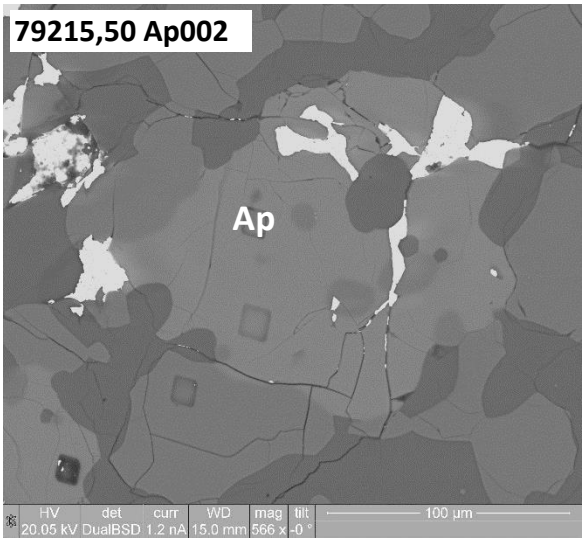
79215,50 Ap002
Ap
HV 20.05 kV
det DualBSD
curr 1.2 nA
WD 15.0 mm
mag 566 x
tilt -0 °
100 µm

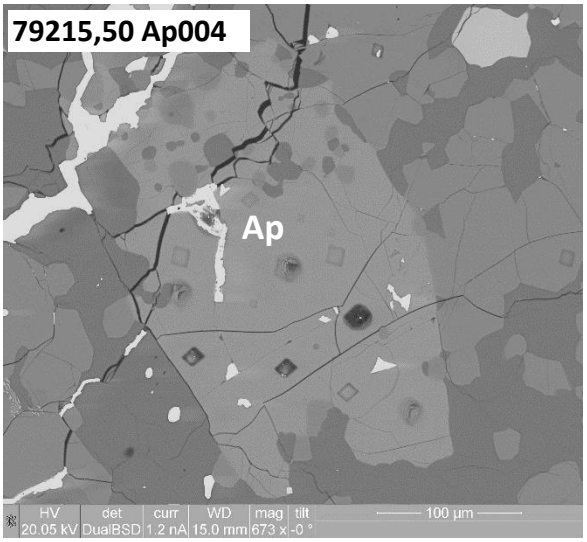
79215,50 Ap004
Ap
HV 20.05 kV
det DualBSD
curr 1.2 nA
WD 15.0 mm
mag 673 x
tilt -0 °
100 µm

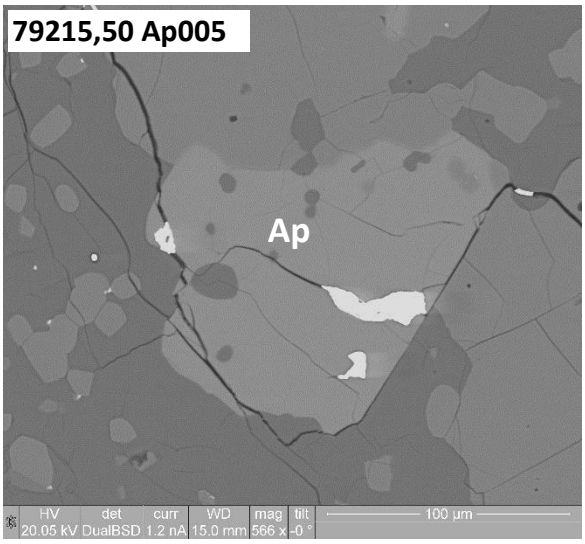
79215,50 Ap005
Ap
HV det curr WD mag tilt
20.05 kV DualBSD 1.2 nA 15.0 mm 566 x -0 °
100 µm

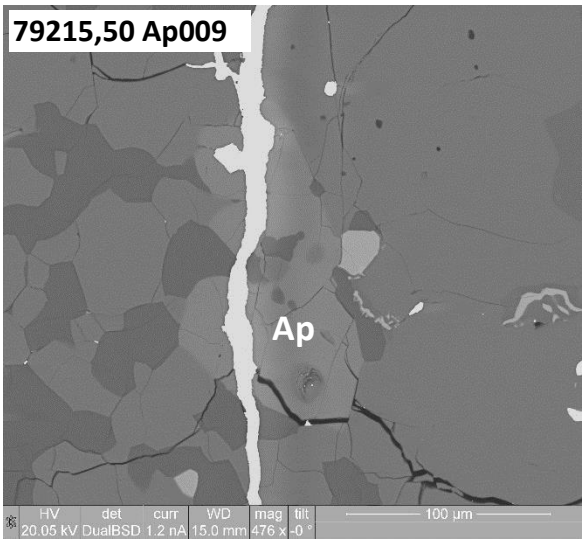
79215,50 Ap009
Ap
HV det curr WD mag tilt
20.05 kV DualBSD 1.2 nA 15.0 mm 476 x -0 °
100 µm

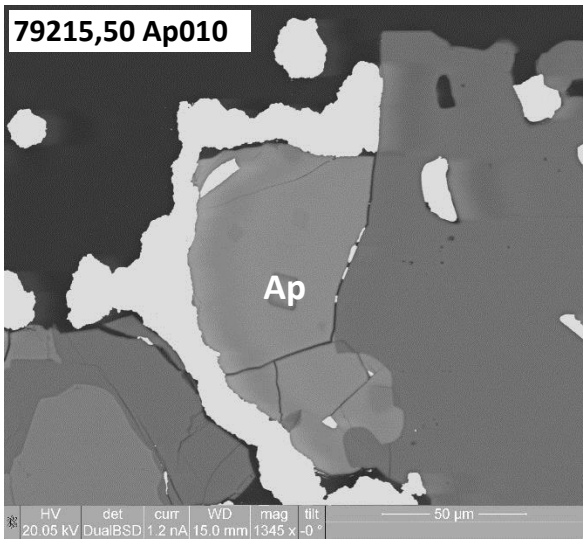
79215,50 Ap010
Ap
HV det curr WD mag tilt
20.05 kV DualBSD 1.2 nA 15.0 mm 1345 x -0 °
50 µm